CFD Modeling of Separation and Transitional Flow in Low Pressure Turbine Blades at Low Reynolds Numbers

Darius Demetri Sanders

A dissertation submitted to the faculty of the Virginia Polytechnic Institute and State University in partial fulfillment of the requirements for the degree of

Doctor of Philosophy

In

Mechanical Engineering

Walter F. O'Brien, Chair
Clinton L. Dancey
Marc D. Polanka
Douglas C. Rabe
Rolf Sondergaard
Danesh Tafti

September 28, 2009

Blacksburg, VA

Keywords: Low Pressure Turbines, Low Reynolds Number, CFD, Turbulence Modeling, Unsteady Aerodynamics

CFD Modeling of Separation and Transitional Flow in Low Pressure Turbine Blades at Low Reynolds Numbers

By

Darius Demetri Sanders

Dr. Walter F. O'Brien, Chair

Mechanical Engineering

(**ABSTRACT**)

There is increasing interest in design methods and performance prediction for turbine engines operating at low Reynolds numbers. In this regime, boundary layer separation may be more likely to occur in the turbine flow passages. For accurate CFD predictions of the flow, correct modeling of laminar-turbulent boundary layer transition is essential to capture the details of the flow. To investigate possible improvements in model fidelity, both two-dimensional and three-dimensional CFD models were created for the flow over several low pressure turbine blade designs. A new three-equation eddy-viscosity type turbulent transitional flow model originally developed by Walters and Leylek was employed for the current RANS CFD calculations. Flows over three low pressure turbine blade airfoils with different aerodynamic characteristics were simulated over a Reynolds number range of 15,000-100,000, and predictions were compared to experiments. The turbulent transitional flow model sensitivity to inlet turbulent flow parameters showed a dependence on free-stream turbulence intensity and turbulent length scale. Using the total pressure loss coefficient as a measurement of aerodynamic performance, the Walters and Leylek transitional flow model produced adequate prediction of the Reynolds number performance in the Lightly Loaded blade. Furthermore, the correct qualitative flow response to separated shear layers was observed for the Highly Loaded blade. The vortex shedding produced by the separated flow was largely two-dimensional with small spanwise variations in the separation region. The blade loading and separation location was sufficiently predicted for the Aft-Loaded L1A blade flowfield. Investigations of the unsteady flowfield of the Aft-Loaded L1A blade showed the shear layer produced a large separation region on the suction surface. This separation region was located more downstream and significantly reduced in size when impinged upon by the upstream wakes, thus improving the aerodynamic performance consistent with experiments. For all cases investigated, the Walters and Leylek transitional flow model was judged to be sufficient for understanding the separation and transition characteristics, and superior to other widely-used turbulence models in accuracy of describing the details of the transitional and separated flow. This research characterized and assessed a new model for low Reynolds number turbine aerodynamic flow prediction and design improvement.

Acknowledgements

Table of Contents

CFD Modeling of Separation and Transitional Flow in
Low Pressure Turbine Blades at Low Reynolds Numbers

CFD Modeling of Separation and Transitional Flow in
Low Pressure Turbine Blades at Low Reynolds Numbers

List of Figures

CFD Modeling of Separation and Transitional Flow in
Low Pressure Turbine Blades at Low Reynolds Numbers

CFD Modeling of Separation and Transitional Flow in
Low Pressure Turbine Blades at Low Reynolds Numbers

CFD Modeling of Separation and Transitional Flow in
Low Pressure Turbine Blades at Low Reynolds Numbers

List of Tables

Nomenclature

A	=	amplitude
b	=	wake width
c	=	phase speed
c_f	=	friction coefficient
C_P	=	pressure coefficient
C_x	=	axial chord
d	=	wall distance
D	=	cylinder diameter, kinetic energy near-wall dissipation
$E(\kappa)$	=	energy spectrum density
f_{shed}	=	vortex shedding frequency
f_{resol}	=	frequency resolution
F	=	nondimensional frequency
H	=	shape factor
k	=	turbulent kinetic energy
$\hat{k}$	=	unit vector in the z-direction
K_t	=	acceleration parameter
l_m	=	integral turbulent length scale
N	=	amplification factor, wave number
N_{avg}	=	averaging interval
n	=	distance normal from the wall
P	=	pressure; production term
q	=	dynamic pressure
q'	=	instability quantity
R	=	bypass transition production term
$\mathfrak{R}_\tau$	=	autocorrelation function
R_{NAT}	=	natural transition production term
Re	=	Reynolds number
Re_Θ	=	Reynolds number based on momentum thickness
s	=	pitch

CFD Modeling of Separation and Transitional Flow in
Low Pressure Turbine Blades at Low Reynolds Numbers

St	=	Strouhal number
T	=	time interval
t	=	time
t_{step}	=	time-step
$TPLC$	=	total pressure loss coefficient
$TLPC_{int}$=		integrated total pressure loss coefficient
Tu	=	freestream turbulence intensity
u	=	freestream velocity magnitude
u^+	=	law of the wall
$\bar{u}$	=	mean velocity
u'	=	streamwise fluctuation
$\hat{u}$	=	nondimensional Reynolds stress
u^+	=	nondimensional velocity
u_p	=	peak velocity deficit
u_{turb}	=	friction velocity
v	=	Kolmogorov velocity scale
$\vec{W}$	=	relative velocity vector
w	=	relative velocity
x	=	directional component
y^+	=	nondimensional wall distance
Z_w	=	Zwiefel blade force coefficient
α	=	wave number, spatial growth rate, absolute flow angle
α_T	=	turbulent diffusivity
β	=	wave number, relative flow angle
γ	=	intermittency function
δ	=	boundary layer thickness
δ^*	=	boundary layer displacement thickness
δ_{ij}	=	Kronecker delta
ε	=	dissipation per unit mass
Θ	=	boundary layer momentum thickness
θ	=	angle
θ_{sep}	=	momentum thickness at separtion

CFD Modeling of Separation and Transitional Flow in
Low Pressure Turbine Blades at Low Reynolds Numbers

κ	=	turbulent scales
λ	=	dimensionless momentum thickness
λ_{eff}	=	effective length scale
λ_T	=	Tayler microscale
η	=	Kolmogorov length scale
ϕ	=	complex disturbance stream function
μ	=	molecular viscosity
μ_t	=	turbulent viscosity
ν	=	kinematic viscosity
ρ	=	density
τ	=	Kolmogorov time scale
τ_{ij}	=	Reynolds stress tensor
τ_w	=	wall shear stress
ω	=	angular frequency, specific dissipation rate
Ω	=	vorticity

Subscripts

0	=	total
c	=	cylinder
i,j	=	indices
in	=	inlet
L	=	laminar
out	=	outlet
tur	=	turbulent

CFD Modeling of Separation and Transitional Flow in
Low Pressure Turbine Blades at Low Reynolds Numbers

CHAPTER ONE

1. Introduction

The range and endurance of turbine-powered aircraft cruising at high altitude is limited by multiple factors, including the operational efficiency of the low pressure turbine (LPT). As aircraft elevation is increased, the operational Reynolds number decreases due to the change in density. The Reynolds number for turbomachinery is defined by the equation

$$\mathrm{Re} = \frac{\rho U C_x}{\mu} \tag{1.1}$$

where C_x is the axial chord length and U is the inlet velocity. It is important to improve the low Reynolds number performance to achieve increased efficiency, reduced fuel consumption, increased range, and longer loiter at high altitudes.

Low Reynolds numbers promote the presence of laminar and transitional flow boundary layers on the suction surface of the LPT blades. Also, the desire to use high-lift LPT blade airfoil designs in order to decrease the total blade count thus, reducing weight and cost of turbomachinery designs. These high-lift LPT blade airfoil designs promotes the increase in the region of adverse pressure gradients located on the aft portion of the blade may cause the laminar flow boundary layer to separate from the surface. Also, the region of the boundary layer that undergoes laminar-turbulent boundary layer transition may increase. Current LPT blades suffer a dramatic increase in losses with decreasing Reynolds number, and this is usually due to the effects of separation [1]. Loss in efficiency due to the aerodynamic losses from boundary layer separation results in a loss in engine efficiency, which reduces the aircraft range and maximum altitude.

CFD Modeling of Separation and Transitional Flow in
Low Pressure Turbine Blades at Low Reynolds Numbers

Chapter 1. Introduction

As a result, there is a need for improved prediction methods for separation and transitional flow using Computational Fluid Dynamics (CFD) for turbomachinery designs. With recent advances in numerical techniques and increased computational resources, CFD is being widely applied to further advance turbomachinery designs. Accurate prediction of aerodynamic losses due to separation and laminar-to-turbulent transitional flow is required for CFD to continue to play an integral role in the design process particularly for optimization. More advanced numerical methods are needed in order to properly resolve the complicated flow physics associated with low Reynolds number flows. The characterization of CFD models using experimental measurements is necessary for further advancement for both numerical methods and physical models. These CFD models can be used to gain more insight to the flow features that are difficult to measure. Yet, these numerical model cannot be so complex that they require excessive amounts of computing power and lengthy simulation times when applied to complicated geometries such as three-dimensional multistage rotating turbomachinery designs. The ideal CFD method is a balance between increased fidelity for accurate modeling of complicated flow physics associated with low Reynolds number effects, increased accuracy over a wide range Reynolds numbers, and yet effective enough to be applied to complex geometries without being too computationally expensive.

The recent development of an improved transition and turbulence model by Walters and Leylek [2] appears to offer the possibility of improved accuracy for low Reynolds number LPT flow predictions using the Reynolds-Averaged Navier-Stokes (RANS) CFD method. It is the purpose of this dissertation to test and evaluate CFD models incorporating the Walters and Leylek [2] model against a number of available benchmark experiments, and to compare experiments results with other widely used turbulence models. The emphasis in this study is on

CFD Modeling of Separation and Transitional Flow in
Low Pressure Turbine Blades at Low Reynolds Numbers

low Reynolds number turbine flows, but it is hoped that the results will be of general use in expanding the validated knowledge base for prediction of transitional flows in turbomachinery.

1.1   Research Program Goals

The goals associated with this research program are as follows:

1. Provide a baseline methodology using LPT cascade models to investigate low Reynolds number aerodynamic effects

    (a) Understand the impact of applying RANS turbulence models to the prediction of separation and transitional flow

    (b) Evaluate the prediction capability of RANS turbulence models within the Ansys® Fluent CFD software

        (i) Choose the best RANS turbulence model based on the criteria of modeling the correct aerodynamic flow physics and the successful prediction of the aerodynamic losses at low Reynolds numbers

    (c) Understand the influence of the inlet turbulent boundary conditions on the prediction capability using the chosen turbulence model

2. Apply the developed methodology to LPT blade airfoils with different pressure loading characteristics

    (a) Show the ability to predict laminar flow separation and laminar-to-turbulent transitional flow

    (b) Predict the resulting total pressure loss from these aerodynamic flow effects

    (c) Characterize predictions for each blade airfoil using experimental cascade database

3. Demonstrate the ability of the new methodology to predict unsteady flowfield of an advanced cascade model with upstream wake generators

CFD Modeling of Separation and Transitional Flow in
Low Pressure Turbine Blades at Low Reynolds Numbers

Chapter 1. Introduction

The ability to predict the performance of LPT blades subjected to high altitude conditions is important to turbine engine designers. This research will apply a new methodology based on an existing prediction method that can effectively predict aerodynamic flows of LPT blade airfoils at high altitude conditions. This study will investigate the low Reynolds numbers flow effects associated with high altitude conditions on LPT cascade geometries. For accurate CFD predictions, correct modeling of laminar-turbulent boundary layer transition and flow separation is essential to capture the details of the flow. It will be determined if the new methodology is capable of providing the improved prediction of low Reynolds number effects for more complex geometries expected for future advanced multistage LPT's for turbine engines. This research will contribute a characterized model for low Reynolds number turbine performance prediction and design improvement.

1.2 Low Pressure Turbine Aerodynamic Flow Effects

The flows found within low pressure turbines are highly unsteady. Each blade row generates flow non-uniformities due to viscous and potential effects that propagate to the adjacent blade rows. Potential effects originate from unsteady variations in the pressure field that propagate both upstream and downstream. There are three types of viscous effects that can occur within the blade passages. The boundary layer along the surface of the airfoils begins as laminar at the leading edge and transition to turbulence can be initiated depending on the main flow conditions, and flow separation can occur due to low Reynolds inlet conditions.

Wakes are created due to the difference in the velocity in the viscous layers emerging from the pressure and suction surfaces at the blade trailing edge. A reduction in the total pressure occurs due to the wake region and increases the aerodynamic losses within the blade row. Boundary layer transition is affected by these passing wakes. As these wakes travel

CFD Modeling of Separation and Transitional Flow in
Low Pressure Turbine Blades at Low Reynolds Numbers

downstream, the region on the blade affected by the wake quickly shifts from transitional flow to turbulent flow and then returns to transitional flow after the wake has passed [3]. Figure 1.2 shows the global effect of the stator wake as it is distorted by the downstream rotor and mitigated across the blade passage. Because of the velocity deficit in the wake, the inlet flow angle to the rotor is changed. The wake is sheared and stretched into a V-shaped segment due to the different velocity field existing within the blade passage. The pressure forces are observed to be driving the low momentum fluid within the wake from the pressure side toward the suction side [4].
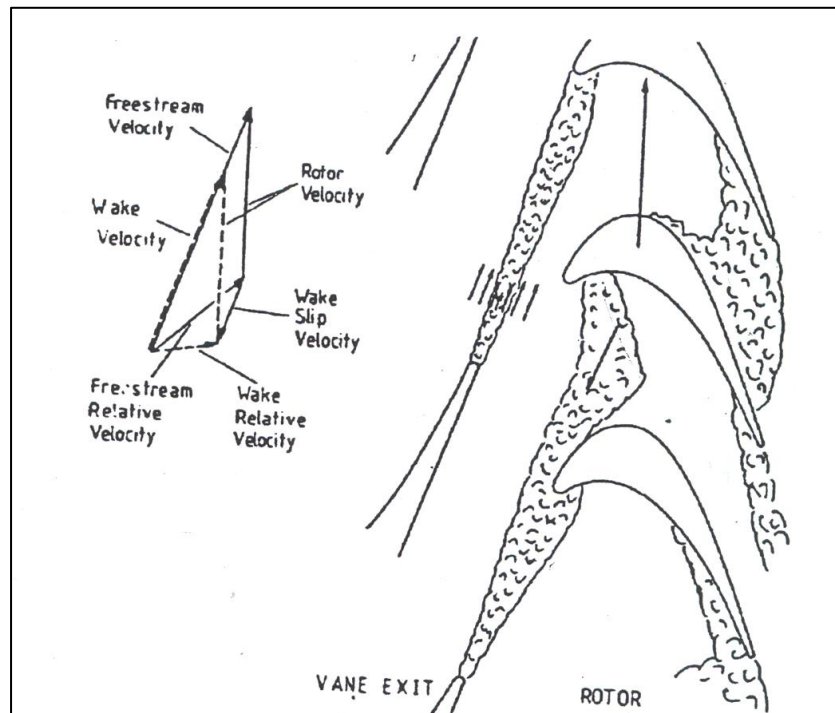
Figure 1.1. Illustration of passing wake behavior across a rotor blade row [5]

Within the passage, boundary layers on the end-walls caused by the incoming flow produces vortical structures called secondary flows. They are generated within the vicinity where the blade leading edge and the end-wall meet. Figure 1.2 shows the two types of vortical structures, a passage vortex formed from the pressure side and counter vortex formed on the suction surface. Both these vortices can interact and become more complex. The resulting total

CFD Modeling of Separation and Transitional Flow in
Low Pressure Turbine Blades at Low Reynolds Numbers

pressure loss from these secondary flows can be another source of aerodynamic loss and cause a reduction in stage efficiency.

As discussed previously, low pressure turbine flows at low inlet Reynolds numbers are dominated by the increase of the laminar-to-turbulent transition region and laminar flow separation within the boundary layer. The flow physics involved with these effects are very complex. A complete understanding of the flow physics involved in low Reynolds number effects is necessary in order to formulate accurate numerical models. To establish the basis for the findings reported in this dissertation, the following sections present fundamental topics involving laminar flow separation, laminar-to-turbulent transition, and turbulent flows.
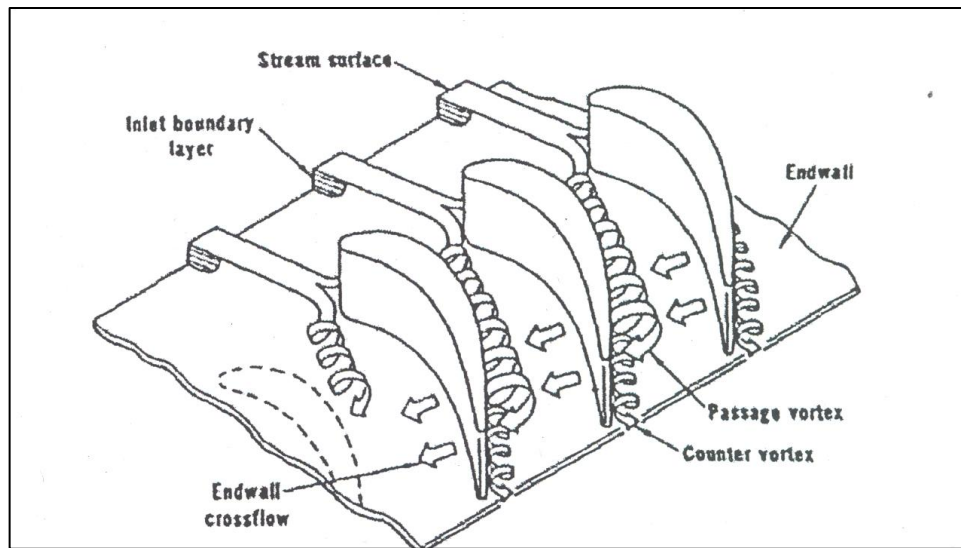
Figure 1.2. Endwall flow within a turbine blade passage [6]

1.2.1 Laminar Flow Boundary Layers

The following summary of classical flow concepts associated with laminar, transitional, turbulent and separating boundary layers is provided for completeness, and to support the discussions of results presented from the CFD modeling. The reader familiar with these

concepts may wish to move directly to Section 1.3, CFD Methods of Predicting Low Reynolds Number Effects in LPT Blades

When fluid flow moves over an object at a velocity U, the presence of viscosity causes the fluid to adhere to the surface of the body. Fluid velocity on the surface is zero following the accepted assumptions of a "no-slip" boundary. The fluid forms a boundary layer on the body surface where viscous effects are significant. The viscous effects within the boundary layer cause a velocity gradient and the velocity profile of the fluid particles found in the boundary layer begins to distort. The fluid velocity increases with distance from the surface of the body. The boundary layer has a finite thickness, defined as the distance from the body surface at which the fluid velocity is approximately 99% of the freestream velocity. Figure 1.3(a) shows a typical boundary layer profile having a thickness δ.
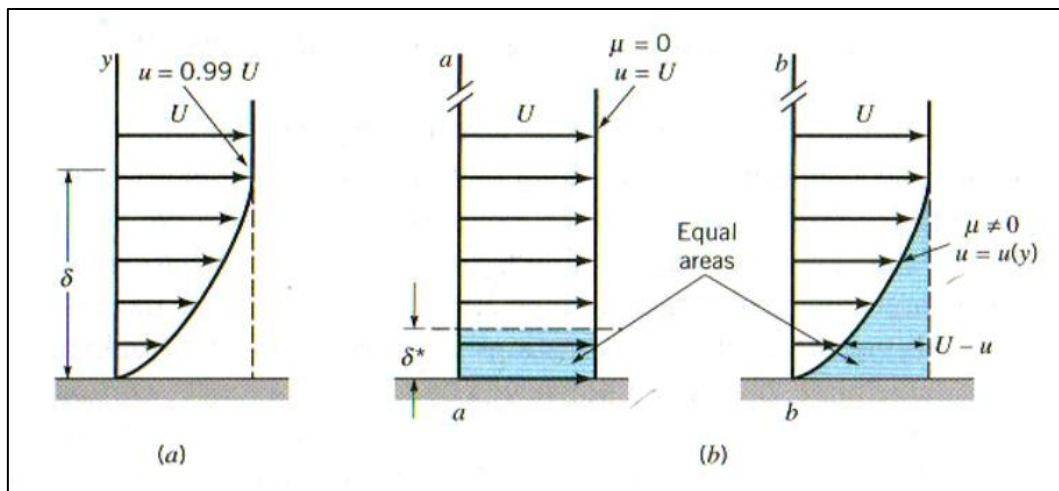
Figure 1.3. Diagram of typical boundary profile (a) and description of displacement thickness (b) [7]

The structure of the boundary layer within the viscous region is mainly dependent on the Reynolds number. The Reynolds number is defined as the ratio of inertia forces to viscous forces. If the Reynolds number is large enough, viscous effects are only important in the

CFD Modeling of Separation and Transitional Flow in
Low Pressure Turbine Blades at Low Reynolds Numbers

boundary layer. Outside the boundary layer, the gradients are relatively small and the flow behaves as if it were inviscid. The simplest case is the development of the boundary layer on a flat plate as shown in Figure 1.4. The Reynolds number based on distance x on the plate is defined as

$$\mathrm{Re}_x = \frac{\rho U x}{\mu} \tag{1.2}$$
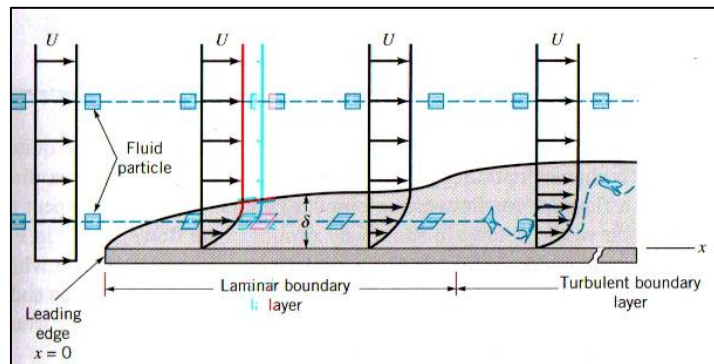
Figure 1.4. Diagram of laminar and turbulent boundary layer flow over a flat plate [7]

At the leading edge, the plate is assumed to have a negligible effect on the fluid flow ahead of it. A laminar flow boundary layer forms starting at the plate leading edge.. Laminar flow is defined as the type of flow in which fluid particles move along a well defined path or streamline. These streamlines are well defined and the fluid particles move in adjacent layers gliding smoothly over each other. The shear stress, τ_w, in a laminar fluid is defined as

$$\tau_w = \mu \frac{\partial U}{\partial n} \tag{1.3}$$

where μ is the laminar coefficient for viscosity which depends on the composition of the fluid and n is the direction normal to the direction of the shear stress. The relation is defined as *Stokes' law* and fluids that obey this law are defined as *Newtonian*.

Chapter 1. Introduction

In general for a flow past objects other than a flat plate the pressure gradient within the freestream is not uniform. The pressure gradient will vary depended on the shape of the body. The component of the pressure gradient in the streamwise direction is variable, although normal to the flow the pressure gradient is assumed negligibly small. The characteristics of the flow are highly dependent on the pressure gradient effects found within the boundary layer.
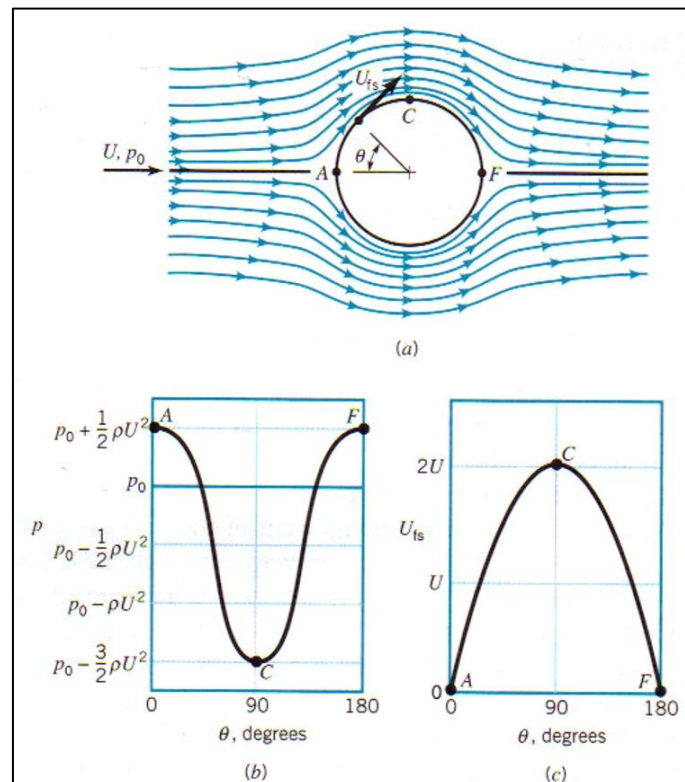
Figure 1.5. Inviscid flow past a cylinder (a) pressure distribution (b) and freestream velocity (c) on the cylinder surface [7]

For example, for a flow at inlet velocity U and static pressure P past a circular cylinder of diameter D, if the flow were inviscid, the Reynolds number would be infinite. The streamlines would be symmetrical as shown in Figure 1.5(a). The velocity and static pressure variation would be as shown in Figure 1.5(b) and Figure 1.5(c) and described with the following equations based on the potential flow method

CFD Modeling of Separation and Transitional Flow in
Low Pressure Turbine Blades at Low Reynolds Numbers

$$P_c = P + \frac{1}{2}\rho U^2(1 - 4\sin^2\theta) \tag{1.4}$$

$$U_c = 2U\sin(\theta) \tag{1.5}$$

The pressure is a maximum at the stagnation point at front and back of the cylinder. The maximum freestream velocity, U_c, would be at the top and bottom of the cylinder. Figure 1.5 shows from $\theta = 0$ to $\theta = 90°$ the pressure decreases in the direction of the flow along front half of the cylinder and is called favorable pressure gradient. At the rear half of the cylinder, the pressure increases in the direction of the flow, producing an adverse pressure gradient. There is exchange between kinetic and potential energy, but there are no energy losses.

Considering viscous effects, the fluid within the boundary layer experiences a loss in energy as it flows along the cylinder surface. This loss of energy means the fluid particle does not have enough energy to travel from the front to the rear of cylinder as the inviscid case. The fluids flows against the adverse pressure gradient as far as it can until the boundary layer separates from the cylinder surface. At the separation point, the velocity gradient and shear stress, τ, at the wall are zero. From applying the momentum equation at the wall, where $u = v = 0$:

$$\left.\frac{\partial \tau}{\partial y}\right|_{wall} = \mu\left.\frac{\partial^2 u}{\partial y^2}\right|_{wall} = -\rho U\frac{dU}{dx} = \frac{dP}{dx} \tag{1.6}$$

$$\left.\frac{\partial^2 u}{\partial y^2}\right| = \frac{1}{\mu}\frac{dP}{dx} \tag{1.7}$$

the second derivative of the velocity is positive at the wall in an adverse gradient and yet must be negative at the outer boundary layer ($y = \delta$) to merge with the mainstream flow, $U(x)$. The second derivative must pass, a point of inflection (PI) for any boundary layer undergoing an adverse pressure gradient. Figure 1.6 shows the effect of pressure gradients on the boundary layer

profile. In the favorable pressure gradient (Fig 1.6(a)), the boundary layer velocity profile is smooth with no point of inflection, so there cannot be any separation. Laminar profiles of this type will be resistant to transition to turbulence. In a zero pressure gradient flow (Fig 1.6(b)), the point of inflection is at the wall with no separation and the flow will eventually transition to turbulent. As the strength of the adverse pressure gradient increases (Fig 1.6(c)), the point of inflection will be located within the boundary layer and it will increase its distance from the wall. Figure 1.6(d) shows the critical situation where shear stress is exactly zero ($\tau_w = 0$), and is defined as the separation point. A increase in the adverse pressure gradient will cause backflow as in Figure 1.6(e).
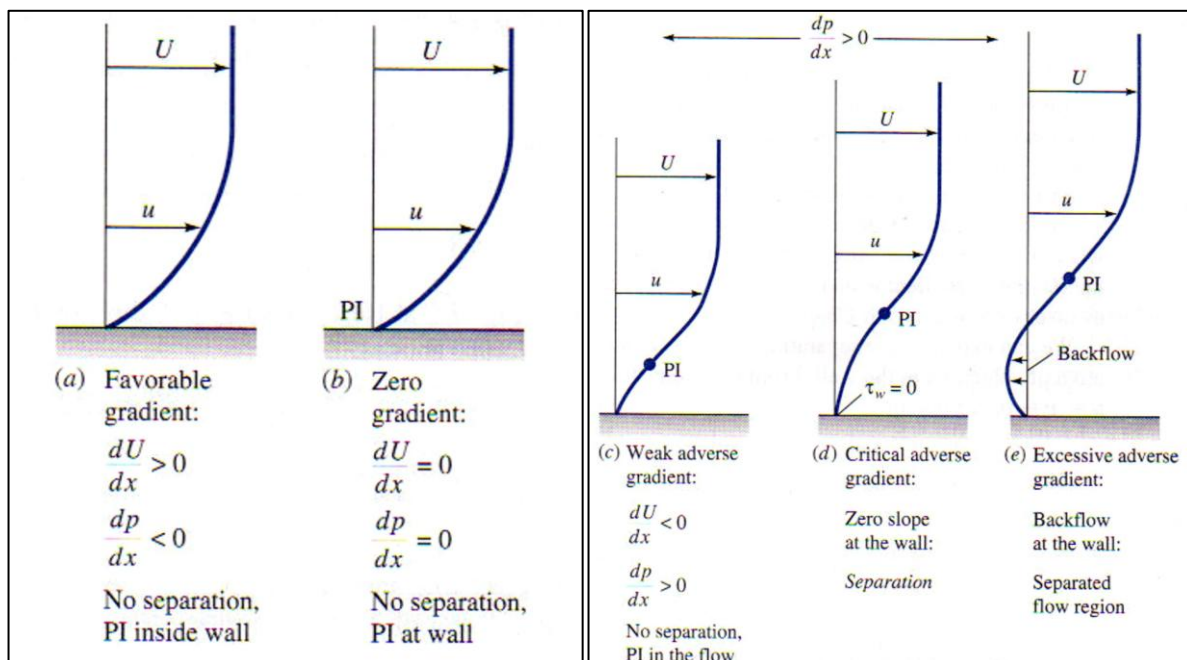
Figure 1.6. The effect of pressure gradients on boundary layer profiles [8]

One widely used numerical method for the estimation of growth of laminar flow boundary layers subjected to pressure gradients is Thwaites integral momentum method. It starts by taking the two-dimensional boundary layer integral relation for variable *U(x)* given as

CFD Modeling of Separation and Transitional Flow in
Low Pressure Turbine Blades at Low Reynolds Numbers

$$\frac{\tau_w}{\rho U^2} = \frac{1}{2}c_f = \frac{d\Theta}{dx} + (2+H)\frac{\Theta}{U}\frac{dU}{dx} \qquad (1.8)$$

where $H(x) = \delta^*(x)/\Theta(x)$ is the ratio of displacement thickness to momentum thickness, of the shape factor. The shape factor is a good indicator of the pressure gradient, the higher the $H(x)$ the stronger the adverse pressure gradient, and laminar flow separation occurs approximately at $H \approx 3.5$. Thwaites determined that the Eq. (1.10) can be correlated by using the dimensionless momentum-thickness variable, λ, and is defined as

$$\lambda = \frac{\Theta^2}{\nu}\frac{dU}{dx} \qquad (1.9)$$

Thwaites was able to integrate Eq. (1.10) in closed form with the result

$$\Theta^2 = \Theta_0^2\left(\frac{U_0}{U}\right)^6 + \frac{0.45\nu}{U^6}\int_0^x U^5 dx \qquad (1.10)$$

where Θ_0 is the momentum thickness at $x = 0$. Separation was found to occur at $\lambda = -0.09$. The non-dimensional shear stress, $S = \tau_w\Theta/(\mu U)$, was also correlated with λ as follows

$$S(\lambda) = \frac{\tau_w\Theta}{\mu U} \approx (\lambda + 0.09)^{0.62} \qquad (1.11)$$

Thwaites method is mainly used to make qualitative assessment of the boundary layer behavior. The range of accuracy is generally less than 10% for favorable pressure gradients, but about 20-30% in strong adverse pressure gradients [9].

1.2.2   Transitional Flow Boundary Layers

The flat plate example in Figure 1.4 shows a region where instabilities within the laminar flow boundary layer grow and become turbulent. The understanding of the origins of turbulent

flow and transition from laminar to turbulent flow are one of the most important unsolved problems in the field fluid mechanics.

Transition occurs in the boundary layer for external flows due to the disturbances in the freestream, such as vorticity or acoustic effects, which enter the boundary layer as steady and/or unsteady fluctuations of the basic state. This process is known as *receptivity* and it provides the initial conditions of amplitude, frequency, and phase for the breakdown of laminar flow. Receptivity may be initially too small to measure and is observed only after the onset of the instability [10]. A variety of different types of instabilities can occur either independently or coupled, and the type instability depends on the Reynolds number, wall curvature, roughness, and initial conditions.

Linear stability theory is used to describe initial growth of these disturbances. For example for flow over a flat plate, the basic state is assumed to be parallel flow where u = u(y). Two-dimensional instabilities are superimposed on the Navier-Stokes equations (Eq. 1.37) which are linearized assuming a normal mode of the instability stated as

$$q'(x, y, t) = q(y)\exp i(\alpha x - \omega t) + C.C. \tag{1.12}$$

where C.C. is the complex conjugate, and q' represents the instability quantity such as pressure or a velocity component. The Orr-Sommerfield equation describes the spatially varying instabilities as

$$\left(D^2 - \alpha^2\right)^2 \phi - iR\left[\left(\alpha \frac{u}{U_\infty} - \omega\right)\left(D^2 - \alpha^2\right)\phi - \left(\alpha D^2 \frac{u}{U_\infty}\right)\phi\right] = 0 \tag{1.13}$$

$$\alpha = \alpha_r + i\alpha_i \tag{1.14}$$

where $D = d/dy$, ϕ is the complex disturbance stream function, ω is the angular frequency, $-\alpha_i$ is

the spatial growth rate, and $c = \omega/\alpha_r$ is the phase speed. The eigenvalues for Eq. (1.15) are

found by looking at $\alpha = \alpha(Re, F)$, where F is the nondimensional frequency defined as

$$F = \frac{2\pi f \nu}{U_\infty^2}$$
(1.15)

The collection of points which $\alpha_i(Re, F) = 0$ is called the neutral stability curve shown in Figure

1.7. For a given frequency in the boundary layer, there can be two values of the Reynolds

number. In the region between the two Reynolds numbers the flow is unstable. Transition

depends on the measure of growth between the higher and lower Reynolds numbers. The

Reynolds number defined where the flow is stable for all frequencies is called the minimum

critical Reynolds number, Re_{crit}.
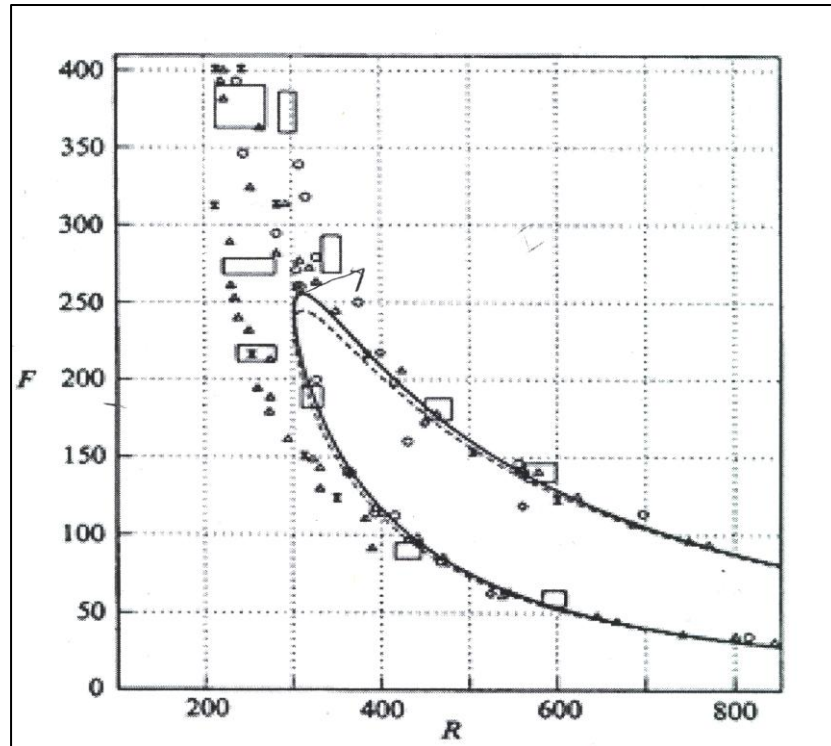
Figure 1.7. The neutral stability curve [10]

CFD Modeling of Separation and Transitional Flow in
Low Pressure Turbine Blades at Low Reynolds Numbers

Chapter 1. Introduction

In the boundary layer of a flat plate, Reynolds number varies along the plate and a disturbance at a given frequency, *F*, is called a Tollmien-Schlichting (T-S) wave. At certain conditions this wave is amplified and three-dimensional nonlinear interactions occur, referred to as secondary instabilities. These disturbances grow rapidly and turbulent spots eventually form where the boundary layer alternates between laminar and turbulent flow states. The formation of turbulent spots occurs at different locations and the spots merge to form fully developed turbulence. This entire process from laminar flow to transition to turbulence through the generation of T-S waves is classified as "natural" transition.

In some instances, boundary layer transition occurs in flows that are laminar and stable and do not follow the natural path of transition. This is known as "bypass" transition, where the formulation and amplification of T-S waves are bypassed due to the presence of forced disturbances of sufficient amplitude. This disturbance can be caused by either higher freestream turbulence or surface roughness. The formation of turbulence spots is the first indication of transition. This process reduces the distance of unstable laminar flow significantly and promotes earlier transition. Under certain conditions, the laminar boundary layer may separate from the surface of the body. Rapid transition occurs within the separated shear layer, providing that the Reynolds number is not too low or the adverse pressure gradient too large. The turbulent layer will reattach to the surface and form a closed region of the flow called a separation bubble. The region beneath the separated shear layer has very low shear stress and approximately constant static pressure. Figure 1.9 illustrates the three processes by which transition to turbulence is known to occur.

CFD Modeling of Separation and Transitional Flow in
Low Pressure Turbine Blades at Low Reynolds Numbers

These Regions bypassed
for bypass transition

| Region 1 | Region 2 | Region 3 | Region 4 | Region 5 |
| TS Waves | Spanwise Vorticity | Three-Dimensional Breakdown | Turbulent Spots | Fully Turbulent Flow |

Stable laminar flow

V_∞ →

LE Re_{crit}

δ

V_∞ →

Laminar |←— Transition —→| Turbulent

a) Tollmien-Schlichting transition (after White, 1974) and bypass transition

TRANSITION REGION

←— LAMINAR SHEAR LAYER —→ | |←— TURBULENT SHEAR LAYER —→

ATTACHED | SEPARATED

SEPARATION   REATTACHMENT

Figure 1.8. Diagram of the Types of Boundary Layer Turbulent Transition [3]

1.2.3   Turbulent Flow Characteristics

As the Reynolds number increases the fluid inertia overcomes the viscous stresses, and the laminar motion becomes unstable. The fluid goes through transitional flow regions as described previously. The pressure and velocity fluctuations become very rapid and the fluid motion becomes inherently three-dimensional and unsteady, which is described as turbulence. The flow in turbulence is a mixture of intertwined eddies or swirls of different sizes. There is a large amount of mixing involved with these finite-sized eddies compared to laminar flow. The

CFD Modeling of Separation and Transitional Flow in
Low Pressure Turbine Blades at Low Reynolds Numbers

three–dimensional eddy structure greatly promotes mixing within the fluid while the mixing is confined to the molecular scale for laminar flow. Fluctuating eddies within the turbulence exists over a large number of wavelengths due to the physical process of vortex stretching. The turbulence gains energy if the vortex elements are primarily oriented in a direction such that they can be stretched by the velocity gradients. This stretching of the vortex elements maintains the fluctuating vorticity and keeps the flow three-dimensional.

Flow properties in turbulence can be described in terms of their mean properties and the fluctuating components. For example, instantaneous velocity in the x-direction, $u = u(x,y,z,t)$, and the time mean is described as

$$\bar{u} = \frac{1}{T} \int_{t_0}^{t_0+T} u(x, y, z, t) dt \tag{1.16}$$

where T is the time interval, which is longer than the period of fluctuations but shorter than unsteadiness of the average velocity. The fluctuating part is of velocity is, u', is related to the mean velocity value by

$$u = \bar{u} + u' \tag{1.17}$$

The fluctuations are equally distributed on either side of the average so the square of the fluctuation quantity, $(u')^2$. The fluctuations within turbulent flow can occur temporally or spatially. Typically, turbulent flows are described as stationary and homogenous if the mean flow does not vary over time and is spatially uniform in all directions. The Reynolds stress components $\overline{u'^2}$, $\overline{v'^2}$, and $\overline{w'^2}$ or the root-mean squared fluctuations are a measurement of the intensity of the turbulent fluctuations. The Reynolds stress is typically normalized relative to the mean flow velocity using the equation

$$\hat{u} = \frac{\sqrt{\overline{(u')^2}}}{\overline{u}} \qquad \hat{v} = \frac{\sqrt{\overline{(v')^2}}}{\overline{v}} \qquad \hat{w} = \frac{\sqrt{\overline{(w')^2}}}{\overline{w}} \tag{1.18}$$

these definitions are known as the relative turbulent intensities. When these relative intensities are approximately equal, the turbulence is referred as isotropic.

Another important turbulence parameter is the period of fluctuations or time scale. This is determined by investigating the relative size of the turbulent eddies. The largest eddies carry most of the energy and enhance the transfer of mass, momentum, and energy. The range of eddies overlap in space, as larger eddies carry smaller eddies. Turbulence incorporates an energy cascade process where kinetic energy is transferred from larger eddies to smaller eddies. The smallest eddies dissipate the kinetic energy through viscous shear into heat.

Kolmogorov's universal equilibrium theory states that the smaller eddies should be in a state where the rate of receiving energy from the larger eddies is equal to the rate which the smallest eddies dissipate the energy to heat. The type of energy being transferred is the called turbulent kinetic energy, k (energy per unit mass) through the cascade process. The Reynolds stress and the turbulence intensity (measured in percent) are related to the turbulent kinetic energy using the equations

$$k = \frac{1}{2}\left(\overline{u'^2} + \overline{v'^2} + \overline{w'^2}\right) \tag{1.19}$$

$$Tu = 100\frac{\sqrt{\overline{(u')^2}}}{\overline{u}} = 100\sqrt{\frac{2}{3}\frac{k}{\overline{u}^2}} \tag{1.20}$$

Chapter 1. Introduction

The motion at the smallest scales should depend upon the rate at which the larger eddies supply the energy, $\varepsilon = -dk/dt$, and the kinematic viscosity, ν. The Kolmogorov scales of length (η), time (τ), and velocity (v) scales are depended on the dissipation rate, ε, and given as

$$\eta = \left(v^3/\varepsilon\right)^{1/4} \quad \tau = \left(\nu/\varepsilon\right)^{1/2} \quad v = \left(\nu\varepsilon\right)^{1/4} \tag{1.21}$$

Like light, turbulent eddies have a range of energies at different wave numbers (κ) or wavelengths ($\lambda = 2\pi/\kappa$). Using the Fourier transform, the turbulent kinetic energy can be described as

$$k = \int_0^\infty E(\kappa)d\kappa \tag{1.22}$$

where $E(\kappa)$ is the energy spectrum density. The spectral representation of turbulence for the large energy-containing eddies is defined as the integral length scale (l_m). The integral length scale is computed by taking the autocorrelation of the measurement of the velocity fluctuations using the equation

$$\mathfrak{R}_\tau = \frac{\overline{u(t)u(t+\tau)}}{\overline{u^2}(t)} \tag{1.23}$$

This autocorrelation function is integrated from the origin to the first zero crossing resulting in an integral time scale. The integral length scale is obtained by multiplying the integral time scale by the freestream velocity using Taylor's frozen turbulence assumption [11]. The Taylor microscale, λ_T, is derived from using the slope and curvature of autocorrelation function, f, at the origin with the equation

$$\lambda_T = \sqrt{\frac{-2}{\left(\partial^2 f/\partial x^2\right)_{x=0}}} \tag{1.24}$$

CFD Modeling of Separation and Transitional Flow in
Low Pressure Turbine Blades at Low Reynolds Numbers

Chapter 1. Introduction

When the turbulence is homogenous and isotropic, the analysis of Taylor shows that the turbulent kinetic energy (k) and dissipation rate (ε) is related to the Taylor microscale with the equation

$$\varepsilon = -\frac{dk}{dt} = \frac{10\nu k}{\lambda_T^{\,2}} \qquad (1.25)$$

Using this relationship and Eq. (1.23), the Kolmogorov length scale (η) can be put in terms of the Taylor microscale (λ_T) as

$$\eta = \frac{(\lambda_T \nu)^{1/2}}{(10k)^{1/4}} \qquad (1.26)$$

Experimental measurements [11] indicate that

$$\varepsilon \approx 0.09 \frac{k^{3/2}}{l_m} \qquad (1.27)$$

Using this correlation, the definition of the Kolmogorov length scale (Eq. 1.23), and combining Eq. (1.27) and Eq. (1.29) yields

$$\frac{\lambda_T}{\eta} \approx 7\left(\frac{l_m}{\eta}\right)^{1/3} \qquad (1.28)$$

Typically the Taylor microscale is estimated to be at least 70 times the Kolmogorov length scale. It involves a quantity characteristic of small, dissipating eddies as well as large, energy-containing eddies. It typically cannot be used to characterize either the large or small eddies. Kolmogorov hypothesized that for a very large Reynolds number there is a range of eddy sizes between the largest and smallest scale for which the cascade process is independent of the

statistics of the energy- containing eddies and the effects of viscosity. He concluded that $E(\kappa)$

depends upon κ and ε only and described with the equation

$$E(\kappa)=C_\kappa\varepsilon^{2/3}\kappa^{-5/3}, \quad \frac{1}{l_m}<<\kappa<<\frac{1}{\eta} \tag{1.29}$$

where C_κ is the Kolmogorov constant. Figure 1.10 shows the typical energy spectrum for

turbulent flow. The Taylor microscale of turbulence is found within the inertial sub-range of the

energy spectrum.
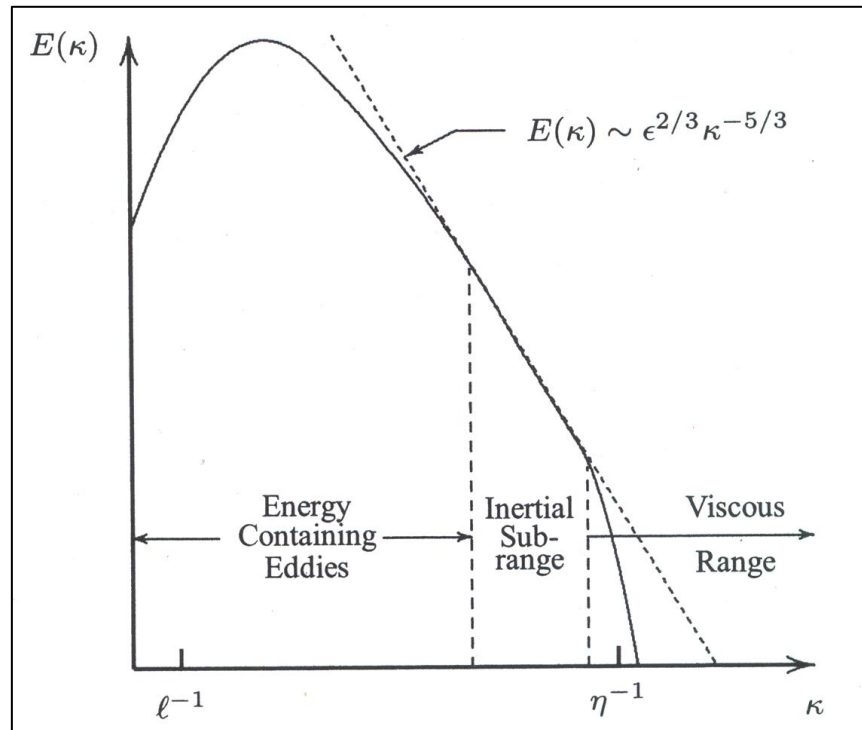
Figure 1.9. Energy spectrum for a turbulent low in log-log scales [11]

These ranges of length scales are randomly transported within the flow resulting in a

relatively large shearing force. The shear stress in turbulent flow is described with the following

equation

$$\tau = \tau_{lam}+\tau_{turb} = \mu\frac{d\overline{u}}{dy}-\rho\overline{u'v'} \tag{1.30}$$

When the flow is laminar, $\overline{u'v'} = 0$. The turbulent shear stress $(-\rho\overline{u'v'})$ is positive hence the stress is greater in laminar flow than turbulent flow. The process of the transfer of momentum and other quantities in turbulence is sufficiently similar mathematically to the molecular process to suggest that an eddy or turbulent viscosity can be defined where:

$$\tau_{turb} = \mu_{turb}\frac{d\overline{u}}{dy} \tag{1.31}$$

The eddy viscosity is a function of the fluid properties and flow conditions and is not easily determined. The sum of the eddy viscosity and fluid viscosity, called the effective viscosity, is sometimes 400 times larger than the fluid viscosity. The reason for the difference is the characteristic length for turbulent flow is the size of the eddies rather than the mean free path of molecules as in laminar flow. The strong diffusiveness helps turbulent flow withstand much stronger adverse pressure gradients than laminar flow without separating.

1.2.4   Turbulent Flow Boundary Layers

The turbulent boundary layer can be treated as a composite layer consisting of an inner and outer region. The inner region of the turbulent boundary layer is much smaller than the outer region. The mean velocity distribution in the inner region is determined by the wall shear stress, density, viscosity, and distance from the wall by an expression known as the law of the wall.

$$u^+ = \frac{u}{u_{turb}} = \phi_1\left(y^+\right) \tag{1.32}$$

where $u_{turb} = \left(\tau_w/\rho\right)^{1/2}$ is the friction velocity. The parameter y^+ is the Reynolds number based on turbulent length scale ($y^+ = yu_{turb}/\nu$). The inner region can be divided into three layers identified as the viscous sublayer, the transitional region, and the fully turbulent region. In the

viscous sublayer, stress is mainly viscous since the turbulent fluctuations become zero at the wall. This region is non-uniform in time and distance along the wall. The effect of viscosity decreases as distance from the wall is increased. Ultimately, the region is reached where the flow is completely turbulent. The transition region, viscous and turbulent stresses are of similar magnitude. The size of the viscous and transition region is quite small compared to the overall turbulent region.

The outer region encompasses 80-90% of the boundary layer thickness. According to experiments [12], the mean velocity distribution in the outer region can be described by the following expression called the velocity deficit law.

$$\frac{(u_e - u)}{u_{turb}} = f\left(\frac{y}{\delta}\right) \tag{1.33}$$

This is not valid close to the wall and depends on the Reynolds number $(\delta u_{turb}/\nu)$ and ratio y/δ. As y→δ the function goes to zero. Although the behavior of turbulent flow in the inner and outer regions is quite different, the regions are coupled by the shear stress-profile and the general diffusivity of turbulence.

The phenomena of laminar and turbulent flow, transition, separation and reattachment are evident in the flows modeled in this investigation, and the related flow theory provides the basis for the interpretation of the CFD predictions. Thus, the above review of fundamental boundary layer, transition and turbulence concepts has been provided as an introduction to the CFD modeling results to be described.

1.3 CFD Methods of Predicting Low Reynolds Number Effects in LPT Blades

The development of high speed digital computers has had a large impact on the way fluid mechanics and heat transfer is applied to design problems in modern engineering practice. Computational Fluid Dynamics (CFD) has been a well known methodology for solving complex problems of fluid mechanics and heat transfer. In CFD, the Navier-Stokes partial differential equations for fluid flow are solved numerically using finite difference methods. The beginning of modern numerical analysis is sometimes attributed to a famous paper by Courant, Friedrichs, and Lewy in 1928. The acronym CFL, frequently used in the CFD literature stands for the last names of these authors. In the paper, uniqueness and existence questions were addressed for the numerical solutions of partial differential equations [13].

Numerical modeling of turbulent flows using CFD has been a challenge due to the inherent randomness, three-dimensionally, and time dependence associated with turbulent flows. An enormous amount of information is required to completely describe a turbulent flow problem. The largest turbulent eddies can in some cases be as large as the width of the flow and are directly affected by the boundary geometry. There is a large range of time scales and length scales that need to be resolved.

There are three primary types of CFD methods used for modeling of turbulent flows. These methods are direct numerical simulations, large eddy simulations, and Reynolds-Averaged Navier-Stokes equations. The suitability of a particular method for a particular flow problem depends on several factors including computational cost, ease of use, range of applicability, and accuracy. It is the decision of the user based on these factors to judge whether a particular method would be suitable for the turbulent flow problem of interest. For this particular study, there is special interest in the accurate prediction of aerodynamic losses of boundary layers

undergoing turbulent transition and separation in turbomachinery geometries. The next sections will discuss the CFD methods of direct numerical simulations (DNS), large eddy simulations (LES), and Reynolds-Averaged Navier-Stokes (RANS) in greater detail including the advantages and disadvantages of each method. Also, a literature review of several studies will be presented where DNS, LES, and RANS CFD methods have been applied to LPT flows for the prediction of separated and transitional flow and compared to experimental cascade results.

1.3.1 Direct Numerical Simulation CFD Method

Advances in computing and storage capacity of high performance computing systems have made possible computations using direct numerical simulations. DNS uses the finite difference form of the three-dimensional imcompressible Navier-Stokes and continuity equations stated below.

Continuity

$$\frac{\partial \rho}{\partial t} + \frac{\partial}{\partial x}(\rho u) + \frac{\partial}{\partial y}(\rho v) + \frac{\partial}{\partial z}(\rho w) = 0 \tag{1.34}$$

Navier-Stokes

$$\rho \frac{Du}{Dt} = \rho f_x - \frac{\partial p}{\partial x} + \frac{\partial}{\partial x}\left[\frac{2}{3}\mu\left(2\frac{\partial u}{\partial x} - \frac{\partial v}{\partial y} - \frac{\partial w}{\partial z}\right)\right] + \frac{\partial}{\partial y}\left[\mu\left(\frac{\partial u}{\partial y} + \frac{\partial v}{\partial x}\right)\right] + \frac{\partial}{\partial z}\left[\mu\left(\frac{\partial w}{\partial x} + \frac{\partial u}{\partial z}\right)\right]$$

$$\rho \frac{Dv}{Dt} = \rho f_y - \frac{\partial p}{\partial y} + \frac{\partial}{\partial x}\left[\mu\left(\frac{\partial v}{\partial x} + \frac{\partial u}{\partial y}\right)\right] + \frac{\partial}{\partial y}\left[\frac{2}{3}\mu\left(2\frac{\partial v}{\partial y} - \frac{\partial u}{\partial x} - \frac{\partial w}{\partial z}\right)\right] + \frac{\partial}{\partial z}\left[\mu\left(\frac{\partial v}{\partial z} + \frac{\partial w}{\partial y}\right)\right]$$

$$\rho \frac{Dw}{Dt} = \rho f_z - \frac{\partial p}{\partial z} + \frac{\partial}{\partial x}\left[\mu\left(\frac{\partial w}{\partial x} + \frac{\partial u}{\partial z}\right)\right] + \frac{\partial}{\partial y}\left[\mu\left(\frac{\partial v}{\partial z} + \frac{\partial w}{\partial y}\right)\right] + \frac{\partial}{\partial z}\left[\frac{2}{3}\mu\left(2\frac{\partial w}{\partial z} - \frac{\partial u}{\partial x} - \frac{\partial v}{\partial y}\right)\right] \tag{1.35}$$

No turbulence modeling is required as in other numerical schemes, as DNS can directly resolve the whole spectrum of turbulent eddy scales. The value of DNS is obvious in that it can be used to understand the turbulent structures and processes for a given flow problem. It can also be viewed as an additional source of experimental data. It allows for detailed analysis of the

complex flow physics involved when separation and transition exist, which cannot be measured using current experimental methods. These results can be obtained only if the DNS simulation has high numerical accuracy and correct boundary and initial conditions. However, the computational cost required for DNS computations is proportional to Re_t^3, where $Re_t = k^{1/2} l_m / \nu$, known as the turbulent Reynolds number. The number of grid points has to be high enough to be able to resolve the smallest eddy. Similarly, the time-step in the computation should be the same order as the Kolmogorov time scale, τ (Eq. (1.23)). Therefore DNS is rarely employed for simulations involving three-dimensional rotating turbomachinery due to the high computational cost even at low Reynolds numbers.

Several studies have been done where computations based on DNS were successfully applied to low Reynolds number flows [14-27] in stationary LPT cascade geometries. Enomoto *et al.* [14] applied DNS to the Pack-B turbine blade airfoil at a Reynolds number of 43,000 and compared the results to the experimental measurements of Lake [18]. The blade loading and total pressure loss coefficient showed a reasonable comparison with experimental results. It was demonstrated that the flowfield is dominated by relatively large eddies near the blade surface and that DNS can be used to simulate low Reynolds number flowfields relatively well. Singh *et al.* [15] simulated flow with Reynolds numbers of 10,000 and 25,000 on the Pack-B blade airfoil using two different boundary conditions, a static inflow boundary condition with extrapolated outflow, and dynamic inflow boundary condition which accounted for the upstream influence in subsonic flow. Results using the static inflow boundary condition showed that the laminar boundary layer on the suction surface becomes separated and forms two-dimensional clockwise vortices, which then become three-dimensional as they convect downstream to the trailing edge due to spanwise instabilities. The location of the onset of separation compared well to

experimental measurements. They observed different behavior at the Reynolds number of 25,000 using the dynamic inflow boundary conditions, where separation was found to be smaller when compared to the results from static boundary condition specification [15].

DNS simulations were advanced further by Rizzetta and Visbal [16,17] by modeling active flow control using vortex generating jets and plasma-based flow control to reduce separation and total pressure loss. It was reported that pulsed vortex generating jets helped to maintain the boundary layer attached for an additional distance of 19-21% along the blade with a 53-56% decrease in total pressure loss [16]. Plasma based flow control using dielectric barrier discharge actuators were simulated at an inlet Reynolds number of 25,000 [17]. Counter-flow plasma injection was found to provide the most effective control, producing vortices that enhanced mixing and brought higher momentum fluid to the boundary layer causing the flow to remain attached to the blade suction surface all the way to the trailing edge.

1.3.2. *Large Eddy Simulation CFD Method*

An alternative to the DNS method is large eddy simulation (LES). It enables the use of coarser meshes and larger time-steps with less computational cost than required by DNS. The governing equations in LES are obtained by filtering the unsteady Navier-Stokes equations using Fourier, Gaussian, or other filters. The filtering process separates the eddies whose scales are smaller than the grid spacing from the resolvable scaled eddies. The subgrid scale eddies are modeled because they are nearly isotropic and have universal characteristics. Some of the types of subgrid-scale models (SGS) are the Smagorinsky SGS model and Dynamic SGS model. Because the large scale eddy unsteady motions are resolved explicitly, LES can be more accurate than most RANS solvers, especially for flows over bluff bodies with unsteady separation and vortex shedding. The dynamics of these large scale eddy motions are computationally expensive

to model. Since the small scale eddy motions are described using simple models, LES has less computational expense than DNS. Nearly all the computation effort in DNS is used in resolving the smallest eddy dissipation. For boundary layer flows with isotropic turbulence, LES typically provides enough frequency modes to resolve 80% of the eddy energy spectrum even at high Reynolds numbers [12]. The grid resolution requirements are still high for boundary layer flows because the size of the near wall eddies within the boundary layer are relatively small. The boundary layer grid resolution increases with $Re_t^{1.8}$. Thus LES has been successfully applied to boundary layer flows at low and moderate Reynolds numbers. At high Reynolds numbers, LES is currently computationally expensive for flows involving aircraft wings and complex geometries such as rotating turbomachinery but it can be used to help improve engineering models of turbulence.

LES has emerged as a viable means for the investigation of transitional and separated flow associated with low Reynolds numbers in low pressure turbine cascade geometries [19-21]. Mittal *et al.* [19] simulated a cascade configuration at Reynolds numbers of 10,000 and 25,000 and found that the dynamics of the separation phenomenon on the suction surface are dominated by Karman vortex shedding and cannot occur without vortices shed from the pressure side. Accurate representation of the pressure side boundary layer is required to capture the separation dynamics on the suction side. Revady *et al.* [20] demonstrated the ability to successfully predict transition and identified a coupling between the separation bubble and the vortex shedding generated by the trailing edge. The effect of passing wakes on LPT blade airfoil surfaces was investigated using LES by Sarkar and Voke [21]. They observed that vortices form over the rear half on the suction surface by the rollup of the shear layer as wakes pass over the separation

region. Large pressure fluctuations were measured on the suction surface due to the wake

passing and showed good agreement with experimental results and a similar DNS simulation.

1.3.3. Reynolds Averaged Navier-Stokes (RANS) CFD Method

The most widely adopted CFD method used for practical engineering applications is the

Reynolds Averaged Navier-Stokes (RANS) equations. All flow quantities are expressed as the

sum of mean and fluctuating parts, where the whole range of turbulent scales is being modeled.

Reynolds averaging assumes a variety of forms involving either an integral or summation. Time

averaging is the most appropriate forms of Reynolds averaging because most engineering

problems involve inhomogeneous turbulence. The RANS equations are developed from the

time-averaging of the Navier-Stokes equations and are given as

$$\rho \frac{\partial U_i}{\partial t} + \rho U_j \frac{\partial U_i}{\partial x_j} = -\frac{\partial P}{\partial x_i} + \frac{\partial}{\partial x_j}\left(2\mu S_{ij} - \rho \overline{u_i' u_j'}\right) \quad S_{ij} = \frac{1}{2}\left(\frac{\partial U_i}{\partial x_j} + \frac{\partial U_j}{\partial x_i}\right)$$

(1.36)

where S_{ij} is the mean-strain rate tensor. Also note the appearance of the term $\overline{u_i' u_j'}$ in the RANS

equation. The RANS equations are solved for the mean fluid properties. In order to compute the

velocity field for turbulent flow, the term $\overline{u_i' u_j'}$ must be defined. This term is the Reynolds stress

tensor and is defined as

$$\tau_{ij} = -\rho \overline{u_i' u_j'}$$

(1.37)

The Reynolds stress is a symmetric tensor where $\tau_{ij} = \tau_{ji}$. For general three-dimensional flows,

the four unknowns of pressure and the three components of the velocity need to be solved along

with the six Reynolds stresses as a result of the Reynolds averaging. The pressure and velocity

components can be resolved from the Reynolds averaged continuity and RANS equations. An

expression for the Reynolds stress is required to obtain a closed form solution. A turbulence

model or directly modeled Reynolds stress transport equation is used to obtain a closed form solution to the RANS equations.

Both the algebraic and transport equation turbulence models are used to bring closure to RANS equations. Algebraic models are based on the Boussinesq eddy-viscosity approximation which states that the Reynolds stress relates to the eddy viscosity, μ_t, with the equation

$$-\rho \overline{u_i' u_j'} = 2\mu_t S_{ij} - \frac{2}{3}\mu_t \frac{\partial U_k}{\partial x_k}\delta_{ij} - \frac{2}{3}\rho k \delta_{ij} \tag{1.38}$$

Algebraic turbulence models are the simplest turbulence models for determining the eddy viscosity. Transport equation models solve for the quantities of the turbulent kinetic energy and dissipation rate of the energy-containing eddies. There many types of turbulence models used to solve engineering flows and each model has its advantages and limitations. All the different types of conventional turbulence models are presented in text such as Wilcox [11]. The particular interest of this study is the type of RANS turbulence models that have been applied to prediction of transitional and separated flows associated with low Reynolds number effects with success.

1.4 Transition Modeling

1.4.1. e^N Method

The e^N method, based on linear stability theory, is one of the most popular methods available for transition prediction. It can be used with either the local stability approach or the non-local linear Parabolized Stability Equations (PSE) approach. The local approach implies that the stability of the flow at a particular location is determined by the local conditions at that

location and independent of all others and assumes the mean flow is locally parallel. The instabilities are described with the equation

$$q'(x, y, z, t) = q(y)\exp(-\alpha_i x)\exp[i(\alpha_r x + \beta z - \omega t)]$$

(1.39)

where z is the spanwise direction, α and β are complex representations of the wave number components in the x and z directions, and ω is the frequency. The non-local linear PSE approach states that the mean flow and amplitude functions is dependent on both x and y, and α depends on x, so that the instabilities are described as

$$q'(x, y, z, t) = q(x, y)\exp\left[i\left(\int_{x_0}^{x} \alpha(X)dX + \beta z - \omega t\right)\right]$$

(1.40)

The stability of the flow at a given location depends the upstream history of the disturbances. The surface of curvature of the body is taken to account by the linear PSE approach because these effects are of the same order of magnitude as the non-parallel effects [10]. Also, the streamwise pressure gradient is automatically taken into account through the shape of the mean velocity profile.

There are three steps in the application of the e^N method. The first involves computing the laminar flow velocity and temperature profiles at different streamwise locations for a given flowfield. Secondly, the amplification rates of the most unstable waves are calculated for each profile. These amplification rates are used to calculate the transition location in the third step. The value for the "N" factor is determined by looking at the amplification rate of the spatial varying wave defined as

$$\ln(A/A_0) = -\int_{x_0}^{x} \alpha_i dx$$

(1.41)

CFD Modeling of Separation and Transitional Flow in
Low Pressure Turbine Blades at Low Reynolds Numbers

where A is the wave amplitude at any location and A_0 is the wave amplitude where that wave becomes unstable at x_0. The "N" factor is calculated as

$$N = \underset{f}{Max}\left[\ln\left(A/A_0\right)\right] \tag{1.42}$$

where the total amplification rate has been determined for a series of instabilities ($f_1, f_2, f_3,..$). The e^N method assumes transition to occur for a predefined value of N factor defined as N_T. This means that the breakdown to turbulence is observed when the most amplified wave has been amplified by a critical ratio, $\exp(N_T)$. The one disadvantage is the value of the N factor is not universal for transition and needs to be validated based on experimental data.

1.4.2. Dorney et al. Model

Dorney *et al.* [22] modified both the Baldwin-Lomax and standard k-ε model to include numerical models for the prediction of separated and transitional flows. A natural transition model called the Abu-Ghannam and Shaw (AGS) model which determines the start of transition based on the momentum thickness is given as

$$\mathrm{Re}_\Theta = 163 + \exp\left[F(\lambda_\Theta) - \frac{F(\lambda_\Theta)}{6.91}Tu\right] \tag{1.43}$$

The relationship of $F(\lambda_\Theta)$ is given in Ref. [22] with more details. This model is considered to be valid up to turbulent intensities of Tu =10%. The end of the transition region is calculated as

$$\mathrm{Re}_L = 31.8\left(\mathrm{Re}_\Theta\right)^{1.6} \tag{1.44}$$

An intermittency function γ was used in the region between the start and end of transition and is calculated as

$$\gamma = 1 - \exp(-4.64\zeta^2) \tag{1.45}$$

This function represents the fraction of the total time that the flow is turbulent. It is equal to zero in laminar flow and unity in fully turbulent flow. The intermittency is multiplied by the turbulent viscosity in the turbulence model. The separated flow region was modeled with the correlation

$$\text{Re}_\Theta = 25000 \log_{10}\left(1/\tanh(0.173205\tau)\right) \qquad (1.46)$$

The Dorney *et al.* [22] model was applied at three inlet Reynolds numbers of 43,000, 86,000, and 172,000 for the Pack-B blade airfoil. The predicted total pressure losses using both of the modified turbulent flow models were greater than the experimental values at all three Reynolds numbers due to the difference in the separation and reattachment locations and the size of the separation region.

1.4.3. *Suzen et al. Model*

A study by Suzen *et al*. [23] used the turbulent viscosity expression from Menter's *k-ω(SST)* model as $\mu_t^* = \gamma\mu_t$. A transport equation was used to solve for the intermittency function, γ, given as

$$
\begin{aligned}
\frac{\partial\rho\gamma}{\partial t} + \frac{\partial\rho u_j\gamma}{\partial x_j} &= (1-\gamma)\left[(1-F)2C_0\rho\sqrt{u_k u_k}\,f(s)f'(s) + F\left(\frac{C_1\gamma}{k}\tau_{ij}\frac{\partial u_i}{\partial x_j} - C_2\gamma\rho\frac{k^{3/2}}{\varepsilon}\frac{u_i}{(u_k u_k)^{1/2}}\frac{\partial u_i}{\partial x_j}\frac{\partial\gamma}{\partial x_j}\right)\right] \\
&+ C_3\rho\frac{k^2}{\varepsilon}\frac{\partial\gamma}{\partial x_j}\frac{\partial\gamma}{\partial x_j} + \frac{\partial}{\partial x_j}\left(\left((1-\gamma)\gamma\sigma_\gamma\mu + (1-\gamma)\gamma\sigma_\gamma\mu_t\right)\frac{\partial\gamma}{\partial x_j}\right)
\end{aligned} \qquad (1.47)
$$

The constants and auxiliary relations were given in more detail in Ref. [23]. The intermittency transport equation was used to obtain the distribution of intermittency in the transitional flow region, while the onset of transition was determined by correlations. The onset of attached transitional boundary layer flow was determined with a correlation for Reynolds number based on momentum thickness, given as

CFD Modeling of Separation and Transitional Flow in
Low Pressure Turbine Blades at Low Reynolds Numbers

$$\text{Re}_{\Theta} = \left(120 + 150Tu^{-2/3}\right)\coth\left[4\left(0.3 - K_t \times 10^5\right)\right] \qquad (1.48)$$

where K_t is called the acceleration parameter. In order to determine the onset of separated flow transition, the Reynolds number, Re_{st}, is expressed in terms of the turbulence intensity (Tu) and momentum thickness Reynolds number of the separation point, $Re_{\Theta s}$ using the correlation as

$$\text{Re}_{st} = 874\,\text{Re}_{\Theta s}^{0.71}\exp\left[-0.4Tu\right] \qquad (1.49)$$

The Suzen *et al*. [23] model was applied to two different cascade grid topologies. Results compared well with three different experiments with differences in separation and reattachment locations.

1.4.4. Prasnier and Clark Model

Another approach by Praisner and Clark [24] used correlations developed from an experimental database for attached flow transition, laminar separation with turbulent attachment, and separated-flow transition. The experimental database consisted of 57 cases of seven different turbomachinery-specific airfoils at various boundary conditions. Laminar flow simulations were performed for experimental cascade configurations at the appropriate in boundary conditions. The pre-transitional boundary layer was modeled using a "quasi-laminar" formulation of the Wilcox k-ω model in the laminar region of the boundary layer. In this formulation, the production of k and ω were kept at a minimum to allow for the convection and diffusion of freestream turbulence into a quasi-laminar boundary layer.

A momentum thickness Reynolds number correlation based on the experimental database was given as

$$\text{Re}_{\Theta} = A\left(Tu \frac{\Theta}{l_m} \right)^{B} \tag{1.50}$$

It was used to determine the onset of attached transitional flow, where A and B were constants equal to 8.52 and 0.956, respectively. The onset of separated-flow transition was modeled using

$$\frac{L_{sep}}{S_{sep}} = C \, \text{Re}_{\Theta-sep}^{D} \tag{1.51}$$

where C and D were constants equal to 173.0 and -1.227, respectively, L_{sep} was the distance between separation and transition onset, and S_{sep} was the surface distance from the stagnation point to the separation location. If the separated-flow transition was predicted to occur downstream of the trailing edge, the simulation was run as fully laminar. Once transition occurred, the Wilcox k-ω model was used to model the fully turbulent flow. The Prasnier and Clark [25] model showed significant improvement over a conventional fully turbulent flow model in the predicted accuracy of the total pressure loss for both linear cascades and multistage LPT rigs.

1.4.5. The Menter et al. γ-Re_{Θ} Model

Menter *et al*. [26] has developed a new transitional flow model called the γ-Re_{Θ} model. Instead of using the momentum thickness Reynolds number to trigger the onset of transition, the γ-Re_{Θ} model was based on the vorticity Reynolds number, Re_{υ}, given as

$$\text{Re}_{\upsilon} = \frac{\rho y^2}{\mu} \frac{\partial u}{\partial y} = \frac{\rho y^2}{\mu} \Omega \tag{1.52}$$

where y is the distance from the wall, and Ω is the vorticity. The maximum value of Re_υ was dependent on the momentum thickness Reynolds number. A transport equation for the intermittency was used to trigger the transition process and defined as

$$\frac{\partial \rho \gamma}{\partial t} + \frac{\partial \rho u_j \gamma}{\partial x_j} = P_{\gamma 1} - E_{\gamma 1} + P_{\gamma 2} - E_{\gamma 2} + \frac{\partial}{\partial x_j}\left[\left(\mu + \frac{\mu_t}{\sigma_f}\right)\frac{\partial \gamma}{\partial x_j}\right] \tag{1.53}$$

Also, a transport equation for the momentum thickness Reynolds number at the transition onset, $Re_{\Theta t}$ was used and given as

$$\frac{\partial Re_{\Theta t}}{\partial t} + \frac{\partial \rho u_j Re_{\Theta t}}{\partial x_j} = P_{\Theta t} + \frac{\partial}{\partial x_j}\left[\sigma_{\Theta t}(\mu + \mu_t)\frac{\partial Re_{\Theta t}}{\partial x_j}\right] \tag{1.54}$$

The intermittency transport equation included two terms that controlled the production of intermittency. These terms were the F_{length} and $Re_{\Theta c}$, which were determined by proprietary empirical correlations. $Re_{\Theta c}$ was defined as the momentum thickness Reynolds number at the point where the intermittency started to increase in the boundary layer and F_{length} controlled the length of the transition zone. The $Re_{\Theta t}$ transport equation outside the boundary layer was forced to follow an experimental empirical correlation. This was then diffused by the boundary layer by a standard diffusion term. When the boundary layer became separated, the transition model was modified so that the intermittency could exceed unity when the boundary layer separated. This modification was given as

$$\gamma_{sep} = \min\left\{8\max\left[\left(\frac{Re_\upsilon}{2.193\,Re_{\Theta c}}\right) - 1,0\right]\exp-\left(\frac{R_T}{15}\right)^4,5\right\}F_{\Theta t} \tag{1.55}$$

where $F_{\Theta t}$ is a blending function within the auxiliary relationship from Eq. (1.54) and is confined the modification to boundary layer flows. Eq. (1.55) allowed for the control of the

CFD Modeling of Separation and Transitional Flow in
Low Pressure Turbine Blades at Low Reynolds Numbers

separation bubble resulting in a larger production of turbulent kinetic energy, which corrected the prediction of reattachment [26]. The γ-Re_{Θ} model transport equation was coupled with the Menter's k-ω(SST) model where the production and destruction terms were modified using intermittency. The γ-Re_{Θ} model has been applied to several 2D and 3D geometries by Langtry *et al.* [27] including the Pack-B cascade, a 3D GE low-pressure turbine vane, and the T106 blade undergoing passing wakes. All simulations agreed well with experiments for all test cases at a wide range of Reynolds numbers and freestream turbulent intensities.

1.4.6.   *The Moore and Moore MARV Reynolds Stress Model*

Moore and Moore [28] developed a Reynolds stress model for application of separated and transitional flows called the MARV Reynolds Stress Model. Traditional Reynolds stress models solved differential equations for the Reynolds stress, $\overline{u_i' u_j'}$, and the dissipation rate, ε. The MARV model specified equations for $q = \sqrt{k}$, $\omega = \varepsilon/k$, and five independent turbulent anisotropies, defined as

$$b_{ij} = \frac{\overline{u_i u_j}}{2k} - \frac{1}{3}\delta_{ij} \qquad (1.56)$$

Also, the MARV model used a non-isotropic viscosity based on DNS calculations. It correctly models the behavior of the strain rate and shear stress within the boundary layer. This behavior was described as the larger velocity fluctuations in the outer portion of the boundary layer pointing toward the wall and becoming more parallel to the mean velocity vectors as the wall is approached, similar to DNS predictions. This behavior was not seen in turbulence models that used the Boussinesq approximation, where the direction of velocity fluctuations were always aligned 45° to the mean velocity vectors. The MARV Reynolds Stress model of Moore and

Chapter 1. Introduction

Moore [28] was applied to a UTRC/Pratt & Whitney cascade design of the JT9D. Reasonable agreement was achieved with experimental results for the location of increased heat transfer on the suction surface due to transition. Also, the trends in the prediction of performance were consistent with the experimental results.

1.4.7. Walters and Leylek k-k_L-ω Model

Walters and Leylek [2] developed a three-equation eddy-viscosity type model named the k-k_L-ω model. This model contained transport equations for the turbulent kinetic energy (k_T), laminar kinetic energy (k_L), and the specific dissipation rate (ω) which were given as

$$\frac{Dk_T}{Dt} = P_{k_T} + R + R_{NAT} - \omega k_T - D_T + \frac{\partial}{\partial x_j}\left[\left(\nu + \frac{\alpha_T}{\sigma_k}\right)\frac{\partial k_T}{\partial x_j}\right] \tag{1.57}$$

$$\frac{Dk_L}{Dt} = P_{k_L} - R - R_{NAT} - D_L + \frac{\partial}{\partial x_j}\left[\nu\frac{\partial k_T}{\partial x_j}\right] \tag{1.58}$$

$$\frac{D\omega}{Dt} = P_\omega + C_{\omega R}\frac{\omega}{k_T}(R + R_{NAT}) - C_{\omega 2}\omega^2 - C_{\omega 3}f_\omega\alpha_T\left(\frac{\lambda_{eff}}{\lambda_T}\right)^{4/3}\frac{\sqrt{k_T}}{d^3} + \frac{\partial}{\partial x_j}\left[\left(\nu + \frac{\alpha_T}{\sigma_\omega}\right)\frac{\partial\omega}{\partial x_j}\right] \tag{1.59}$$

The influence of the laminar and turbulent kinetic energy on the Reynolds stress term was included through the prescription of the total eddy viscosity as given in Eq. (1.60).

$$-\overline{u_i'u_j'} = \nu_{TOT}\left(\frac{\partial u_i}{\partial x_j} + \frac{\partial u_j}{\partial x_i}\right) - \frac{2}{3}k_{TOT}\delta_{ij} \tag{1.60}$$

The laminar kinetic energy was used to describe the low frequency, high amplitude fluctuations that originated from the pre-transitional boundary layer. These fluctuations primarily occurred at one scale and almost all energy was contained in a single streamwise component. The production of laminar kinetic energy was assumed to occur due to a "splat

CFD Modeling of Separation and Transitional Flow in
Low Pressure Turbine Blades at Low Reynolds Numbers

mechanism". This "splat mechanism" redirected the normal fluctuations of the freestream turbulence into a streamwise component while creating local pressure gradients in the boundary layer, increasing the low frequency fluctuations. These fluctuations grow to the development of turbulent spots and then to full turbulence. A local transition parameter that depended on the turbulent energy, effective length scale, and fluid viscosity determined when this occurred. Once this parameter reached a threshold value, a transfer of energy began from streamwise fluctuations (k_L) to turbulent fluctuations (k_T). In the near-wall region, the turbulent kinetic energy was split into small-scale and large-scale energy. The small-scale energy contributed to the turbulent production, and the large-scale energy contributed to the laminar kinetic energy.

Both natural, mixed, and bypass transition were resolved in the Walters and Leylek [2] model. The production terms in this model controlled the transfer from streamwise fluctuations to full turbulence which depended on the laminar kinetic energy and the local mean velocity in order to include natural and mixed transition. For the onset of transition, a parameter was calculated from the turbulent kinetic energy, kinematic viscosity, and the wall distance. When this parameter exceeded a certain threshold, transition was assumed to start. The onset of transition was associated with the reduction of laminar kinetic energy and the increase in the turbulent kinetic energy. A full description of all model constants and auxiliary equations was presented by Walters and Leylek [2].

The Walters and Leylek [2] model has been applied to the cases of a zero-pressure-gradient flat plate at various freestream turbulent intensities [2] and a circular cylinder at subcritical, critical, and supercritical Reynolds numbers [29] with good results. Also, the capability of the new model to predict transitional flow behavior has been demonstrated on a

highly loaded turbine blade airfoil with and without film cooling [30] and a flat plate with pressure distribution similar to an axial compressor undergoing passing wakes [31].

In the foregoing material, fundamental boundary layer theory and examples of CFD models applied to turbomachinery have been reviewed. This supports the dissertation goal to examine representative turbulence models and RANS solvers for LPT flow modeling and, if possible, to offer a new, characterized model for the applicability of low Reynolds numbers flow predictions.

2. Description of Experimental Cascade Configurations Utilized in the Investigation

Linear cascades have long been important in the testing of axial flow turbines and compressors. A cascade is a stationary array of blades constructed for the measurement of aerodynamic effects around the blades. Flowfield conditions are varied independently of each other in order to yield performance and efficiency data, relate flow turning angles to the blade geometry, or give qualitative clues about conditions for separation. Cascade testing has brought about the development of correlations that have been used for many current day design procedures [32]. In the present study, experimental cascade results provided reliable data of the aerodynamic properties to validate the CFD predictions.

2.1 Linear Cascade Geometry

The cascade geometry shown in Figure 2.1 is typical of compressor/turbine blade cascade test setups. The spacing (s) or pitch is defined as the distance in the tangential direction between corresponding points on adjacent blades. The chord (c) is equal to the linear distance between the front or leading edge and the rear or trailing edge of the blade. The camber line is the mean line of the blade profile. It extends from the leading edge to the trailing edge, midway between the pressure and suction surface. The stagger angle (ξ) is the angle between the chord line and axial turbine direction. The inlet and outlet flow angles are defined as the angle between the fluid flow direction and machine axial direction at the blade inlet and outlet, respectively. The inlet and exit velocities can be broken down into their axial (x) and tangential (y) components to form typical velocity triangles (Fig. 2.1). The solidity or the ratio of c/s is another important

parameter for cascade aerodynamics. The higher this ratio, the more closely packed are the

blades.
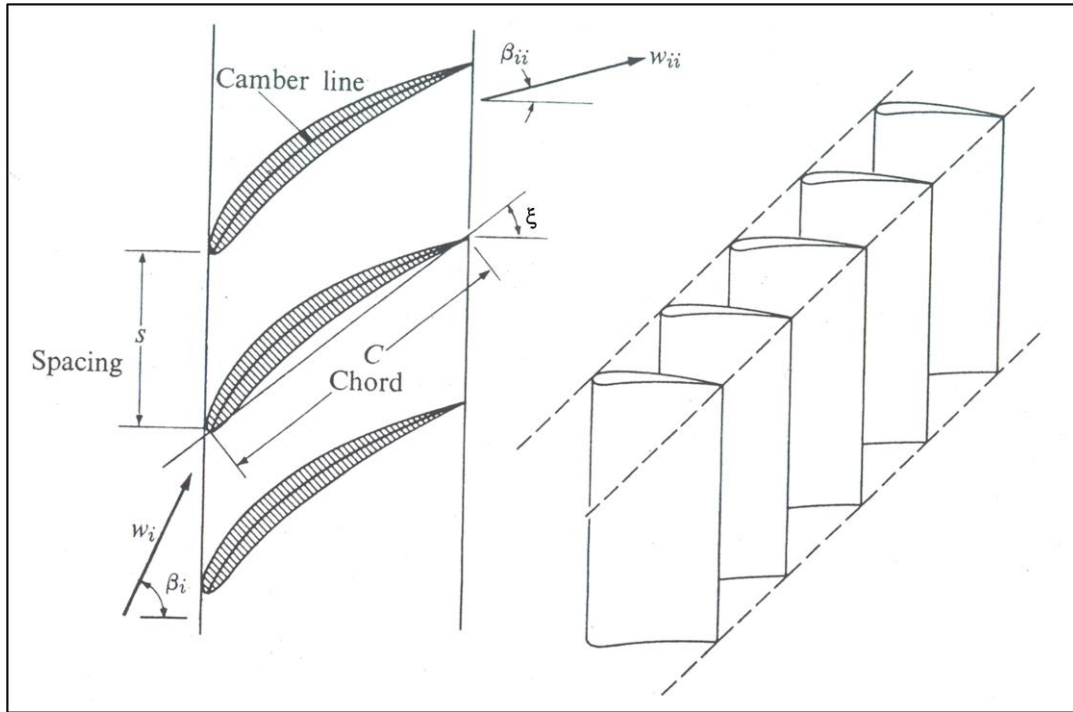
Figure 2.1. Diagram of a typical rectilinear cascade geometry [32]

2.2   The AFRL Low Speed Wind Tunnel

The experimental investigations used for comparisons with the CFD results were

conducted in the Air Force Research Lab (AFRL) Low Speed Wind Tunnel (LSWT) at Wright

Patterson Air Force Base [18,34-40]. The wind tunnel was a modified Aerolab Corporation open

loop tunnel. A photo of facility and a schematic of the test section is shown in Figure 2.2. The

inlet bell-mouth was 3.05m wide and 2.67m tall. The wind-tunnel test section is 1.22m wide and

0.85m tall at the inlet and houses the linear turbine case cascade. A 125-hp electric motor drives

an axial flow fan which is capable of producing air speeds up to 80m/sec. A honeycomb flow

straightener led to a convergent nozzle which reduced the flow area by 87%. Stryofoam inserts

were placed in the flow straightener to help minimize corner vortices and to provide freestream

uniformity of better than 1% with a turbulence intensity of approximately 0.5%. An optional turbulence grid can be installed yielding freestream turbulence levels up to a maximum of approximately 4%. Turbulent length scales with these grids have been characterized by both Lake [18] and McQuilling [33].

The test section of the cascade wind tunnel (Fig. 2.2(b) had a central hinge pivot joint that allowed the inlet and outlet flow angles to be set for the referenced tests involving all airfoils studied in this research. Eight airfoils with an outboard pressure surface blade were bolted to acrylic endplates and placed in the test section. The blade axial chord was 0.18m with span of 0.88m to ensure two-dimensional flow over the midspan region of the blade. The cascade test section exhibited good uniformity and periodicity as confirmed by Lake [18].
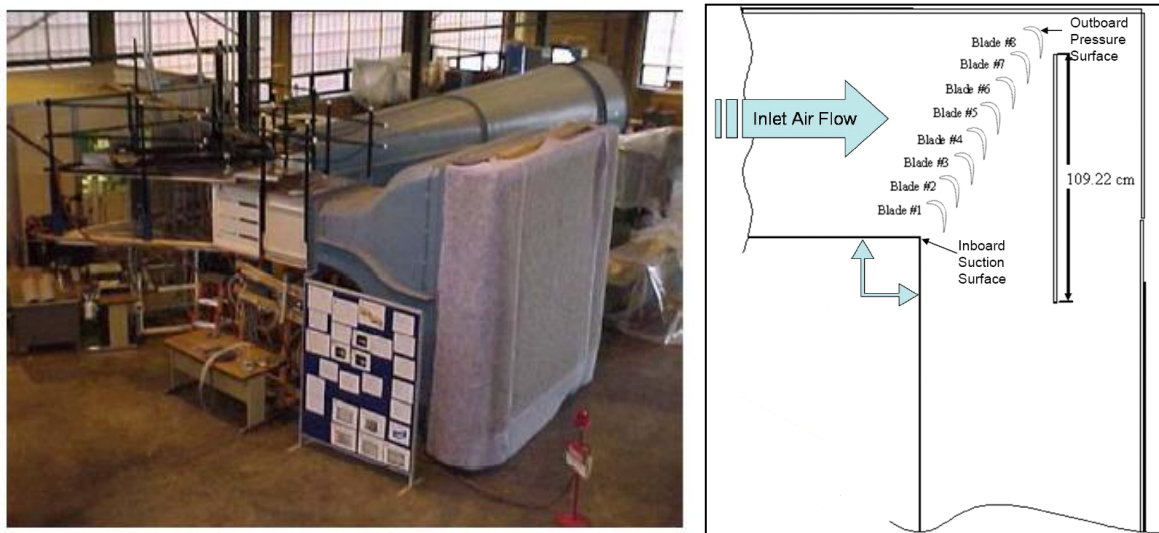
Figure 2.2. (a) AFRL Low Speed Wind Tunnel Facility[35] and (b) view of the test section [36]

2.2.1 Design of Moving Bar Wake Generator

A moving bar wake generator was designed by Nessler *et al.* [37] for the AFRL Low Speed Wind Tunnel in order to simulate the conditions in a low pressure turbine stage. The objective was to produce periodic unsteadiness in the flow impinging on the linear cascade to

CFD Modeling of Separation and Transitional Flow in
Low Pressure Turbine Blades at Low Reynolds Numbers

simulate the effect of upstream vane wake shedding [37]. The wake generator consisted of 0.318cm diameter unidirectional carbon fiber rods spaced 17.9cm apart which matched the trailing edge boundary layer and blade spacing of the Aft-Loaded L1A blade to be presented and discussed in further detail in Section 3.1.3. The rods were oriented vertically and fastened to a hollow pin chain which was directed through a series of sprockets and chain guides. A 3 horsepower variable frequency motor drove the chain system at speeds up to 5.0m/sec to match inlet flow velocities for Reynolds numbers below 50,000. A design optimization routine produced a track configuration with a length of 8.4m using 18 cylindrical rods equally spaced across a 3.04m span. The configuration maximized the number of primary wakes being measured while minimizing the cycle time before the first secondary wake passed through the cascade inlet. Figure 2.3 shows a track configuration and a CAD model of the wake generator.

Linear spring tensioner
Chain Guides
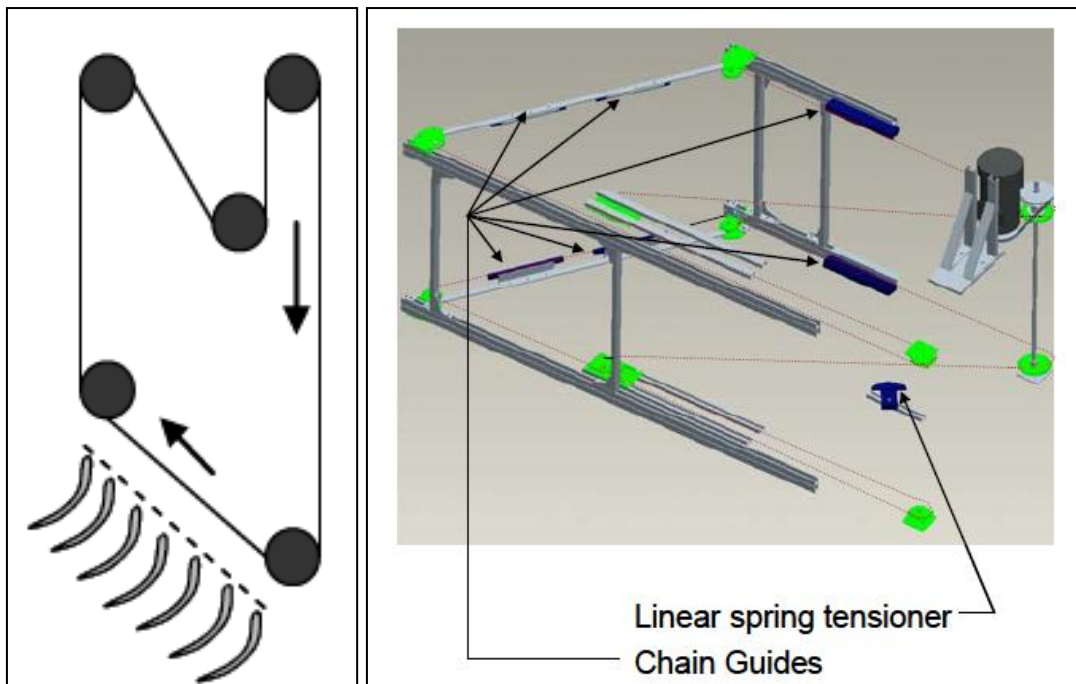
Figure 2.3. (a) Track configuration and (b) mechanical design CAD model of moving wake generator track [37]

CFD Modeling of Separation and Transitional Flow in
Low Pressure Turbine Blades at Low Reynolds Numbers

2.3 Measurement Techniques

Flow measurements from several different experimental studies in the AFRL LSWT were used for comparison with the CFD results. All experimental measurements were done on the middle blade to reduce side-wall effects from the cascade. Inlet Reynolds numbers were set based on inlet velocity measurements and the blade axial chord length. Surface static pressure, Particle Image Velocimetry, and wake loss measurements were made over a wide range of Reynolds numbers and freestream conditions. The next sections describe each measurement technique in greater detail.

2.3.1 Surface Static Pressure Measurements

Static pressure measurements were made using up to forty static pressure taps placed around the blade pressure and suction surface.   A Druck pressure transducer with a measurement range of 0-2.0 in-H_2O was used for static pressure coefficient calculations. The static pressure coefficient (C_p) is calculated using Eq. (2.1),

$$C_p = \frac{\left(\overline{P_{0,i}} - \overline{P_s}\right)}{\overline{q_i}}$$

(2.1)

where $\overline{P_{0,i}}$ is the average inlet total pressure, $\overline{q_i}$ is the average inlet dynamic pressure, and P_s is the static pressure on the surface of the blade. Measurements taken by Bons *et al.* [38] and Marks *et al.* [35] were used for static pressure coefficient comparisons with the CFD results.

2.3.2 Wake Loss Measurements

An upstream Pitot-static probe and a downstream total pressure Kiel probe were used to measure the static and total pressure upstream and the downstream blade wake total pressure. Each of the probes was mounted on a pitchwise traverse. A -0.2 to 0.8 in-H_2O Druck pressure

transducer was used for the wake loss measurements. The local total pressure loss coefficient was calculated based on these measurements using Eq. (2.2) by taking the time-averaged difference between the inlet and outlet total pressure and dividing by the difference between the time-averaged inlet total and static pressure.

$$TPLC = \frac{\overline{\left(P_{0,inlet} - P_{0,outlet}\right)}}{\overline{\left(P_{0,inlet} - P_{inlet}\right)}} \qquad (2.2)$$

The integrated total pressure loss coefficient was calculated for one pitch (*s*) using Simpson's rule based on the local total pressure loss coefficient with the equation

$$TPLC_{\text{int}} = \frac{1}{s}\int_{-s/2}^{s/2}\left(\frac{P_{0,inlet} - P_{0,outlet}}{P_{0,inlet} - P_{inlet}}\right)ds \qquad (2.3)$$

Performance of the blade airfoils was evaluated based on the total pressure loss coefficient, which is an indirect measurement of the entropy generation. As entropy is generated, the total pressure at the outlet decreases due to the blade airfoil trailing edge wake and the loss coefficient increases. Inlet and outlet turbulence intensity measurements were made at the same locations using a single element hot film.

2.3.3 Particle Image Velocimetry

Particle Image Velocimetry (PIV) involves two main steps. First, a plane within the flowfield is created by illuminating seeding particles with a thin, laser-light sheet. The laser-light sheet was formed using a combination of optical lenses. The light scattered by seeding particles in the illumination plane was recorded using double-exposure photographs. In the second step, the ratio of the measured displacement between successive images of the same seed particles and the known change in time was used to calculate the local fluid velocity.
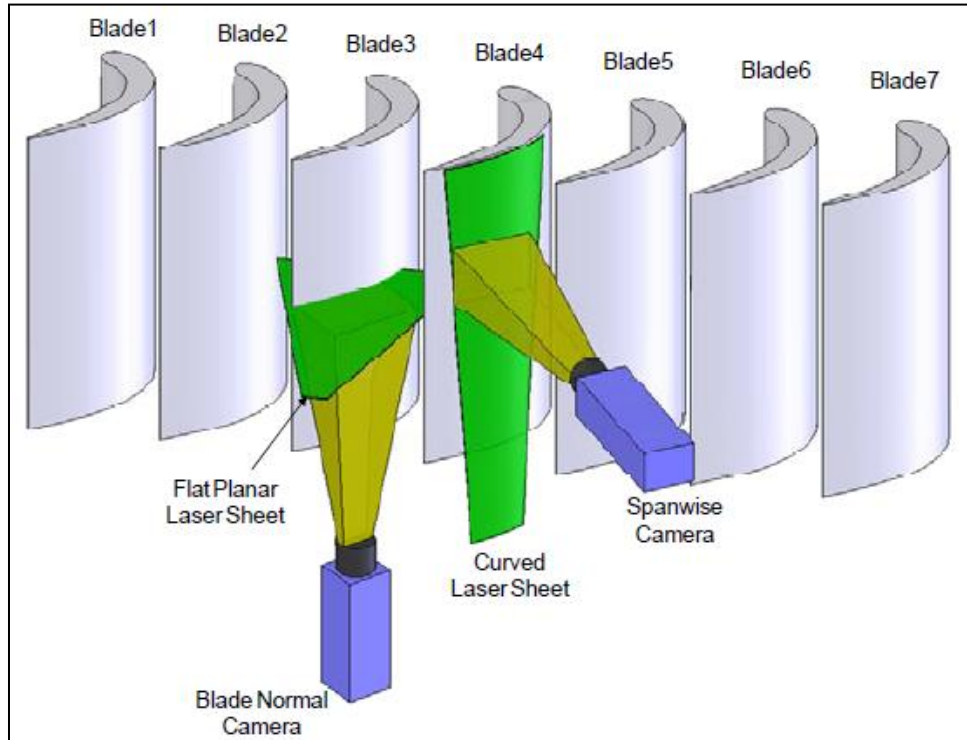
Figure 2.4. Schematic of PIV setup of laser and camera[35]

A PIV system was implemented in the Low Speed Wind Tunnel facility as shown in Figure 2.4. The lasers and cameras were mounted underneath and adjacent to the cascade. A dual-head, flashlamp-pumped Nd:YAG laser was used as the laser source, capable of dual 120mJ pulses at 15Hz repetition rate. Scattering from the seed particles was recorded on high resolution CCD digital camera sensors with a 1600x1200 pixel resolution at a maximum framerate of 30frames/sec. Two frames can be recorded sequentially with a time spacing of 100-200μsec depending on the flow velocity and magnification. Image pairs from the CCD cameras were recorded at a frequency of 10Hz. The camera lens provided a field of view of 119x158mm. The uncertainty PIV measurements was found to be associated with the velocity calculation that involves the displacement of pixels, the time intervals between exposures, and the magnification of the digital image relative to the object. It was found the uncertainty in the velocity to yield a maximum error of <2% in the freestream velocity and ~10% in the viscous region [35].

CFD Modeling of Separation and Transitional Flow in
Low Pressure Turbine Blades at Low Reynolds Numbers

The blade normal PIV images were primarily used for flowfield comparisons with the CFD results. Boundary layer velocity profiles were extracted normal to the blade surface from the PIV experiments of Marks *et al.* [35] and Woods *et al.* [39]. This PIV technique has successfully demonstrated the resolution necessary for examining flow features in complex flowfields [41].

2.4 Description of LPT Blade Airfoil Geometries

The three different LPT blade airfoils used in this study have different blade loading characteristics. The Zweifel blade force coefficient was used as the parameter to compare the blade loading for each LPT blade airfoil. The incompressible form of the Zweifel blade force coefficient, Z, is calculated with Eq. (2.4)

$$Z = 2\frac{s}{C_x}\cos^2\alpha_{out}\left(\tan\alpha_{in} - \tan\alpha_{out}\right) \tag{2.4}$$

where C_x is the axial chord, α_{in} and α_{out} is the inlet and outlet flow angles, respectively and s, is defined as the blade pitch. The Zweifel coefficient is a measure of the amount of work which can be extracted from a turbine blade and was originally developed to determine the number of blades and solidity needed for optimal turbine performance [33].

A study done by Curtis *et al.* [42] used LPT blade airfoils with a $Z_w \approx 1$ where the suction surface pressure distribution was changed using flaps and inserts over Reynolds number range of 70,000 - 400,000. They proposed that the two most significant factors that determine the suction surface velocity distribution are the degree of deceleration along the blade surface and the location of the velocity peak. The degree of deceleration was defined as the magnitude of the adverse pressure gradient along the suction surface of the LPT blade airfoil. The location of the velocity peak describes the loading characteristic of the LPT blade where the minimum pressure

is located on the airfoil. LPT blade designs were given the classification of front-loaded, mid-

loaded, or aft-loaded depending on the location of the velocity peak on the blade suction surface.
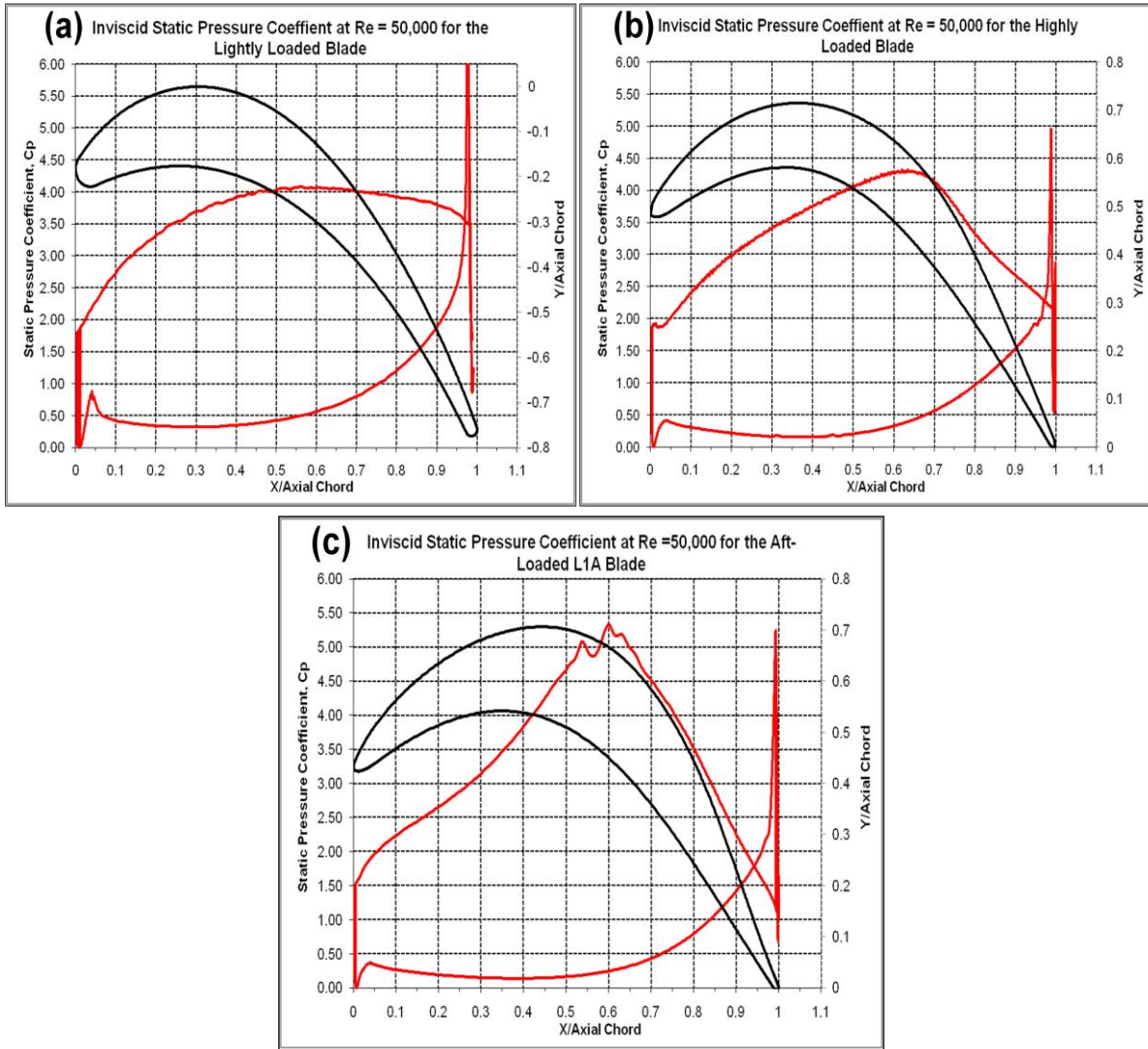
Figure 2.5. Inviscid static pressure coefficient distributions and blade profiles for the (a) Lightly Loaded, (b) Highly Loaded, and (c) Aft-Loaded L1A blade airfoils at Re =50,000

2.4.1   The "Lightly Loaded" LPT Blade Airfoil

The LPT blade airfoil defined as "Lightly Loaded" with a Z_w = 0.94 was based on the

midspan airfoil of a typical three-dimensional LPT rotor blade. The axial chord length, C_x, and

axial solidity were 17.78cm and 1.20, respectively.   The inlet and outlet flow angle for the

Lightly Loaded blade airfoil were 30.75° and 60.94°, respectively. Figure 2.5(a) shows the blade

CFD Modeling of Separation and Transitional Flow in
Low Pressure Turbine Blades at Low Reynolds Numbers

profile for the Lightly Loaded blade airfoil and the inviscid distribution of the static pressure coefficient along the blade surface at Re = 50,000. The location of the peak velocity corresponded to the same location of the peak pressure coefficient. This peak was found at the 56.0% axial chord location, indicating that the Lightly Loaded blade is more of a mid-loaded blade design. The more upstream the peak velocity location, the more the blade will be intrinsically separation resistant when operated at low Reynolds numbers. Also, the slope of the pressure coefficient downstream of the peak pressure location is relatively flat indicating a very weak adverse pressure gradient. Flow separation is less likely to occur because there is little total pressure change from the peak velocity location to the trailing edge.

Experimental measurements of the flow over the Lightly Loaded blade were performed by Garmoe [36] in the LSWT. Wake total pressure loss measurements were collected at an inlet Reynolds number range of 10,000-100,000 and inlet turbulence intensity, Tu = 1%. Figure 2.6 show the total pressure loss coefficient profiles along with the integrated total pressure loss coefficient. The integrated value of the loss coefficient was plotted as a function of the inlet Reynolds number including the experimental error bars calculated based on the Reynolds number variance. The trend in both plots indicated that as the Reynolds number decreased, the magnitude and width of the loss coefficient distribution increased. Also, boundary layer velocity profiles were taken at several locations normal to the blade suction surface and indicated very little evidence of separation on suction surface, not even at the lowest inlet Reynolds number. It was later discovered that the hot-film anemometers used in the study were incorrectly calibrated, so only the wake loss coefficient distributions were used for comparisons with the CFD results [36].
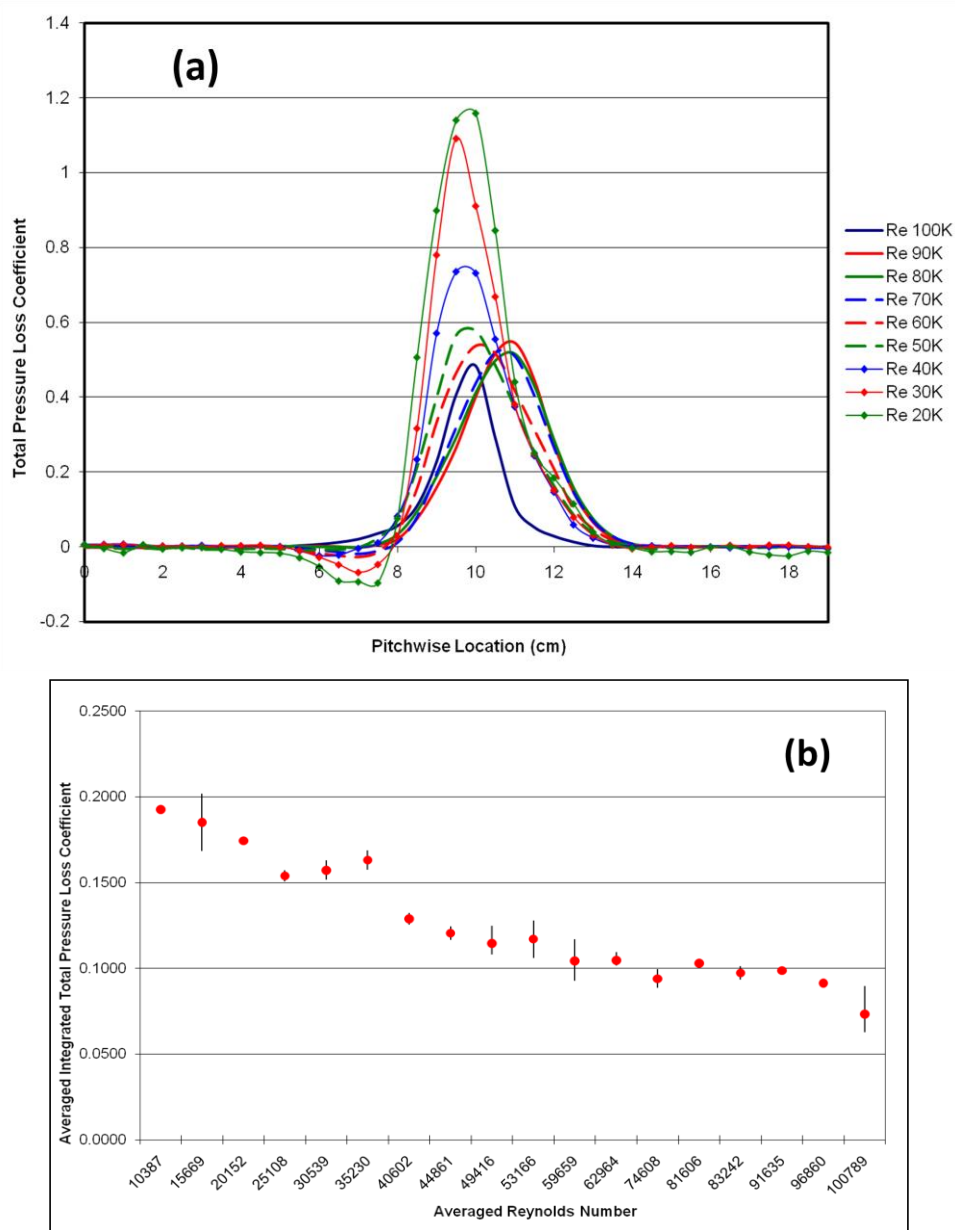
Figure 2.6. (a) Wake total pressure loss coefficient profiles (b) and integrated loss coefficient with error bars at Re =10,000-100,000 for the Lightly Loaded blade airfoil

2.4.2 The "Highly Loaded" LPT Blade Airfoil

The second LPT blade geometry used was the Pack-B research LPT blade with a $Z = 1.07$ and defined as "Highly Loaded". Pratt & Whitney introduced the Highly Loaded LPT design in order to provide a current higher lift design with an improved low Reynolds number efficiency [33]. The Highly Loaded blade is an incompressible Mach number scaled version of a

*CFD Modeling of Separation and Transitional Flow in
Low Pressure Turbine Blades at Low Reynolds Numbers*

conventional LPT geometry used in a commercial aircraft turbine engine. The axial chord length

was 17.78cm with an axial solidity of 1.13. The inlet and outlet flow angle was 35° and 60°,

respectively. Figure 2.5(b) indicates the peak velocity location was 62.1% of the axial chord for

the Highly Loaded blade and was located more downstream compared to the Lightly Loaded

blade. The Highly Loaded blade is therefore an aft-loaded blade design [34]. The slope of the

pressure coefficient is downstream of the peak velocity location creating a strong adverse

pressure gradient on the blade suction side. The strength of the adverse pressure gradient and

lower solidity makes flow separation more likely to occur at low Reynolds numbers.
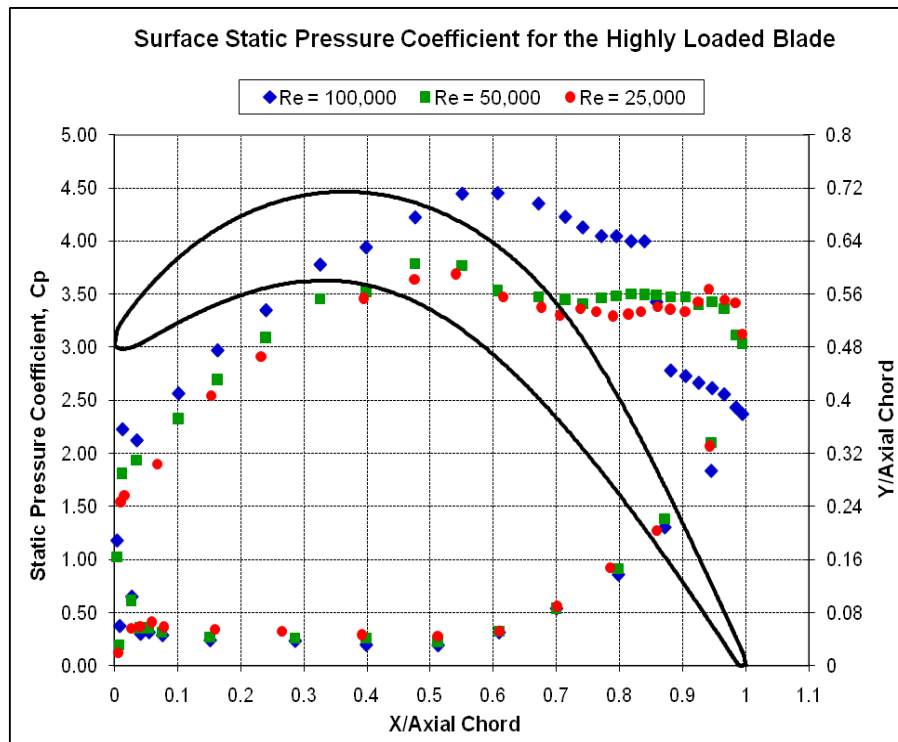
Figure 2.7. Experimental measurements of the static pressure coefficient for the Highly
Loaded blade airfoil taken by Bons *et al.* [38]

The Highly Loaded blade has been extensively tested in the LSWT in several different

experimental studies [36-40] mainly due to its aerodynamic characteristics at low Reynolds

numbers. Those studies indicated the Highly Loaded blade tends to separate at Reynolds

numbers of 100,000 and below. Figure 2.7 shows the static pressure coefficient measurements

taken by Bons *et al.* [38] at Re = 25,000, 50,000, and 100,000. The formation of a plateau where

the static pressure remained constant after the maximum C_p location was an indicator of

boundary layer separation on the suction surface. At the Re = 100,000, this plateau began at the

75% axial chord and continued downstream to 88% axial chord. The decrease in C_p downstream

of 88% axial chord indicated that the boundary layer reattached to the blade surface, forming a

closed separation bubble on the suction surface. The distribution of the static pressure for Re =

50,000 and 25,000 show the same trend where the constant C_p plateau begins at approximately

60% axial chord and continues downstream of that location to the blade trailing edge which

indicates a separation region at the rear of the blade.
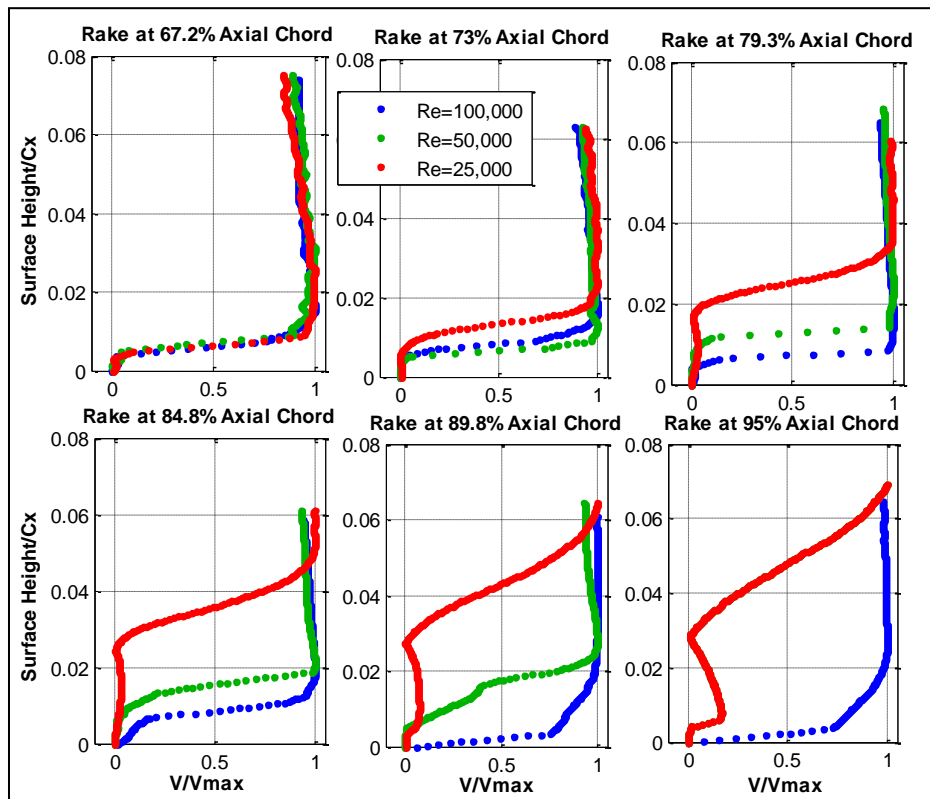
Figure 2.8. Mean boundary layer velocity profiles extracted from PIV measurements of Woods *et al.* [39] for the Highly Loaded blade

Chapter 2. Description of Experimental Cascade Configurations Utilized in the Investigation

Mean boundary layer velocity profiles were extracted from the PIV experiments taken by Woods *et al.* [39] shown in Figure 2.8 at all three Reynolds numbers and 0.6% freestream intensity. These profiles were extracted normal to the blade surface at 67.2%, 73%, 79.0%, 84.8%, 89.8%, and 95% axial chord locations. At the Re = 100,000, the boundary layer profiles reconfirmed the trend observed from the static pressure measurements that a closed separation bubble was present on the suction surface. This separation bubble was formed due to the high energy present in the freestream flow caused the shear layer re-energizing the boundary layer and reattaching the flow to the blade surface. This flow behavior is known as separation-induced turbulent-transition as described by Halsted *et al.* [3]. At the Re = 50,000, the boundary layer profiles indicated the separation region extended to the trailing edge because there was not enough energy present in freestream to cause boundary layer reattachment. The further decrease in the Reynolds for the Re = 25,000 case caused the separation region to increase compared to the higher Reynolds number cases.
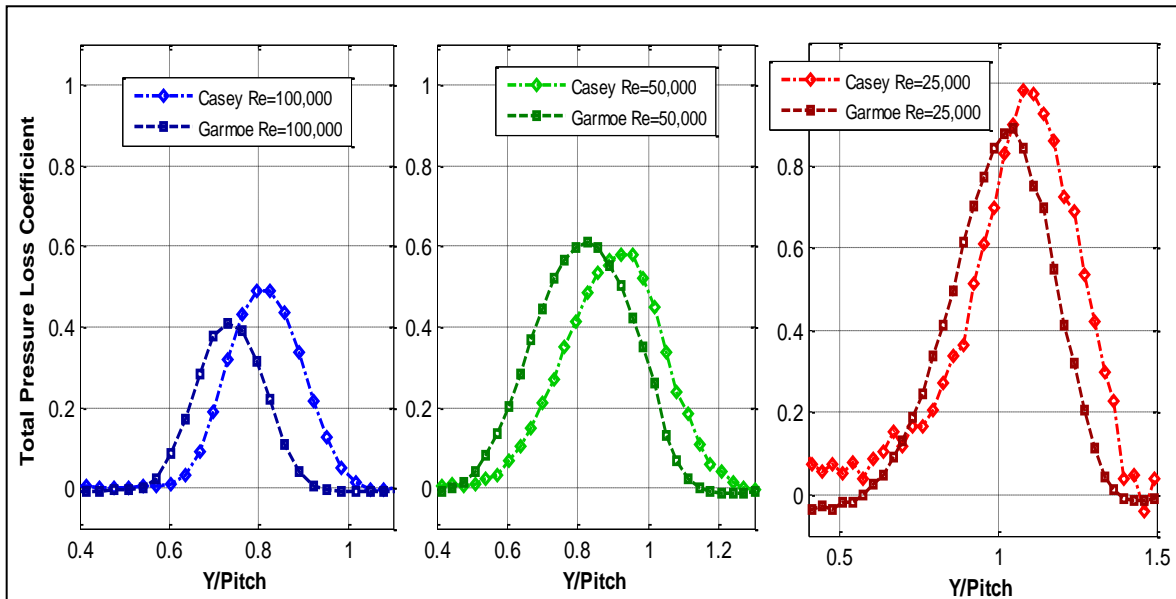
Figure 2.9. Wake total pressure loss coefficient measurements of Garmoe [36] and Casey *et al.* [40] for the Highly Loaded blade

Figure 2.9 shows the wake total pressure loss coefficient profiles as measured by Garmoe [36] and Casey *et al.* [40] for all three inlet Reynolds numbers. The discrepancy in the measurement of the wake loss coefficient between the two experiments was due to the difference in the inlet turbulent boundary conditions. For the Re =100,000 Garmoe [36] reported the inlet turbulence intensity as 0.735% compared with 0.437% for Casey *et al*. [40] measurements. As the Reynolds number decreased, the magnitude of the loss coefficient and the width of the region increased due to growth of the separation region. The Re = 100,000 case showed that even though a closed separation bubble was present, the total pressure loss was not significantly higher due to the attached turbulent boundary layer downstream of the separation bubble. An approximate 50% increase in the peak loss coefficient compared to Re = 100,000 was observed for the Re = 50,000 due to the increase in the amount of separated flow on the suction surface. The inlet turbulence intensity was 0.34% for the Casey *et al*. [40] measurements and 0.84% for Garmoe's [36] measurement at Re = 50,000. At Re = 25,000, a Tu = 0.36% was used in the Casey *et al.* [40] experiment while a Tu = 0.89% was used in the Garmoe [36] experiments. The amount of separated flow was the highest for the Re = 25,000 case, and as a result the peak loss coefficient was the highest and the width of the wake region was larger than for the higher inlet Reynolds number cases.

2.4.3 The "Aft-Loaded L1A" LPT Blade Airfoil

Clark and Koch [43] designed an aft-loaded LPT blade airfoil with Z_w = 1.23, a 15% increase in the blade loading compared to the Highly Loaded blade. The blade was designated as the "Aft-Loaded L1A" LPT blade airfoil. The axial chord length was 17.76cm with an axial solidity of 0.99. The inlet and outlet flow angle was 35° and 60°, respectively as set with the Highly Loaded blade. The peak velocity location at 60% axial chord location had a similar peak

CFD Modeling of Separation and Transitional Flow in
Low Pressure Turbine Blades at Low Reynolds Numbers

velocity location as the Highly Loaded blade (Figure 2.5(c)). Yet, the adverse pressure gradient

was much stronger than was observed for the Highly Loaded blade, which was due to the

decrease in the blade solidity. This indicated that the Aft-Loaded L1A blade will be more prone

to flow separation on the suction surface than both Lightly Loaded and Highly Loaded blades.
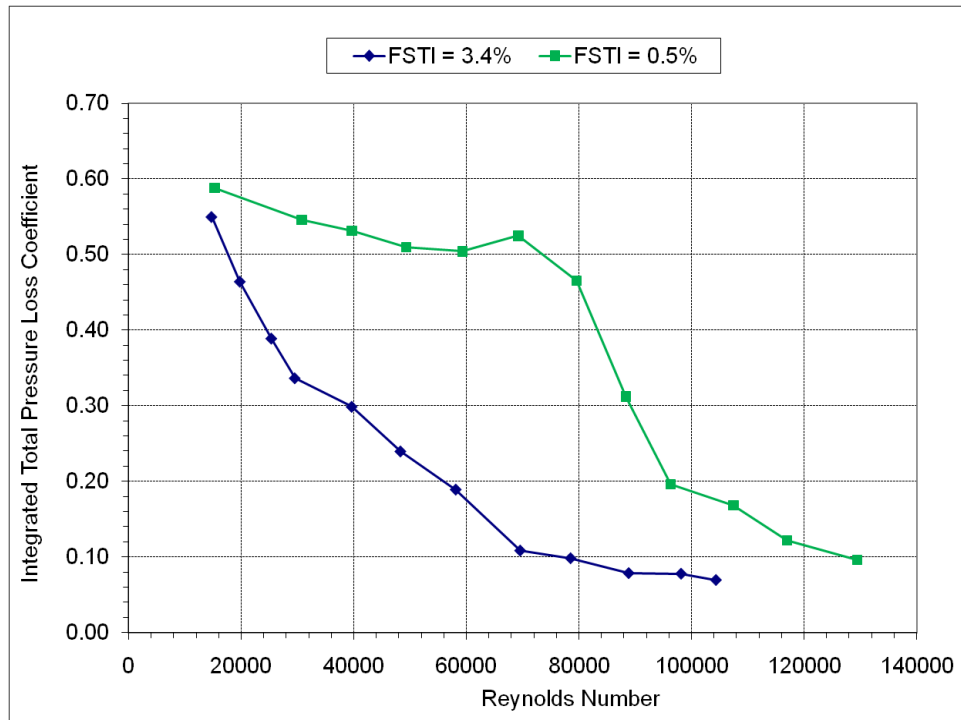
Figure 2.10. Integrated wake total pressure loss coefficient measurements of Marks *et al.* [40] for the Aft-Loaded L1A blade at high and low turbulent intensities

Marks *et al.* [35] experimentally investigated the aerodynamic characteristics of the Aft-

Loaded L1A blade in the LSWT. The wake loss coefficient and the static pressure distribution

along the blade surface were measured at both low and high freestream turbulent intensities.

Also, flow visualizations were completed using PIV measurements in the blade normal direction

at Re = 15,000-120,000. Figure 2.10 shows the inlet Reynolds number effect on the integrated

total pressure loss coefficient calculated using Eq. 2.3 at both turbulence intensity levels. The

loss profile for Tu = 0.5% showed a gradual increase in the loss coefficient with decreasing

Reynolds number down to Re ≈ 96,000. This was followed by a more rapid rise at Re ≈ 60,000-

CFD Modeling of Separation and Transitional Flow in
Low Pressure Turbine Blades at Low Reynolds Numbers

96,000, and then a more gradual increase as Reynolds number was decreased further. The Re ≈ 60,000-96,000 region was referred to as the loss knee and its behavior was attributed to flow separation without reattachment on the suction surface [44]. The loss profile at Tu = 3.4% has a gradual increase in the loss coefficient with decreasing Reynolds number compared to the loss knee of the Tu = 0.5% case. Also, the magnitude of the loss coefficient decreased compared to the Tu = 0.5% case, which was due to the elevated amount of freestream turbulence causing a reduction in flow separation and lower total pressure loss.
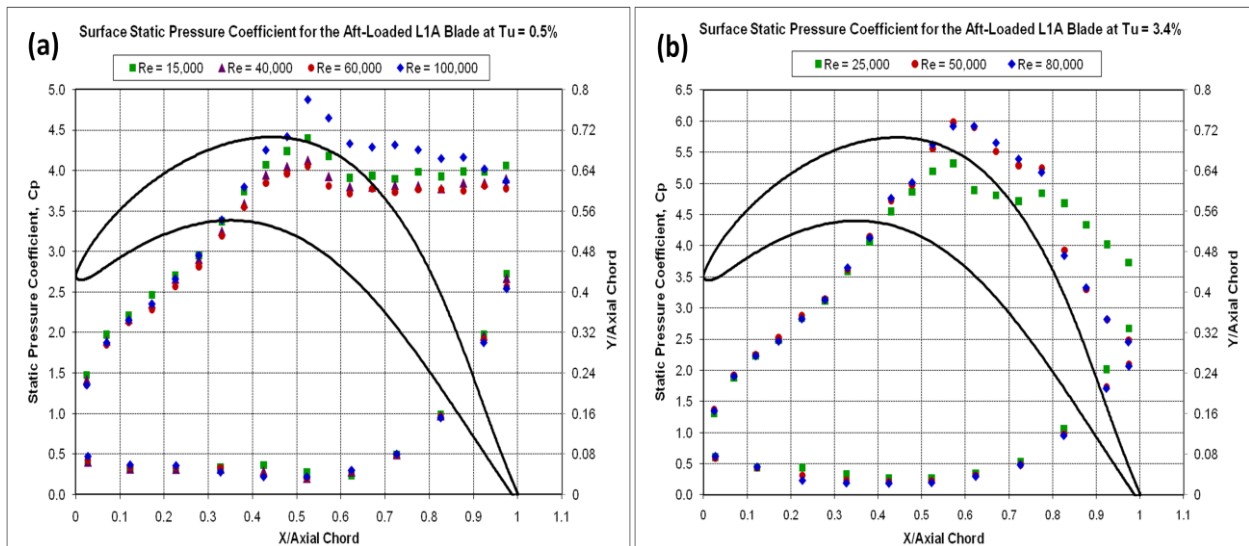
Figure 2.11. Measurements of the Surface static pressure coefficient of Marks *et al.* [40] for the Aft-Loaded L1A blade at high and low turbulent intensities

The surface static pressure coefficient is shown in Figure 2.11 for both low and high turbulent intensities. The C_p distribution at the Tu = 0.5% indicated a separated flow region on the suction surface continuing to the blade trailing edge for all Reynolds numbers shown. The separation location was approximately 57% axial chord for Reynolds number below 60,000 and 62% axial chord for the Re = 99,000 case. A closed separation bubble was observed for the Tu = 3.4% C_p measurements (Fig 2.11(b)) at Re = 50,000 and 80,000 which began at approximately 62% axial chord and reattached between the 78% and 83% axial chord. The separated flow

CFD Modeling of Separation and Transitional Flow in Low Pressure Turbine Blades at Low Reynolds Numbers

region starting at the 62% axial chord location extended all the way to the trailing edge for the

Re = 25,000 case.
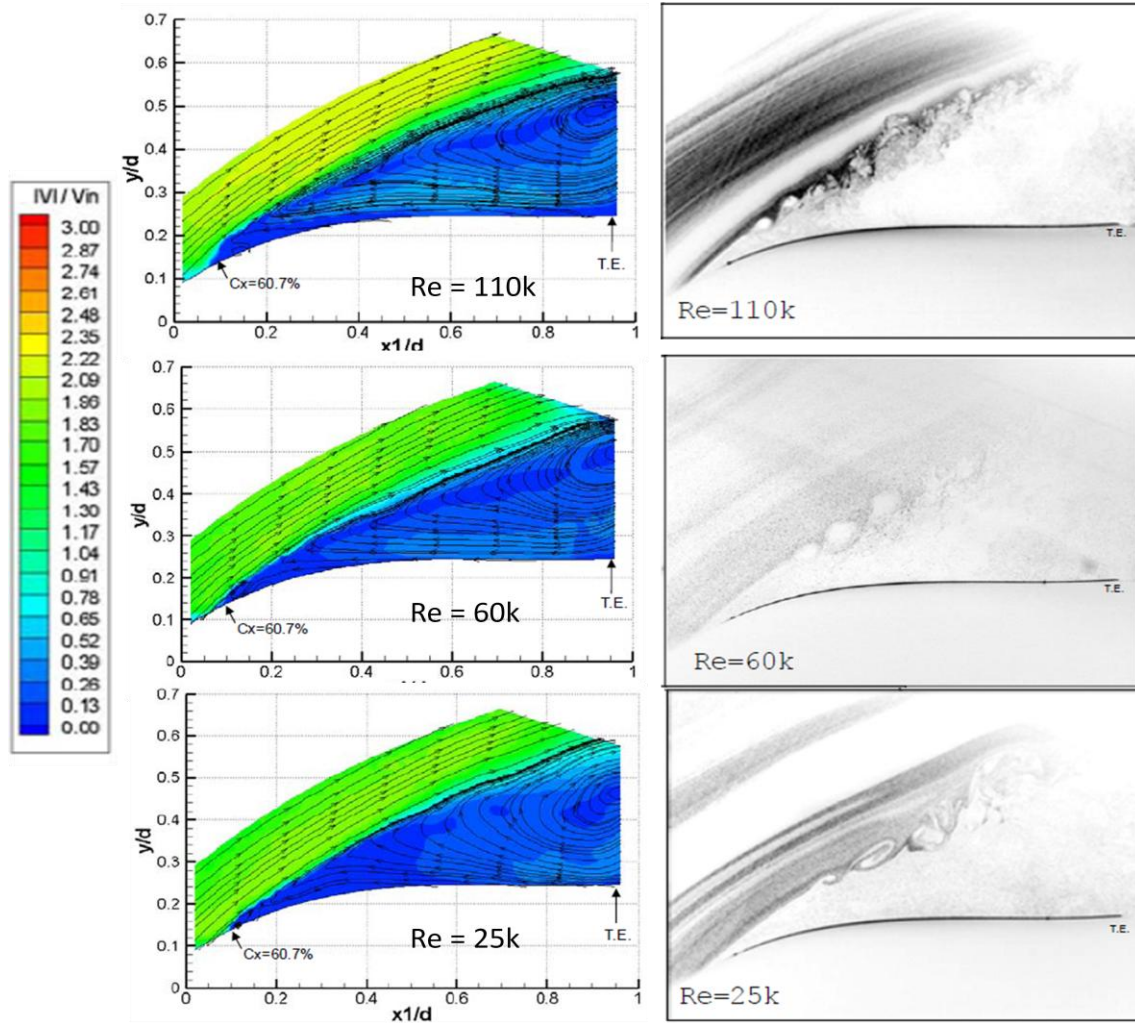
Figure 2.12. Mean velocity contours obtained from PIV measurements and instantaneous flow visualizations of Marks *et al.* [40] for the Aft-Loaded L1A blade at Tu = 0.5%

The PIV measurements confirmed the trends observed from the behavior of the static pressure distribution. Figure 2.12 shows contour plots of the average velocity magnitude obtained using the PIV measurement technique including instantaneous flow visualizations at Tu = 0.5%. At the lowest Reynolds number of 25,000, the flow visualizations show that the separated shear layer produced large vortices that traveled downstream. As the Reynolds

number was increased to the Re = 60,000 and 110,000 cases, these vortices reduced in size and transitioned to turbulent vortices. The average velocity contours for all Reynolds numbers did not show the unsteady vortices as a result of the flow averaging but, a recirculation region was present due to separated flow. In Figure 2.13, the instantaneous flow visualizations at Tu = 3.4% show that at Re = 90,000, the initially laminar flow boundary layer grew in thickness and transitioned to turbulence. The PIV average velocity contour plot showed a separation bubble present between approximately the 60% and 85% axial chord locations, which was consistent with the static pressure measurements. At the Re = 50,000, the separation bubble region increased in thickness and at the Re = 90,000 case, the boundary layer became attached to the blade surface and underwent turbulent transition. The flow remained separated without reattachment for the Re = 25,000 case, similar to the lower turbulence intensity result. The instantaneous flow visualizations showed vortices generated from the separated shear layer and recirculation region present in the PIV results.

In summary, the aerodynamic characteristics and performance at low Reynolds numbers were experimentally measured for each blade airfoil. CFD models were created based on the experimental configuration of the LSWT. The experimental results presented here will be used to validate the CFD predictions and provide more insight on the flow features produced at low Reynolds numbers.
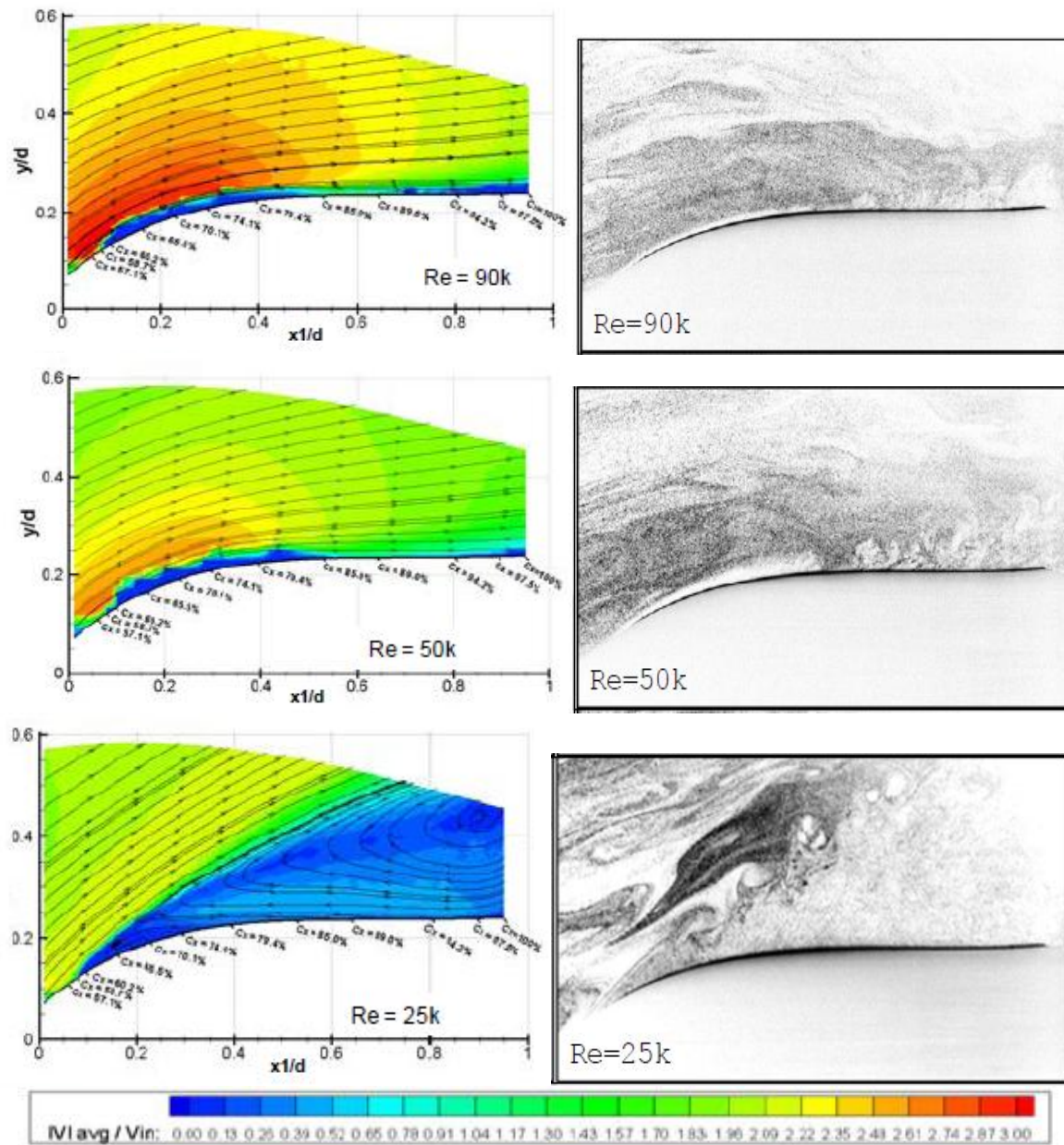
Figure 2.13. Mean velocity contours obtained from PIV measurements and instantaneous flow visualizations of Marks *et al.* [40] for the Aft-Loaded L1A blade at Tu = 3.4%

CHAPTER THREE

3. Computational Model Methodology

Numerical methods used for the current study included grid generation techniques, the CFD numerical scheme, the applied boundary conditions, discussion on the choice of turbulence models, CFD post-processing methods, and computational resources available for this study. The design of each LPT blade airfoil will be presented including a brief discussion of LPT blade design parameters. The design of the grid topology for LPT cascade geometries will be discussed including grid independence studies completed. The numerical schemes used within the CFD solver are presented along with appropriate boundary conditions. A brief summary of the current transitional flow model functionality is given including transport equations. Lastly, a description of the computational resources used to complete the CFD simulations including computing platforms available for large model simulations is provided.

3.1 Computational Grid Design Method

One key element in CFD for successful application to the modeling of fluid flow is the process of grid construction. Grids or meshes are made of discrete elements or volumes where the numerical form of the conservation laws are applied. Grid generation is an important part of completing successful CFD simulations. A well constructed grid greatly improves the quality of the CFD solution, and conversely, a poorly designed grid can lead to difficultly with the CFD simulation and poor numerical results. Grids that contain elements that are quadrilateral or hexahedral shaped cells are called structured grids. Unstructured grids contain only triangular, tetrahedral, pyramidal, and/or prismatic elements. A grid that contains both structured and unstructured grid elements is as defined as a hybrid grid.

Chapter 3. Computational Model Methodology

Structured grids have considerable advantage over other grid methods because they allow a high degree of control and high amount of skewness and stretching within a cell before the solution is drastically affected. Also, a higher degree of accuracy is achieved because the grid is often aligned with the flow. Structured grids typically require a lower amount of memory for a given mesh size and have faster convergence rate than unstructured grid solvers. The main drawback with structured grids is they require more construction time when dealing with complex geometries. Cells elements can become highly skewed and stretched in areas with high degree of curvature as are typically associated with turbine blade geometries. Most of the current grid generation software contains elliptical solvers that can be used to optimize grid smoothness and reduce the cell skewness on topologies containing a high degree of curvature.

Unstructured grids use an arbitrary collection of elements to fill the domain, typically with triangles for 2D grids and tetrahedrons for 3D grids. Automated algorithms within unstructured grids typically involve meshing the boundary and adding elements on the boundary surface or adding points in the interior and reconnecting the elements. The main advantage of using an unstructured grid is that the gridding method is highly automated and requires less construction time. They are capable of handling complicated geometries providing that the CAD geometry is of good quality. If the CAD model contains even minor errors, it can cause grid failures with the CFD solver. The triangle and tetrahedral cell elements are usually isotropic and do not stretch well. So, if refinement within a region such as a viscous layer is needed, the entire grid must be made finer in order to provide the required grid resolution. Unstructured flow solvers typical require more memory and have longer run times compared to structured flow solvers with a similar mesh size.

CFD Modeling of Separation and Transitional Flow in
Low Pressure Turbine Blades at Low Reynolds Numbers

Chapter 3. Computational Model Methodology

Hybrid grids are designed to take advantage of positive aspects of both structured and unstructured grids. Typically hybrid grids use structured grids for the local regions, for instance within the boundary layer, and unstructured grids in the main flow domain. The hybrid grid method provide full control of the shape and distribution of the structured grid in local regions, while providing automated unstructured cell creation in the main flow region. Hybrid grids do require more user expertise than unstructured meshes for design of the grid topology. CFD flow solvers using hybrid grids require the same computing requirements as unstructured grids, but the overall cells size can be reduced when compared to a purely unstructured grid.

Both two-dimensional and three-dimensional hybrid grid topologies were used to construct the CFD models for this study. The topologies were designed to provide enough resolution to capture the viscous effects within the boundary layer and wake region. The grids were designed to be adequately fine, and to reduce the amount of computational time needed for the simulations. The grid geometries were based on the experimental cascade configuration of the AFRL Low Speed Wind Tunnel. The next sections describe the grid construction technique used for each LPT blade airfoil cascade CFD model. Also, the three-dimensional grid technique used for the Highly Loaded blade airfoil will be presented.

3.1.1   Grid Technique for the 2D Cascade CFD Models

The two-dimensional grid for the cross section of the each blade airfoil is shown in Figure 3.1. The inlet and outlet of the computational domain was placed one axial chord length upstream and one axial chord downstream of the blade leading and trailing edge, respectively, for the Lightly Loaded and Highly Loaded blades. The inlet domain was located 22.86 cm from leading edge of the Aft-Loaded L1A blade, while the outlet domain was placed two axial chords downstream in the streamwise direction of the blade trailing edge. The location of the inlet and

CFD Modeling of Separation and Transitional Flow in
Low Pressure Turbine Blades at Low Reynolds Numbers

outlet domains was placed far enough from the LPT blade to encompass the experimental loss coefficient measurement locations. The mid-passage flow around the blade airfoil was modeled with the passage length equal to the blade pitch. Periodic boundaries were applied to model an infinite cascade.

Figure 3.1. Two dimensional hybrid O-H grid of the (a) Lightly Loaded, (b) Highly Loaded, and (c) Aft-Loaded L1A LPT blade airfoils
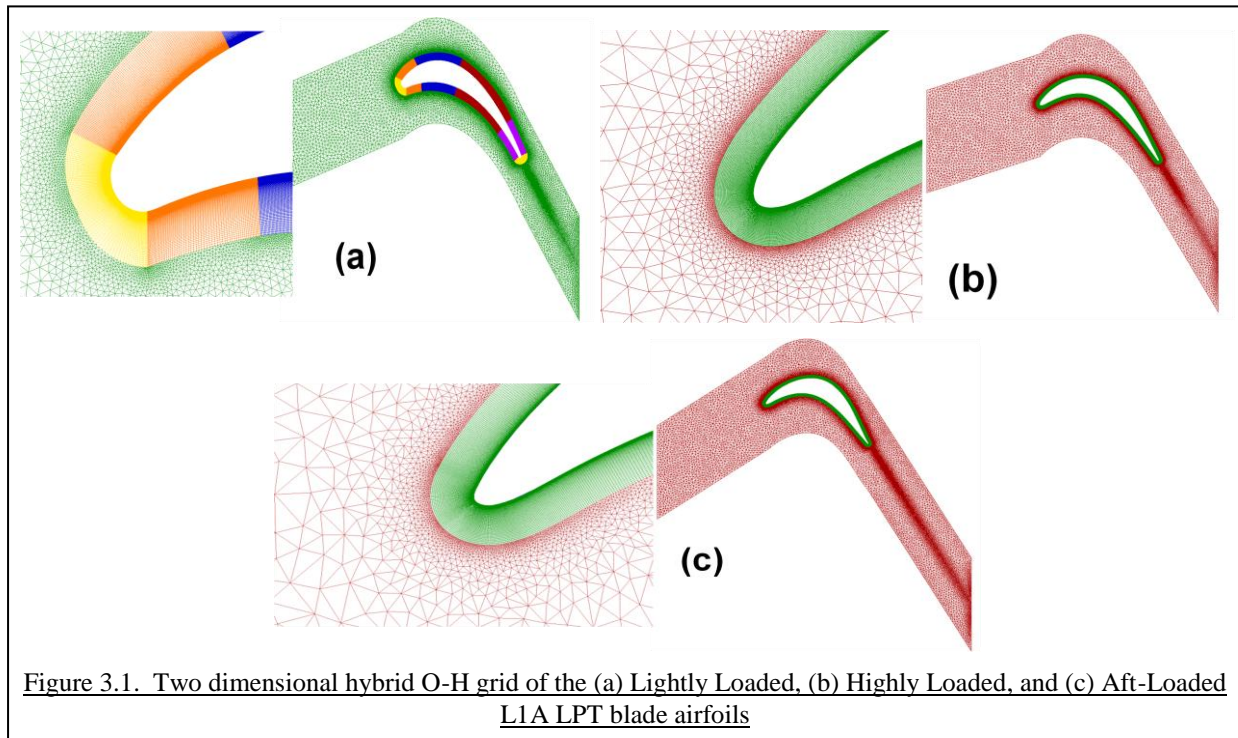
CFD Model	O-Grid Dimensions	H-Grid Dimensions	Cells	Aft-Loaded L1A Blade with Wake Generators			
				Domain	O-Grid Dimensions	H-Grid Dimensions	Total Cells
Lightly Loaded Blade	1749×110	33,209	221,081				
Highly Loaded Blade	1749×67	44,091	150,392	Inflow		733	
Aft-Loaded L1A Blade	1099×71	16,399	108,011	Wake Generator	249×46	20,266	172,904
3D Highly Loaded Blade	1099×67×51	15,698×51	5,116,700	Aft-Loaded L1A Blade	1099×71	23,018	

Table 3.1. Grid Dimensions of each Cascade CFD Model

The computational meshes used consisted of a hybrid O-H grid topology created with Gridgen® 15 mesh generation software (Figure 3.1). A structured O-grid was extruded normal to each blade surface in order to provide the resolution needed to resolve the boundary layer. The first cell wall distance was such that the y^+ was less than unity at every grid point around the

blade airfoil surface, satisfying the y^+ tolerance requirement for the transitional flow model. The average aspect ratio for each grid topology was 6.5:1, but was as high as 30:1 in cells close to the blade surface. An unstructured mesh was placed in the main flowpath consisting of triangles generated by a modified Delauney method. Triangular cell clustering was increased to provide enough resolution for the wake region generated by the trailing edge. Table 3.1 shows the grid dimensions for the structured O-grid and unstructured H-grid for each LPT blade airfoil.
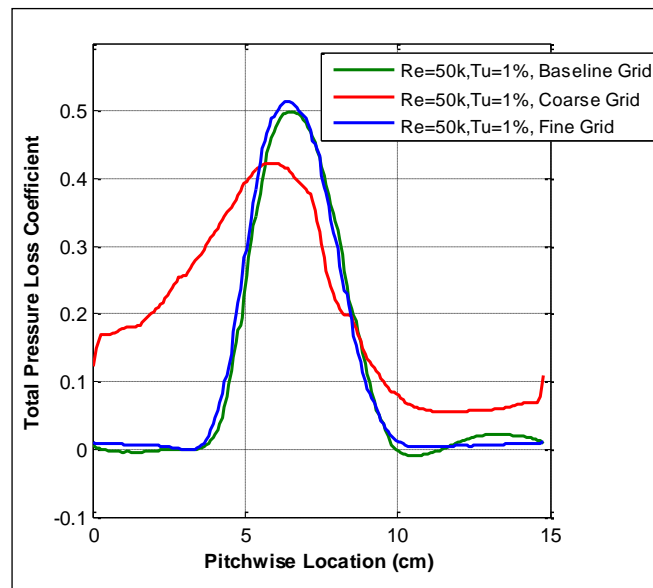
Figure 3.2. Comparison of the total pressure loss coefficient for the Lightly
Loaded blade airfoil at different grids spatial resolutions

A grid independence study was completed using the Lightly Loaded blade mesh to determine if the selected meshing scheme provides enough spatial resolution to capture the features of the flowfield within the computational domain. Two additional grid topologies were created by increasing and decreasing the number of nodes on the blade surface and in the main flowfield by 50% while maintaining the same hybrid O-H grid topology. The coarse and fine grids contained 94,846 and 451,866 cells, respectively while the baseline grid contained 238,230 cells. All three grid topologies were used in a computation at an inlet Reynolds number of 50,000, with an inlet freestream turbulence intensity of 1%, and an average turbulent length scale

CFD Modeling of Separation and Transitional Flow in
Low Pressure Turbine Blades at Low Reynolds Numbers

of 5 mm using a 2nd order spatial accurate steady flow pressure-based solver in Fluent 6.3$^{®}$. The y^{+} was less than unity around the blade surface and the turbulent transition point was the same for all three grid topologies. The wake total pressure loss coefficient in Figure 3.2 shows the effect of the wake distribution at the different grid spatial resolutions. The results from the coarse grid showed a distorted total pressure loss coefficient due to the low cell count in the wake region while the baseline and fine grid indicated a similar total pressure loss coefficient distribution. The fine grid has only 2% difference in prediction of the peak loss coefficient, while the coarse grid has 15% difference compared to the baseline grid. This indicated that the baseline grid provided enough spatial resolution to capture the effects of the flowfield in the boundary layer and within the wake. The additional grid points in the fine grid were not needed, thus making the overall grid size smaller and reducing the computational cost of running simulations. Based on these results, the resolution provided with the baseline meshing scheme was used for all three cascade CFD models.
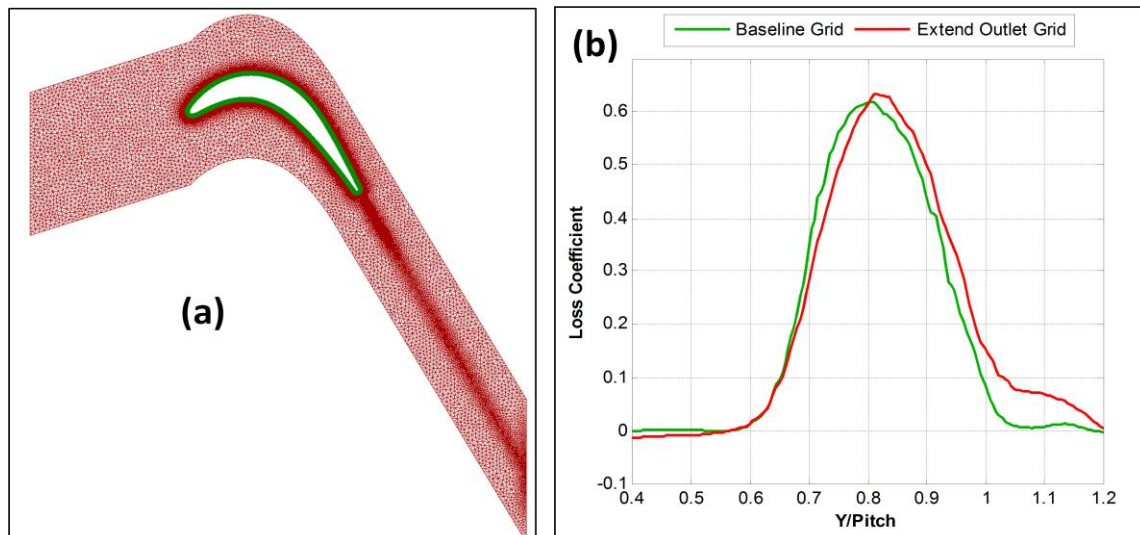
Figure 3.3. (a) Grid of the Highly Loaded blade with the extended outlet and (b) loss coefficient comparison of the baseline grid to the extended outlet grid

The length of the outlet domain from the trailing edge was varied using the Highly Loaded blade grid to determine how far the outlet boundary needed to placed from the simulated wake measurement location. A grid shown in Figure 3.3(a) was created that placed the outlet boundary two axial chord lengths in the streamwise direction from the blade trailing edge while, the baseline grid outlet boundary was one axial chord length from the blade trailing edge (Fig. 3.1(b)). Unsteady simulations were completed at a Re = 50,000 at an inlet freestream turbulence intensity of 0.6% and average turbulent length scale of 50 mm. The total pressure loss coefficient was measured across the pitch length using a 200 point simulated rake placed one axial chord length from the blade trailing edge. Figure 3.3(b) compares the loss coefficient obtained from the baseline grid to the extend outlet grid. There was a 3% difference the prediction in the peak loss coefficient for the extended outlet grid compared to the baseline result. Based on these results, the baseline grid outlet boundary was judged to be the correct length from the blade trailing edge to provide adequate measurements of wake region at a reduced overall grid size.

3.1.2   Aft-Loaded L1A Blade with Upstream Wake Generators

Figure 3.4. Two dimensional hybrid O-H grid of the Aft-Loaded L1A blade with upstream wake generators
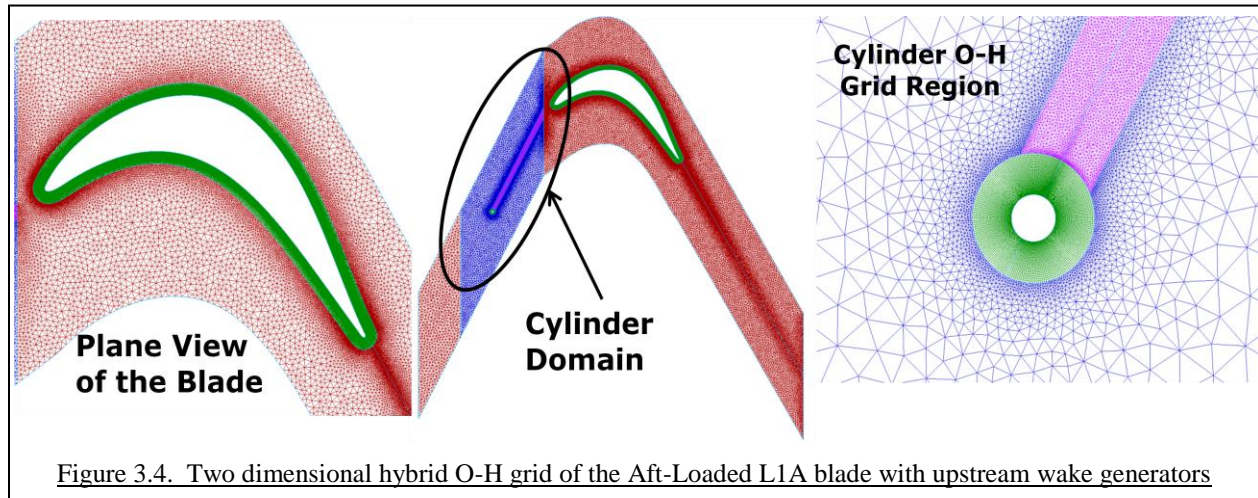
Chapter 3. Computational Model Methodology

A CFD grid of the Aft-Loaded L1A blade with upstream wake generators was constructed based on the experimental setup of Nessler *et al.* [40]. The grid consisted of a modified hybrid O-H grid of the Aft-Loaded L1A blade as shown in Figure 3.4. The inlet to the L1A blade domain was reduced to 1.53cm in the axial direction from blade leading edge. Also, the number of cells within the unstructured H-grid was increased to resolve the unsteady viscous effects within this region. The outlet of the Aft-Loaded L1A blade domain was placed 2 axial chord lengths downstream of the trailing edge in the streamwise direction to encompass the experimental loss coefficient measurement location.

Another hybrid O-H grid for a circular cylinder with a diameter of 0.318cm was placed upstream of the L1A blade. The center of the cylinder was placed a distance of 8.88cm in the axial flow direction from the leading edge of the Aft-Loaded L1A blade. The cylinder was used to generate unsteady wakes similar to the actual wakes generated from an upstream LPT vane. The cylinder grid was translated in order to simulate the effect of a passing wake from the upstream vane. The translating motion of the circular cylinder was modeled using the sliding mesh technique within Fluent 12.0. Interface zones were set up at the inlet and outlet of the circular cylinder domain at the points where the domain was moved relative L1A blade domain. The inlet boundary was placed 22.86cm in the streamwise direction from the cylinder center. The shape of the cylinder domain was based on the inlet relative flow angle, $\beta = 62.54°$, which corresponded to a flow coefficient ($\Phi = u_{axial}/u_{rod}$) of 0.817 and cylindrical rod speed, $u_{rod} = -2.298$m/sec as set in the experimental [40] results. A structured O-grid was placed around the cylinder and the unstructured H-grid was placed in the flowpath and the cylinder wake region. The unstructured cell count and clustering was made fine enough to resolve the small vortical structures produced from the cylinder (Fig. 3.4).

CFD Modeling of Separation and Transitional Flow in
Low Pressure Turbine Blades at Low Reynolds Numbers

3.1.3   Grid Technique for the 3D Cascade CFD Models

Figure 3.5 shows the three-dimensional grid domain for the Highly Loaded blade. The baseline two-dimensional structured O-grid dimensions were (1099×67) and the unstructured H-grid contained 15,698 cells in the main flowpath.   The O-grid dimensions were reduced compared to the two-dimensional grid topology in order to reduce the overall size of the grid and conserve computational resources. The grid was created by taking the original two-dimensional grid and performing a geometric extrusion to 20% of the axial chord length in the spanwise direction.   The length of the spanwise extent of the Highly Loaded blade was based on the recommendations suggested by Rizzetta and Visbal [45]. The grid provided enough spanwise distance to resolve the effects of spanwise instabilities, while keeping the grid size reasonable for successful completion of unsteady computations. The final three-dimensional structured O-grid dimensions were (1099×67×51) with the unstructured H-grid contained prism-shaped cells with the dimensions of (33,209x51). Prism-shaped cells were used instead of tetrahedral cells in order reduce overall cell count while maintaining cell quality and to reduce the three-dimensional cells skewness. The total grid size was 5,116,700 cells.
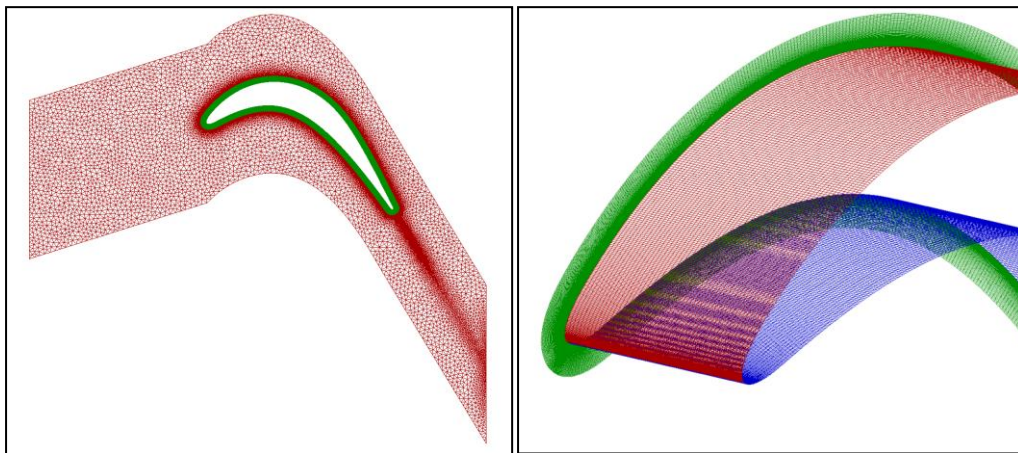
Figure 3.5. Three-dimensional hybrid O-H grid of the Highly Loaded LPT blade airfoils

CFD Modeling of Separation and Transitional Flow in
Low Pressure Turbine Blades at Low Reynolds Numbers

3.2 CFD Numerical Scheme

CFD simulations were performed using ANSYS Fluent 6.3$^{®}$ which is based on a finite volume method. The domain was discretized onto a finite set of control volumes and the general conservation equations for mass and momentum were solved on this set of control volumes. The partial differential equations based on the RANS equations shown in Eq.(3.1) and Eq. (3.2) were discretized algebraically and solved for the mapping of the flowfield.

$$\frac{\partial \rho}{\partial t} + \frac{\partial}{\partial x_i}(\rho u_i) = 0 \tag{3.1}$$

$$\frac{\partial}{\partial t}(\rho u_i) + \frac{\partial}{\partial x_j}(\rho u_i u_j) = -\frac{\partial p}{\partial x_i} + \frac{\partial}{\partial x_j}\left[\mu\left(\frac{\partial u_i}{\partial x_j} + \frac{\partial u_j}{\partial x_i} - \frac{2}{3}\delta_{ij}\frac{\partial u_i}{\partial x_j}\right)\right] + \frac{\partial}{\partial x_j}\left(-\rho\overline{u_i'u_j'}\right) \tag{3.2}$$

All solution variables represent ensemble or time averaged values. The Reynolds stress term $-\rho\overline{u_i'u_j'}$ is resolved according to the chosen turbulence model in order to close the equation. The RANS equations were discretized using the pressure-based coupled algorithm which solved a coupled system of equations comprising the momentum equations and the pressure-based continuity equation.

Steady flow solutions were initialized based on the inlet boundary conditions and iteratively run with a first-order upwind scheme until the residual tolerance for continuity, linear momentum, and turbulence variables were below 10^{-4}. Then the second-order upwind discretization scheme was used until the minimum convergence tolerance for all flow parameters was below 10^{-5}. Also, the drag and lift coefficients were monitored to determine if the steady state solution was adequately converged. Unsteady flow cases were initialized with the first-order discretization steady flow solutions and run using a second-order upwind spatial discretization with a second-order implicit temporal solver. Time steps were chosen in order to

obtain enough temporal resolution to allow the solution to converge locally within 20-30 iterations per time step.

The sliding mesh model was used in order to simulate the translating motion of the wake generators placed upstream of the Aft-Loaded L1A blade. The relative motions of stationary and rotating components were accounted for using the sliding mesh models. It is the most accurate method for simulating flows in multiple moving reference frames and yet the most computationally demanding. Unsteady interactions due to the potential flowfield, and convecting wakes needed to be accounted for, so a time-dependent solution procedure was required. Each cell zone was bounded by at least one "interface zone" where it met the opposing cell zone. The interface zones of adjacent cell zones are associated with each other to form a "grid interface". The two cell zones will move relative to each other along the grid interface in discrete steps during the calculation. The flux at the interface was computed using the intersection between interface zones at each new time step. The resulting intersection produced one zone with fluid cells on both sides and one or more periodic zones. The number of faces in these intersection zones will vary as the interface zones moves relative to each other. Grid interfaces were set up at the inlet and outlet of the wake generator domain.

3.3 The Choice of Turbulence Model

The choice of the turbulence model was known to be critically important for success in predicting the turbine blade flowfields at low Reynolds numbers. Section 1.3.3 reviewed the feature of turbulence models that were candidates for selection for the present investigation. It was decided that the model that promised the best accuracy, and that could be readily applied without the need of code development for implementation would be used. All turbulence models already implemented within available CFD software were researched to determine which could

best provide the prediction capability needed for this study. To close on the selection, a test case described in Section 3.3.1 below of the flow over the Lightly Loaded blade airfoil was simulated. Three turbulence models were evaluated; the Realizable k-ε [46] model with enhanced wall treatment, Menter's k-ω(SST) turbulence model [46] using a low Reynolds number correction to the turbulent viscosity, and the Walters and Leylek [2] k-k_L-ω transitional flow model. The Realizable k-ε model was tested because it was known to provide improved prediction of turbulent flows involving rotation, boundary layers under strong pressure gradients, separation, and recirculation [46]. The Realizable k-ε model transport equations are calculated using Eq. (3.3) and (3.4)

$$\frac{\partial}{\partial t}(\rho k) + \frac{\partial}{\partial x_j}(\rho k u_j) = \frac{\partial}{\partial x_j}\left[\left(\mu + \frac{\mu_t}{\sigma_k}\right)\frac{\partial k}{\partial x_j}\right] + G_k + G_b - \rho\varepsilon - Y_M + S_k \tag{3.3}$$

$$\frac{\partial}{\partial t}(\rho\varepsilon) + \frac{\partial}{\partial x_j}(\rho\varepsilon u_j) = \frac{\partial}{\partial x_j}\left[\left(\mu + \frac{\mu_t}{\sigma_k}\right)\frac{\partial\varepsilon}{\partial x_j}\right] + \rho C_1 S_\varepsilon - \rho C_2 \frac{\varepsilon^2}{k + \sqrt{\nu\varepsilon}} + C_{1\varepsilon}\frac{\varepsilon}{k}C_{3\varepsilon}G_b + S_\varepsilon \tag{3.4}$$

The k-ω(SST) turbulence model was examined because it is known to be more accurate for adverse pressure gradient flows and has a low Reynolds number correction to the turbulent viscosity. This feature dampens the production of the turbulence and reduces the possibility of over-prediction of viscous effects for flows that may not be fully turbulent. The Realizable k-ε model transport equations are calculated using Eq. (3.5) and (3.6)

$$\frac{\partial}{\partial t}(\rho k) + \frac{\partial}{\partial x_j}(\rho k u_j) = \frac{\partial}{\partial x_j}\left[\Gamma_k \frac{\partial k}{\partial x_j}\right] + \tilde{G}_k - Y_k + S_k \tag{3.5}$$

$$\frac{\partial}{\partial t}(\rho\omega) + \frac{\partial}{\partial x_j}(\rho\omega u_j) = \frac{\partial}{\partial x_j}\left[\Gamma_\omega \frac{\partial\omega}{\partial x_j}\right] + G_\omega - Y_\omega + D_\omega + S_\omega \tag{3.6}$$

Chapter 3. Computational Model Methodology

All auxiliary equations and constants are given in the ANSYS Fluent® User's Manual [46] for both the Realizable k-ε and k-ω(SST) turbulence models. In the end, the model judged to have the most potential to provide the prediction capability needed was the Walters and Leylek [2] k-k_L-ω transitional flow model. This turbulence model was designed to model the laminar-to-turbulent transition process using three transport equations. The k-k_L-ω model was implemented in Ansys® Fluent 6.3.26 as a beta version.

3.3.1   Comparisons of the RANS Turbulence Models

The inlet Reynolds number was set to 100,000 using the Lightly Loaded blade airfoil with inlet turbulence intensity of 1% and inlet turbulent length scale of 10.4 mm. The transition to turbulence, the boundary layer integral parameters, and the wake total pressure loss coefficient were compared for all three turbulence models. Figure 3.6 shows the turbulent kinetic energy around the blade suction surface for the three RANS turbulence models. A sudden increase in the magnitude of the turbulent kinetic energy was used as an indicator of the turbulent transition point. The k-ω(SST) and the k-k_L-ω model both produced transition at 65% axial chord. The k-ω(SST) model generated much less turbulent kinetic energy after the transition point when compared to the k-k_L-ω model. It was discovered that the specific dissipation rate around the blade surface was higher for the k-ω(SST) model than for the k-k_L-ω model. So, the turbulent kinetic energy that was being generated in the boundary layer was being converted into viscous losses at a much higher rate than the k-k_L-ω model. The k-ω(SST) model was not designed to model the laminar-to-turbulent transitional flow process within its transport equations, making it less desirable for the purpose of completing the goals of this research program. In contrast, the k-ε model became turbulent from the leading edge and exhibited no transition behavior, which is not the correct boundary layer behavior for these types of flows.
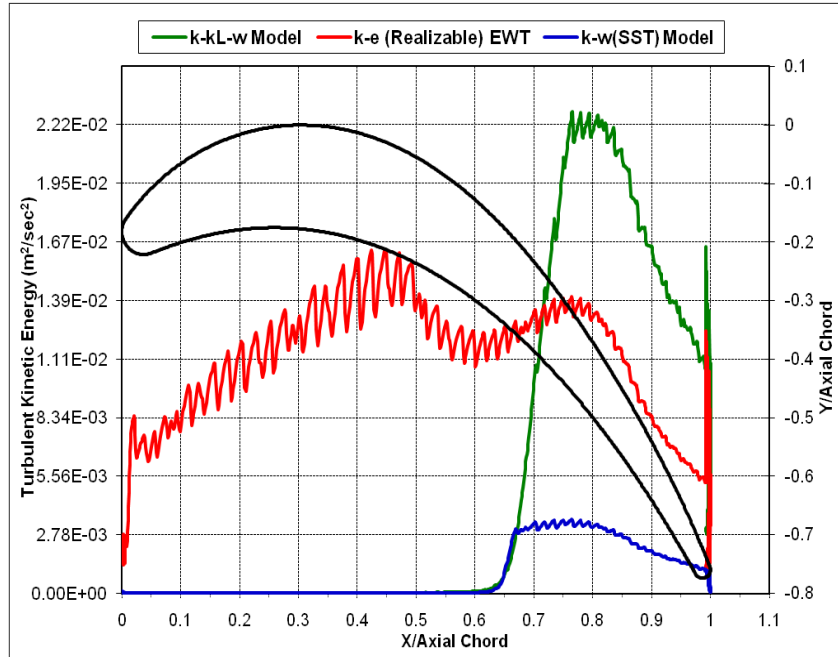
Figure 3.6. Turbulence model comparison of the suction surface turbulent kinetic energy at Re = 100,000, Tu =1%, l_m = 10.4mm for the Lightly Loaded blade airfoil
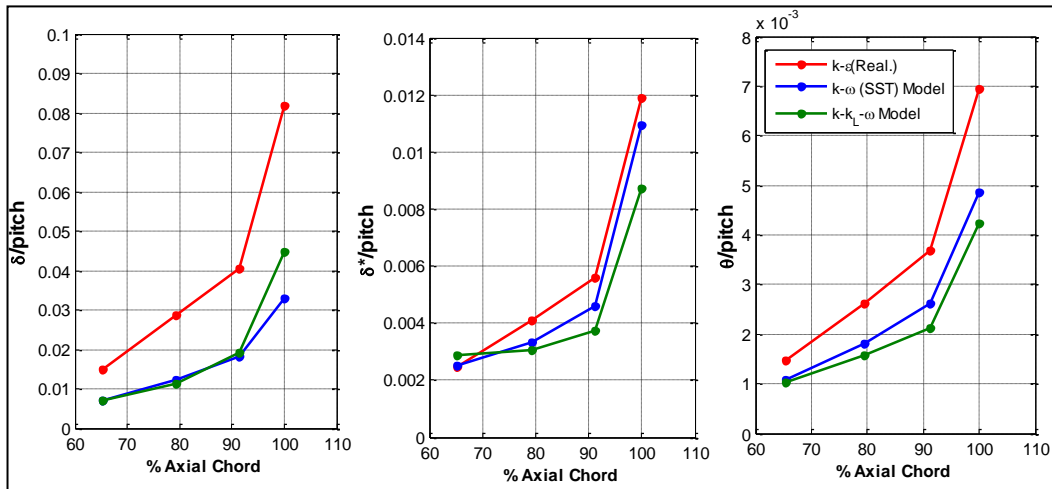
Figure 3.7. Comparison of the boundary layer integral parameters of all three turbulence models at Re = 100,000 for the Lightly Loaded blade airfoil

Boundary layer integral parameters were calculated from the velocity profiles at four axial chord locations of 65.3%, 79.4%, 91.3%, and 100% normal to the Lightly Loaded blade airfoil surface. Figure 3.7 compares the predicted boundary layer thickness, displacement thickness, and momentum thickness for all three turbulence models. The k-ε model result has the largest boundary layer thickness because the boundary layer was fully turbulent from the leading

edge. This resulted in a faster growth of the boundary layer thickness than for the boundary layers undergoing transition as with the k-ω(SST) and k-k_L-ω models. The momentum thickness plot showed that the k-ε model yielded a higher momentum loss than both the k-ω(SST) and k-k_L-ω models, indicating a more turbulent boundary layer. The boundary layer thickness for the k-ω(SST) and k-k_L-ω models were in good agreement with each other until the 100% axial chord location, where the boundary layer of the k-k_L-ω model grew at a higher rate after transitioning to turbulence. The k-ω(SST) model exhibited a higher displacement and momentum thickness which indicated a larger mass deficit in the boundary layer with a slightly higher momentum loss as compared to the k-k_L-ω model. This was attributed to the large amount of specific dissipation produced in the boundary layer from the k-ω(SST) model. Even though the flow was transitional, the high specific dissipation rate produced more viscous losses in the boundary layer, which resulted in larger mass deficit and momentum loss than the k-k_L-ω model.

The total pressure loss coefficient plot shown in Figure 3.8 indicated that the k-ε model produced the highest amount of total pressure loss because the flow was predicted as fully turbulent. The high momentum loss observed in the boundary layer created a larger total pressure loss in the wake region, which was over-predicted compared to the experimental results [36]. The most interesting result was for the case using the k-ω(SST) model. The total pressure loss was as high as the fully turbulent k-ε model even though the boundary layer exhibited transitional flow behavior. The momentum loss was slightly higher in the boundary layer than with the k-k_L-ω model. This again can be attributed to the specific dissipation present in the wake for the k-ω(SST) model which was observed to be about 20 times larger than the level

predicted with the k-k_L-ω model. Agreement with respect to the experimental results was calculated using Eq. (3.7)

$$\% \, agreement = \left[1 - \frac{\left(X_{CFD} - X_{exp} \right)}{X_{exp}} \right] \times 100 \qquad (3.7)$$

where X is the compared flowfield parameter. The total pressure loss prediction made with the k-k_L-ω model achieved 98% agreement with the experimental results [36] for the peak value of the loss coefficient while the k-ε and k-ω(SST) models obtained 17% and 20% agreement, respectively. When compared to the integrated value of the loss coefficient, the k-k_L-ω model showed 99% agreement with the experimental results. The k-ε and k-ω(SST) model produced a 56% and 96% agreement, respectively with the experimental result in the prediction of the integrated loss coefficient. Thus, the k-k_L-ω model achieved the best agreement with experimental results for the prediction of the amount of viscous losses produced and the magnitude of the total pressure loss in the wake region. So, this demonstrated that for the turbulence models evaluated, the k-k_L-ω transitional flow model has superior ability to predict transitional flow behavior associated with low Reynolds number flows than the k-ε and k-ω(SST) turbulence models. The Walters and Leylek [2] k-k_L-ω transitional flow model was chosen as the turbulence model to be used in this study because it was shown to be an effective model for laminar-to-turbulent transitional flow and was considered more suitable for the successful completion of the research program goals.
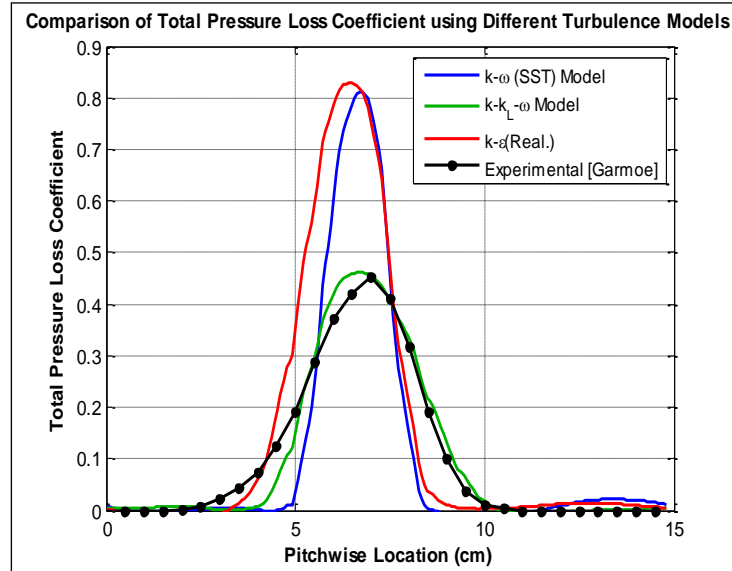
Figure 3.8. Comparison of total pressure loss coefficient for turbulence models at Re = 100,000, Tu = 1% for the Lightly Loaded blade airfoil

Turbulence Model	Integrated Total Pressure Loss Coefficient	
	CFD	Garmoe [36]
$k\text{-}k_L\text{-}\omega$	0.1033	
$k\text{-}\omega(SST)$	0.1066	0.1026
$k\text{-}\varepsilon$	0.1473	

Table 3.2. Turbulence model comparison of the integrated total pressure loss coefficient with the experimental [36, 40] results for the Lightly Loaded blade airfoil

Recently, an updated version of the $k\text{-}k_L\text{-}\omega$ model has been fully integrated in the newest software release as Ansys® Fluent 12.0. CFD simulations of the Lightly Loaded and Highly Loaded blades were completed using the Fluent 6.3 version of the $k\text{-}k_L\text{-}\omega$ model while all simulation of the Aft-Loaded L1A blade were completed using the Fluent 12.0 version of the model. This version was used for the simulations using the Aft-Loaded L1A blade because only the Fluent 12.0 version of the model can be used in combination with the sliding mesh model, which was needed for the Aft-Loaded L1A blade simulations using the passing wake generators. Flowfield comparisons of the Aft-Loaded L1A blade were made using the 6.3 and 12.0 versions Fluent with the Walters and Leylek [2] $k\text{-}k_L\text{-}\omega$ model and are discussed in Appendix I. In

CFD Modeling of Separation and Transitional Flow in
Low Pressure Turbine Blades at Low Reynolds Numbers

summary, the Fluent 12.0 version of the model showed similar results to the Fluent 6.3 version for unsteady prediction of the flowfield at low turbulent intensities, but it showed improved prediction of the blade loading and flowfield at higher turbulent intensities with respect to Fluent 6.3 version of model.

3.4   CFD Boundary Conditions

CFD boundary conditions were set to mirror the experimental cascade test conditions. The inlet boundary condition for the steady flow cases was specified as a total pressure inlet where static pressure was set according to an experimentally determined value of 98870 Pa. The inlet total pressure reflected the chosen Reynolds number based on the axial chord. Unsteady cases used a mass flow inlet boundary condition permitting the total pressure to be calculated from the interior solution which aided the local convergence per time step. The mass flow was calculated based on the normal component of the velocity and inlet domain length (kg/sec·m). Simulations were run for a Reynolds number range of 10,000-100,000. The axial and tangential components of the flow direction were set based on the design inlet flow angle for each blade. The inlet flowfield was uniformly distributed across the pitch length of the inlet boundary as measured by the experimental results. The experimental cascade blade airfoil geometries were scaled-up, causing the inlet Mach number to be less than 0.03 for a given inlet Reynolds number. Each blade airfoil in the CFD model had the same dimensions as the blade airfoil used in the LSWT. The flow was assumed to be incompressible in the CFD simulations because of the low Mach number. The inlet turbulence intensity and turbulent length scale were chosen based on user specification or experimental values, when available. The inlet laminar kinetic energy was set to 10^{-6} m^2/sec^2 in accordance with specifications of the turbulence model. No-slip conditions were assigned to the blade surface, and turbulence parameters used a zero-flux boundary

CFD Modeling of Separation and Transitional Flow in
Low Pressure Turbine Blades at Low Reynolds Numbers

condition. The initial static pressure boundary condition at the outlet was estimated using conservation of mass of the axial velocity, the ideal outlet flow angle, and the assumption that no total pressure loss occurred between the inlet and outlet planes following Eq. (3.8) and (3.9).

$$u_{out} = u_{in} \left[\frac{\cos(\alpha_{in})}{\cos(\alpha_{out})} \right] \tag{3.8}$$

$$P_{out} = P_0 - \frac{1}{2} \rho u_{out}^2 \tag{3.9}$$

This assumption of the outlet static pressure provided an initial guess for the pressure-based solver and was adjusted during the calculation to account for the actual total pressure loss. The target mass flow rate option was implemented at the pressure outlet for the steady flow solutions in order to adjust the pressure at the outlet to meet the mass flow rate. The target mass flow rate option was not used for the unsteady cases because the mass flow was set in the inlet boundary condition.

3.5   Computational Resources

The computational resources shown in Figure 3.9 for this work were provided by the U.S. Department of Defense, AFRL Distributed Computing Research Center, High Performance Computing facility at Wright-Patterson AFB, OH. Three different supercomputing systems were available for performing the CFD simulations. The HP XC Opteron high performance super-computer has 2048 AMD[®] Opteron 2.8GHz processors with 2 Gigabytes of memory per processor. The SGI Altix 3700 super-computer has 2048 Intel[®] Itanium 2, 1.6GHz processors with 1 Gigabyte of memory per processor. The largest super-computing system is the SGI Altix 4700 with 9216 core processors and 2 or 4 Gigabytes of memory per processor. There are two cores per 1.6GHz Intel[®] Itanium2 processor.

CFD Modeling of Separation and Transitional Flow in
Low Pressure Turbine Blades at Low Reynolds Numbers

The double-precision parallel version of Fluent 6.3® was run on a HP XC Opteron super-computer for two-dimensional cascade simulations. A total of 8-10 processors were used for the steady simulations and 16-32 processors for the transient two-dimensional cascade simulations. The three-dimensional cascade simulations were run on the SGI Altix 4700 using 80-104 processors.

Figure 3.9. AFRL Major Shared Resource Center HP XC Opteron (top left), SGI Altix 3700 (top right), and SGI Altix 4700 (bottom center) Super-Computers

3.6 CFD Post Processing and Analysis

Once the CFD simulations were completed, a number of different software tools were used to complete the analysis of the CFD results. Mathematical rakes were created in Fluent using the Rake Creation Tool for measurements of flow quantities. The locations of these rakes correspond to the same measurement locations as the experimental rakes. Table 3.2 shows the location of rakes, total length, and total number of points for each CFD model. Text files containing the CFD rake data were exported from Fluent to a Microsoft® Excel file for further

analysis. Two-dimensional plots were made within Microsoft® Excel or using Mathworks® Matlab 2008.

Flow visualizations were completed using Intelligent Light® FieldView 12.0 CFD post-processing and visualization software. FieldView files (.fvuns & .fvuns.fvreg) were exported from Fluent after the completion of steady flow simulations or during calculations for unsteady simulations every 10-20 time-steps. Contour plots and animations were made to visualize steady and unsteady aerodynamic flow characteristics.

CFD Model	Rake Type	Total Pts.	Length	Location
Lightly Loaded Blade	Inlet	200	One pitch length	One C_x from leading edge (streamwise)
	Outlet Wake	200	One pitch length	One C_x from trailing edge (streamwise)
	Boundary Layer	300	30.0cm	65.3% C_x, 79.4% C_x, 91.3% C_x, 100% C_x (normal to blade surface)
Highly Loaded Blade	Inlet	200	One pitch length	One C_x from leading edge (streamwise)
	Outlet Wake	200	One pitch length	One C_x from trailing edge (streamwise)
	Boundary Layer	300	30.0cm	67.2% C_x, 73.0% C_x, 79.3% C_x, 84,8% C_x, 89.8% C_x, 95.0% C_x, (normal to blade surface)
Aft-Loaded L1A Blade	Inlet	200	One pitch length	22.86cm from leading edge (streamwise)
	Outlet Wake	200	One pitch length	25.4cm from trailing edge (streamwise)
	Boundary Layer	300	30.0cm	57.0% C_x, 58.8% C_x, 60.4% C_x, 65.5% C_x, 70.0% C_x, 74.1% C_x, 79.4% C_x, 85.0% C_x, 89.0% C_x, 94.2% C_x (normal to blade surface)
Aft-Loaded L1A Blade with Wake-Generators	Inlet	200	One pitch length	21.27cm from cylinder center (streamwise)
	Outlet Wake	200	One pitch length	17.46cm from trailing edge (streamwise)
	Boundary Layer	300	30.0cm	57.0% C_x, 58.8% C_x, 60.4% C_x, 65.5% C_x, 70.0% C_x, 74.1% C_x, 79.4% C_x, 85.0% C_x, 89.0% C_x, 94.2% C_x (normal to blade surface)
	Point Probe	1		Mid-pitch at the blade leading edge axial location

Table 3.3. CFD mathematical rake measurement locations created in Fluent CFD software

CHAPTER FOUR

4. The Lightly Loaded Blade CFD Results

The Lightly Loaded blade geometry was used for the initial baseline study because of its low blade loading level. As previously described, it was used to determine which RANS turbulence model within Fluent was the most capable for the prediction of low Reynolds number aerodynamic flow effects. To obtain the following results of this Section, the Walters and Leylek [2] k-k_L-ω model was applied to flows over a Reynolds number range of 15,000-100,000 using the Lightly Loaded blade airfoil. The simulation results were compared to available data from experimental studies to determine if total pressure loss was successfully predicted. Additionally, parametric studies of the k-k_L-ω model sensitivity to inlet freestream turbulence intensity and turbulent length scale were conducted to investigate how the inlet turbulence parameters affect boundary behavior and total pressure loss.

4.1 Performance Prediction at Different Inlet Reynolds Numbers

The Lightly Loaded blade airfoil flow was simulated at individual Reynolds numbers of 100,000, 75,000, 50,000, 40,000, and 15,000 to determine if the k-k_L-ω transitional flow model could adequately predict the varying Reynolds number performance. The inlet freestream turbulence intensity for the CFD simulations was set to the average inlet turbulence intensity measured in the experimental [36] results with the turbulent length scale, $l_m = 5mm$. The steady and time-mean velocity contour plots at each inlet Reynolds number are shown in Figure 4.1. The flow around the Lightly Loaded blade airfoil behaved similarly at Reynolds number from 100,000 to 50,000, where the flow was predicted as transitional and boundary layer was well attached to the blade surface producing a turbulent wake similar to Figure 4.3(c). The freestream

length scales as modeled by the specific dissipation rate (ω) transport Eq. (1.59) were small enough to couple with the k-k_L-ω model and cause transition to turbulence in the boundary layer. When the Reynolds number decreased below 50,000, the flow around the suction side of the blade became laminar and began to separate, resulting in a von Kàrmàn vortex street in the wake region of the blade (Fig. 4.3(b)). The freestream length scales at these Reynolds number ranges were large enough to decouple with the k-k_L-ω model and contribute to the growth in the laminar kinetic energy [2] resulting in a laminar boundary layer and vortex shedding in the wake region.

At the inlet Reynolds number of 15,000, the steady flow simulation (Fig. 4.1(e)) predicted a very large separation region beginning at the 70% axial chord on the suction side of the blade. However, the unsteady simulation (Fig. 4.1(f)) predicted a separation beginning at approximately 90% axial chord with the presence of von Kàrmàn vortex shedding at a frequency of 75Hz in the wake region. A Strouhal number, $St = 0.0220$, was calculated based on the observed vortex shedding frequency, freestream velocity, and momentum thickness at separation with Eq. (4.1).

$$St = \frac{f_{shed}\theta_{sep}}{U_\infty} \tag{4.1}$$

The presence of the vortex shedding caused the boundary layer to remain attached for an additional 20% chord than for the steady flow solution. The separation region was reduced due to the unsteady generation of vortices from the trailing edge of the blade. The unsteady simulation provided a better prediction of the flowfield because unsteady effects from the separated shear layers on pressure and suction side were allowed form into discrete vortices. However, unsteady flow simulations require significantly larger computational resources

compared to steady flow simulations because the solution must be converged spatially for every

time-step and run until the solution is time-periodic.
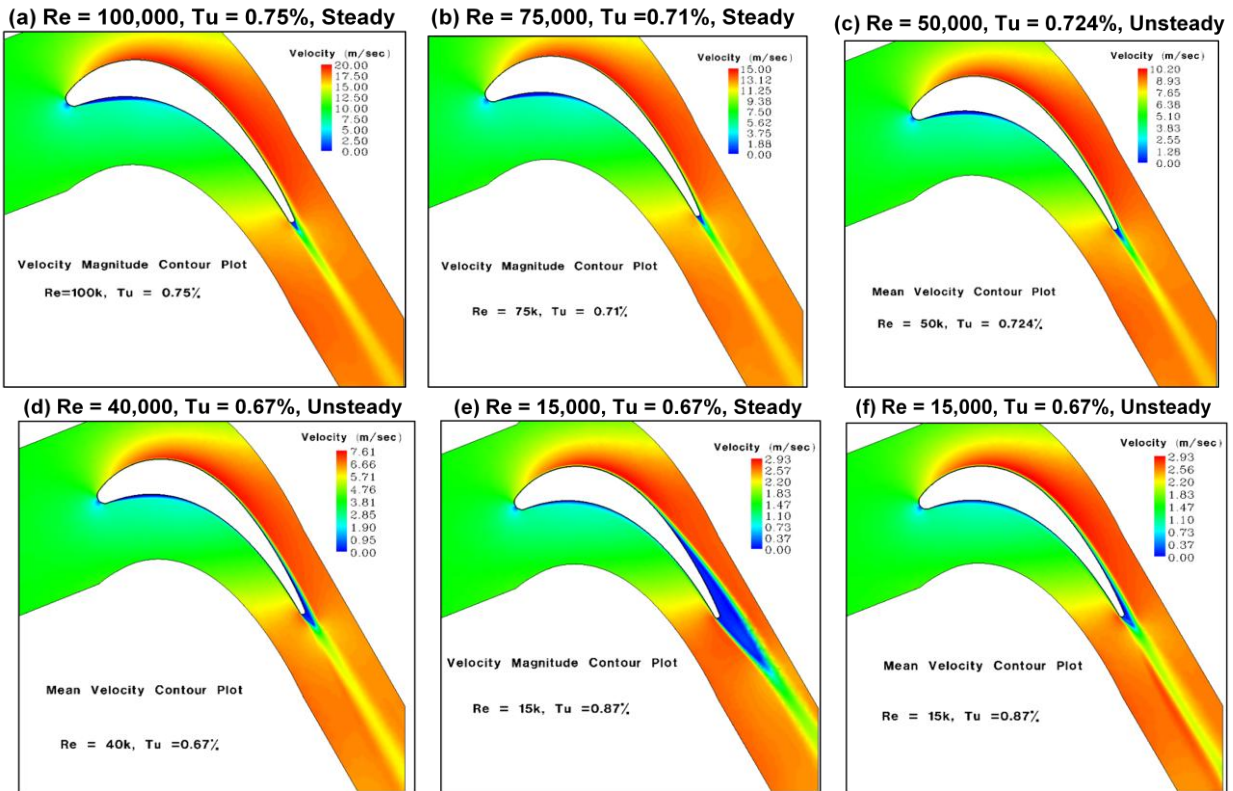
Figure 4.1. Velocity magnitude contour plots of the Lightly Loaded blade airfoil simulated at a range of inlet Reynolds numbers
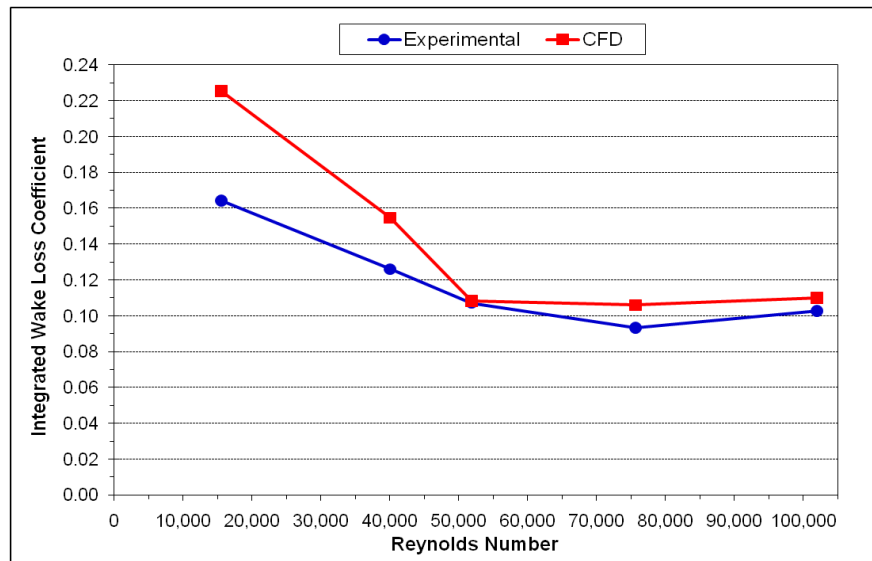
Figure 4.2. Comparison of the CFD and experimental [36] integrated wake loss coefficient at a range of inlet Reynolds numbers for the Lightly Loaded blade airfoil

Chapter 4. The Lightly Loaded Blade CFD Results

Aerodynamic performance was evaluated based on the total pressure loss coefficient, which was used as an indicator the viscous losses. The integrated loss coefficient was used as an indicator of the total amount of viscous losses generated in the wake region, and the peak loss coefficient was used as an indicator of the strength of the wake region and how the viscous losses were distributed within the wake region. The integrated and maximum value of the wake total pressure loss coefficient are plotted in Figures 4.2 and 4.3 versus the inlet Reynolds number for both the experimental and the CFD results to show the Reynolds number performance of the Lightly Loaded blade airfoil. Figure 4.2 shows the integrated wake loss coefficient was over-predicted by 23% and 37% for the Reynolds number of 40,000, and 15,000, respectively. This was attributed to the width of the wake region being larger in the CFD predictions than the experimental result [36]. The specific dissipation rate calculated from the k-k_L-ω model which was set based on the inlet turbulent length scale and its effect on integrated and peak loss coefficient was investigated in Section 4.2.1. The CFD predictions at the other Reynolds numbers showed better than 88% agreement with the experimental results [36]. Also, the gradual increase of the integrated loss coefficient with decreasing Reynolds number was predicted in the CFD results.

The CFD results showed better than 90% agreement with the experimental results [36] at inlet Reynolds numbers of 100,000, 75,000, and 40,000 for the prediction of the peak value of the loss coefficient as shown in Figure 4.3. Discrepancies existed between the experimental and CFD predictions at 50,000 and 15,000. The CFD results for the Re = 50,000, Tu = 0.724% case predicted that the flow does not transition until 85% axial chord, causing the total pressure loss coefficient to be 20% under-predicted with respect to the experimental result [36]. At a Reynolds number of 15,000, the unsteady case resulted in 83% agreement of the total pressure

CFD Modeling of Separation and Transitional Flow in
Low Pressure Turbine Blades at Low Reynolds Numbers

loss coefficient with the experimental result [36] due to the presence of vortex shedding, caused by an increased amount of losses present in the wake. Overall, the CFD simulations using the k-k_L-ω model demonstrated the ability to adequately predict the inlet Reynolds number aerodynamic loss trends for the Lightly Loaded blade airfoil. Based on comparisons of the integrated and peak loss coefficient, the k-k_L-ω model was able to effectively predict the amount of losses generated and their distribution within the wake region. Based on the prediction of aerodynamic losses and comparisons with other turbulence model presented in Section 3.3.1, the k-k_L-ω model showed the potential to provide improved prediction low Reynolds number flow effects. This provided confidence in its capability for providing the same type of results for more highly loaded turbine blade airfoil geometries such as the Highly Loaded and Aft-Loaded L1A blade to be presented Section 5 and 6, respectively.
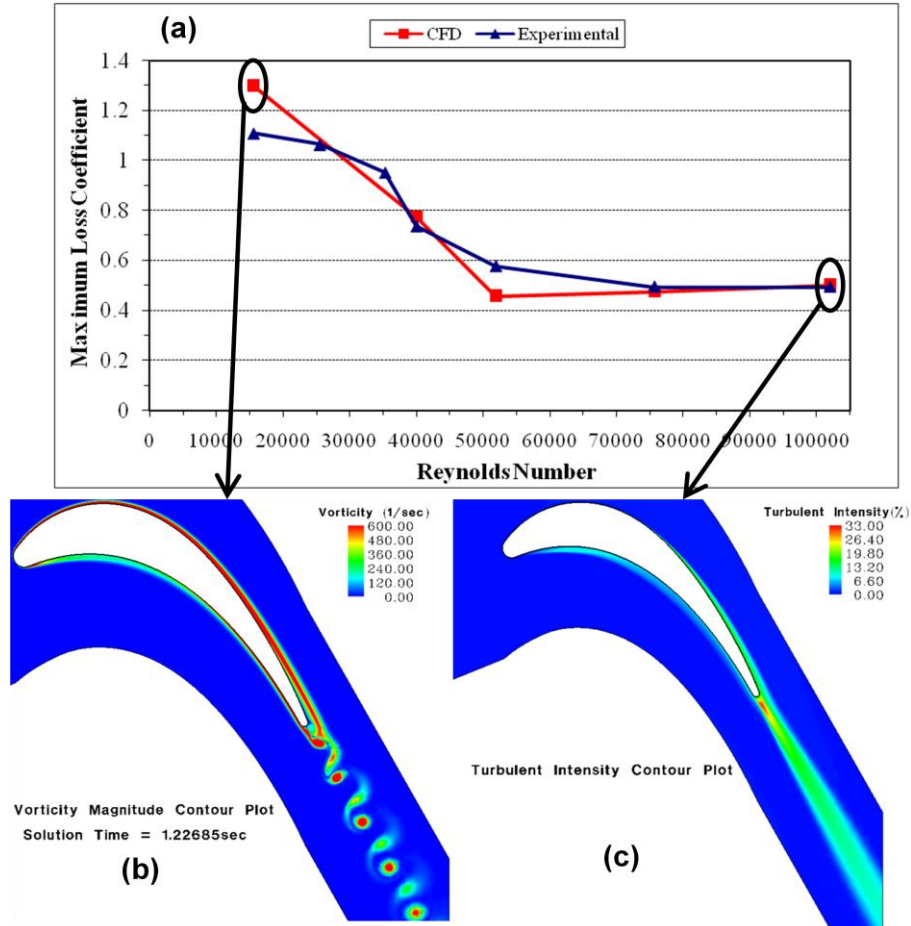
Figure 4.3. Comparison of the CFD and Experimental [36] Maximum Loss Coefficient
at a Range of Inlet Reynolds Numbers for the Lightly Loaded Blade Airfoil

4.2 Effect of Inlet Turbulence Parameters on Transition and Performance Predictions

Since the k-k_L-ω transitional flow model was a newly formulated model, an understanding of how the inlet turbulence parameters affected the CFD predictions of aerodynamic effects at low Reynolds numbers was needed. Simulations were completed at Re = 50,000 using the Lightly Loaded blade airfoil where either the inlet turbulent length scale was held constant and the inlet turbulence intensity was varied, or inlet turbulence intensity was held constant and the inlet turbulent length scale was varied. The effect of these inlet turbulent boundary condition variations was investigated on the turbulent transition point, the behavior of the boundary layer, and the total pressure loss coefficient.

CFD Modeling of Separation and Transitional Flow in
Low Pressure Turbine Blades at Low Reynolds Numbers

(a) Inlet Length Scale Parametric Study Re = 50,000, Tu = 1%					(b) Inlet Turbulent Intensity Parametric Study Re = 50,000, l_m = 5mm			
l_m (mm)	X_{trans}/C_x		Max. TPLC	ITPLC	Tu (%)	X_{trans}/C_x	Max. TPLC	ITPLC
2	0.831		0.471	0.1099	0.724	0.879	0.455	0.1076
3.5	0.761		0.495	0.1136	0.75	0.862	0.457	0.1084
4	0.753		0.498	0.1141	1	0.747	0.499	0.1144
5	0.747		0.499	0.1144	1.5	0.615	0.546	0.1239
6	0.749		0.497	0.1143				
8	0.778		0.523	0.1249				
14	0.823		1.052	0.1313				
l_m (mm)	X_{sep}/C_x	St	Max. TPLC	ITPLC	Tu (%)	X_{sep}/C_x	St	Max. TPLC	ITPLC
20	0.938	0.015	0.988	0.1527	0.5	0.931	0.014	0.718	0.1364
25	0.942	0.015	1.069	0.1630					
30	0.944	0.015	1.040	0.1814	Experimental Result [36]				
40	0.966	0.015	1.000	0.1733	Tu (%)			Max. TPLC	ITPLC
50	0.947	0.015	1.015	0.1652	0.724			0.577	0.1083

Table 4.1. Summary of inlet turbulence parameters on transition/separation location and maximum loss coefficient for the Lightly Loaded Blade

4.2.1 Inlet Turbulent Length Scale Study

An estimate of the inlet turbulent length scale range was needed for the boundary condition specification because measurements of the inlet turbulent length scale were unavailable for the Lightly Loaded blade airfoil cascade experiments. Typically, integral length scale measurements obtained from experiments were used to set the inlet turbulent length scale in Fluent CFD software. The sensitivity of the k-k_L-ω transitional flow model to the inlet turbulent length scales was investigated in order to determine the prediction accuracy tolerance to the inlet turbulent length scale. The inlet turbulent length scale (l_m) specification in Fluent CFD software was used to set the initial inlet specific dissipation rate (ω) in the k-k_L-ω model with the Eq. (5.2)

$$\omega = \frac{k^{1/2}}{C_\mu^{1/4} l_m}$$

(4.2)

where the empirical constant $C_\mu = 0.09$ used was specified in the k-k_L-ω model. Then the specific dissipation rate was calculated within the flowfield according to the transport equation in Eq. (1.59). The specific dissipation controls the rate of transfer of turbulent kinetic energy to viscous losses. RANS turbulence models use the dissipation transport equation to model the energy cascade of turbulence where the turbulent kinetic energy is transferred from larger eddies to smaller eddies and the smallest eddies dissipate the kinetic energy into viscous heat. The difference with the k-k_L-ω model compared to conventional turbulence models is that it divides the eddy sizes according to a cutoff eddy size called the effective length scale. Length scales smaller than the effective length scale interacted with the mean flow as typical turbulence and larger scales contribute to the production mechanism for laminar kinetic energy [2].

The separation/transition to turbulence point on the blade suction side and the wake total pressure loss coefficient were used to study this effect. The inlet Reynolds number for these steady and unsteady flow simulations was set to 50,000 with an inlet turbulence intensity, $Tu = 1\%$. The turbulent length scale was varied over a range of *2 – 50 mm* as shown in Table 4.1(a). Over a range of $l_m = 3.5$ - *8mm*, Table 4.1(a) shows that the location of the transition region does not vary significantly. For the $l_m = 2mm$ case, the transition region moved further downstream to the 83% axial chord position indicating that as the length scale becomes very small, the transition region will move downstream. This is consistent with the fact that the magnitude of the disturbance that couples with the boundary layer will be reduced as the turbulent length scale decreases. The $l_m = 14mm$ case, showed a similar turbulence transition point as the $l_m = 2mm$ case. This indicated a nonlinear variation in the location of the turbulent transition point at the inlet turbulent length scale range of $l_m = 2$ - *14mm*. At a turbulent length scale of $l_m = 20mm$ and above, the flow within the boundary layer remained laminar and separated. The turbulent length

scale has grown large enough that the freestream eddies no longer couple to the boundary layer through the turbulence model, hence the boundary layer does not transition to turbulent.
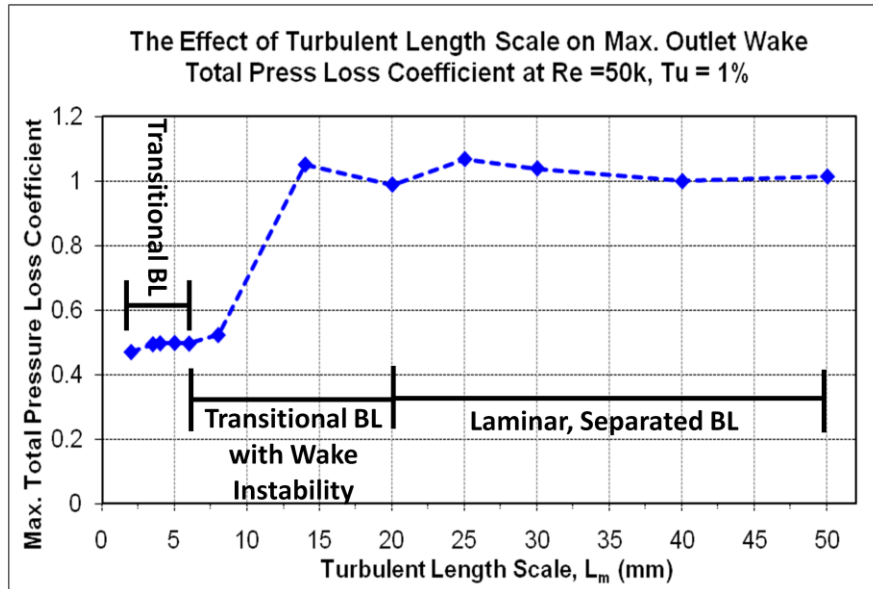
Figure 4.4. Maximum wake loss coefficient verses inlet turbulent length scale for the Lightly Loaded blade

The maximum value of the wake total pressure loss coefficient shown in Figure 4.4 also shows no significant variation for the l_m = 3.5 - 6mm range. The lowest value of the maximum total pressure loss coefficient was calculated for the l_m = 2mm case due to the transition region being located far downstream in comparison to the other cases. This resulted in a lower momentum loss in the boundary layer. The l_m = 8mm and 14mm cases showed an increase in the loss coefficient even though the boundary layer was transitional. This increase was due to a wake instability present in the flowfield. It caused the vortex shedding similar to the separated flow cases at the higher inlet turbulent length scales shown in the contour plots in Figure 4.5. For the l_m = 8mm case (Fig. 4.5(a)) the wake instability was weak, causing the initial trailing edge vortex shedding to dissipate. The wake instability was the strongest for the l_m = 14mm case (Fig. 4.5(b)) and caused a higher loss coefficient compared to the l_m = 8mm case. The total pressure loss remained constant at turbulent length scales above 20mm because the separation

CFD Modeling of Separation and Transitional Flow in
Low Pressure Turbine Blades at Low Reynolds Numbers

within the laminar flow boundary layer caused vortex shedding within the wake region (Fig. 4.5(c)). The turbulent length scale must be within a range of $l_m = 2 - 6mm$ in order to couple with the boundary layer and affect turbulent transition. Also, a length scale range of $l_m = 8 - 14mm$ was found to cause transition in the boundary layer and produce eddies that were large enough to cause instabilities in the wake and produce vortex shedding.
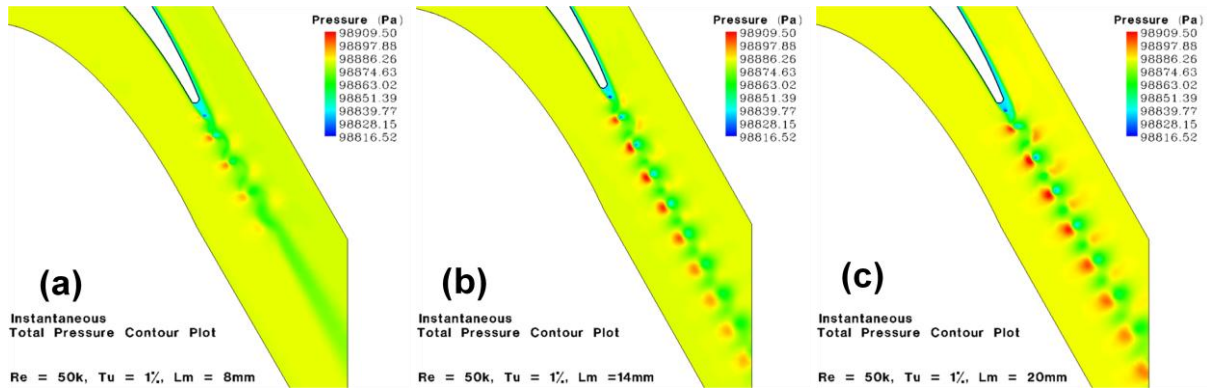
Figure 4.5. Wake region total pressure contours for the Lightly Loaded Blade at (a) $l_m = 8mm$, (b) $l_m = 14mm$, and (c) $l_m = 20mm$

Figure 4.5 shows the integrated total pressure loss coefficient that was calculated at each inlet turbulent length scale. The trends were similar to the maximum loss coefficient plot in Figure 4.4. The integrated loss coefficient remained essentially constant from $l_m = 2 - 6mm$ and it began to linearly increase from $l_m = 6 - 30mm$ due to an increase in the width of the wake region and the peak loss coefficient. At length scales above $l_m = 30mm$, the integrated loss coefficient decreased as the inlet turbulent length scale was increased, mainly due to the decrease in the wake region.
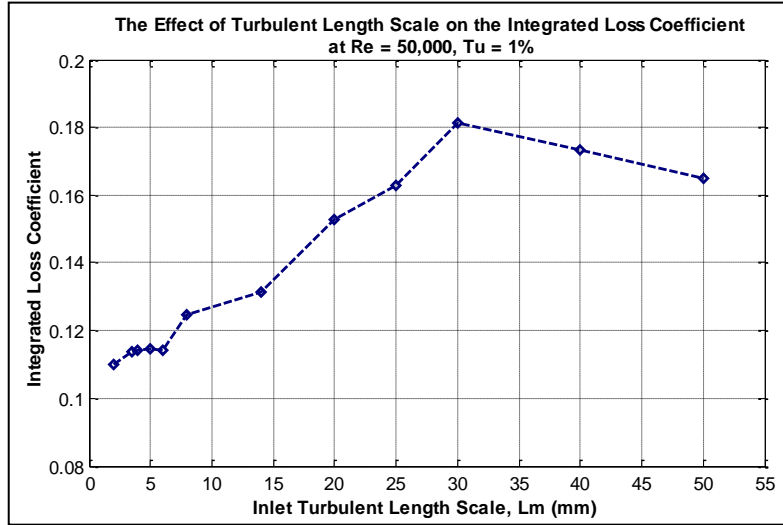
Figure 4.5. Integrated wake loss coefficient verses inlet turbulent length scale for the Lightly Loaded blade

4.2.2 Inlet Turbulence intensity Study

Sensitivity to the inlet turbulence intensity level on the turbulent transition location and the total pressure loss coefficient was investigated. The inlet turbulence intensity was used to set the initial value of the turbulent kinetic energy in the k-k_L-ω model using Eq. (5.3).

$$k = \frac{3}{2}\left(u_{inlet}Tu\right)^2$$

(4.3)

The transport equation (Eq. (1.59)) was used to calculate the turbulent kinetic within the flowfield. Steady flow simulations at Re = 50,000 for the Lightly Loaded blade airfoil were also completed at inlet turbulent intensities of 0.75%, 1%, and 1.5%. Unsteady flow simulations were completed at inlet turbulent intensities of 0.5% and the experimentally [36] measured inlet turbulence intensity of 0.724%. There was a significant amount of unsteadiness present in the flowfield for the $Tu = 0.5\%$ case due to separation and vortex shedding whereas the $Tu = 0.724\%$ case was quasi-steady with no significant flow unsteadiness present in the flowfield. All these cases used a constant turbulent length scale of *5mm*. Figure 4.6 and Table 4.1(b) shows the

effect of varying the inlet turbulence intensity on transition. The location of turbulent transition on the suction side moved downstream as inlet freestream turbulence intensity was decreased, while the transition on the pressure side remained unchanged. The low-frequency high amplitude fluctuations in the pre-transitional boundary layer took longer to develop because the freestream turbulence was reduced, causing transition on the suction surface to be further delayed. In the 0.5% inlet turbulence intensity case, the boundary layer did not transition along the blade surface and flow remained laminar. The presence of laminar flow caused vortex shedding at a frequency of 325Hz with a *St = 0.014*, and explained the origin of the increase in the turbulent kinetic energy at the trailing edge.
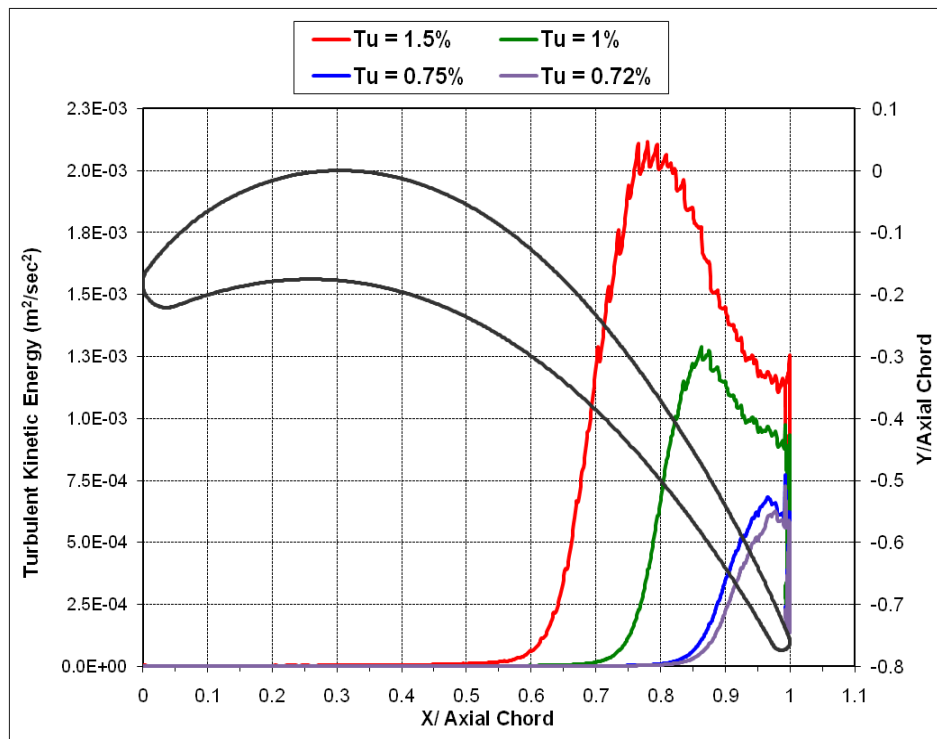
Figure 4.6. Comparison of the suction surface turbulent kinetic energy at different inlet turbulent intensities for the Lightly Loaded blade at Re = 50,000, l_m = 5mm

Boundary layer velocity profiles were then obtained at four axial locations of 65.3%, 79.4%, 91.3%, and 100% normal to the Lightly Loaded blade surface. The profiles shown in

Figure 4.7(a) revealed that the flow remained attached for all four measured locations except for the $Tu = 0.5\%$ case. The flow separated at the 100% axial chord location due to the initial creation of vortices from the shear layer on suction side. The boundary layer thickness, displacement, and momentum thickness shown in Figure 4.7(b) were calculated from the velocity profiles. The largest boundary layer thickness was found in the $Tu = 1.5\%$ case because the boundary layer transitioned to turbulent farthest upstream of all the cases and underwent more of the exponential growth associated with turbulent boundary layers. It also contained the highest momentum thickness because of the larger amount of turbulence present in the mean flow. At the 65.3% axial chord location, the boundary layer thickness was approximately the same for all cases. The smallest boundary thickness was found for the $Tu = 0.75\%$ and $Tu = 0.724\%$ cases, because the transition locations are more downstream than the $Tu = 1\%$ and $Tu = 1.5\%$ cases. The displacement thickness at the four axial chord locations increased as the inlet turbulence intensity decreased. The largest displacement thickness was found in the $Tu = 0.5\%$ case because the flow around the suction side of the blade was laminar and separated at the 100% axial chord location.
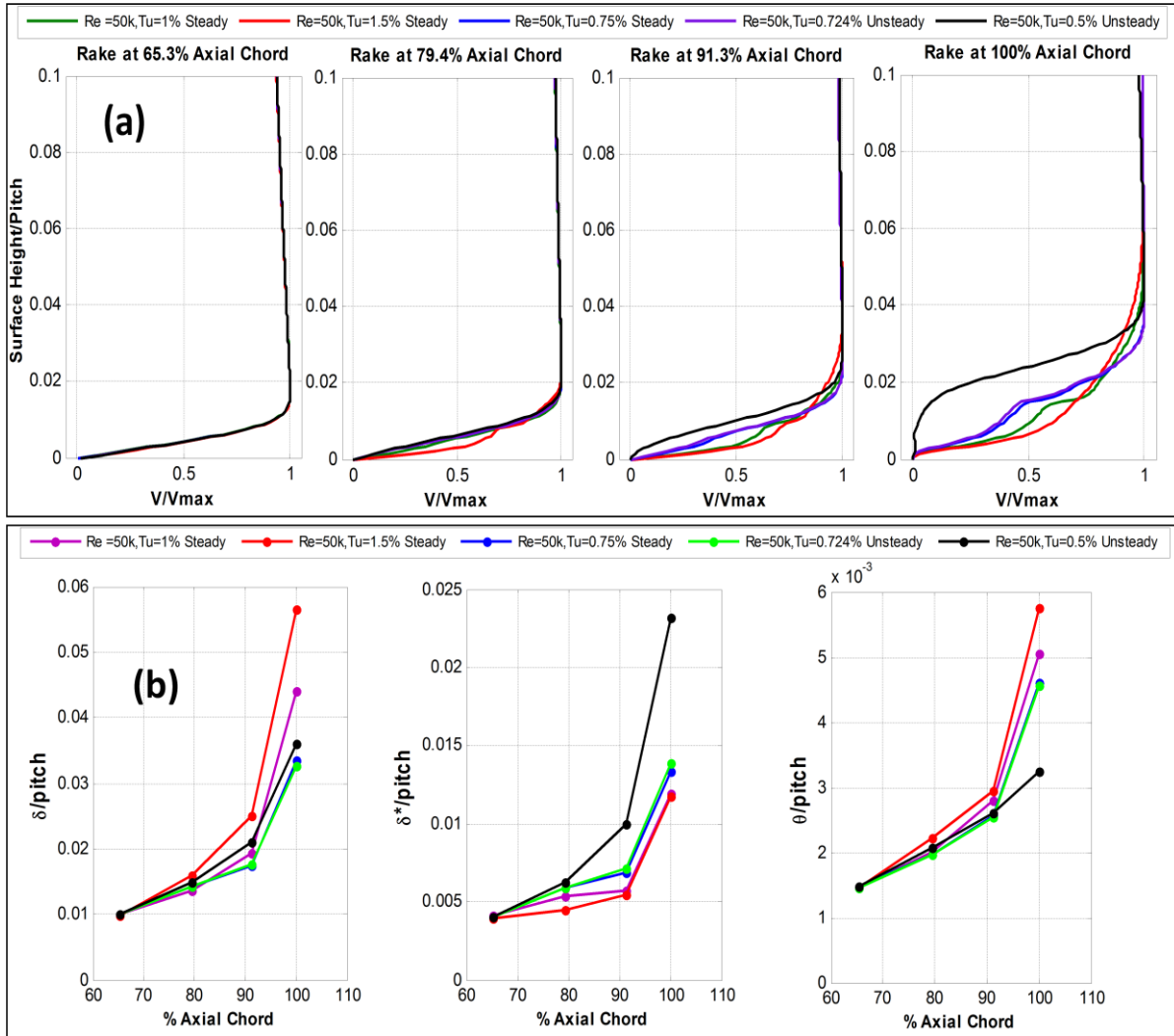
Figure 4.7. Comparison of (a) boundary layer velocity profiles and (b) integral parameters at different inlet freestream turbulent intensities at Re = 50,000, l_m = 50mm for the Lightly Loaded blade airfoil

The behavior of the boundary layer at the various inlet turbulent intensities was reflected in the calculation of the total pressure loss coefficient. In Table 4.1 and Figure 4.8(a), the total pressure loss coefficient for the several freestream inlet turbulent intensities were compared to the Tu = 0.724% experimental result and showed the best agreement with the Tu = 1.5% case. The Tu = 0.5% and Tu = 1.5% cases show that large values of the total pressure losses can be produced by two different types of flow behaviors. High values of turbulence intensity caused turbulent transition further upstream of the blade resulting in higher momentum loss in the boundary layer. This high momentum flow leads to a higher total pressure loss. In contrast, at

CFD Modeling of Separation and Transitional Flow in
Low Pressure Turbine Blades at Low Reynolds Numbers

low turbulence intensity the flow remains laminar and separated, thus causing a von Kàrmàn vortex street (Fig 4.8(b)). The vortices shed from the trailing edge increased the total pressure loss in the wake. The $Tu = 0.724\%$ CFD result predicted the flow to transition furthest downstream of all the cases. The total pressure loss coefficient was under-predicted because the momentum loss within the boundary layer was the lowest of all the cases where the flow transitioned. Figure 4.8(c) shows the wake was narrow with relatively low total pressure loss. The experimental [36] loss coefficient result indicated that the flow was more laminar than predicted with the CFD. So, if the inlet turbulence intensity was set in the CFD result between $Tu = 0.5\%$ and $Tu = 0.724\%$ such that the flow did not transition but remained laminar, better agreement might be achieved with the experimental results.
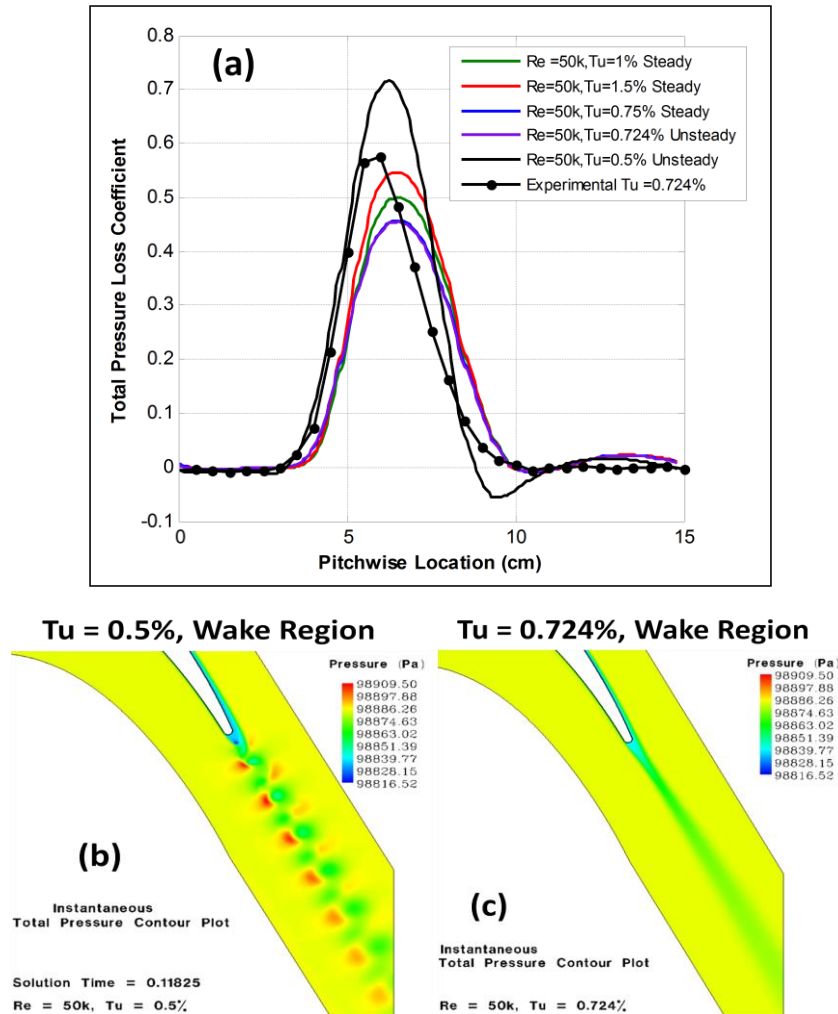
Figure 4.8. (a) Inlet turbulence intensity effect on the wake total pressure loss coefficient and instantaneous wake total pressure contours at (b) Tu = 0.5% and (c) Tu = 0.724%, Re = 50,000 for the Lightly Loaded blade airfoil

Table 4.1 summarizes the results of the predicted turbulent transition point and the peak and integrated value of the loss coefficient as inlet turbulent length scale and turbulence intensity was varied. The k-k_L-ω transitional flow model does show that the inlet turbulence intensity has a first order effect on transition and prediction of the total pressure loss coefficient. Clearly, setting the correct inlet turbulence intensity was crucial to being able to predict performance at low Reynolds numbers when using current transitional flow model. The CFD simulation demonstrated that high total pressure loss can originate from high freestream turbulence or laminar flow with the presence of vortex shedding. The inlet turbulent length scale had a second

CFD Modeling of Separation and Transitional Flow in
Low Pressure Turbine Blades at Low Reynolds Numbers

order effect on transition and total pressure loss coefficient and needs to be in the correct range in order to penetrate the boundary layer to affect transition and allow for successful performance prediction.

4.3   Summary of Results

A new three-equation eddy-viscosity type turbulent transitional flow model developed by Walters and Leylek [2] was tested to predict the performance a CFD model of LPT cascade configuration. A Lightly Loaded blade airfoil was simulated for inlet Reynolds numbers from 15,000 to 100,000. Walters and Leylek's [2] k-k_L-ω transitional flow model showed the ability to predict the transitional flow behavior associated with low Reynolds number flows for the Lightly Loaded blade airfoil. The k-k_L-ω transitional flow model provided a more accurate method for performance predictions compared to conventional RANS turbulence models. Sensitivity of the inlet turbulence boundary conditions to the turbulent length scale and freestream inlet turbulence intensity was investigated to determine the effect on prediction of the total pressure loss coefficient. The turbulent transition point and total pressure loss coefficient showed strong sensitivity to changes in the inlet freestream turbulence intensity, and second order sensitivity effect to the inlet turbulent length scale. Good agreement was obtained for the effect of Reynolds number sensitivity with the experimental results. The ability to adequately predict the Reynolds number effect was demonstrated for the Lightly Loaded blade airfoil.

CHAPTER FIVE

5. The Highly Loaded Blade CFD Results

Walters and Leylek's [2] k-k_L-ω transitional flow model was applied to the Highly Loaded blade airfoil to determine if it could effectively predict the low Reynolds number aerodynamic flow effects associated with this geometry. Experimental studies [36,38-40] reported that the flowfield was largely separated when the Highly Loaded blade airfoil was subjected to low inlet Reynolds numbers due the increased loading level and strong suction surface adverse pressure gradient. Two-dimensional simulations were compared to experimental cascade results and investigations of the unsteady flowfield were made at various inlet Reynolds numbers. The inlet turbulent length scale was varied to investigate its effect on the unsteady flowfield and the loss coefficient predictions. Additionally, a three-dimensional cascade model was developed and run to study the effect of the spanwise dimension on the CFD predictions for the Highly Loaded blade airfoil.

5.1   Two-Dimensional CFD Comparisons with Experimental Results

The two-dimensional cascade model of the Highly Loaded blade airfoil (Fig. 3.5(b)) was simulated at an inlet Reynolds number of 25,000, 50,000, and 100,000. Unsteady simulations were run with an inlet $Tu = 0.6\%$ for all inlet Reynolds numbers. The inlet turbulent length scale was set for Re = 50,000 and 25,000 at l_m = *5mm* and *50mm* to investigate the impact of the length scale on the CFD predictions using the k-k_L-ω model. The Re = 100,000 case, the inlet turbulent length scale was set as l_m = *50mm*. The next sections present the comparisons of the static pressure coefficient, boundary layer profiles, and total pressure loss coefficient with the

CFD Modeling of Separation and Transitional Flow in
Low Pressure Turbine Blades at Low Reynolds Numbers

experimental measurements taken at the AFRL Low Speed Wind Tunnel. Also, the unsteady features of the flowfield predicted with the k-k_L-ω model were discussed.

5.1.1 Surface Static Pressure Coefficient

In Figure 5.1, the mean static pressure coefficient distributions on the blade airfoil suction and pressure side were compared to the measurements of Bons *et al.* [38] and the three-dimensional LES results of Rizzetta and Visbal [45]. The present CFD result predicted a higher static pressure on the suction side of the blade for the Re = 100,000 case (Fig 5.1(a)), but it did predict the flow separation and reattachment and followed the same trend as the experimental [38] results. The flow separated at 70% axial chord location and then underwent turbulent reattachment at approximately the 93% axial chord location. The uncertainty separation location was 0.1% axial chord in the CFD whereas experimental results were 3% axial chord. The experiment showed that separation began more downstream at 75% axial chord and there was reattachment at 88% axial chord. On the pressure side of the blade, the predicted values were in excellent agreement with the experimental values.

At 50,000, the current CFD results showed similar blade loading characteristics as the LES simulation up to the 80% axial chord location (Fig. 5.1(b)). There was a large amount of unsteadiness present on the suction and pressure sides due to the production of vortices from the separated shear layers. The pressure coefficient trend downstream of the 80% axial chord location was due to the motion of suction side vortices. The k-k_L-ω model predicted the suction side vortex in a time-averaged perspective to be fixed in space. As a result, the pressure coefficient has a sharp increase and then decreases further downstream. The decrease in the inlet turbulent length scale from $l_m = 50mm$ to $l_m = 5mm$ caused the localized increase of the pressure coefficient to extend further downstream. The experimental result [38] for the Re = 50,000 cases

CFD Modeling of Separation and Transitional Flow in
Low Pressure Turbine Blades at Low Reynolds Numbers

showed that the flow at 60% axial chord remained separated all the way to the trailing edge of the blade. The discrepancy in the CFD and experimental results could be attributed to possible differences in inlet turbulent boundary conditions.
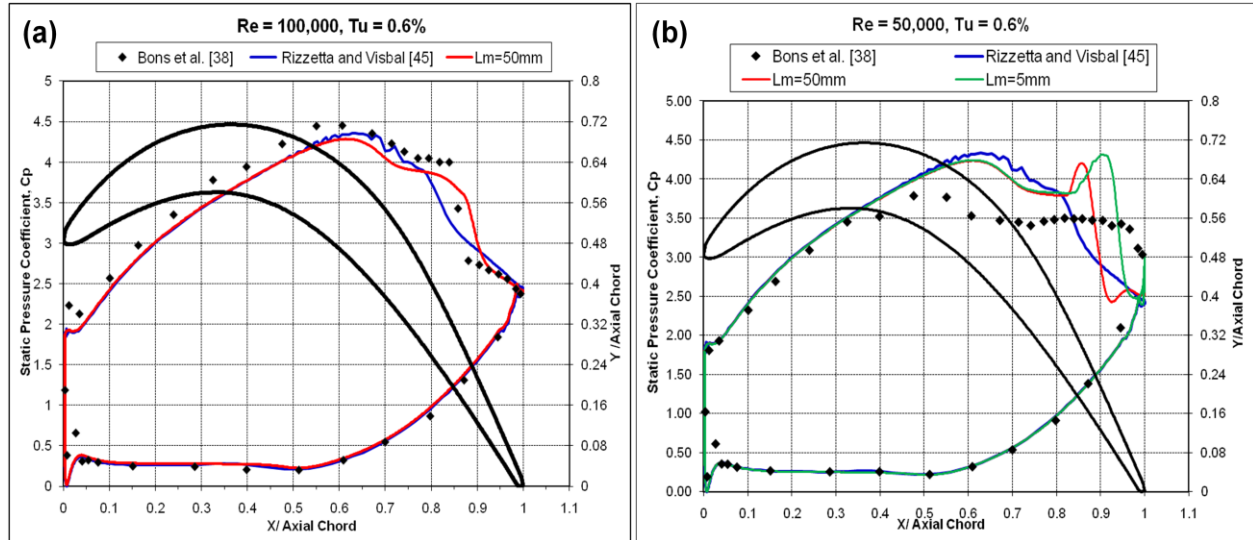
Figure 5.1. Comparison of surface static pressure coefficient with 3D LES [45] simulations and experimental results [38] at inlet Reynolds numbers of a) 100,000 and b) 50,000 for the Highly Loaded blade airfoil

The pressure coefficient on the suction side was predicted to be higher than the experimental result [38] for the Re = 25,000 case as shown in Figure 5.2. The location where the separation first began was the 60% axial chord location for both the experimental result and the current CFD prediction. The CFD was able to adequately reproduce the static pressure distribution on the pressure side of the blade. There was a large unsteadiness present in the Re = 25,000, $l_m = 50mm$ case due to vortex shedding from the separation bubble as the Re = 50,000 case, which caused a small increase in the pressure coefficient beginning at 95% axial chord. When the inlet length scale was decreased to $5mm$, the increase in the pressure coefficient began at the 85% axial chord location. The unsteady vortex shedding caused a larger localized increase in the pressure coefficient as observed in the Re = 50,000 CFD results.

CFD Modeling of Separation and Transitional Flow in
Low Pressure Turbine Blades at Low Reynolds Numbers

Chapter 5. The Highly Loaded Blade CFD Results

The LES results from Rizzetta and Visbal [45] predicted separation and turbulent reattachment for all simulated inlet Reynolds numbers. At Re = 100,000, the separated and turbulent reattachment region was smaller and located more upstream of the blade than found in the Bons *et al.* [38] experimental result. The separation and reattachment region increased as inlet Reynolds number decreased from 100,000 to 25,000. In summary, this shows that the k-k_L-ω transitional flow model was very suitable for the prediction of the qualitative flow response of the Highly Loaded blade airfoil to separated shear layers in low Reynolds number turbine flows. It demonstrated the improved prediction of the static pressure distribution and the unsteady effects of the separation and reattachment behavior.
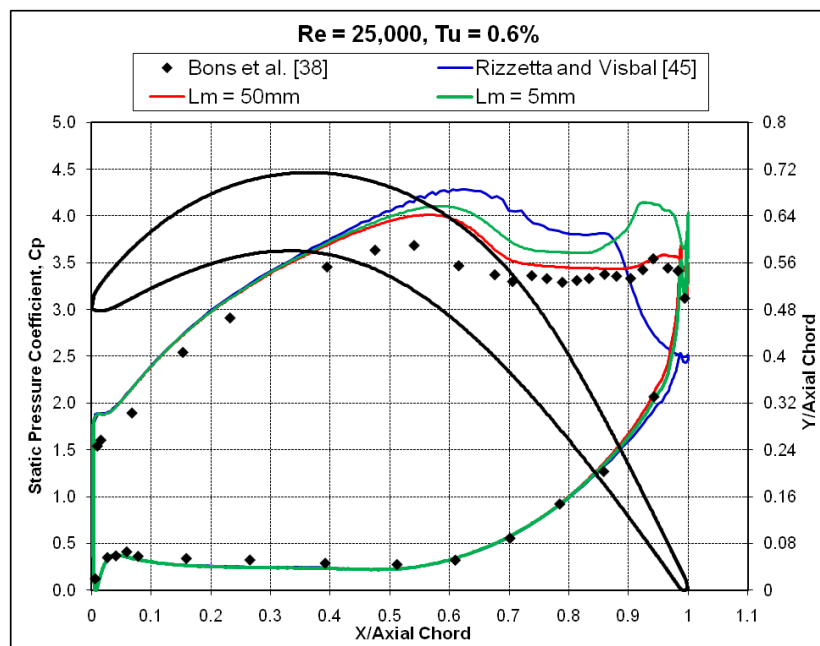
Figure 5.2. Comparison of surface static pressure coefficient with 3D LES [45] simulations and experimental results [38] at inlet Reynolds numbers of 25,000 for the Highly Loaded blade airfoil

5.1.2 *Boundary Layer Velocity Profiles*

Time-averaged values of the boundary layer velocity profiles obtained at six axial chord locations of 67.2%, 73.0%, 79.3%, 84.8%, 89.8%, and 95.0% normal to the blade surface are shown in Figure 5.3 and Figure 5.4, with boundary layer velocity measurements from the PIV

CFD Modeling of Separation and Transitional Flow in
Low Pressure Turbine Blades at Low Reynolds Numbers

experiments of Woods *et al.* [39] extracted at the same locations. The high Reynolds number at Re = 100,000 caused the separated shear layer to re-energize and undergo transition to turbulence, causing the flow to reattach to the blade surface. The CFD predicted the flow to be reattached before the 95% axial chord location, while the experiments showed turbulent flow reattachment to occur upstream at approximately the 90% axial chord location. For the Re = 50,000 case, (Fig. 5.3(b)) the velocity profile at the 73% axial chord location in the CFD prediction was in good agreement with the experimental results [39] at both inlet turbulent length scales. The size of the separation region was slightly over-predicted for the CFD results at the 84.8% axial chord location with the l_m =5mm case having a larger separation region. Both inlet length scale results showed the presence of a recirculation region at 84.8% axial chord location while the experimental results showed the flow remained separated. At the 95% axial chord location, the boundary layer reattached to the blade surface for the l_m = 50mm case, where the l_m = 5mm case flow remained separated. The experimental result showed a recirculation region had formed at the 95% axial chord location.
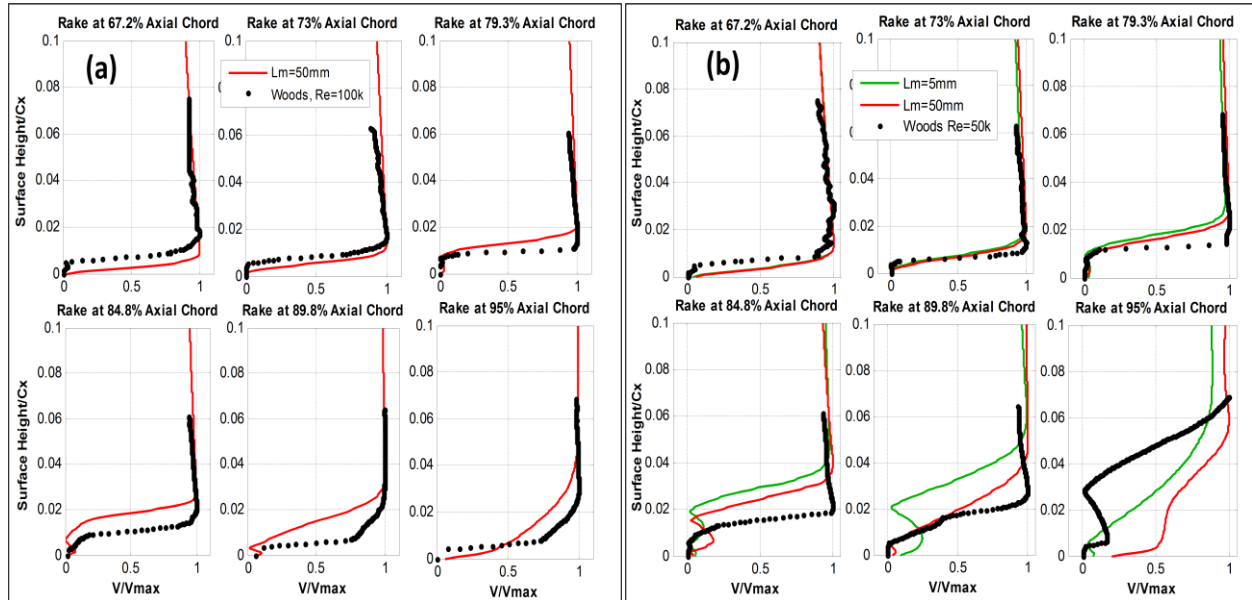
Figure 5.3. Comparison of the boundary layer velocity profiles at inlet Reynolds numbers of a) 100,000 and b) 50,000 with the experimental results [39] for the Highly Loaded blade airfoil

Figure 5.4 shows the Re = 25,000 case where the shape of velocity profiles were in good agreement with experimental results [39] at the 73% axial chord location for both inlet turbulent length scales. Downstream of those locations, the CFD predicted a larger separation region than the experimental results [39]. The time-averaged behavior of the recirculation region caused by the separation bubble was shown to be similar for both the CFD and experimental results. Figure 5.4 shows that the separated flow region decreased when the inlet turbulent length scale was decreased to *5mm*. The opposite trend was observed for the Re = 50,000 when the inlet turbulent length scale was decreased to *5mm*. The CFD results did follow the same trend as the experimental results [39] in that the separation grew as the Reynolds number was decreased. There were differences in the boundary layer behavior of the separation region compared to the experimental results [39]. The effect of neglecting the spanwise dimension was found not to be the reason for the discrepancy, which will be discussed in Section 5.2. The k-k_L-ω transitional flow model demonstrated that it can show a qualitative response to separated boundary layers.

There were differences using the k-k_L-ω transitional model in the prediction of the size of the separation region for all Reynolds number cases. It is noted that the k-k_L-ω flow model was not specifically designed to model boundary layer transition in separated shear layers [30]. It was intended to model attached transitional flows.
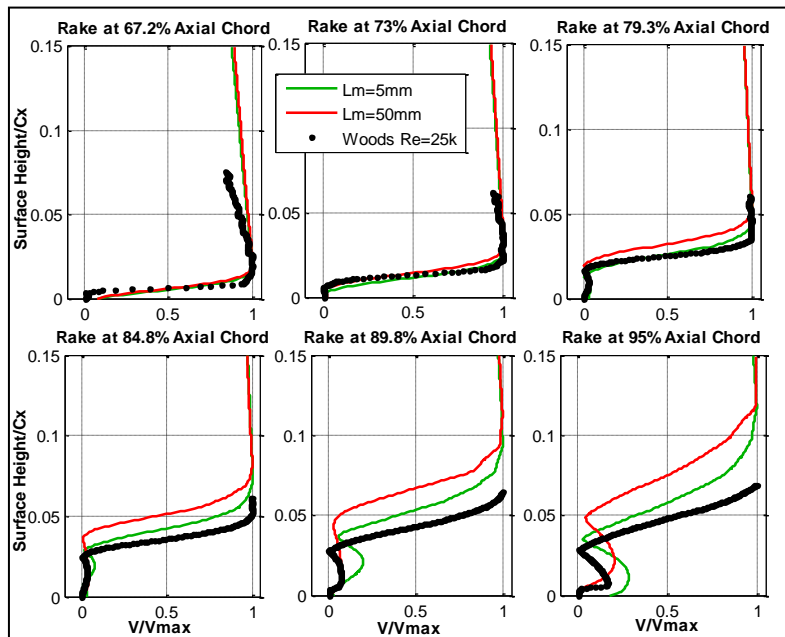
Figure 5.4. Comparison of the mean boundary layer velocity profiles at 25,000 with the experimental results [39] for the Highly Loaded blade airfoil

5.1.3   Unsteady Features of the Flowfield

The features of the unsteady flowfield were investigated to gain insight on the behavior of the unsteady flow separation and vortex generation. Instantaneous "snapshots" of the predicted flowfield were taken for all three Reynolds number simulations. For the Re = 100,000 case, a total of 44,700 time-steps or 0.223sec were utilized for averaging of mean-flow quantities with a flow time-step of 5μsec. The flow-time, which is described as the time interval it takes for the simulated fluid flow to travel from the inlet to the exit CFD domain, was 0.0654sec. The mean-flow averaging time-interval was calculated with Eq. (5.1)

$$\text{flow - time interval} = \frac{\text{mean - flow averaging time interval}}{\text{flow - time}}$$ (5.1)

was 3.41 flow-time intervals. Upon investigation of the unsteady flow features, separation and reattachment were seen to occur at every time step as representatively indicated in Figure 5.5. The separated shear layer on the suction side produces two clockwise vortical structures that move downstream. These vortical structures break down and reduce in magnitude when the separated boundary layer becomes reattached to the blade surface.
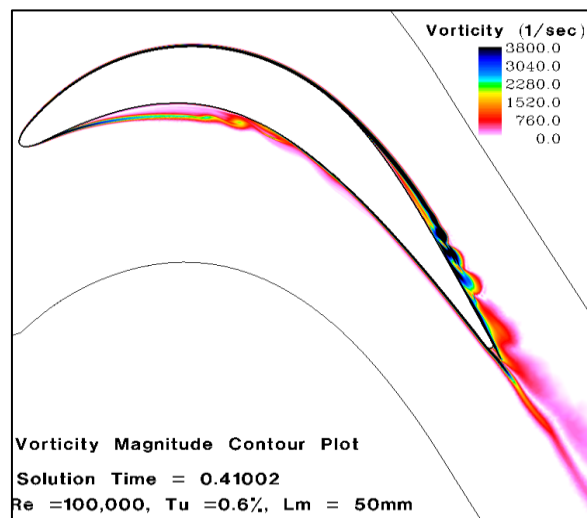
Figure 5.5. Instantaneous vorticity contour plot at Re = 100,000 for the Highly Loaded blade airfoil

The inlet turbulent length scale had a significant effect on the flow unsteadiness for the Re = 50,000 simulations. For the $l_m = 50mm$ case, a total of 70,000 time-steps or 0.07074sec were utilized for averaging of mean-flow quantities with a flow time-step of 1μsec. The total flow-time was 0.131sec and mean flow-averaging was 0.54 flow-time intervals as calculated with Eq. (5.1). As in the Re = 100,000 case, the separated shear layer produced vortices on the blade suction side, but they were larger in size. Once the suction side vortex formed, it traveled downstream and rolled off the blade surface and into the freestream as shown in Figure 5.6(a)-(b). The boundary layer became reattached once the suction side vortex moved into the

freestream giving the boundary layer velocity profiles in Figure 5.3 its unique shape. For the l_m = *5mm* case, a total of 64,100 time-steps 0.1284sec or were used for averaging of mean-flow quantities with a flow time-step of 2μsec with 0.98 flow-time intervals. The suction side vortices created from the separated shear layer were larger compared to the l_m = *50mm* case and this was verified from the velocity profiles in Figure 5.3(b). Also there were smaller vortices created within the shear layer as shown in Figure 5.6(c)-(d). The suction side vortex exhibited the same behavior of forming and rolling off the blade surface as in the l_m = *50mm* case, but occurred slightly more downstream and closer to the blade trailing edge.
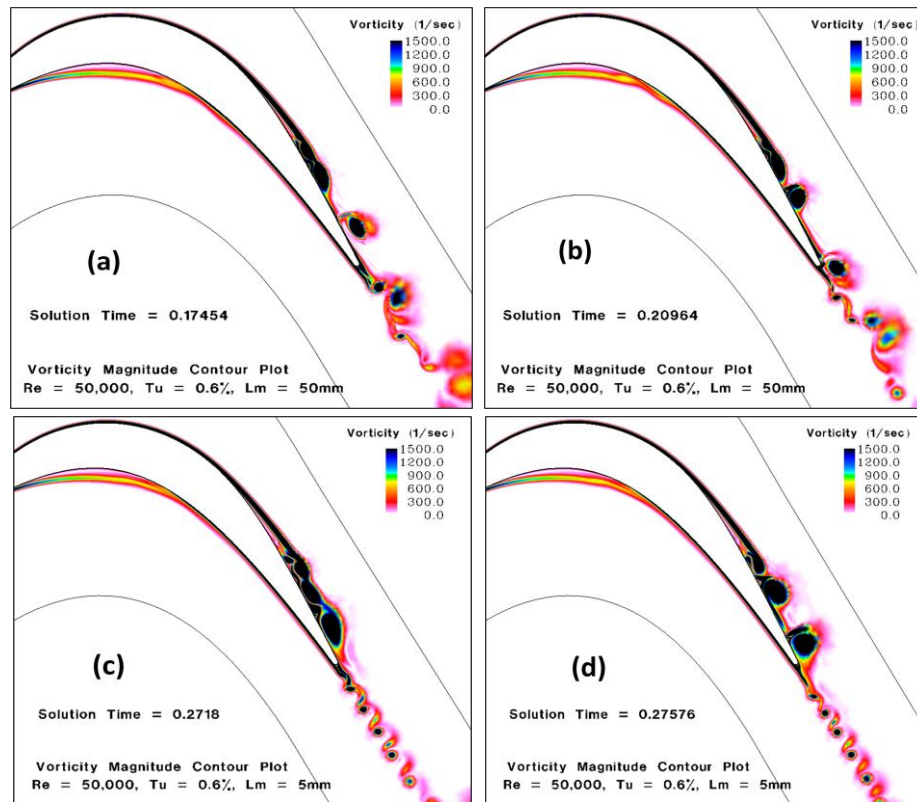
Figure 5.6. Instantaneous vorticity contours at Re = 50,000 for the Highly Loaded blade airfoil at l_m = 50mm (a&b) and l_m = 5mm(c&d)

The time signal of the drag coefficient was calculated by summing the dot product of the pressure and viscous forces with the force vector along the blade surface boundary as shown in Figure 5.7. A Fast-Fourier Transform (FFT) was performed to examine the frequency content

present in the time signal of the drag coefficient. The frequency resolution (f_{resol}) was based on

the time-step (t_{step}) and the averaging interval (N_{avg}) and calculated based on the equation

$$f_{resol} = \frac{1}{t_{step}(N_{avg})}$$
(5.2)

The frequency resolution was 8Hz and 14Hz for the l_m = *5mm* and l_m = *50mm* cases,

respectively. The dominant frequencies present in the FFT calculation originated from the

vortex generation on the pressure and the suction side caused by the separated shear layers.

Also, Figure 5.7(c)-(d) and Figure 5.9(c)-(d) shows the shedding frequency for each vortical

structure for the Re = 50,000 and 25,000 cases, respectively. Table 5.1 shows the comparison of

the separation location, shedding frequencies, and Strouhal number based on Eq. (4.1) for both

inlet turbulent length scales. The shedding frequency and Strouhal number was higher for the

l_m=50mm case due to the lower specific dissipation rate while the separation point was

approximately the same for both inlet turbulent length scales.
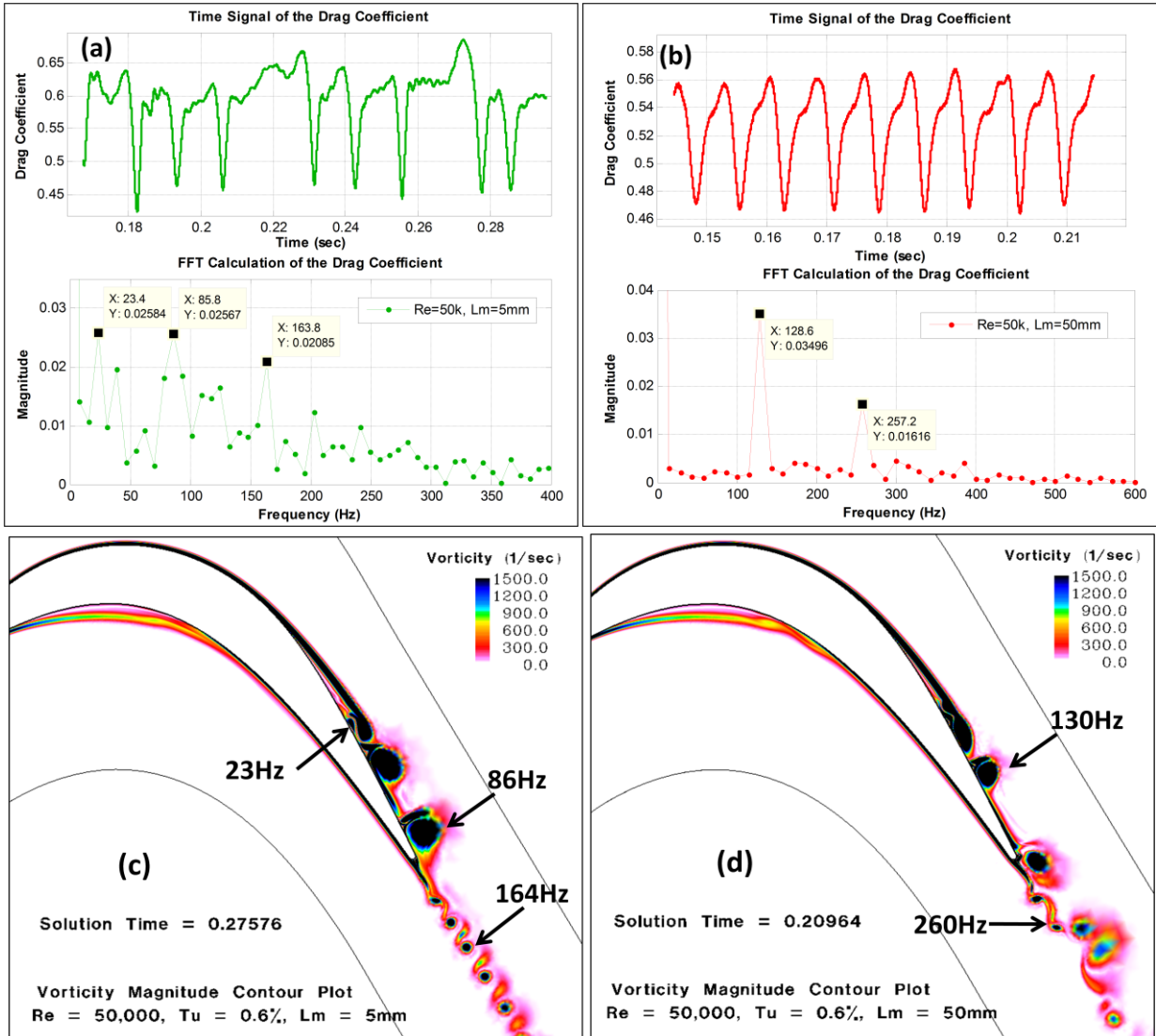
Figure 5.7. Time signal, FFT calculation of the drag coefficient, instantaneous vorticity contours at Re = 50,000 for the Highly Loaded blade airfoil at l_m = 5mm (a) & (c) and l_m = 50mm (b) & (d)

In Figure 5.8(a)-(b), the unsteady nature of the Re = 25,000, l_m = 50mm case is shown. The flow time-step was 10μsec and 43,000 time-steps or 0.4297sec was completed for mean flow averaging. The total flow-time was 0.262sec and mean flow-averaging was 1.64 flow-time intervals. The separated shear layer on the suction side produced a clockwise vortex, while the pressure side shear layer produced a counterclockwise vortex that moved from the trailing edge to the wake region. The decrease in length scale to *5mm* caused the opposite effect as the Re = 50,000 case where the separation region decreased when the turbulent length scale decreased as

CFD Modeling of Separation and Transitional Flow in
Low Pressure Turbine Blades at Low Reynolds Numbers

shown in Figure 5.8(c)-(d). Also, the vortex shedding frequencies on pressure and suction side remained unchanged unlike the Re = 50,000 case (Fig. 5.9). This could be due to the separation region in the Re = 25,000 cases being significantly larger than the Re = 50,000 cases. The suction side vortex was formed above the blade surface and became insensitive to changes in the inlet turbulent length scale. The same trend was found for the inlet Re = 25,000 and 50,000 cases in which decreasing the turbulent length scale caused the separation location to occur slightly more downstream as indicated in Table 5.1.
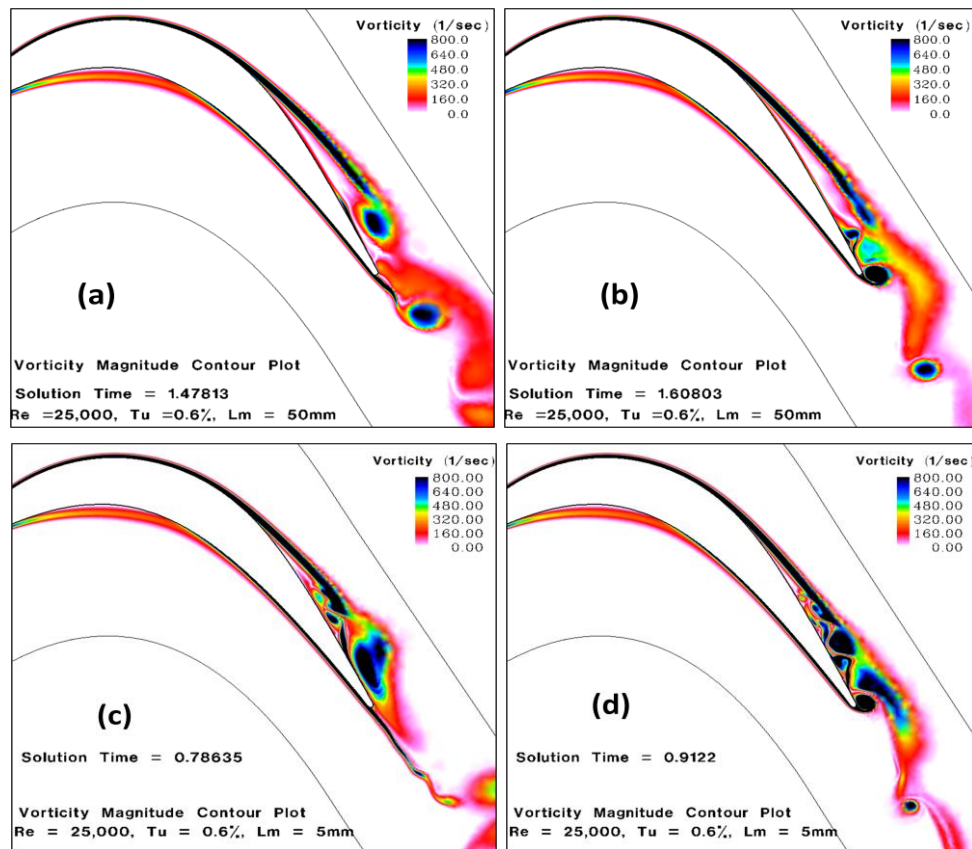
Figure 5.8. Instantaneous Vorticity Contours at Re = 25,000 for the Highly Loaded Blade Airfoil at l_m = 50mm (a&b) and l_m = 5mm (c&d)

			Pressure Side		Suction Side			
Re	$l_m(mm)$	X_{sep}/C_x	f_{shed}	St	f_{shed}	St	f_{shed}	St
25,000	5	0.709	45	0.0045	10	0.0010	20	0.0020
25,000	50	0.722	45	0.0045	12	0.0012	20	0.0020
50,000	5	0.717	164	0.0050	23	0.00070	86	0.0026
50,000	50	0.726	260	0.0082	130	0.0041	-	-
100,000	50	0.713	-	-	-	-	-	-

Table 5.1. Summary of the separation location and Strouhal number for the Highly Loaded blade airfoil
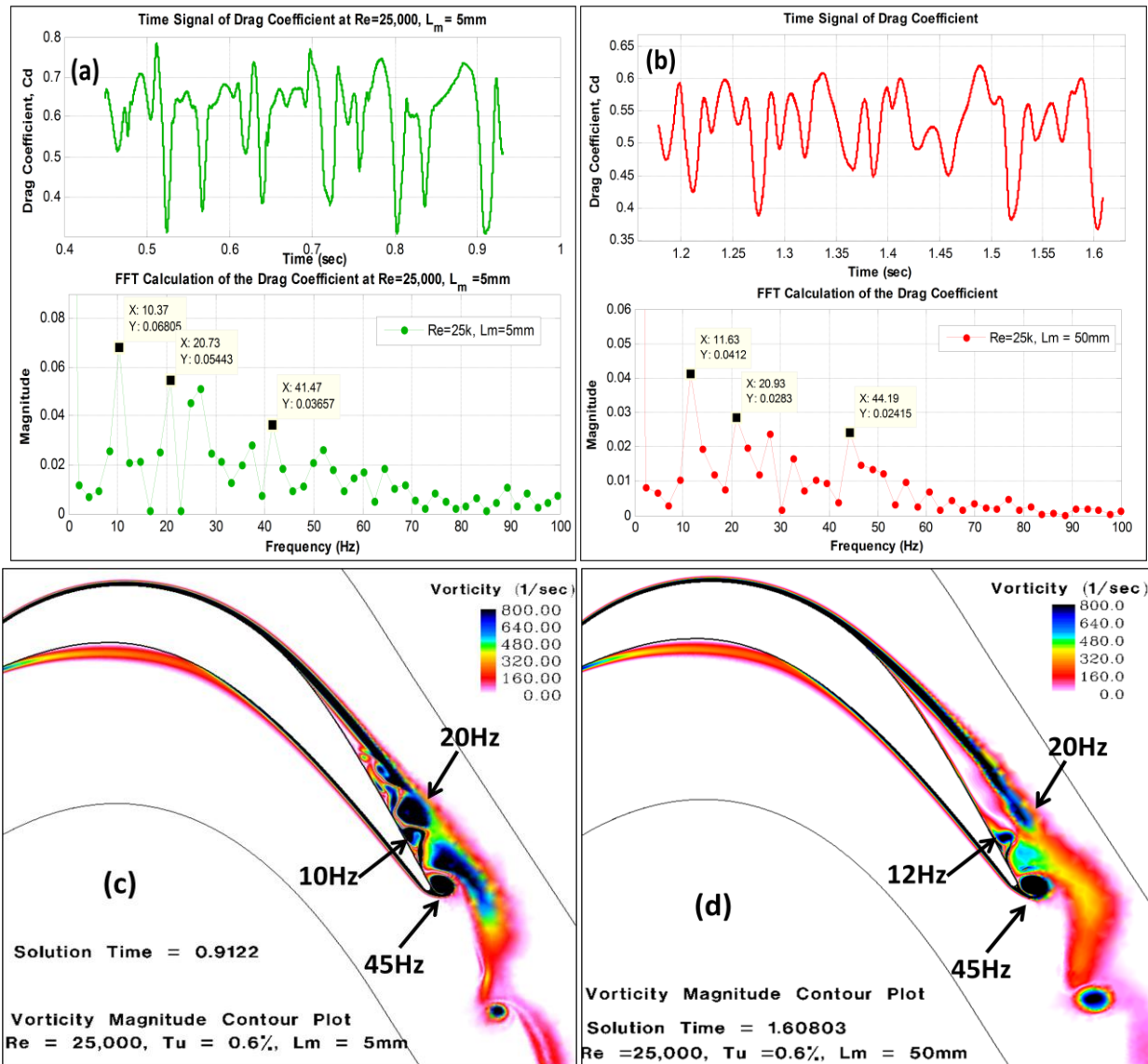
Figure 5.9. Time signal, FFT calculation of the drag coefficient, instantaneous vorticity contours at Re = 25,000 for the Highly Loaded blade airfoil at l_m = 5mm (a) & (c) and l_m = 50mm (b) & (d)

5.1.4   Total Pressure Loss Coefficient Predictions

The total pressure loss coefficient predictions using the k-k_L-ω transitional model for all three Reynolds number simulations are shown in Figure 5.10. The CFD results are compared to experimental wake measurements taken by Garmoe [36] and Casey [40] for a total of two pitch lengths. The major difference in the experimental measurements at Re = 100,000 (Fig. 5.10(a)) was in the average inlet turbulence intensity, which was reported as 0.785% for the Garmoe [36] measurements and 0.437% for the Casey [40] measurements. For the Re = 100,000 case, the CFD results under-predicted the loss coefficient, with 88% and 60% percent agreement with the Garmoe [36] and Casey [40] measurements, respectively. It was expected that the CFD prediction would lie between the two experimental results since the computational inlet turbulence intensity was 0.6%. The reason for the under-prediction was due to the turbulent boundary layer reattachment point being located further downstream on the blade than the experimental measurements, resulting in a lower predicted momentum loss than experimentally measured. Table 5.2 showed a 62% and 72% agreement in the integrated loss coefficient comparisons with Garmoe [36] and Casey [40] experimental results, respectively due to differences in the width of wake region and the maximum value of the loss coefficient.

The total pressure loss coefficient prediction at Re = 50,000 (Fig. 5.10(b)) was found to have good agreement with respect to both Casey's [40] measurement made at an inlet Reynolds number of 45,000 and inlet turbulence intensity of 0.34%, and Garmoe's [36] measurement at Re = 50,000 with a turbulence intensity of 0.84%. Changing the inlet turbulent length scale was observed to have no effect on the peak loss coefficient predictions. Both CFD results were with 93% agreement with experimental results [36, 40] on the peak value of the loss coefficient. A length scale effect was observed in the integrated loss coefficient with the l_m = 5mm case having

CFD Modeling of Separation and Transitional Flow in
Low Pressure Turbine Blades at Low Reynolds Numbers

the largest value. The higher dissipation rate caused the wake width to increase across the pitch length thus increasing the integrated loss coefficient. Comparison with the experimental results indicated a 60% and 68% agreement for the $l_m = 50$mm and $l_m = 5$mm cases, respectively which was attributed to the width of the wake region being larger in the experimental results.

For the Re = 25,000 cases, (Fig. 5.10(c)) the size of the separation region was over-predicted by the CFD, yet the total pressure loss predictions were lower than both experimental results. The decrease in the inlet turbulent length scale caused the wake region to spread and further decrease the maximum value to the loss coefficient. A similar trend was observed in the Re = 50,000 case. The increase in specific dissipation rate, which resulted from lowering inlet turbulent length scale, increased the width of the wake instead of transferring the turbulent flow being generated from the boundary layer to viscous losses at a higher rate which should have caused an increase in the loss coefficient predictions. Better agreement with the experimental results of integrated loss coefficient was achieved with an 84% and 79% agreement with Garmoe [36] and Casey [40], respectively. Also, the CFD prediction of the integrated loss coefficient was independent of changes in inlet turbulent length scale which indicated the amount of viscous losses generated in the wake region was similar in both CFD cases. This confirmed the previous observation that a higher inlet length scale caused only the width of wake region to increase and did not affect the peak value of the loss coefficient.
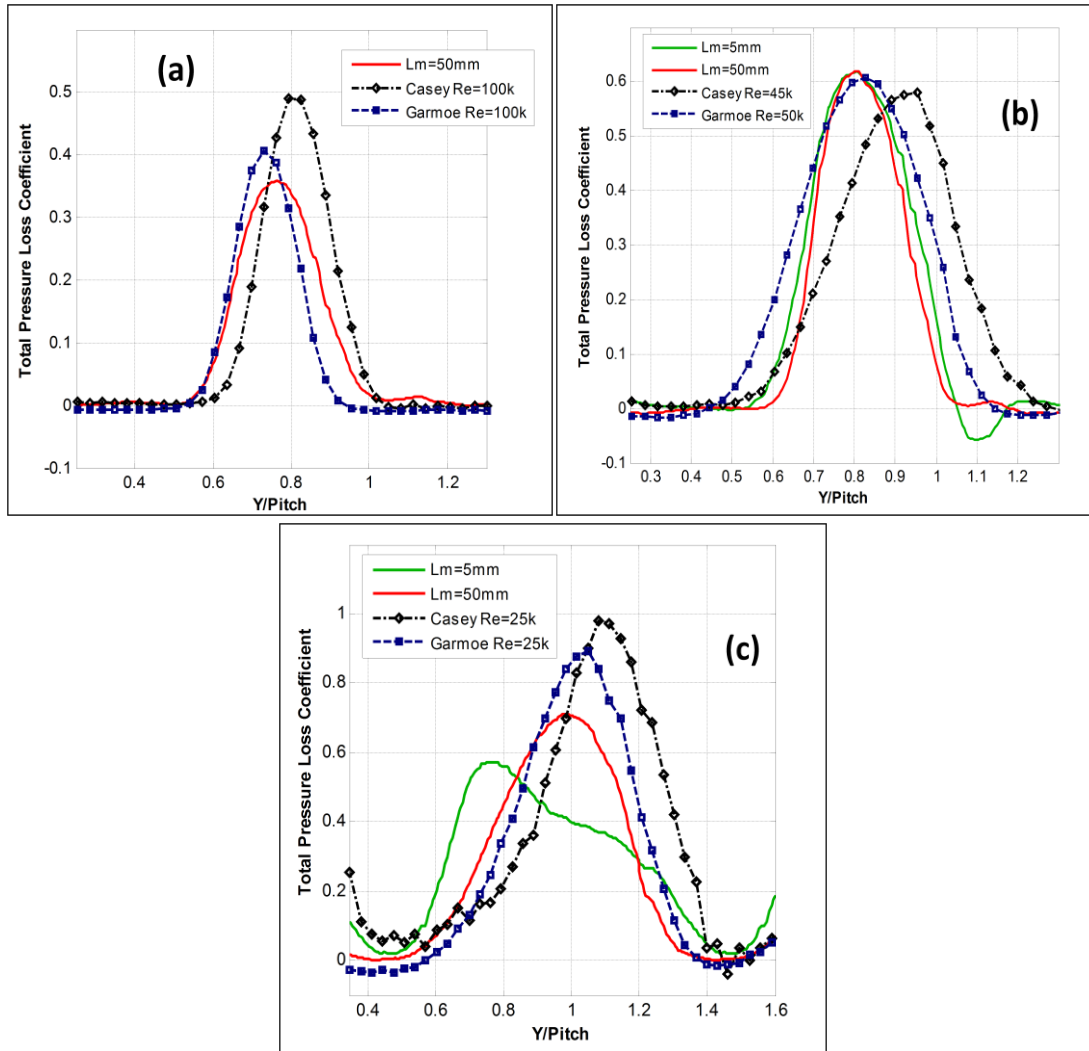
Figure 5.10. Comparison of total pressure loss coefficient with experimental [36,40] results at inlet Reynolds numbers of (a) 100,000, (b) 50,000, and (c) 25,000 for the Highly Loaded blade airfoil

Re	l_m(mm)	Integrated Total Pressure Loss Coefficient		
		CFD	Garmoe [36]	Casey [40]
25,000	5	0.3045	0.3562	0.3808
	50	0.3018		
50,000	5	0.1708	0.2472	0.2494
	50	0.1490		
100,000	50	0.0896	0.06535	0.1242

Table 5.2. Integrated total pressure loss coefficient comparison with the experimental [36, 40] results for the Highly Loaded blade airfoil

5.2 Three-Dimensional CFD Comparisons with Experimental Results

An unsteady simulation was completed using the three-dimensional cascade CFD model of the Highly Loaded blade airfoil presented in Section 4.3.1 at inlet Reynolds number of 25,000. The main goal was to determine the effect of the added spanwise dimension on the flowfield predictions using the k-k_L-ω model. The inlet turbulence intensity was set to Tu = 0.6% with an inlet turbulent length scale at l_m = 50mm. The flowfield of the three-dimensional simulation was compared to the two-dimensional CFD results completed at same inlet conditions and experimental results. Spanwise-averaged surface static pressure coefficient, boundary layer velocity profiles, and the wake total pressure loss coefficient were used for comparisons. Also, the unsteady features of separation and vortex shedding were investigated qualitatively.

5.2.1 Surface Static Pressure Coefficient

Figure 5.11 compares the blade surface static pressure coefficient of both the two and three-dimensional simulations using the k-k_L-ω model to the measurements of Bons *et al.* [38] and three-dimensional LES results of Rizzetta and Visbal [45]. A similar distribution of the suction side blade loading was observed for both the two and three-dimensional results to the 90% axial chord location. Downstream of that location, the three-dimensional results showed a larger increase in the local pressure peak due to the motion of shed vortices compared to the two-dimensional result. The mean-flow averaging time interval in the three-dimensional prediction was 14.6 times smaller compared to the two-dimensional prediction. This caused an increase in the effect that the intermittent vortex shedding had on the static pressure distribution. The LES results from Rizzetta and Visbal [45] predicted separation and turbulent reattachment for Re = 25,000 while the experimental [38] results show separation to the trailing edge. This indicated the addition of the spanwise dimension did not have significant effect on the blade loading and

the two-dimensional result provided adequate prediction of the surface static pressure coefficient

for the Highly Loaded blade airfoil.
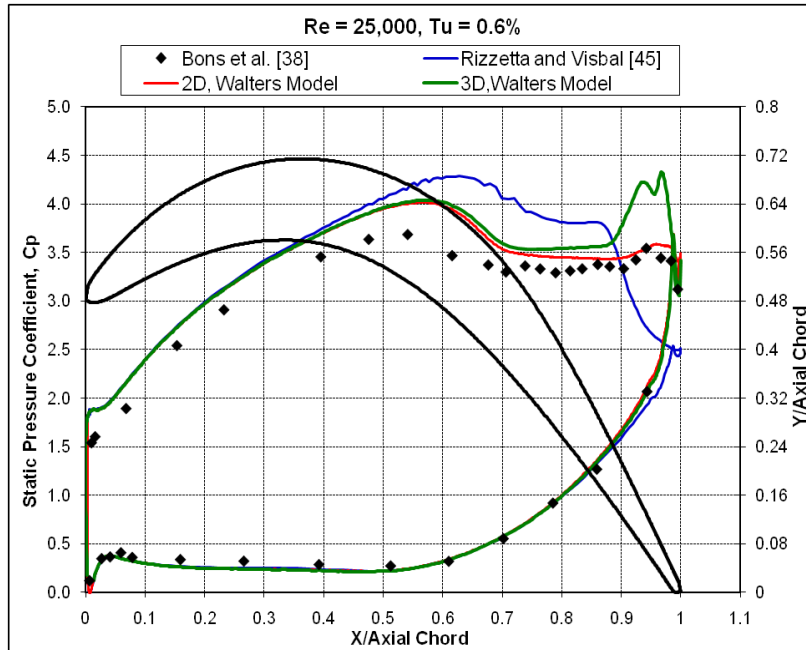
Figure 5.11. Dimensional comparison of surface static pressure coefficient with 3D LES [45] simulations
and experimental results [38] at inlet Reynolds numbers of 25,000 for the Highly Loaded blade airfoil

5.2.2   Mean Velocity Boundary Layer Profiles

The spanwise-averaged boundary layer profiles of the mean velocity obtained from the

three-dimensional simulation were compared to the two-dimensional k-k_L-ω model prediction

and experimental [39] results at the same axial chord locations. Figure 5.12 shows the three-

dimensional predictions were in good agreement with the experimental results to the 79.3% axial

chord location. Downstream of those locations, the three-dimensional result predicted a slightly

smaller separation region compared the two-dimensional results, but showed a larger separation

region than the experimental results [39]. The shape of boundary layer profiles starting at the

84.8% axial chord location in the three-dimensional prediction was due to the spanwise

averaging. The suction surface separation point was located at 71.2% axial chord location

CFD Modeling of Separation and Transitional Flow in
Low Pressure Turbine Blades at Low Reynolds Numbers

similar to the 72.2% separation location in the two-dimensional simulation. The added spanwise

dimension did produce a slightly smaller separation region as reported in Rizzetta *et al.* [45] thus

provided somewhat better agreement with the experimental result.
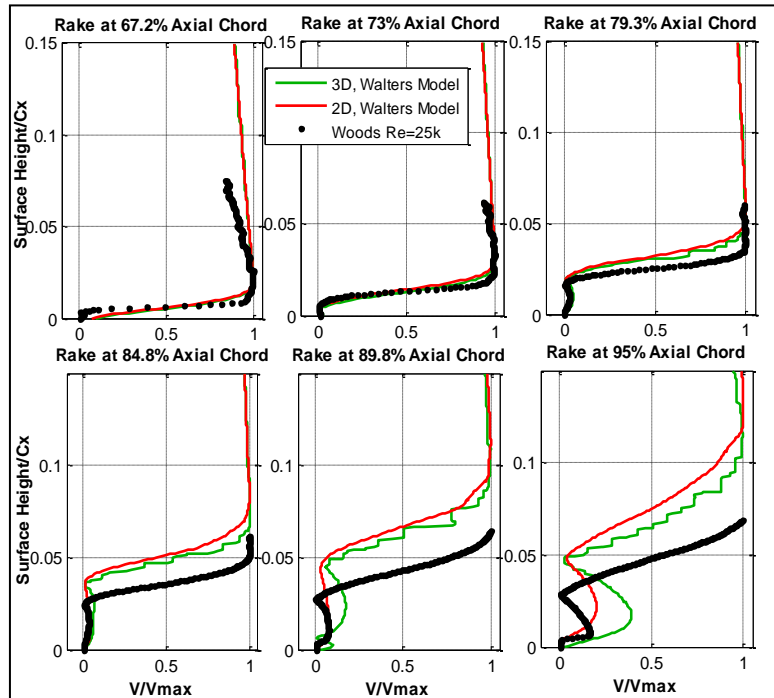
Figure 5.12. Two and three-dimensional comparisons of the mean boundary layer velocity
profiles at 25,000 with the experimental results [39] for the Highly Loaded blade airfoil

5.2.3 Unsteady Features of the Flowfield

The features of the unsteady flowfield have been investigated for the three-dimensional

simulation of the Highly Loaded blade in order to compare with the unsteady flowfield

predictions from the two-dimensional results. Instantaneous contours of the vorticity magnitude

at mid-span location (0.01778m) were compared to the two-dimensional result as shown in

Figure 5.13. A total of 5898 time-steps (0.113 flow-time intervals or 0.02949sec) were utilized

for averaging of mean-flow quantities with a flow time-step of 5μsec which was significantly

smaller time interval compared to the two-dimensional simulation. Unsteady averaging of the

flowfield for a large number of time-steps using the three-dimensional Highly Loaded blade

D. Sanders   117
CFD Modeling of Separation and Transitional Flow in
Low Pressure Turbine Blades at Low Reynolds Numbers

CFD model could not be made because of the large amount of processors and long simulation times required. The current flow-averaging interval was considered adequate to show the three-dimensional unsteady effects due to vortex shedding. Figure 5.13 shows that similar unsteady effects were seen in both the two and three-dimensional results. The separated shear layer produced a large clockwise vortex (Fig 5.13(a) &(c)) and a smaller counter-clockwise vortex seen in the two and three-dimensional result in Figure 5.13(b) and 5.13(c), respectively. Also, a counter-clockwise vortex was produced from the pressure side at the blade trailing edge (Fig 5.13(b) &(d)).
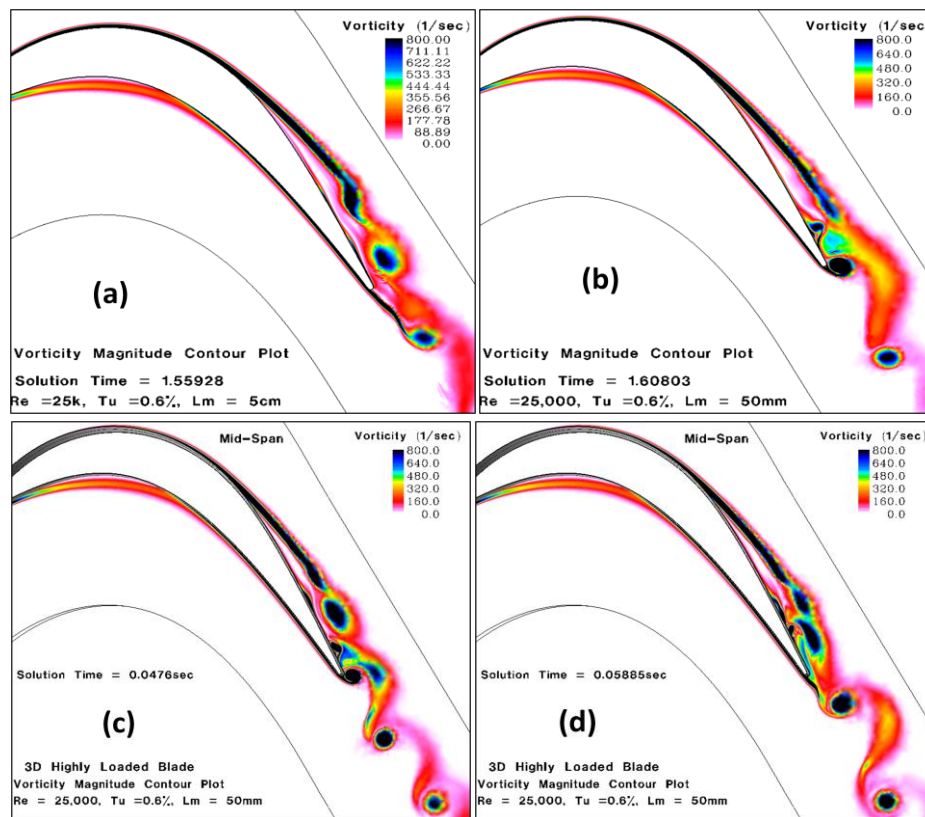
Figure 5.13. Comparison of the instantaneous vorticity contours at Re = 25,000, Tu = 0.5% for the (a)-(b) 2-D and (c)-(d) 3-D simulations of the Highly Loaded blade airfoil

Iso-surfaces of the vorticity were made to show the three-dimensional structure of the vortices shed from the separated shear layers. Figure 5.14 shows iso-surfaces of constant

D. Sanders   118
CFD Modeling of Separation and Transitional Flow in
Low Pressure Turbine Blades at Low Reynolds Numbers

vorticity of 800, 600, 400, and 150 sec^{-1} in the separated flow region. The vortices shed from the pressure and suction surfaces were largely two-dimensional in shape as shown in Figure 5.14(a)-(c). Also, there were small three-dimensional vortical structures present in the separation and wake region (Fig 5.14(d)) that broke-up in the spanwise direction. The vortical flow structure was largely laminar and the two-dimensional simulation was effective in predicting the shape of the unsteady vortices at the Re = 25,000 for the Highly Loaded blade.
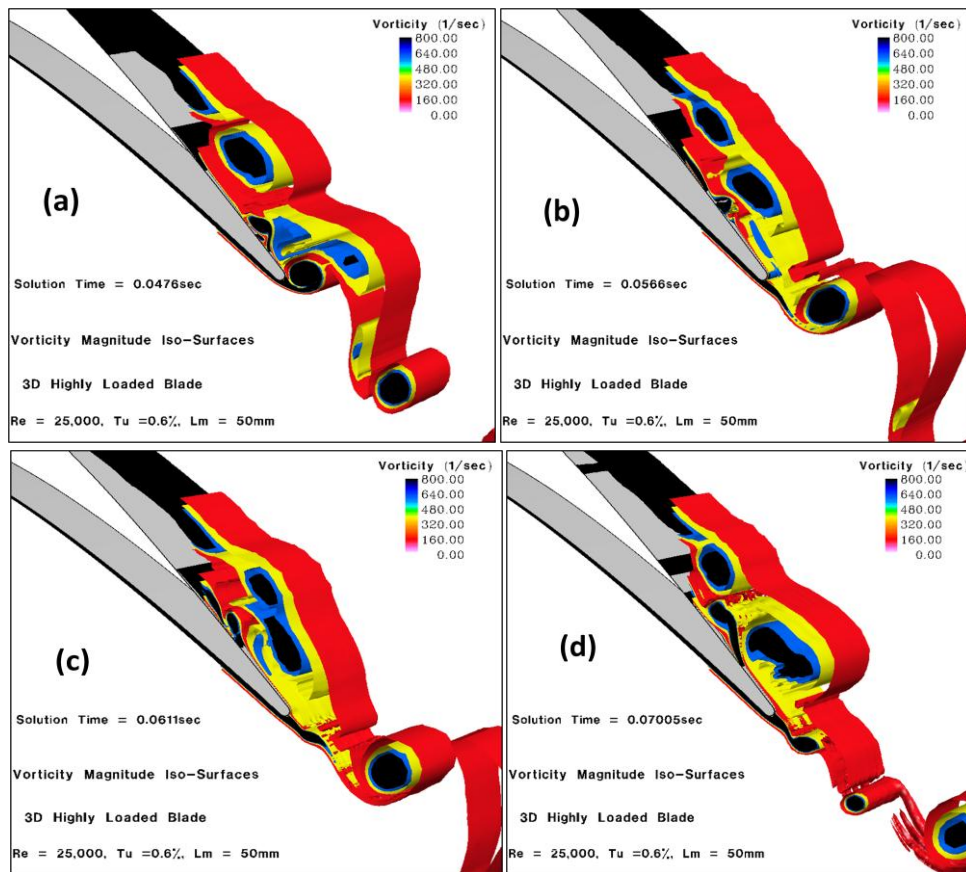
Figure 5.14. Iso-surfaces of instantaneous vorticity for the 3-D simulation of the Highly Loaded blade airfoil at Re = 25,000, Tu = 0.5%

Similar results were obtained in a LES study by Visbal [47] on an oscillating SD7003 airfoil at low inlet Reynolds numbers. Figure 5.15 shows the comparison of the instantaneous spanwise vorticity for two and three-dimensional simulations at Reynolds numbers of 10,000 and

40,000. At Re = 10,000, the two and three-dimensional results were in good agreement with each other over a significant portion of the airfoil as shown in 5.15(a)-(b). The vortices were mostly two-dimensional in shape with some three-dimensional effects due to spanwise breakdown from transitional flow effects [47] (Fig. 5.15(b)). At Re = 40,000, significant differences were observed between two and three-dimensional results (Fig. 5.15(c)-(d)). The coherent vortices observed from the two-dimensional simulations breakdown in the spanwise direction into small-scale structures. The higher Reynolds number caused the increase in the spanwise breakdown in vortices due transitional flow effects.
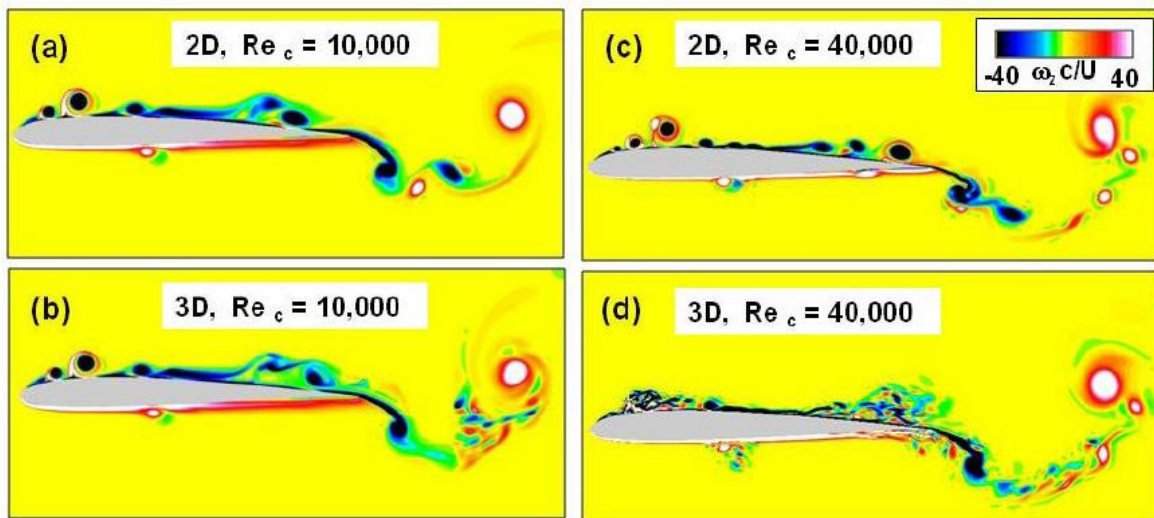
Figure 5.15. Comparisons of instantaneous spanwise vorticity for 2-D and 3-D LES simulation by Visbal [47]

The three-dimensional Highly Loaded blade CFD model was run at Re = 25,000, the midpoint between the Reynolds numbers simulated in the Visbal [47] LES results. As seen in Fig 5.15(c)-(d), vortical structures broke down in the spanwise direction. So, a larger amount of spanwise instabilities were expected to be present than shown at Re = 10,000 condition run by Visbal [47]. However, the Walters and Leylek [2] k-k_L-ω model is based on the RANS CFD method and modeled transitional flow due to only streamwise instabilities. Thus, the present

CFD Modeling of Separation and Transitional Flow in
Low Pressure Turbine Blades at Low Reynolds Numbers

three-dimensional Highly Loaded blade CFD model will not be able to capture spanwise instabilities due to transitional flow. Based on this fact, the trends observed in comparing the two and three-dimensional simulations at Re = 25,000 for the Highly Loaded blade airfoil with the present model will be expected to be similar for simulations at higher inlet Reynolds numbers.

5.2.4   Total Pressure Loss Coefficient Predictions

The wake total pressure loss coefficient distribution and the integrated value are shown in Figure 5.16 and Table 5.3, respectively. The three-dimensional simulation indicated a 41% over-prediction in the peak loss coefficient with 87% agreement in the integrated loss coefficient compared to Casey's [40] experimental result. The two-dimensional predictions showed better comparison to Garmoe's [36] experimental result with a 29% under-prediction in the peak loss coefficient and 84% agreement with the integrated loss coefficient. The over-prediction and distribution in the loss coefficient was significantly different in the three-dimensional simulation due to the mean-flow-averaging time interval which was 14.6 times smaller than for the two-dimensional simulation. A longer mean-flow-averaging time interval would have resulted in a decrease in the effect that the intermittent vortex shedding had on the total pressure loss in the wake region. So, if the averaging interval of the three-dimensional simulation were increased, the loss coefficient would be reduced significantly. Good agreement was achieved in the prediction of the integrated loss coefficient indicating the amount of viscous loss generated from the vortex shedding was predicted sufficiently.
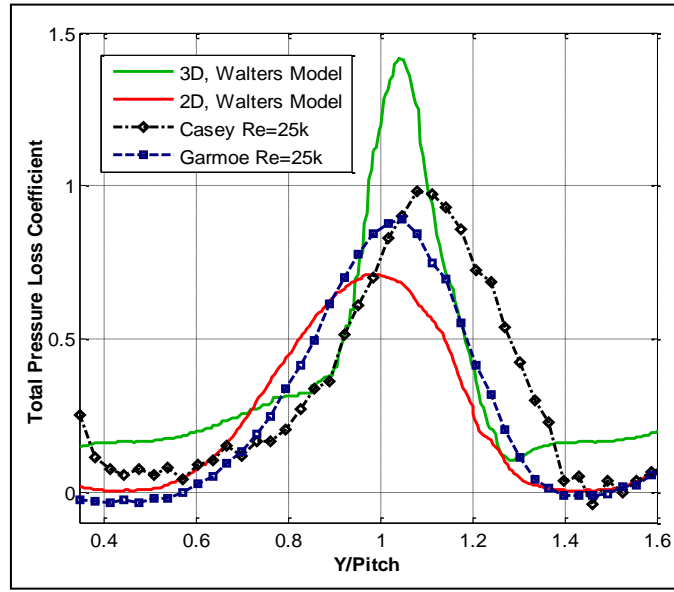
Figure 5.16. 2-D and 3-D comparison of total pressure loss coefficient with experimental [36,40] results at Re = 25,000 for the Highly Loaded blade airfoil

Re	CFD Model	Tu (%)	$l_m(mm)$	Integrated Total Pressure Loss Coefficient		
				CFD	Garmoe [36]	Casey [40]
25,000	2D	0.5	50	0.3018	0.3562	0.3808
	3D	0.5	50	0.4279		

Table 5.3. Dimensional comparison of the integrated total pressure loss coefficient with the experimental [36, 40] results for the Highly Loaded blade airfoil

5.3 Summary of Results

Flows over the Highly Loaded blade airfoil were simulated at inlet Reynolds numbers of 100,000, 50,000, and 25,000. The unsteady features of separation and vortex generation of the flowfield were qualitatively investigated. Boundary layer velocity profiles, surface static pressure distributions, and the wake total pressure loss coefficient were compared to the available experimental data. The CFD simulations showed good agreement with the experimental results in prediction of separation and reattachment. The k-k_L-ω transitional flow model showed a better qualitative response to separated shear layers as seen in the experimental measurements, but quantitative inaccuracies in the size of the separation region were observed.

CFD Modeling of Separation and Transitional Flow in Low Pressure Turbine Blades at Low Reynolds Numbers

Chapter 5. The Highly Loaded Blade CFD Results

Compared to the Lightly Loaded blade airfoil, the flowfield for the Highly Loaded blade airfoil was very complex involving unsteady separated shear layers. The separated flow is known to produce three-dimensional vortical structures, so a three-dimensional CFD model of the Highly Loaded blade was simulated at Re = 25,000 and compared to the two-dimensional CFD predictions. The addition of the spanwise dimension did not have significant effect on the blade loading and the surface static pressure coefficient distribution was similar to the two-dimensional result. The two and three-dimensional results were in good agreement with each other on the prediction of the separation region, but the three-dimensional result predicted a slightly smaller separation region. This produced closer agreement with the experimental [39] results but, the separation region was still over-predicted compared to the experiments. Investigations on the three-dimensional shape of the unsteady vortices showed the vortices shed were very coherent and largely two-dimensional in shape similar to the LES results by Visbal [47]. The k-k_L-ω model did not take into account transitional flow due to spanwise instabilities, so it does not capture the same effects like the more superior LES CFD method. The peak value of the loss coefficient was over-predicted compared to the experimental result because of the short averaging interval for the mean flow predictions. The three-dimensional result showed good agreement with the experimental result in the prediction of the amount of viscous loss generated within the wake region. This study provided an evaluation on how well the k-k_L-ω model captures the separation and unsteady characteristics observed in the Highly Loaded blade airfoil.

CHAPTER SIX

6. The Aft-Loaded L1A Blade CFD Results

The last blade geometry used for the invesitgation of Walters and Leylek's [2] k-k_L-ω transitional flow model was the Aft-Loaded L1A blade airfoil. The low Reynolds number aerodynamic effects of the Aft-Loaded L1A blade were the most challenging to predict because of very high loading level and strong adverse pressure gradient present on the aft portion of the suction surface. Two-dimensional flow simulations were completed at both high and low inlet turbulence levels and compared to experimental results of Marks *et al.* [35] and CFD results of Clark *et al.* [25]. Investigations of the unsteady flowfield were made at low and high inlet turbulent intensities. The inlet turbulent length scale was varied at the high inlet turbulence intensity to investigate its effect on the total pressure loss predictions. This study will serve as a baseline study for the flowfield comparisons with simulations completed using the Aft-Loaded L1A blade with upstream wake-generators CFD model.

6.1 CFD Predictions at Low Inlet Turbulence intensity

The performance of the two-dimensional cascade CFD model of Aft-Loaded L1A blade airfoil (Fig. 3.5(c)) was simulated at an inlet Reynolds number of 31,000 and 50,000. Unsteady simulations were run with an inlet freestream turbulence intensity of 0.5% for all inlet Reynolds numbers. The inlet turbulent length scale was set as l_m = *50mm* which was based on simulations of the Highly Loaded blade since updated length scale measurements were not available for the LSWT at low inlet turbulent intensities. The next sections present the comparisons of the static pressure coefficient, boundary layer profiles, and total pressure loss coefficient with the experimental measurements taken by Marks *et al.* [35] in the LSWT. Also comparisons were

made with CFD result of Clark *et al.* [25] which used the Praisner and Clark [24] correlation based transitional flow model.

6.1.1 Surface Static Pressure Coefficient

In Figure 6.1, the mean static pressure coefficient distributions were compared to the measurements of Mark *et al.* [35] and the CFD results of Clark [25].   At the Re = 50,000 (Fig 6.1(a)), the k-k_L-ω model results showed good agreement with Clark's CFD result to the 55% suction surface axial location. The present CFD results predicted a lower peak pressure than Clark's CFD result but both predictions over-predicted the peak pressure compared to the experimental results. Downstream of the peak static pressure location, the k-k_L-ω model result predicted that the flow would separate at the 62.8% axial chord location. There was a large amount of unsteadiness present on the suction surface due to the vortical production from the separated shear layer. The local peak pressure coefficient at 82% axial chord location was due to the motion of the vortices as they lifted of the blade surface and traveled downstream to the wake region. The Clark CFD results predicted the separation point at approximately 68% axial chord which was more downstream than observed in both experimental and k-k_L-ω model results. The static pressure distribution downstream of the separation point of the Clark CFD results predicted flow separation and reattachment which indicated a closed separation bubble present on the suction surface.   The experimental measurements were taken at inlet Re = 60,000, but all measurement at Tu = 0.5% indicated a separated non-reattaching boundary layer. The separation location was between 57% and 62% axial chord, which was in good agreement with the k-k_L-ω model results.
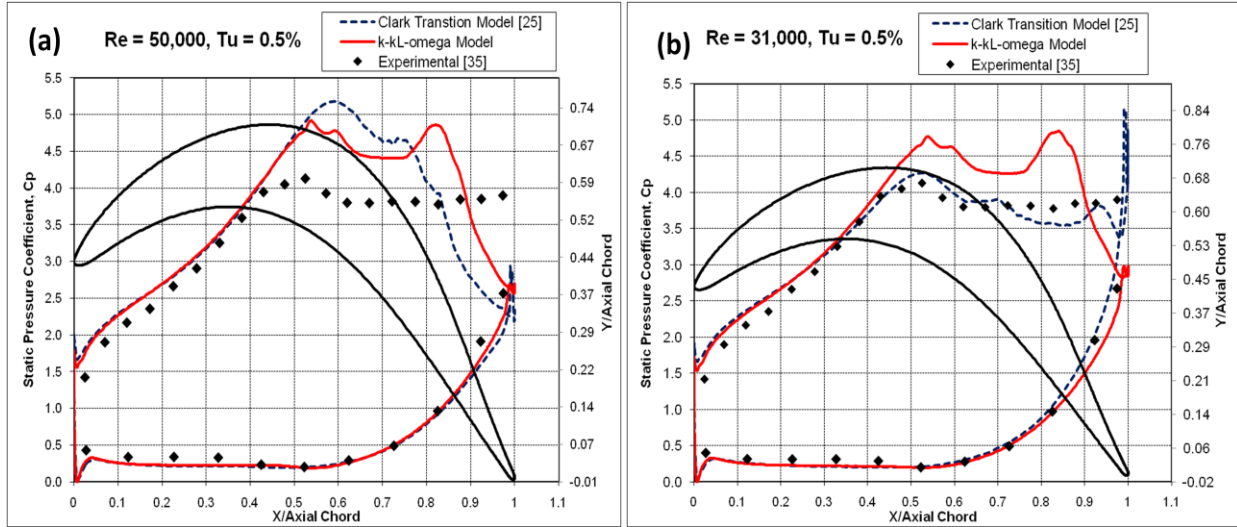
Figure 6.1. Comparison of surface static pressure coefficient with Clark *et al.* [25] simulations and experimental results [35] at inlet Reynolds numbers of a) 50,000 and b) 31,000, Tu = 0.5% for the Aft-Loaded L1A blade airfoil

A similar distribution of the static pressure coefficient was predicted with the k-k_L-ω model at Re = 31,000 as shown in Figure 6.1(b). The boundary layer separation location at 62.8% axial chord location was in good agreement with experimental (Re =40,000) and Clark's CFD results of approximately 62% axial chord. The local pressure peak at the 82% axial chord location was due to the unsteady vortex shedding on the suction surface as observed in the Re = 50,000 case. Clark's CFD results showed the same local pressure peak located at the 95% axial chord, which was more downstream than the k-k_L-ω model result. The experimental results taken at inlet Re = 40,000 showed separated flow to the trailing edge. Yet, there was no evidence of the local pressure peaks within the separated flow region. This could be due to frequency response limitations or the time-averaging of the pressure transducers used in the experimental measurements. In summary, the k-k_L-ω transitional flow model was adequate in the prediction of the blade loading at low inlet turbulent intensities. Good agreement was achieved with the experimental result in the prediction of the separation location. The k-k_L-ω

model demonstrated the ability to predict the static pressure distribution and the qualitative flow

response to the separated shear layers observed in the Aft-Loaded L1A blade airfoil.
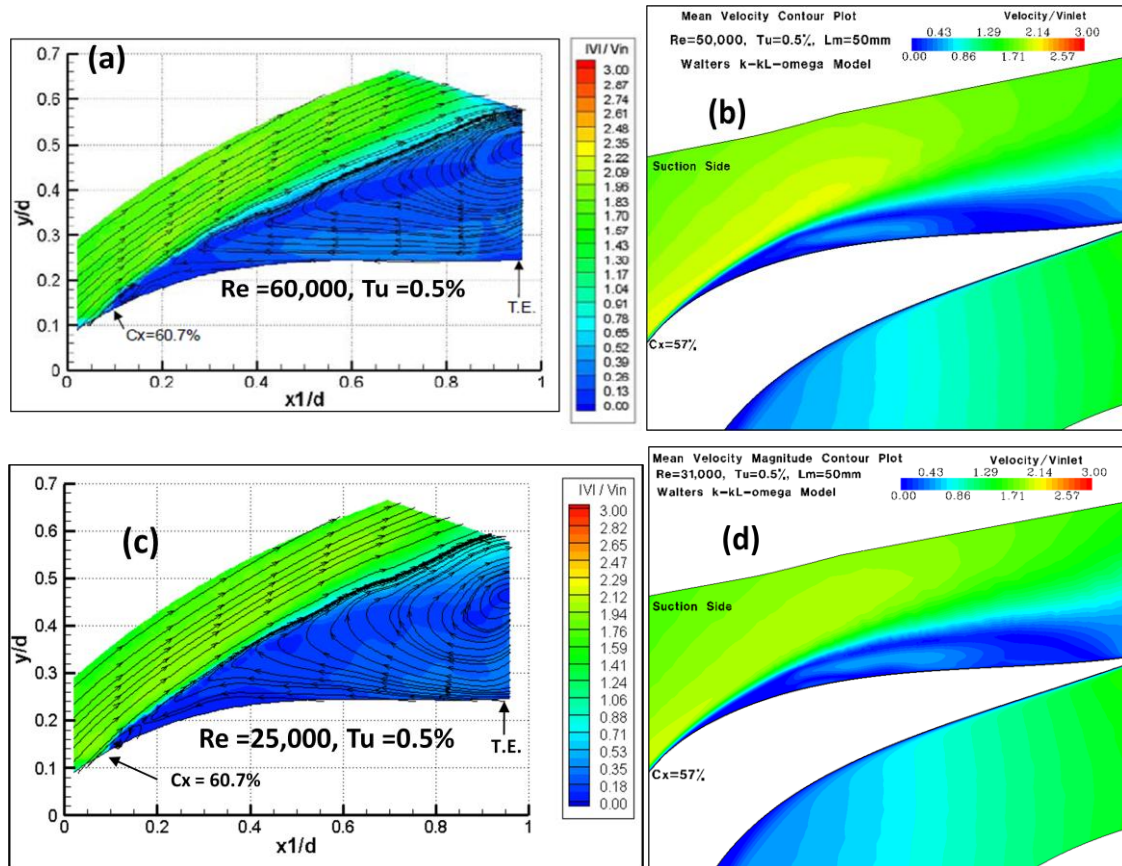
Figure 6.2. Mean velocity contours plots of the (a) PIV results at Re=60,000, (b) the CFD results at Re = 50,000, (c) PIV results at Re = 25,000, and (d) CFD results at Re = 31,000 for the Aft-Loaded L1A blade airfoil

6.1.2   Velocity Contours and Boundary Layer Profiles

Mean velocity magnitude contour plots from the CFD were compared to the PIV contour

plots taken by Marks *et al.* [35] in Figure 6.2. The PIV results for the Re = 50,000 (Fig 6.2(a))

showed the flowfield on the suction surface of the blade starting at approximately the 50.0% to

the 94% axial chord location, while the Re = 25,000 result showed from 57.0% to the 100% axial

chord location. The CFD results were oriented in a similar manner to aid the comparisons. Both

the CFD and experimental results indicated a significant amount of separated flow present on the

suction surface with the experimental result having a larger region of separated flow. The experimental separation region was also larger than the CFD for the Re = 25,000 shown in Figure 6.2(c)-(d). The behavior of the streamlines showed a recirculation region in the separated flow area at both inlet Reynolds numbers (Fig 6.2(a)&(c)).
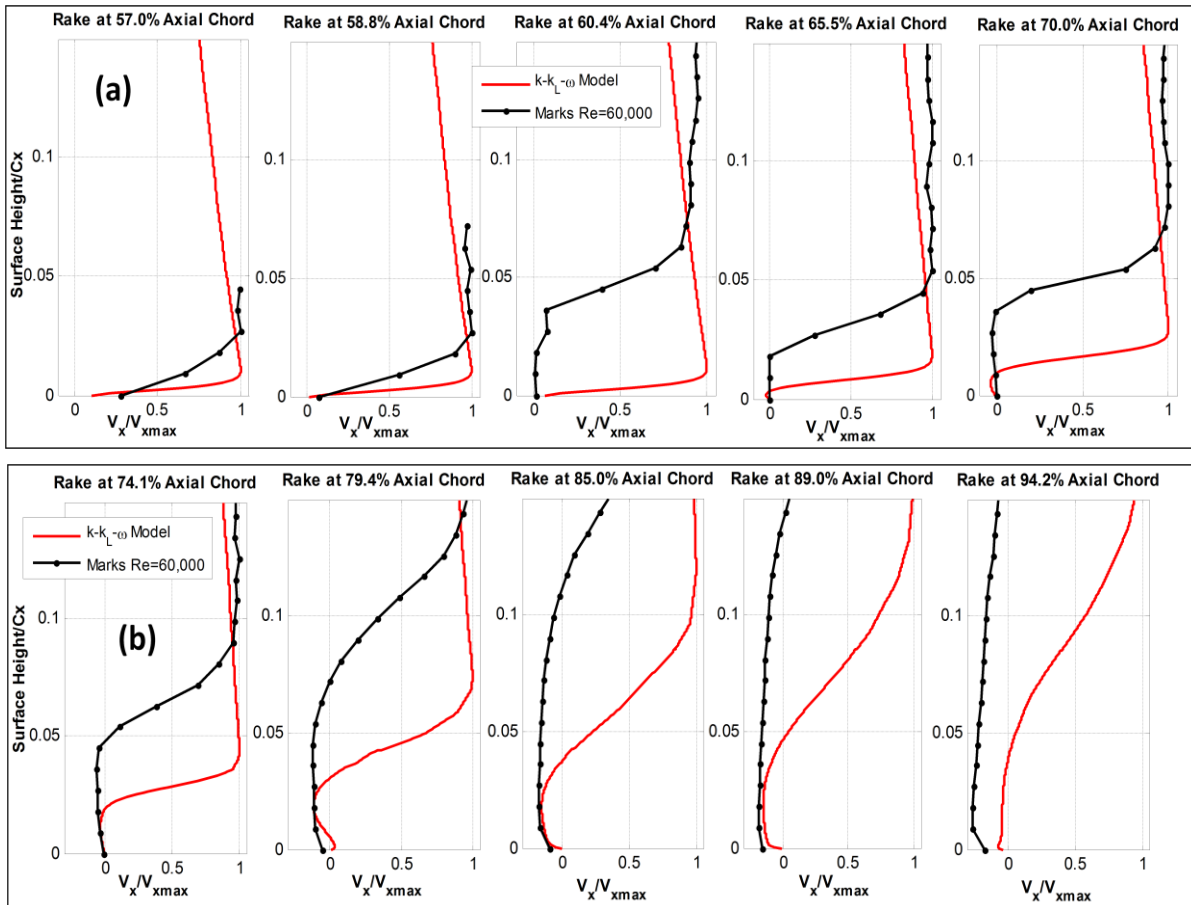
Figure 6.3. Comparison of the mean boundary layer profiles of axial velocity with experimental (Re=60,000) results [35] at inlet Re = 50,000 for the Aft-Loaded L1A blade airfoil

Time-averaged values of the boundary layer velocity profiles obtained at ten axial chord locations of 57%, 58.8%, 60.4%, 65.5%, 70%, 74.1%, 79.4%, 85%, 89.0%, and 94.2% normal to the blade surface from both the CFD and experimental PIV results. The axial component of the velocity was used in order to compare the amount of reversed flow present in the separation region. The separation point for the Re = 50,000 case was predicted to occur at the 62.8% axial

CFD Modeling of Separation and Transitional Flow in
Low Pressure Turbine Blades at Low Reynolds Numbers

chord location, which was in 96% agreement with the experimental result at Re = 60,000. Figure 6.3(a) indicated the separation point at 58.8% and 60.4% axial chord location for the experimental results. The CFD under-predicted the separation region compared to the experimental results starting at the 60.4% axial chord location and continued for every downstream location (Fig. 6.3(a)-(b)). In Figure 6.4(a), the experimental result indicated the boundary layer separation point was located between the 58.8% and 60.4% axial chord location which was more upstream than the static pressure distribution indicated. The CFD predicted the separation point more downstream at the 64.4% axial chord location which is in 93% agreement with the experimental results. Similar trends were observed for the Re = 50,000 where the separation region was significantly under-predicted compared to experimental results (Fig 6.4(a)-(b)).
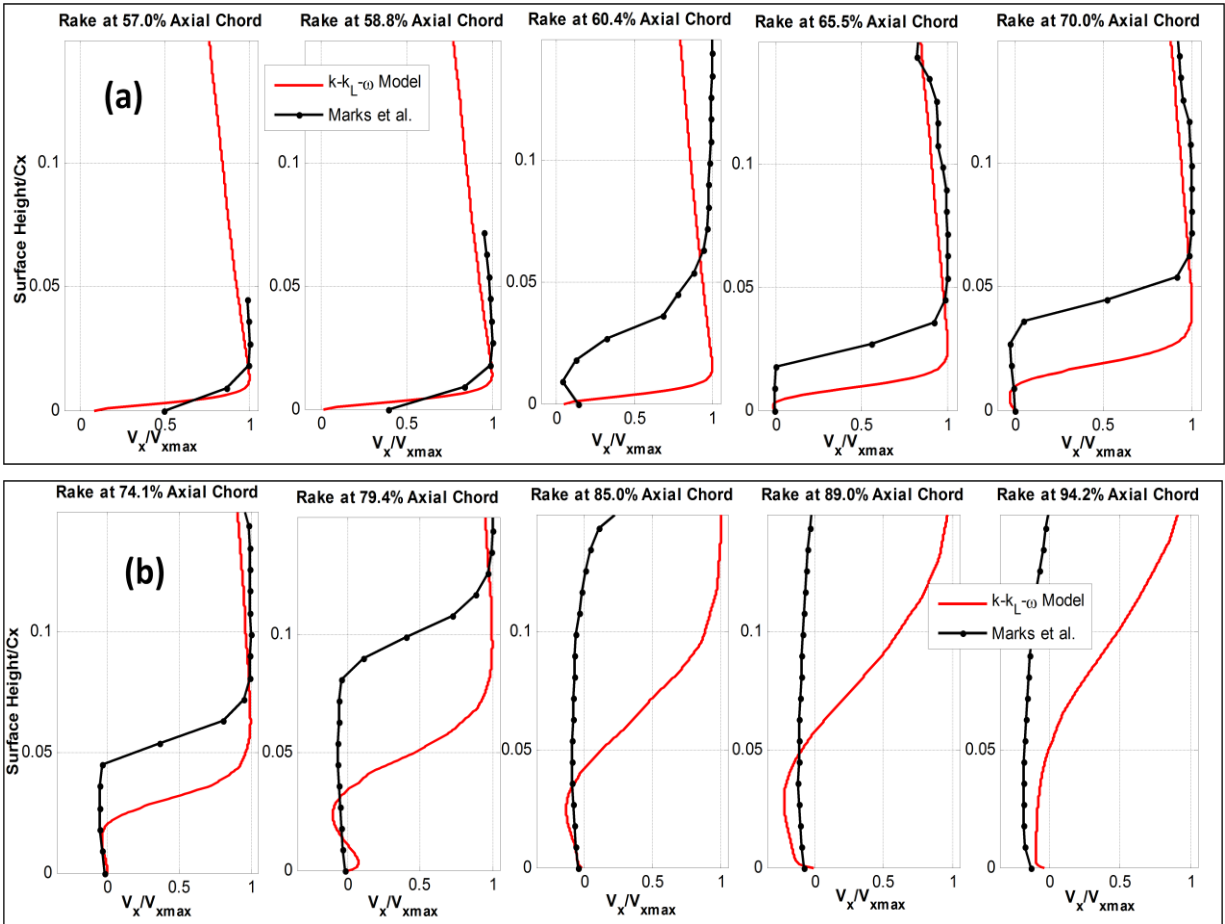
Figure 6.4. Comparison of the mean boundary layer profiles of axial velocity with experimental (Re = 25,000) results [35] at inlet Re = 31,000 for the Aft-Loaded L1A blade airfoil

6.1.3   Unsteady Features of the Flowfield

The unsteady features of the flowfield were investigated to understand the behavior of the flow separation and vortex generation. Instantaneous contour plots of vorticity were used to visualize the features of the flowfield. The flowfield was periodically repeated for two pitch lengths to aid the visualization of vortex shedding in the wake region. For the Re = 50,000 case, a total of 221,549 time-step or 0.425sec were used for averaging of mean flow quantities with a flow time step of 2 μsec. The total flow-time was 0.181sec and mean flow-averaging was 2.35 of the flow-time interval calculated with Eq. (4.1). In Figure 6.6(a)-(b), the separated shear layer on blade suction surface consistently produced a clockwise vortex, while smaller counter-

CFD Modeling of Separation and Transitional Flow in
Low Pressure Turbine Blades at Low Reynolds Numbers

clockwise vortices were present beneath the separated shear layer vortex. As the separated shear layer vortex traveled downstream, it disrupted the smaller vortices originally located beneath it and continued to move downstream into the wake region as shown in Figure 6.6(c)-(d). Once this vortex reached the wake region it began to dissipate rapidly across the pitch. Also, the pressure surface shear layer from the trailing edge produced small counter-clockwise vortices that moved downstream in the wake region (Fig 6.6(a)). The structure of the shear layer vortex was similar to the experimental flow visualization completed by Marks *et al.* [35] at Re = 60,000 shown in Figure 6.5(a). The suction side vortices in CFD predictions stayed near the blade surface whereas the experiment indicated the vortices moved into the freestream.
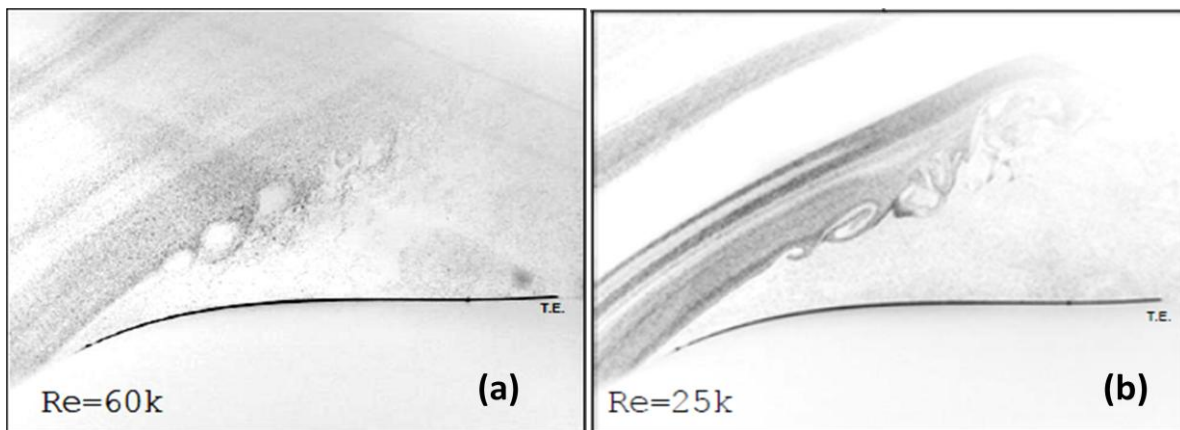
Figure 6.5. Instantaneous flow visualizations of Marks *et al.* [35] at (a) Re = 60,000 and (b) 25,000, Tu = 0.5% for the Aft-Loaded L1A blade airfoil. Image view taken 52.5% axial chord location to the trailing edge.
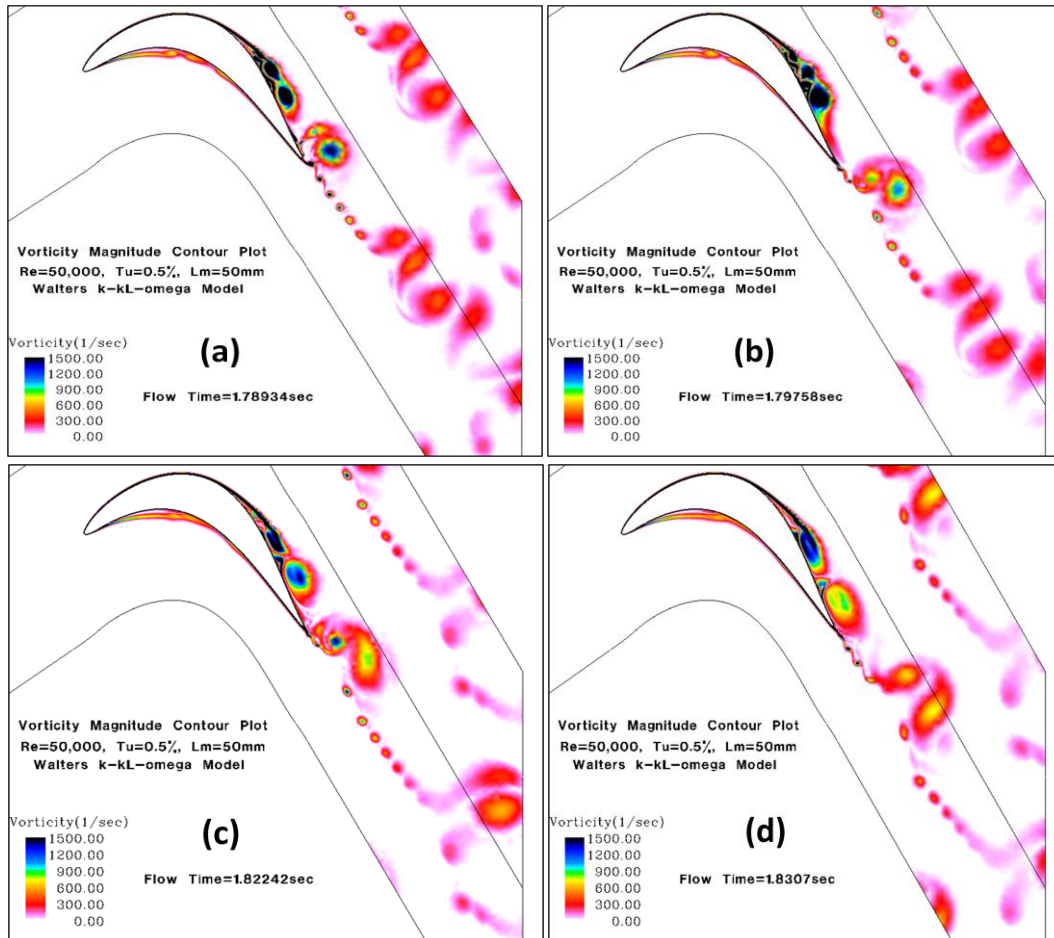
Figure 6.6. Instantaneous vorticity contours at Re = 50,000, Tu = 0.5%, l_m = 50mm for the Aft-Loaded L1A blade airfoil

In Figure 6.7(a)-(d), the flowfield unsteadiness of the Re = 31,000 case is shown. The flow time-step was 10μsec with 99,245 time-steps or 0.990sec being used for mean-flow averaging. The total flow-time was 0.292sec and mean flow-averaging was 3.39 of the flow-time interval. The suction side separated shear layer produced a clockwise vortex that was similar in size as the Re = 50,000 case. Also, the structure of the separated shear layer vortex was comparable to the experimental flow visualizations at Re = 25,000 in Figure 6.5(b). As in the Re = 50,000 case, there was a thin shear layer located directly beneath the separated shear layer vortex as it lifted off the blade surface. This thin shear layer separated from the blade surface and produced small counterclockwise vortices that interacted with the separated shear

CFD Modeling of Separation and Transitional Flow in
Low Pressure Turbine Blades at Low Reynolds Numbers

layer vortex and traveled downstream to the wake region. The trailing edge shear layer produced

a small counterclockwise vortex that would periodically increase in size, roll up on the suction

side near the trailing edge, and interact with the separated shear layer vortex. These vortices

began to dissipate across the pitch length as they reached the wake region.
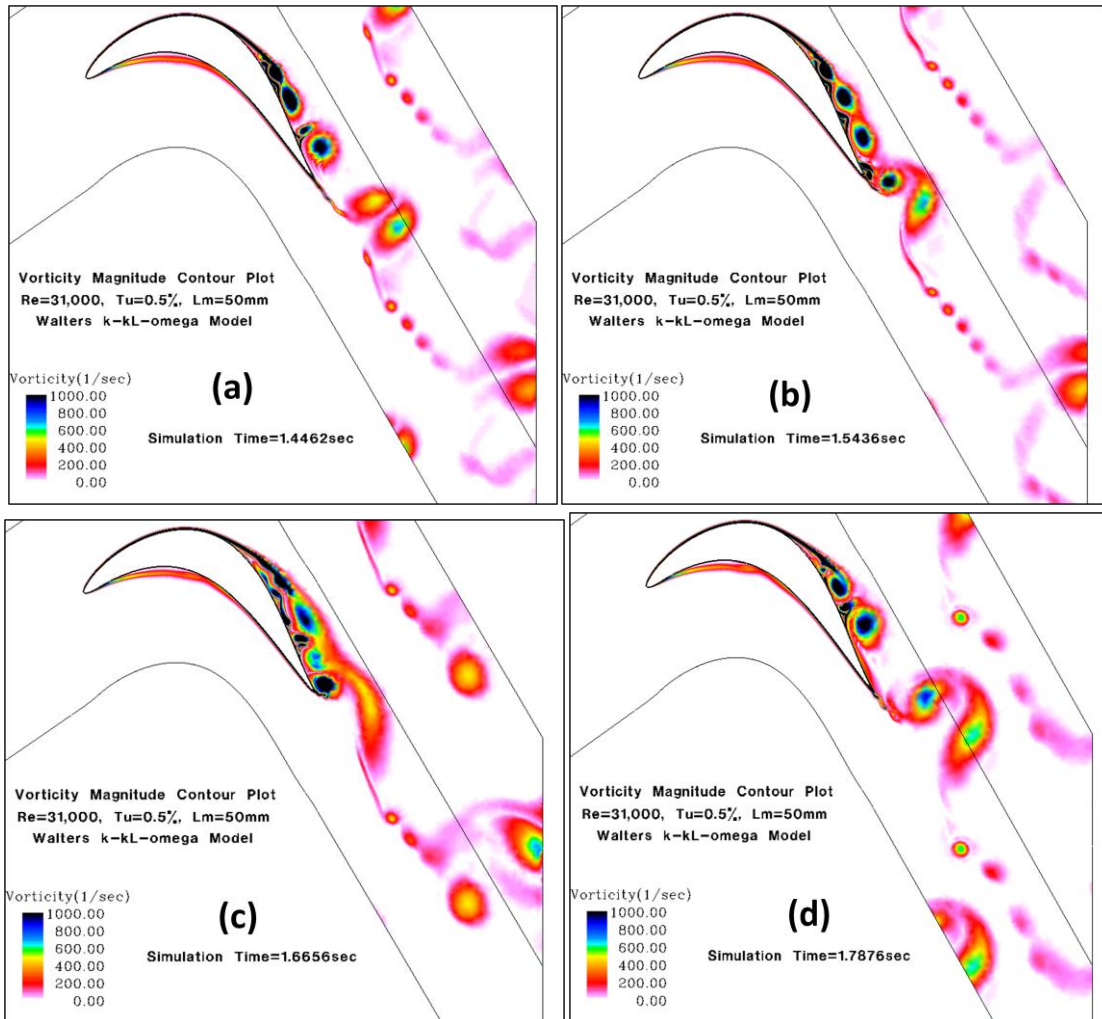
Figure 6.7. Instantaneous vorticity contours at Re = 31,000, Tu = 0.5%, l_m = 50mm for the Aft-Loaded L1A blade airfoil

The time signal and the FFT of the drag coefficient were calculated for the Aft-Loaded

L1A blade for both Reynolds numbers at low turbulence intensity. The frequency resolution was

2Hz and 1Hz for the Re = 50,000 and Re = 31,000 cases, respectively. In Figure 6.8(a), there

were several dominant and harmonic frequencies calculated using the FFT for the Re = 50,000 case. An animation of the last 41,400 time-steps was made to help determine the shedding frequency for the main vortices present in the flowfield. The shedding events were counted individually, divided by the animation time interval of 0.0828sec to estimate the shedding frequency, and compared to frequencies calculated from the FFT. Also, Figure 6.8(c)-(d) and shows the shedding frequency for each vortical structure for the Re = 50,000 and 31,000 cases, respectively. It was determined that the separated shear layer vortex was being shed at frequency of 108Hz, while the smaller suction side vortices were shed at approximately 33Hz and 75Hz. Also, the vortex created by the pressure side separation region was shedding at a frequency of 48Hz. The trailing edge vortices had little impact on the blade drag coefficient because the vortex shedding did not occur until the shear layer reached the wake region (Fig 6.8(c)). A vortex shedding frequency of 350Hz was estimated for the smaller trailing edge vortex. At Re = 31,000 (Fig 6.8(b)) the shedding frequencies were estimated from the animation time interval of the last 0.3941sec mean flow-averaging. It was determined the separated shear layer vortex was being shed at a frequency of 51Hz, while the smaller suction side vortices were shed at approximately 18Hz and 32Hz. The large trailing edge vortex would periodically roll-up on the suction surface at a frequency of 22Hz while the smaller trailing edge vortices were shedding in the wake region at 102Hz (Fig 6.8(d)). Table 6.1 shows the separation location, shedding frequencies, and corresponding Strouhal numbers calculated from Eq. 4.1.
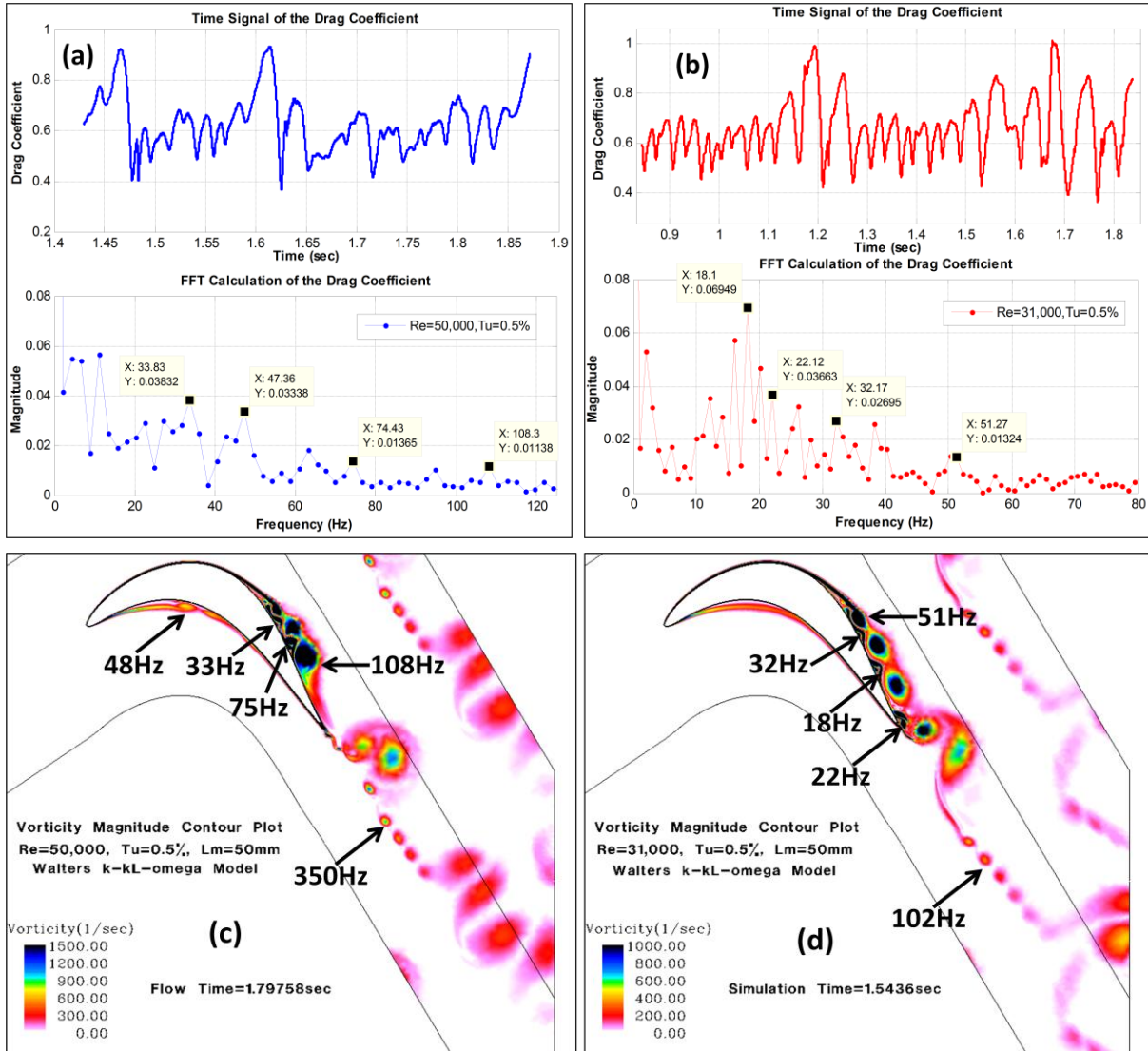
Figure 6.8. Time signal, FFT calculation of the drag coefficient, instantaneous vorticity contours at (a)-(c) Re = 50,000 and (b)-(d) Re = 31,000, Tu = 0.5%, and l_m = 50 mm

			Pressure Side		Suction Side						Trailing Edge	
Re	l_m(mm)	X_{sep}/C_x	f_{shed}	St	f_{shed}	St	f_{shed}	St	f_{shed}	St	f_{shed}	St
50,000	50	0.628	48Hz	0.0010	108Hz	0.0010	75Hz	0.0016	33Hz	0.00071	350Hz	0.0076
31,000	50	0.633	32Hz	0.0016	51Hz	0.0025	18Hz	0.00087	32Hz	0.0015	102Hz	0.0049

Table 6.1. Summary of the separation location and Strouhal number for the Aft-Loaded L1A blade at Tu = 0.5%

6.1.4   Total Pressure Loss Coefficient Predictions

The total pressure loss coefficient obtained from the CFD was compared to the experimental results of Marks *et al.* [35] as shown in Figure 6.9. The CFD using the Walters and

CFD Modeling of Separation and Transitional Flow in
Low Pressure Turbine Blades at Low Reynolds Numbers

Leylek [2] k-k_L-ω transitional model significantly under-predicted the maximum value of the loss

coefficient compared to the experimental results for both inlet Reynolds numbers. Also, the

width of the wake region was over-predicted due to the unsteady vortices being spread across the

wake region. The high numerical specific dissipation rate calculated from the k-k_L-ω model

caused the total pressure loss from vortices created from the separated shear layers to be under-

predicted and over-predict the width of the wake region. Table 6.1 shows that better agreement

was achieved when comparing the integrated loss coefficient with 81% and 97% agreement for

Re = 50,000 and Re = 31,000 to the experimental results, respectively. This indicated that the k-

k_L-ω model predicted an adequate amount of viscous losses but the distribution of the viscous

losses across the wake region was not well predicted. This could be due to the limitation of the

k-k_L-ω model to dampen the production of any small scale turbulent structures. The dynamic

behavior of the small scale turbulence is not present to attribute to viscous losses. The large

coherent vortices produced from the separated shear layer dissipate more across the wake region.
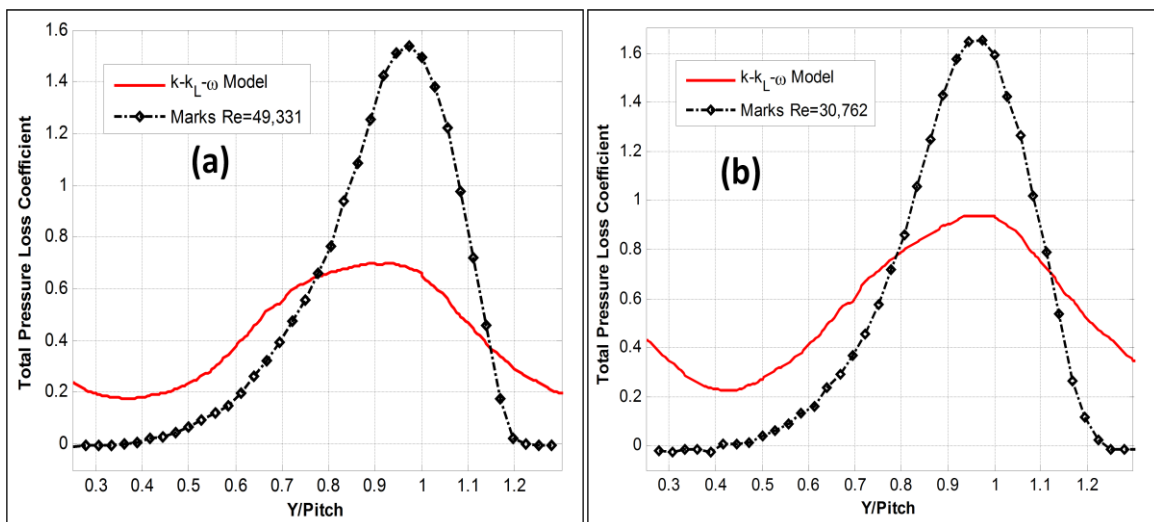
Figure 6.9. Comparison of total pressure loss coefficient with experimental [35] result at inlet Reynolds numbers of (a) 50,000 and (b) 31,000 for the Aft-Loaded L1A blade airfoil

Re	l_m(mm)	Integrated Loss Coefficient		Maximum Loss Coefficient	
		CFD	Marks *et al.* [35]	CFD	Marks *et al.* [35]
50,000	50	0.4131	0.5099	0.7001	1.5974
31,000	50	0.5715	0.5526	0.9391	1.6549

Table 6.2. Maximum and integrated total pressure loss coefficient comparison with the experimental [35] results for the Aft-Loaded L1A blade airfoil

6.2   CFD Predictions at High Inlet Turbulence intensity

Simulations were completed with the Aft-Loaded L1A blade at higher inlet turbulent intensities to determine if prediction capability using the k-k_L-ω model would improve at similar inlet Reynolds numbers.   The inlet turbulence intensity was set to 3.4% corresponding to experiments completed with the turbulence grid placed at the inlet of the LSWT.   Unsteady simulations were completed at Re = 50,000 and 25,000 and compared to experiments taken by Marks *et al.* [35], CFD simulations completed with Menter's k-ω(SST) turbulence model and the Clark *et al.* [24] transition model. The inlet turbulent length scale was measured as $l_m = 40mm$ by McQuilling [34] at *Tu = 3.4%* for the LWST. Simulations were also completed at $l_m = 4mm$, *Tu = 3.4%* to investigate the impact of the length scale on the CFD predictions at high inlet turbulent intensities. Comparisons were made using the surface static pressure coefficient, mean and RMS velocity contours, and total pressure loss coefficient.

6.2.1   Surface Static Pressure Coefficient

In Figure 6.10, the mean static pressure coefficient distributions were compared to the measurements of Marks *et al.* [35] and CFD results of Clark [25].   Also, CFD simulations completed with the k-k_L-ω model at $l_m = 4mm$ & 40mm and k-ω(SST) model at $l_m = 40mm$ were included in Figure 6.10(a)-(b). At Re = 50,000, the k-k_L-ω model at both inlet turbulent length scales predicted a similar pressure distribution due to flow separation and turbulent reattachment

CFD Modeling of Separation and Transitional Flow in
Low Pressure Turbine Blades at Low Reynolds Numbers

which were comparable to Clark's CFD results. The turbulent reattachment point from the Clark's CFD results indicated that reattachment location was slightly upstream than the k-k_L-ω model results. The experimental result had higher suction surface peak velocity than all the CFD simulations which indicated the experimental results had a higher loading level. However, the shape of the pressure distribution due to the reattaching separation bubble in the experimental results was similar to the CFD results using the k-k_L-ω and Clark and Praisner [24] transitional flow models. The CFD prediction using Menter's k-ω(SST) turbulence model did not show an indication of a closed separation bubble on the blade suction surface. The pressure distribution showed an indication of a separation region starting at the 80% axial chord location.

When the Reynolds number was decreased to 25,000, the length of the separation region on the suction surface increased for all results (Fig 6.10(b)). Both the k-ω(SST) turbulence model and Clark's CFD results predicted a separated flow region to the trailing edge and showed a constant pressure starting at the 60% axial chord location which was not measured in the experimental results. The experiment as in Re = 50,000 case had a higher loading level than CFD results but the k-k_L-ω model produced the best agreement with experimental results on the static pressure behavior of the separation region. Also, the prediction of the static pressure distribution was independent of inlet turbulent length scale using the k-k_L-ω model.
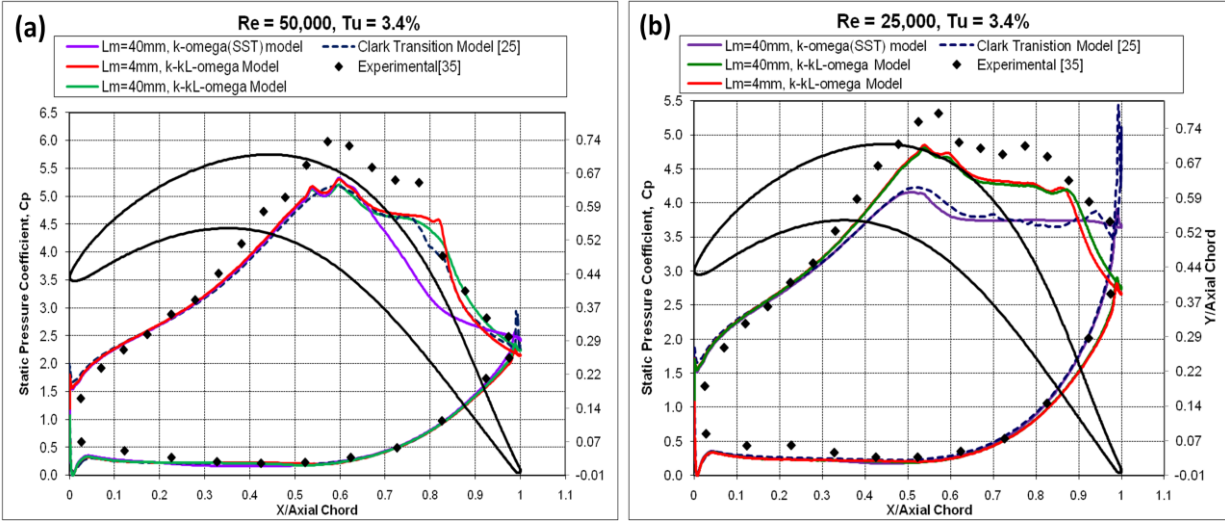
Figure 6.10. Comparison of surface static pressure coefficient with Clark *et al.* [25] simulations and experimental results [35] at inlet Reynolds numbers of a) 50,000 and b) 25,000, Tu = 3.4% for the Aft-Loaded L1A blade airfoil

6.2.2 Mean and RMS Velocity Contours

A CFD comparison of the mean and RMS velocity contours was made with the experimental PIV measurements taken by Marks *et al.* [35] at high turbulent intensities. The RMS contours have been modified to include the unsteadiness due to turbulence because a significant portion of the flow unsteadiness goes into the production of turbulence using the k-k_L-ω model. The RMS velocity was calculated using Eq. (6.1).

$$u_{RMS} = u_{RMS(global)} + (Tu)u_{avg} \qquad (6.1)$$

Isotropic turbulence was assumed in order to relate the turbulent intensity to the RMS velocity using Eq. (1.20). The flow unsteadiness from the separated shear layers contributed 10% of the total RMS velocity whereas 90% the flow unsteadiness went into the production of turbulence. The k-k_L-ω model is based on the RANS CFD method. The limitation with k-k_L-ω model was any small scale unsteadiness present in the flowfield went into the production of turbulence at the high inlet turbulent intensity predictions even if the simulation was run as unsteady.

Chapter 6. The Aft-Loaded L1A Blade CFD Results

For the k-k_L-ω model simulations, a total of 50,000 time-steps were used for averaging of mean flow quantities with a flow time step of 40μsec, while all the steady flow simulations were completed with Menter's k-ω(SST) model at both Reynolds numbers. For the Re = 50,000 case in Figure 6.11, there was a difference in the prediction of the separation region in the k-k_L-ω model results. The lower dissipation present in the l_m = 40mm case (Fig 6.11(b)) caused the separation region to increase on the blade surface compared to the l_m = 4mm case in Fig 6.11(a). This same observation was made with the Lightly Loaded blade in Section 4.2.2, e.g., that the freestream eddies no longer couple to the boundary layer through the turbulence model causing the increase in the separation region. The l_m = 4mm case closely resembled the experimental PIV result which indicated a closed separation region starting at approximately the 60% axial chord location. The fully turbulent flow simulation using the k-ω(SST) model predicted a larger separation region than the k-k_L-ω model at the same length inlet turbulent length scale, which was not observed in the experimental result.

The RMS velocity contour plots in Figure 6.12 show the flow unsteadiness produced from the separated shear layer in the k-k_L-ω model result was under-predicted compared to the experimental result (Fig 6.12(c)) particularly in the 57%-79.4% axial chord locations. Downstream of the 79.4% axial chord location, a similar amount of unsteadiness was observed in the k-k_L-ω model and experimental results. The increase in the inlet turbulent length caused the amount of unsteadiness in the separation region to slightly increase (Fig 6.12(b)) in the k-k_L-ω model results. The experimental flow visualizations in Fig. 6.12(d) show a closed separation region with turbulent structures immediately downstream. These structures were not present in the instantaneous flowfield predictions in the k-k_L-ω model results due to the limitation of model at high inlet turbulent intensities.
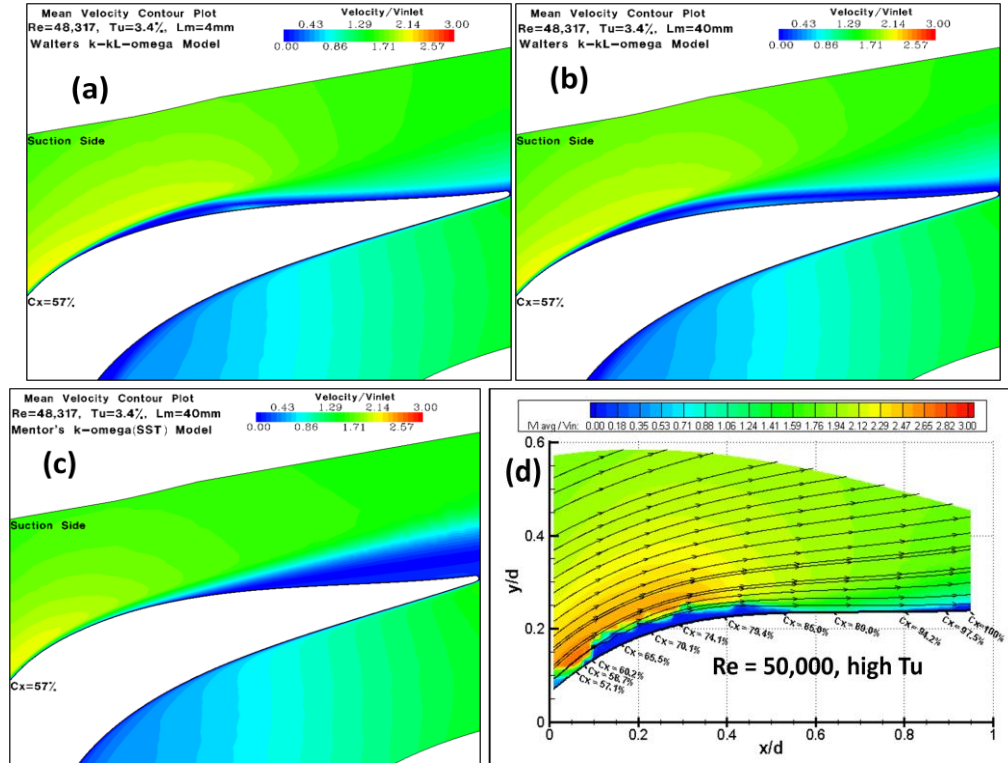
Figure 6.11. Mean velocity contour comparisons of k-k_L-ω model at (a) $l_m = 4mm$, (b) $l_m=40mm$, (c) k-ω(SST) model at $l_m =40mm$, and (d) PIV result of Marks *et al.* [35] at Re=50,000, Tu=3.4% for the Aft-Loaded L1A blade airfoil
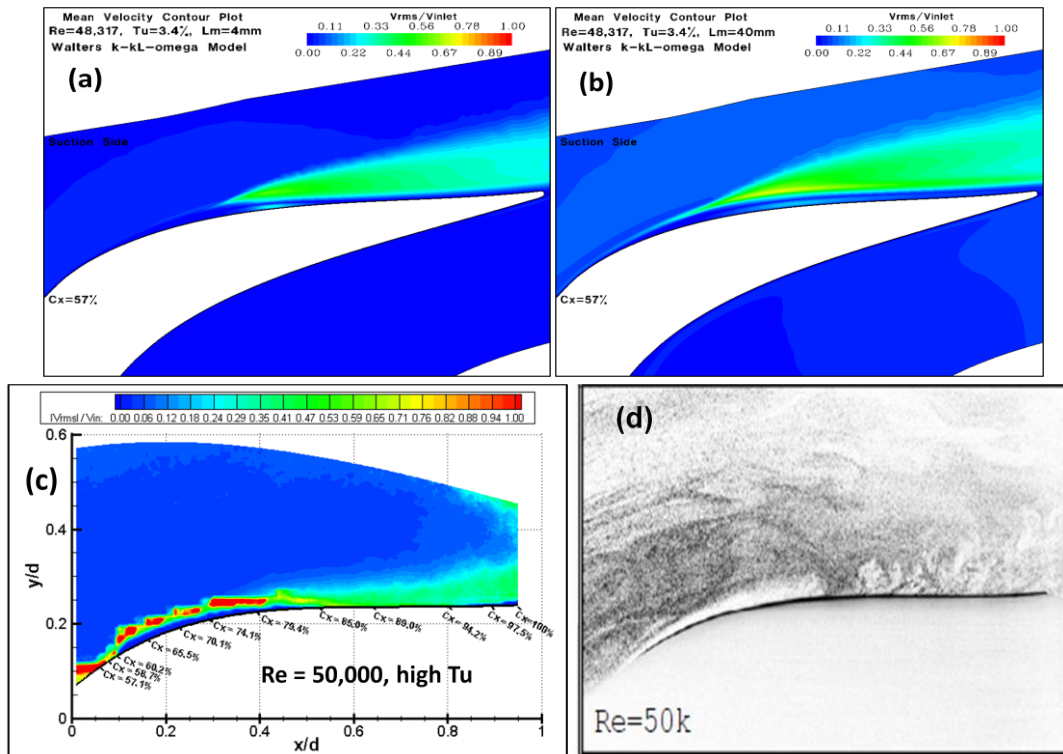
Figure 6.12. RMS velocity contour comparisons of k-k_L-ω model at (a) $l_m = 4mm$, (b) $l_m=40mm$, (c) PIV result, and (d) flow visualizations of Marks *et al.* [35] at Re=50,000, Tu=3.4% for the Aft-Loaded L1A blade airfoil

CFD Modeling of Separation and Transitional Flow in
Low Pressure Turbine Blades at Low Reynolds Numbers

At the Re = 25,000, both the k-k_L-ω model result at l_m = *4mm* and *40mm* showed a similar prediction of the separation region as shown in Figure 6.13(a)-(b). Both simulations predicted a separation region to the trailing edge as the experimental result shown in Figure 6.13(d), yet the CFD result using the k-k_L-ω model predicted a smaller separation compared to experimental result. The fully turbulent flow simulation in Figure 6.13(c) using the k-ω(SST) model was found to be more comparable with the experimental result on the prediction on the size of the separation region. The RMS velocity contour plot comparison in Figure 6.14(a)-(b) for the k-k_L-ω model showed the RMS velocity produced from the separated shear layer was under-predicted compared to the experimental PIV results (Fig. 6.14(c)). This was due to the dampening of the effect the separated shear layer had on the flowfield unsteadiness similar to the Re = 50,000 case. According to the flow visualizations by Mark *et al.* [35] (Fig 6.14(d)), laminar flow eddies were generated from the separated shear layer and transitioned to turbulence further downstream of the separation point. The dampening of the global unsteady effects using the k-k_L-ω model at high inlet turbulence intensity was observed for both inlet Reynolds numbers. A significant portion of the flow unsteadiness went into the production of turbulence. As a result, there was not any vortex shedding observed in the wake region as seen at the lower inlet turbulent intensities.
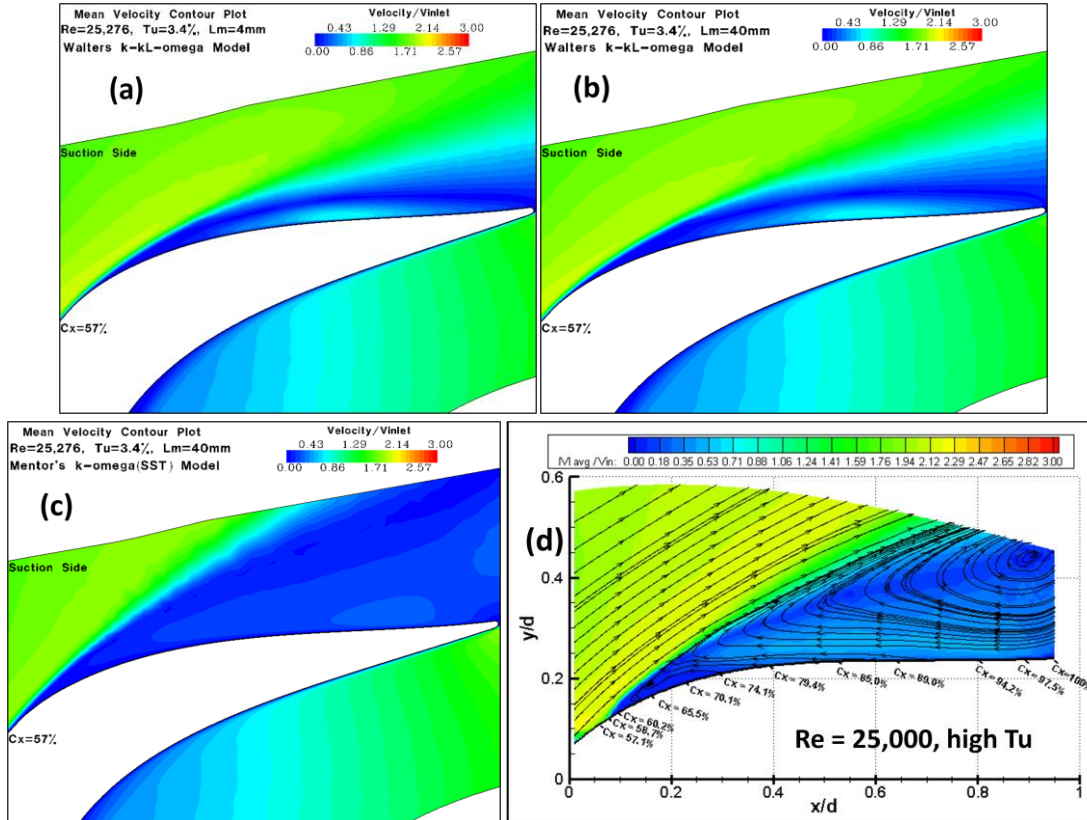
Figure 6.13. Mean velocity contour comparisons of k-k_L-ω model at (a) $l_m = 4mm$, (b) $l_m=40mm$, (c) k-ω(SST) model at $l_m =40mm$, and (d) PIV result of Marks *et al.* [35] at Re=25,000, Tu=3.4% for the Aft-Loaded L1A blade airfoil
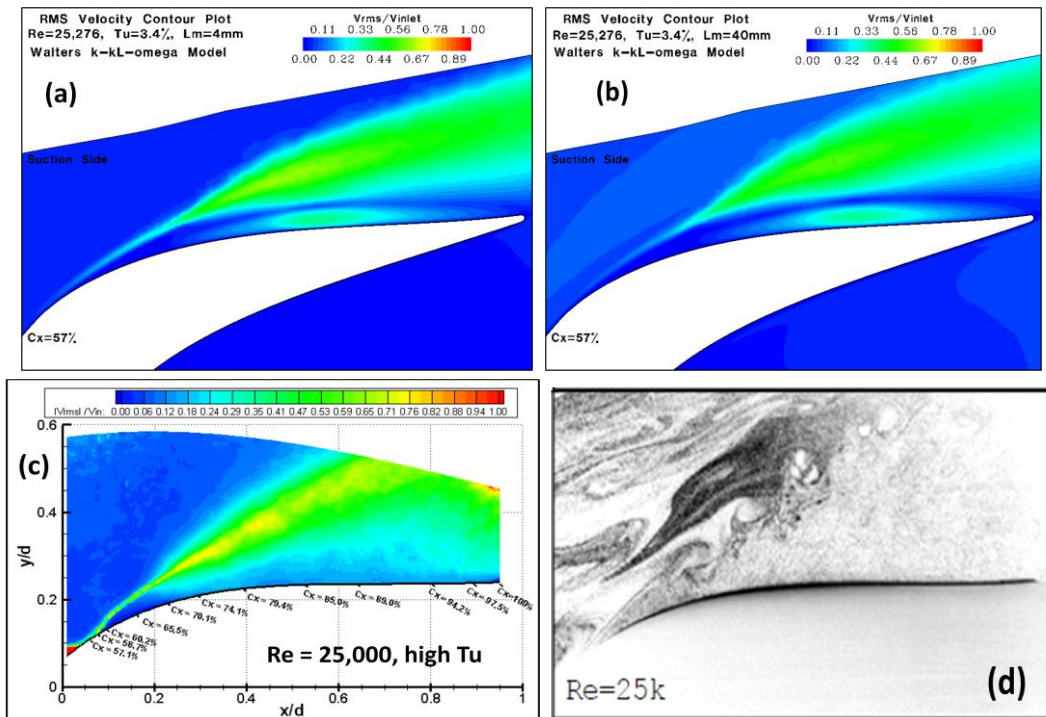
Figure 6.14. RMS velocity contour comparisons of k-k_L-ω model at (a) $l_m = 4mm$, (b) $l_m=40mm$, (c) PIV and (d) flow visualizations of Marks *et al.* [35] at Re=25,000, Tu=3.4% for the Aft-Loaded L1A blade airfoil

CFD Modeling of Separation and Transitional Flow in
Low Pressure Turbine Blades at Low Reynolds Numbers

6.2.3   Boundary Layer Velocity Profiles

The time-averaged axial velocity profiles were obtained at ten axial chord locations for Re = 50,000 and 25,000 at Tu = 3.4% as shown in Figure 6.15 and Figure 6.16, respectively. For Re = 50,000, all three CFD results were in good agreement with each other on the prediction of the thickness of the boundary layer up to the 60.4% axial chord location. Yet, all the CFD under-predicted the boundary layer thickness compared to the experimental results starting at the 57% and up to the 74.1% axial chord location. The separation point was reported to be near ≈62% axial chord location and the flow reattached between the 79.4 and 85% axial chord for experimental result. The $k\text{-}\omega(SST)$ model case predicted the separation point at 79.2% axial chord location and the boundary layer remained separated to the trailing edge. In the $k\text{-}k_L\text{-}\omega$ model results, the separation point was more downstream compared to the experimental results at the 65.9% and 65.1% axial chord location for the $l_m = 4mm$ and $l_m = 40mm$ cases, respectively. The increase in length scale caused a larger separation region with more reversed flow compared to the $l_m = 4mm$ case. Also, reversed flow was present to the trailing edge for the $l_m = 40mm$ case whereas, the $l_m = 4mm$ case showed the boundary layer being reattached at the 89% axial chord location.
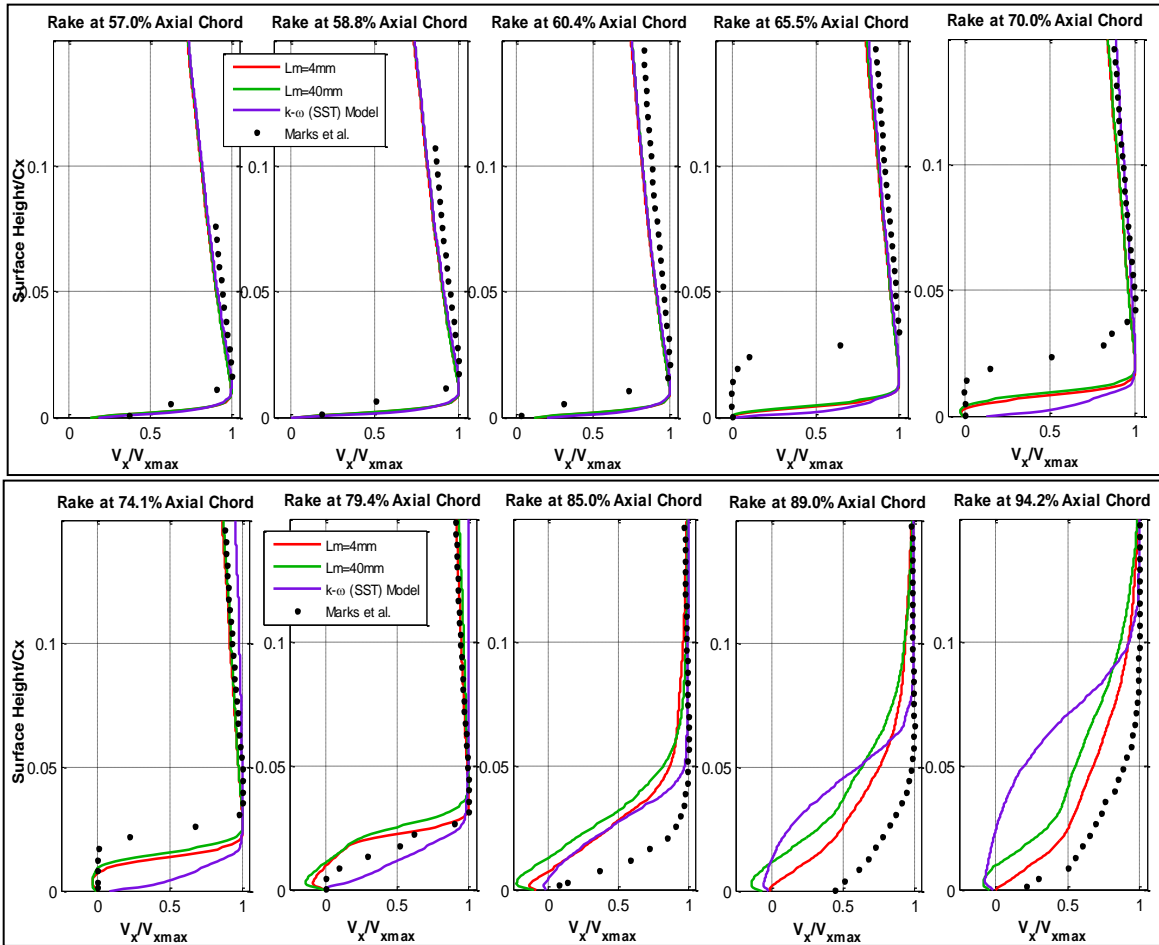
Figure 6.15. Comparison of the mean boundary layer profiles of axial velocity with experimental results [35] at inlet Re = 50,000 for the Aft-Loaded L1A blade airfoil at Tu = 3.4%

The prediction of the separation point at 63% axial chord was independent of the inlet length scale variation for the k-k_L-ω model at Re = 25,000. The $l_m = 40mm$ case predicted a slightly larger separation region approaching the trailing edge as shown at the 94.2% axial chord location. Yet, both of the k-k_L-ω model predictions under-predicted the separation region compared to the experimental results starting at the 60.4% axial chord location. The best agreement was achieved with the experimental results with the k-ω(SST) model prediction with the separation point at 63.2% axial chord location. The size of the separation region and the amount of reversed flow was good agreement with experimental results to the 89% axial chord location where the k-ω(SST) model over-predicted the amount of reversed flow.

CFD Modeling of Separation and Transitional Flow in
Low Pressure Turbine Blades at Low Reynolds Numbers
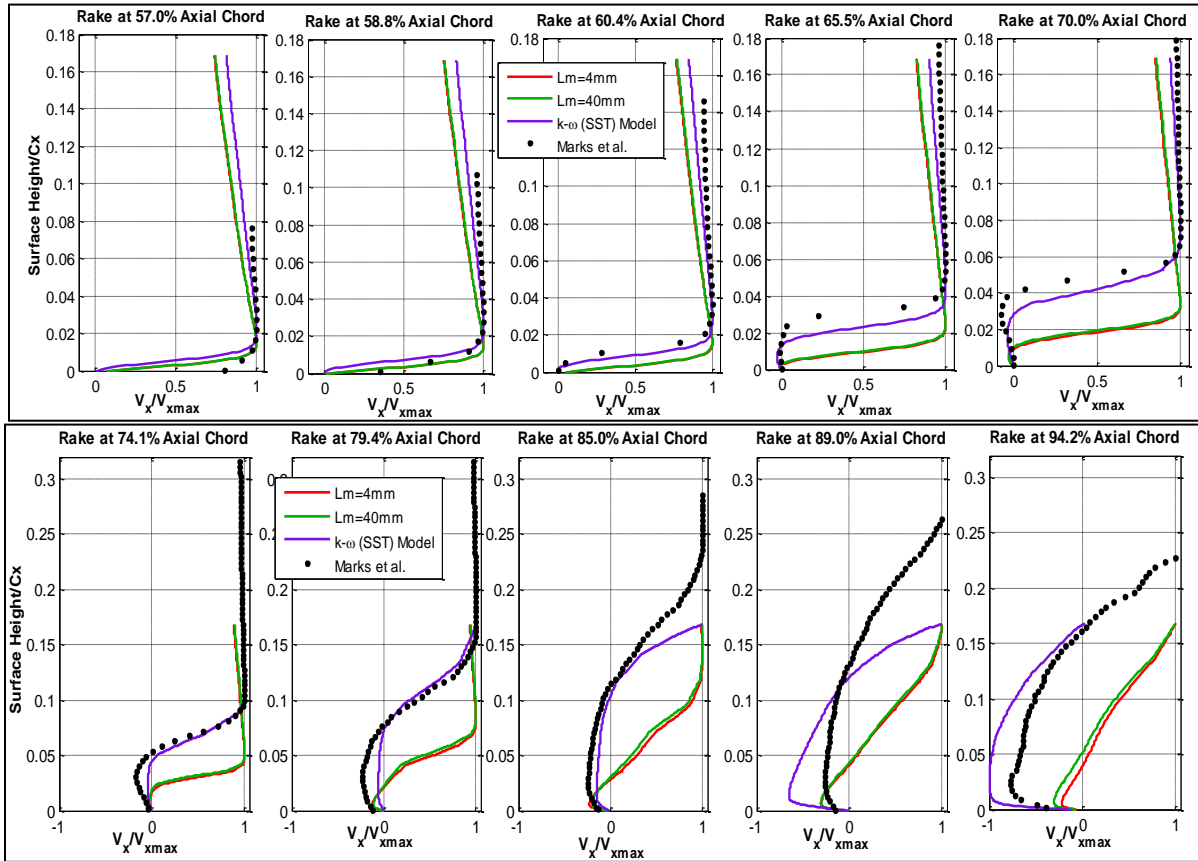
Figure 6.16. Comparison of the mean boundary layer profiles of axial velocity with experimental results [35] at inlet Re = 25,000 for the Aft-Loaded L1A blade airfoil at Tu = 3.4%

6.2.4 Total Pressure Loss Coefficient Predictions

The wake loss coefficient obtained from the CFD predictions at inlet high turbulence intensity was compared to experimental results in Figure 6.17. For the Re = 50,000 case, both of the k-k_L-ω model results under-predicted the loss coefficient compared to the experimental results with 60% and 65% agreement in the peak loss coefficient for the $l_m = 4mm$ and $l_m = 40mm$ cases, respectively. The reason for this was due to the under-prediction of the separation region and the absence of the unsteady vortex shedding observed in the experimental results. Better agreement was achieved when comparing the integrated wake loss coefficient with 83% agreement with the experimental results for the $l_m = 40mm$ case. This indicated the amount of viscous losses produced by the k-k_L-ω model, $l_m = 40mm$ case was similar to the experimental

results but the viscous losses were dissipated across the wake more causing a reduction in the peak loss coefficient. The increase in the inlet turbulent length scale caused a 9% increase in the peak loss coefficient and 33% increase in the integrated wake loss coefficient due to the larger separation region present on the blade suction surface and lower dissipation present in the wake region. The $k\text{-}\omega(SST)$ model produced an 89% and 72% agreement in the peak and integrated loss coefficient with the experimental results, respectively. Yet, the behavior of the blade loading and separation on suction side did not qualitatively agree with the experimental results.

The same trend was observed for the Re = 25,000 where the $k\text{-}k_L\text{-}\omega$ model results under-predicted the loss coefficient, with 70% and 66% agreement in the peak value of the loss coefficient for the $l_m = 4mm$ and $l_m = 40mm$ cases, respectively compared to the experimental result. Better comparisons were made with the integrated wake loss coefficient. The $k\text{-}k_L\text{-}\omega$ model results produced 92% and 87% agreement with the experimental results. For the Re = 50,000 case, the $k\text{-}k_L\text{-}\omega$ model predicted the amount of viscous losses but the distribution across the wake region was different. Also, the absence of vortex shedding caused the $k\text{-}k_L\text{-}\omega$ model to under-predict the peak loss coefficient. Figure 6.17(b) shows that the $k\text{-}\omega(SST)$ model grossly over-predicted the peak loss coefficient by 112% mainly due to the over-prediction of the extent of the separation region in the wake region.
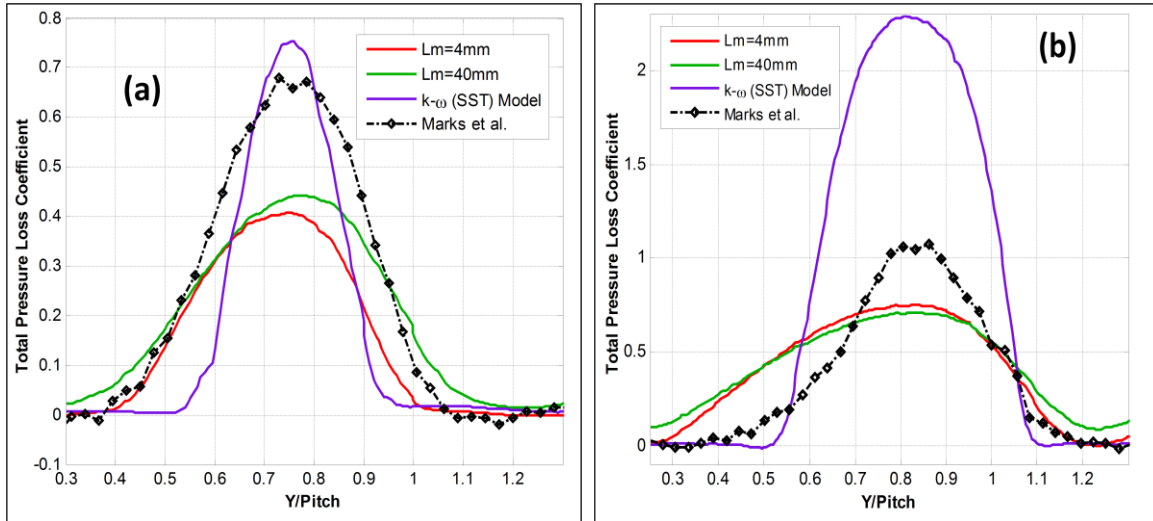
Figure 6.17. Comparison of total pressure loss coefficient with experimental [35] result at inlet Reynolds numbers of (a) 50,000 and (b) 25,000 for the Aft-Loaded L1A blade airfoil at Tu = 3.4%

Re	l_m(mm)	CFD Model	Integrated Loss Coefficient		Maximum Loss Coefficient	
			CFD	Marks *et al.* [35]	CFD	Marks *et al.* [35]
50,000	4	k-k_L-ω	0.1502	0.2397	0.4083	0.6791
	40	k-k_L-ω	0.2000		0.4432	
	40	k-ω(SST)	0.1714		0.7549	
25,000	4	k-k_L-ω	0.4208	0.3893	0.7494	1.0774
	40	k-k_L-ω	0.4383		0.7119	
	40	k-ω(SST)	0.8471		2.2932	

Table 6.3. Maximum and integrated total pressure loss coefficient comparison with the experimental [35] results for the Aft-Loaded L1A blade airfoil at Tu = 3.4%

6.3   Summary of Results

The flowfield of the Aft-Loaded L1A blade airfoil was simulated at inlet Reynolds numbers of 50,000 and 25,000. The flowfield was very complex due to the very high loading level and strong suction surface adverse pressure gradient.   The surface static pressure distribution, boundary layer profiles, and the wake total pressure loss coefficient were compared to available experimental and CFD data. Also, the unsteady features of separation were qualitatively investigated at high and low inlet turbulent intensities.   Good agreement was

achieved with the experimental results on the prediction of the separation location and the blade loading at low turbulent intensities. The k-k_L-ω model demonstrated the ability to predict the qualitative flow response to the unsteady vortex shedding due to the separated shear layers as observed in the experimental flow visualizations. Yet, the CFD results at both Reynolds numbers under-predicted the size of the separation region which resulted in the under-prediction of the peak value of the loss coefficient. Better comparisons were achieved in the prediction of the integrated loss coefficient with 80% or better agreement with the experimental results. This indicated that the amount viscous losses produced was comparable to the experimental results, but, the higher dissipation caused those losses to be distributed more across the wake.

Similar trends were observed for simulations at the higher inlet turbulent intensities. The qualitative effects of the blade loading were adequately predicted, but, the size of the separation region was under-predicted with the k-k_L-ω model. Also, the unsteady vortex generation from the separated shear layers was not present in the CFD results using the k-k_L-ω model. The absence of the unsteady effects from vortex shedding the caused the under-prediction of the maximum value of wake loss coefficient. Increasing the inlet turbulent length scales from $l_m = 4\ mm$ to $l_m = 40mm$ caused an increase in the size of separation region due to the lower dissipation present in the flowfield with a similar static pressure distribution. As in the low turbulence intensity cases, better agreement was achieved with the integrated wake loss coefficient. The fully turbulent k-$\omega(SST)$ model was simulated at the same inlet Reynolds number to determine if it would provide a better prediction than the k-k_L-ω model at higher turbulent intensities. Better agreement with the experimental result was achieved at Re = 50,000 in comparing the peak loss coefficient but, the qualitative flow effects of the blade loading and the separation location did not agree well with experimental results. At Re = 25,000, good

CFD Modeling of Separation and Transitional Flow in
Low Pressure Turbine Blades at Low Reynolds Numbers

agreement was achieved on the size of the separation region yet, the loss coefficient was grossly over-predicted using the k-ω(SST) model. Overall, the Walters and Leylek's [2] k-k_L-ω transitional model flow was achieved better prediction of the low Reynolds number aerodynamic flow effects than the conventional k-ω(SST) turbulence model for the Aft-Loaded L1A blade airfoil at higher turbulent intensities.

7. **Aft-Loaded L1A Blade with Upstream Wake Generators**

The CFD model of the Aft-Loaded L1A blade with upstream wake generators presented in Section 3.1.2 was run at Re = 25,000 at high and low inlet turbulent intensities. The inlet turbulent boundary conditions for the low turbulence intensity case were set to *Tu* = 0.5% with an inlet turbulent length scale, $l_m = 50mm$, whereas the high turbulence intensity case was simulated at *Tu* = 3.4% and $l_m = 40mm$. These inlet turbulent boundary conditions corresponded to the baseline CFD simulations completed without upstream wakes. In the cascaded experiment on the L1A blade, circular cylinders were used to generate an upstream translating wake impinging on the downstream blade. The purpose of this study was to simulate the periodic disturbances associated with rotor/vane flow interactions encountered in a multistage LPT geometry, where wakes shed from an upstream vane propagate and impinge on the downstream rotor blade.

Unsteady simulations were completed for both the high and low turbulence intensity cases based on the experimental results of Nessler *et al.* [37,48] taken in the AFRL LSWT. This included matching the flow coefficient ($\Phi = u_{axial}/u_{rod}$) of 0.817 and cylindrical rod speed, $u_{rod} = 2.298$m/sec. The low turbulence intensity case utilized a total of 112,799 time-steps or 0.2256sec for averaging of mean-flow quantities with the flow time-step of 2μsec. The total flow-time interval through the CFD domain was 0.436sec and the mean-flow averaging interval represented 0.516 flow-time intervals. The high turbulence intensity cases used 112,199 time-steps or 0.2244sec for mean flow-averaging and this interval represented 0.514 flow-time

CFD Modeling of Separation and Transitional Flow in
Low Pressure Turbine Blades at Low Reynolds Numbers

intervals. The flowfield of the upstream wake configuration of the Aft-Loaded L1A blade airfoil

was compared with the CFD predictions and experiments of the baseline Aft-Loaded L1A blade

cases.

7.1   CFD Predictions for the Wake Generator

The flowfield of the upstream wake generators was investigated in order to characterize

the wake produced by the circular cylinder that impinged upon the downstream Aft-Loaded L1A

blade airfoil.   The inlet Reynolds number based on diameter of the cylinder and the relative

velocity was 794. Flowfield comparisons were made against reported theory, since the flowfield

around a circular cylinder has been presented in many fluid dynamics texts [7-9]. The cylinder

surface static pressure, vortex shedding behavior, and wake properties were calculated for at high

and low inlet turbulent intensities and the results are discussed in the next sections.

7.1.1   Surface Static Pressure Coefficient

Figure 7.1 shows the wake generator mean surface static pressure coefficient for both

high and low turbulent intensities as calculated with Eq. (7.1)

$$C_p = \frac{(P_{surface} - P_{in})}{\frac{1}{2}\rho w_{in}^2} \tag{7.1}$$

where the w_{in} is the inlet relative velocity. The static pressure coefficient was plotted as a

function of angular surface location (θ) from the stagnation point. The CFD-predicted static

pressure distribution was similar to that reported results in several fluid dynamic texts [7,8]

where the boundary layer remained attached in the favorable pressure gradient for θ up to $75°$,

and separated from the wake generator surface once it reached the adverse pressure gradient

portion of the wake generator surface. The static pressure distribution was very similar for both the low and high turbulence intensity cases with a predicted separation location of 103.5°. This location corresponded to a laminar boundary flow separation point and was within 95% agreement of the 108.8° separation point for laminar flow around a circular cylinder calculated using the Blasius series [49]. Investigations indicated that the turbulent kinetic energy around the wake generator was an order of magnitude smaller than the freestream value and confirmed that the boundary layer was predicted as laminar.
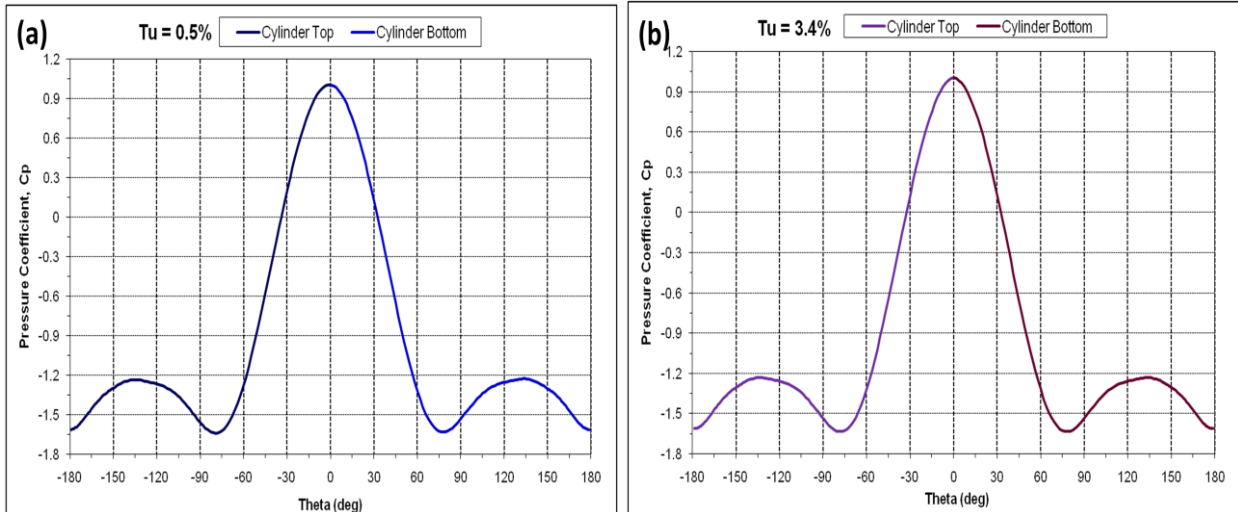
Figure 7.1. The mean surface static pressure coefficient at $Re_D = 794$ at (a) $Tu = 0.5\%$, $l_m = 50mm$ and (b) $Tu = 3.4\%$, $l_m = 40mm$ for the wake generator

7.1.2   Unsteady Features of the Flowfield

Contour plots of the vorticity in the spanwise or z-direction were made to show unsteady vortex generation of the upstream wake generator as shown in Figure 7.2. The z-vorticity (Ω_z) was calculated using Eq. (7.2)

$$\Omega_z = \left(\nabla \times \vec{W}\right) \cdot \hat{k} \qquad (7.2)$$

where $\hat{k}$ is the unit vector in the z-direction and $\vec{W}$ is the relative velocity vector. Figure 7.2 shows the separated shear layer from the wake generator produced two large vortices. Both the low and high inlet turbulence intensity cases produced very similar vortex shedding behavior. The shear layer on the top surface of the wake generator produced a clockwise vortex as indicated by the positive z-vorticity whereas, the shear layer on the bottom portion of the wake generator produced a counter-clockwise vortex with negative z-vorticity. This shedding pattern is known as a von Karman vortex street [48]. The FFT calculation of the dynamic drag coefficient showed that the vortex shedding frequency was 296 ± 4Hz for both the low and high turbulence intensity cases. The Strouhal number was calculated using Eq. (7.3)

$$St = \frac{fD}{u_{in}} \tag{7.3}$$

with the result $St = 0.23$ for the both the low and high turbulence intensity cases. Table 7.1 shows the vortex shedding frequency and Strouhal number based on characteristic length and momentum thickness at separation for both the upstream wake generator and the Aft-Loaded L1A blade.
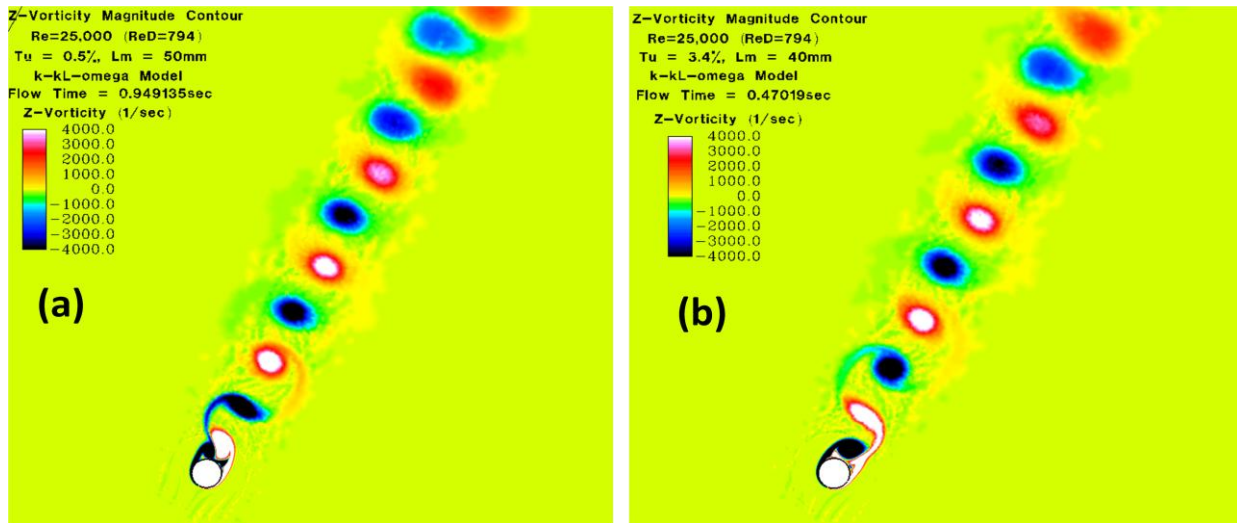
Figure 7.2. Instantaneous Z-vorticity contours at $Re_D = 794$ at (a) $Tu = 0.5\%$, $l_m = 50mm$ and (b) $Tu = 3.4\%$, $l_m = 40mm$ for the wake generator

7.1.3   Downstream Wake Characteristics

Several single point measurements of the velocity were made downstream of the wake generator. The first velocity probe was located one-half of the blade axial chord length (8.9cm) downstream from wake generator center and one-half of the blade pitch length (8.95cm) in the axial and pitchwise flow directions, respectively. Figure 7.3 shows the time-signal of this single point velocity probe measurement for the CFD and experimental results [37]. The experimental measurements were taken with a single element hot-film probe and represented a 100 blade passes ensemble time-averaged measurements of the velocity. The mean-flow averaging was completed for a total of 2.9 wake passes for both CFD results based on a wake passing frequency of 12.77Hz. The wake profiles were similar for the CFD results due to the laminar boundary layer present on the wake generator surface with the same separation location. The wake was quantified using wake width b, and the peak velocity deficit, u_p. The peak velocity deficit was calculated using Eq 7.4.

$$u_p = \frac{U - u_0}{U} \tag{7.4}$$

where U is the average velocity outside the wake region and u_0 is the minimum velocity within

the wake region as given in Table 7.1. Both CFD result had a 122% higher peak velocity deficit

and 35% smaller wake width compared to the experimental results. This could be attributed to

the surface of the actual wake generator not being perfectly circular and smooth. The boundary

layer of the real hardware may have been turbulent, thus reduced the wake peak velocity deficit

in the experimental results. Currently, a simulation of the wake generator is being completed at

the same inlet conditions as the low and high turbulence intensity cases using the fully turbulent

form Wilcox [11] $k\text{-}\omega$ model. This will determine the difference between a wake produced from

a turbulent boundary layer compared to a laminar boundary layer around the wake generator. If

there is a significant difference between the results, future work will explore methods of tripping

the boundary layer around the wake generator to become turbulent using the Walters and Leylek

[2] $k\text{-}k_L\text{-}\omega$ model.

Chapter 7. The Aft-Loaded L1A Blade with Upstream Wake Generators
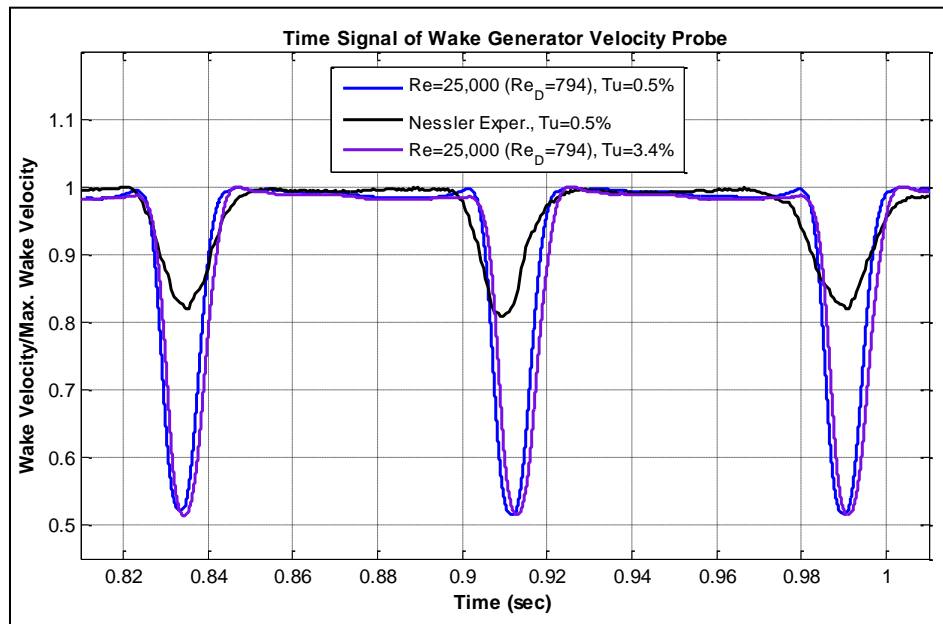
Figure 7.3. Comparison of the time-signal of the wake generator velocity for CFD at Tu = 0.5% and 3.4% with experimental [37] single point hot-film velocity measurements at Tu = 0.5% for Re = 25,000

For the high inlet turbulence intensity condition, single point velocity measurements of the wake were made at two different locations within the blade passage. Velocity Probe #1 was placed at the 66.25% axial chord position, 3.71 cm above and normal to the blade surface whereas, Velocity Probe #2 was placed at the 80.63% axial chord position, 2.87 cm above and normal to the blade surface. Figure 7.4 shows a comparison at $Tu = 3.4\%$ between the CFD and experimental results of the time signal of the blade passage velocity at the Probe #1 and #2 locations. The CFD predictions showed a higher amplitude change of velocity compared to the experimental results for both probe locations. This was due to a higher peak velocity deficit produced by the upstream wake generator in the CFD predictions. Also, the time variation of Probe #1 was significantly different in CFD predictions for the time interval of $0.76< t< 0.81$ sec range (Fig. 7.4(a)) when compared to the experimental results. This was attributed to the CFD only having 3 wake passes to average over instead of the 100 wake passes for flow-averaging in the experimental results causing the local peaks in this range to be significantly reduced. In

CFD Modeling of Separation and Transitional Flow in
Low Pressure Turbine Blades at Low Reynolds Numbers

Figure 7.4(b), the flow-averaging effect was reduced because of the higher amplitude change of the velocity at the Probe #2 location in the experimental result. The periodic pattern of the velocity variation for Probe #2 in the CFD predictions was slightly different compared to experimental result with a much larger amplitude change of the velocity.
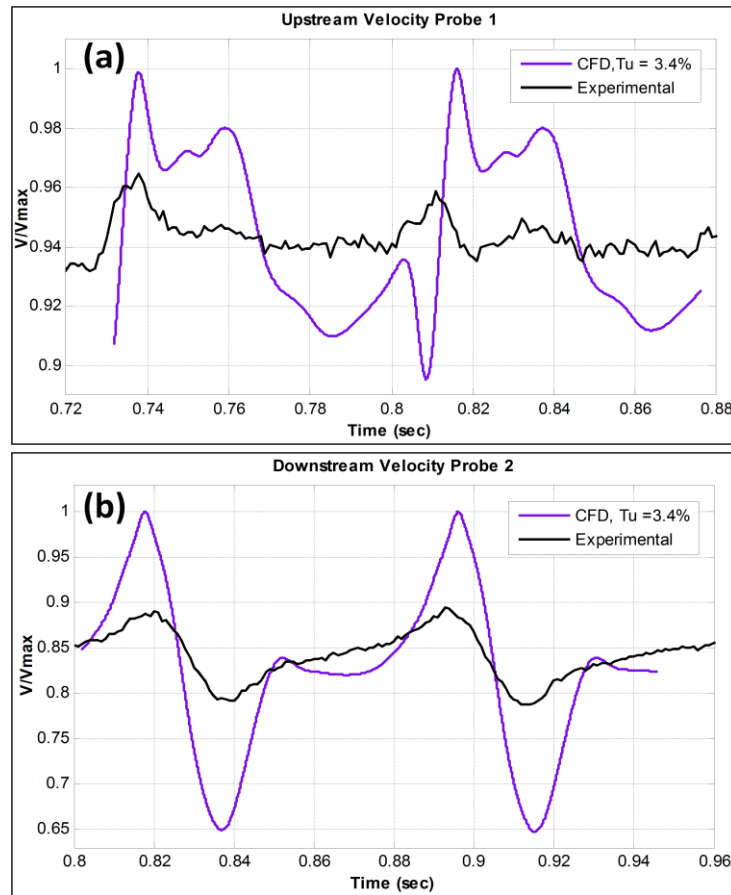
Figure 7.4. Comparison of the velocity (a) Probe #1 and (b) #2 blade passage locations with the experimental [48] single point hot-film velocity measurements at Re = 25,000, Tu = 3.4%

	Re	Tu	$l_m(mm)$	Re$_D$	θ_{sep}	f_{shed}	St (Eq. 5.1)	St (Eq. 7.3)	b (m)	U_p
CFD	25,000	0.5%	50	794	103.5°	296Hz	1.65×10^{-3}	0.23	0.0684	0.476
	25,000	3.4%	40	794	103.5°	298Hz	1.65×10^{-3}	0.23	0.0637	0.477
Exp.	25,000	0.5%	-	761	-	-	-	-	0.0861	0.214

Table 7.1. Summary of the separation location, Strouhal number, and wake properties for the wake generator

Chapter 7. The Aft-Loaded L1A Blade with Upstream Wake Generators

7.2 CFD Predictions for the Aft-Loaded L1A Blade

The effect of the traversing upstream wakes was investigated on the flowfield of the Aft-Loaded L1A blade. The traversing wakes had a significant effect on the blade loading, behavior of the boundary layer, unsteady vortex shedding, and total pressure loss coefficient. These properties of the flowfield were explored at low and high turbulent intensities and compared to the baseline simulations of the Aft-Loaded L1A blade. Comparisons were also made with PIV images of the unsteady flowfield and total pressure loss coefficient measurements taken by Nessler *et al.* [37].

7.2.1 *Unsteady Features of the Flowfield*

The unsteady features of the flowfield were investigated to understand the behavior of the upstream wake on the separation and vortex shedding. The upstream wake traversing event was divided into six phases with the first phase beginning with the rod positioned directly in front of the blade leading edge and in line with the inlet flow direction. A diagram of the six different phases is shown in Figure 7.5. Also, the time location was determined for each phase with respect to the freestream velocity Probe #2 as shown in Figure 7.6 for both the CFD and experimental results. Each phase in the CFD was positioned at different locations with respect to the experimental results for the Probe #2 time signal because the CFD predictions had a larger wake deficit thus producing a time-signal of the velocity. The time location of Phase #1 was verified by making sure the location of the wake generator was in the correct relative position to the blade.

Chapter 7. The Aft-Loaded L1A Blade with Upstream Wake Generators
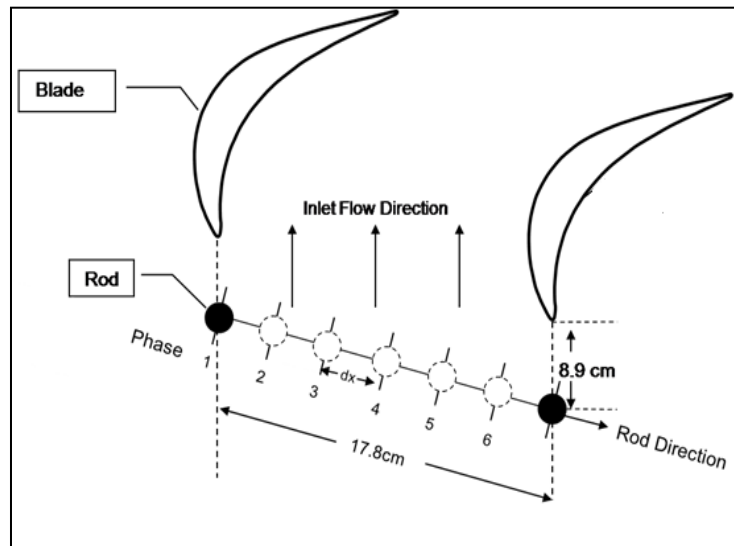
Figure 7.5. Diagram of the different wake generator locations for each of the six phases [37]
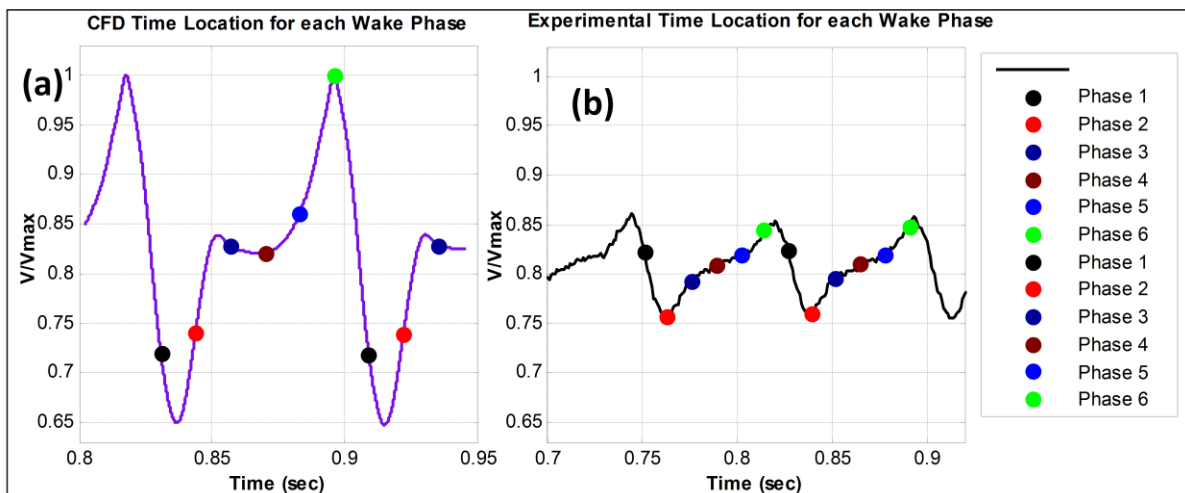
Figure 7.6. (a) CFD and (b) experimental time location for each phase with respect to the Probe #2 time signal of the freestream velocity [48]

Instantaneous contour plots of z-vorticity were used to visualize the features of the flowfield for each of the six phases. The flowfield was periodically repeated for three pitch lengths to aid the visualization of the traversing wake generator and the vortex shedding in the wake region of the downstream blade. The z-vorticity contours for each phase for the Re = 25,000, $Tu = 0.5\%$, $l_m = 50$mm and the Re = 25,000, $Tu = 3.4\%$, $l_m = 40$mm cases is shown in Figure 7.7 and 7.8, respectively. Both simulations showed identical unsteady behavior of the

CFD Modeling of Separation and Transitional Flow in
Low Pressure Turbine Blades at Low Reynolds Numbers

traversing wake and the vortex shedding caused by the blade surface separated shear layers. Phase #1 and #2 (Fig 7.7(a)-(b) and Fig 7.8(a)-(b)) shows the traversing wake affecting the boundary layer separation of the pressure side of the blade. The vortex created on the pressure side was clockwise in direction as indicated by positive z-vorticity. The freestream pressure field in the blade passage caused the traversing wake to form into the V-shape as shown in Figure 7.7(c)-(e) and Figure 7.8(c)-(e) for Phases #3-#5. The wake began to reach the aft portion of the blade and affected the vortices created by the separated shear layer in Phase #6 and #1.

Figure 7.9 presented a magnified view of the vortices produced by suction surface separated shear layer for the Re = 31,000, Tu = 0.5% baseline case compared to the Re = 25,000, Tu = 0.5% with the addition of wakes. The baseline case was divided into six phases corresponding to the same time interval as the Re = 25,000 case with the wakes. The vortices were significantly smaller compared to the baseline case for all six phases (Phase #1, #3, & #6 only shown in Fig. 7.9). The traversing wake caused an increased amount of turbulence present in the freestream and reduced the separation region compared to the baseline case. The separated shear layers produced clockwise vortices that were lifted off the blade surface by the traversing wake. The separated shear layer from the trailing edge produced a similar counter-clockwise vortex as in the baseline case.

The time signal and the FFT of the drag coefficient were calculated for the Aft-Loaded L1A blade with upstream wake generators for both low and high turbulence intensity cases. Within the frequency resolution, 4Hz based Eq. (5.1) for both low and high inlet turbulence intensity cases, the dominant and harmonic frequencies were similar. The suction side separated shear layer vortex was being shed at a frequency of 75Hz as shown in Figure 7.10. Also, evident

is the pressure side separation region was shedding at a frequency of 27Hz. The trailing edge counterclockwise vortex was shedding in the wake region at 36Hz as shown in Fig. 7.9(b). Table 7.2 shows the separation location, shedding frequencies, and corresponding Strouhal number calculated from Eq. (4.1).
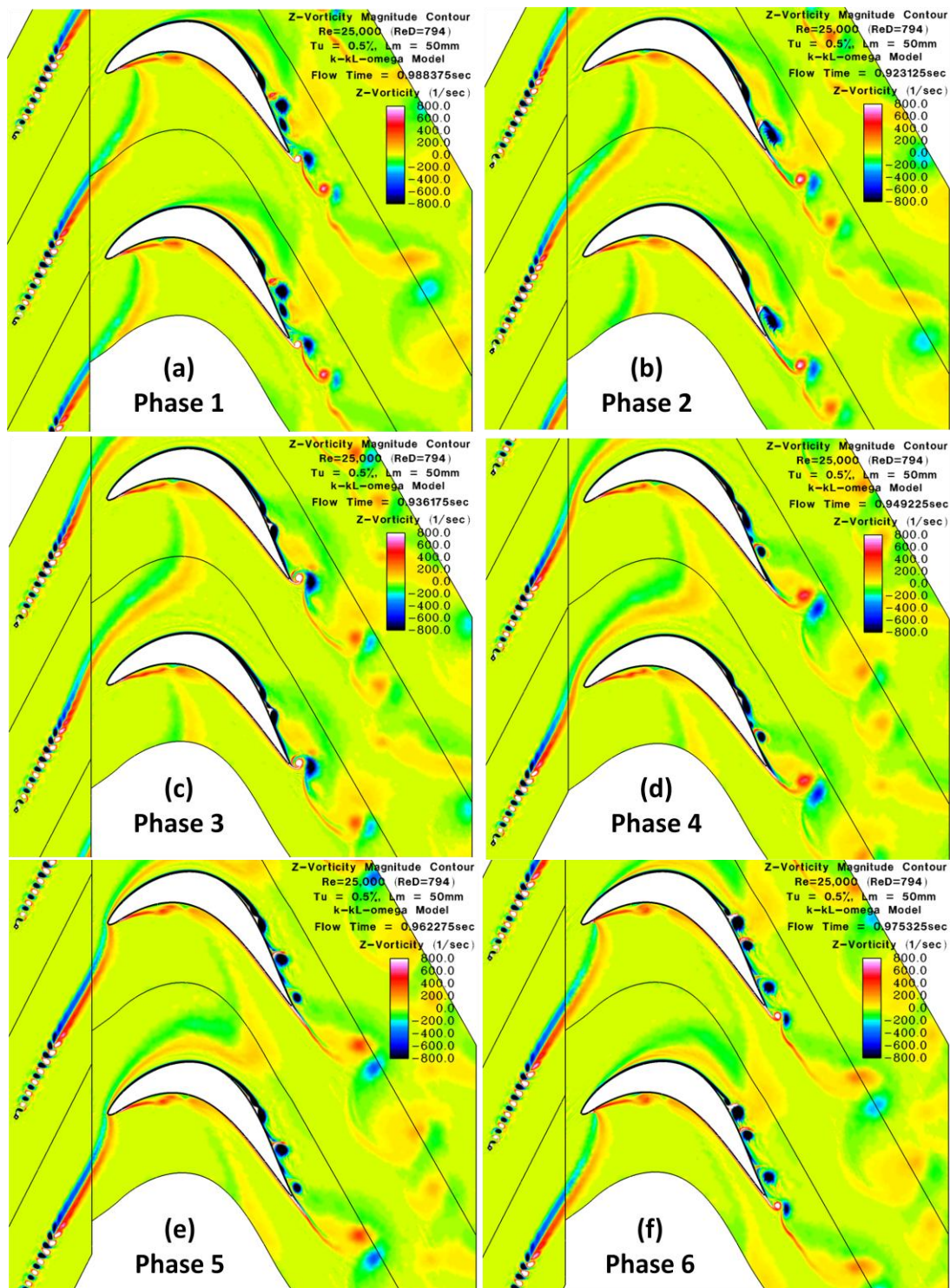
Figure 7.7. Instantaneous z-vorticity contour plots for each of the six phases at Re =25,000, Tu = 0.5%, l_m = 50mm

CFD Modeling of Separation and Transitional Flow in
Low Pressure Turbine Blades at Low Reynolds Numbers

Figure 7.8. Instantaneous z-vorticity contour plots for each of the six phases at Re =25,000, Tu = 3.4%, l_m = 40mm

CFD Modeling of Separation and Transitional Flow in
Low Pressure Turbine Blades at Low Reynolds Numbers
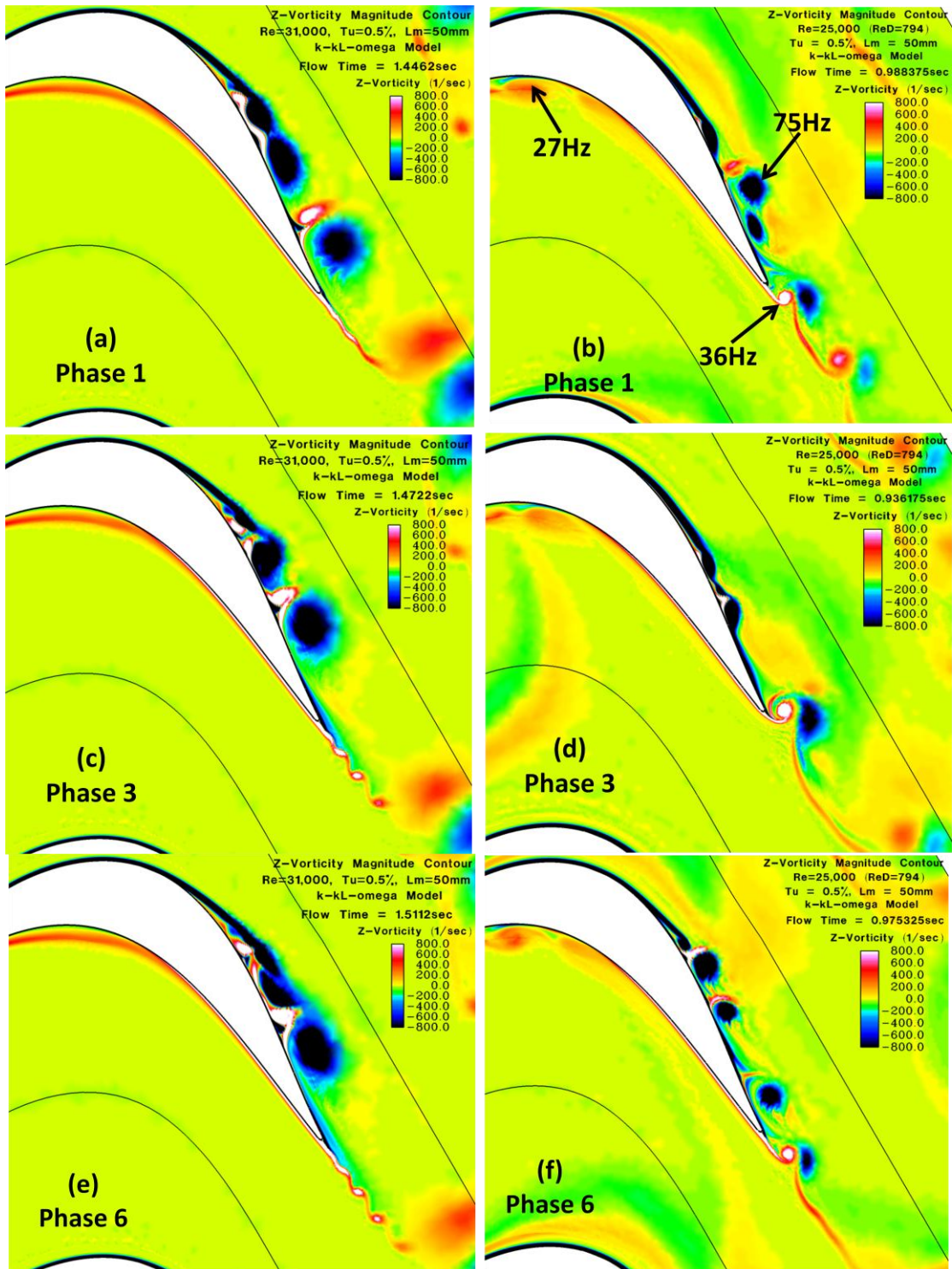
Figure 7.9. Comparisons of the instantaneous z-vorticity contours of the separation region at Phase #1, #3, and #6 for baseline Re = 31,000 and Re = 25,000 with wakes, at Tu = 0.5%, l_m = 50mm

Chapter 7. The Aft-Loaded L1A Blade with Upstream Wake Generators
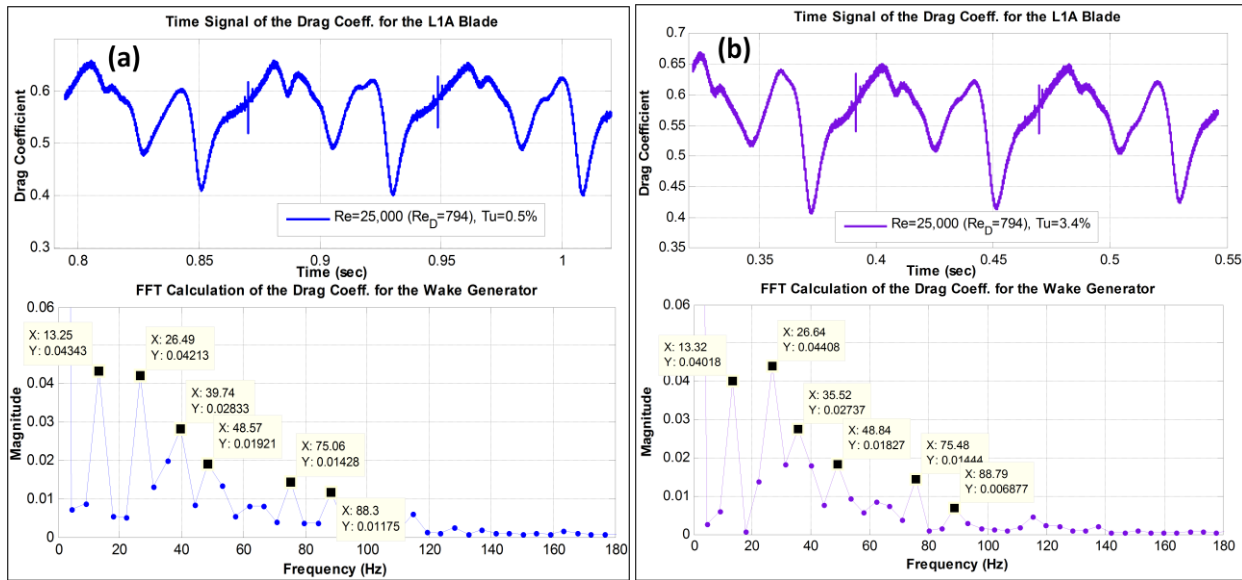
Figure 7.10. Time signal and FFT calculation of the drag coefficient for the Aft-Loaded L1A blade airfoil with upstream wake generators at Re = 25,000 (a) Tu = 0.5%, l_m = 50mm and (b) Tu = 3.4%, l_m = 40mm

				Pressure Side			
Re	$l_m(mm)$	Tu	X_{sep}/C_x	f_{shed}	St		
25,000,Passing Wake	50	0.5%	0.690	25Hz	1.92×10^{-3}		
31,000, Baseline	50	0.5%	0.633				
25,000,Passing Wake	40	3.4%	0.673	27Hz	1.83×10^{-3}		

Suction Side						Trailing Edge	
Re	f_{shed}	St	f_{shed}	St	f_{shed}	St	f_{shed}	St
25,000, Passing Wake	75Hz	5.76×10^{-3}	13Hz	1.00×10^{-3}	-	-	40Hz	3.07×10^{-3}
31,000, Baseline	51Hz	2.46×10^{-3}	18Hz	8.69×10^{-4}	32Hz	1.55×10^{-3}	102Hz	4.93×10^{-3}
25,000, Passing Wake	76Hz	5.15×10^{-3}	13Hz	8.81×10^{-4}	-	-	36Hz	2.44×10^{-3}

Table 7.2. Summary of the separation location and Strouhal number for the Aft-Loaded L1A blade airfoil with upstream wake generators

7.2.2   Comparison of Phase Velocity Contours with Experimental PIV Results

Experimental PIV images were taken by Nessler *et al.* [37] of the blade passage for each of the six phases. Velocity magnitude contours were made based on the PIV images for the comparisons with CFD prediction at the high inlet turbulence intensity cases as shown in Figure 7.11 - 7.13. Figure 7.11(a) shows for Phase #1 the flow was attached with a separation region

CFD Modeling of Separation and Transitional Flow in
Low Pressure Turbine Blades at Low Reynolds Numbers

present in the aft portion of the blade downstream of 90% axial chord location for both the CFD and experimental result. Also, the negative z-vorticity region shown in Figure 7.8(a) corresponded to the same region of high velocity whereas the positive z-vorticity regions corresponded to the low velocity regions and was found for all six phases. There was a larger high velocity region in the CFD prediction compared to the experimental result due to a much larger velocity deficit in the CFD predictions. In Phase #2 (Fig. 7.11(b)), the separation region moved more downstream near the blade trailing edge with attached flow across the visible length of the suction surface in the PIV results. The high velocity region returned along the blade surface with the location of the wake moving out of the view for the PIV and CFD results in Phase #3 as shown in Fig. 7.12(a). Similarly in Phase #2 and #3, the CFD prediction had a larger region high velocity region compared to experimental PIV result. The high velocity region moved more downstream, indicating that a new wake was entering the blade passage in Phase #4 (Fig 7.12(b)). For Phase #5 and #6, in Figure 7.13, the high velocity region continued to move downstream with a localized separation region approximately at the 89% axial chord region in Phase #5 and moving near the trailing edge in Phase #6. The high velocity region was in the CFD prediction similar in size as the PIV result for Phases #4 - #6 because the upstream wake was not present on the aft portion of the blade for these phases.
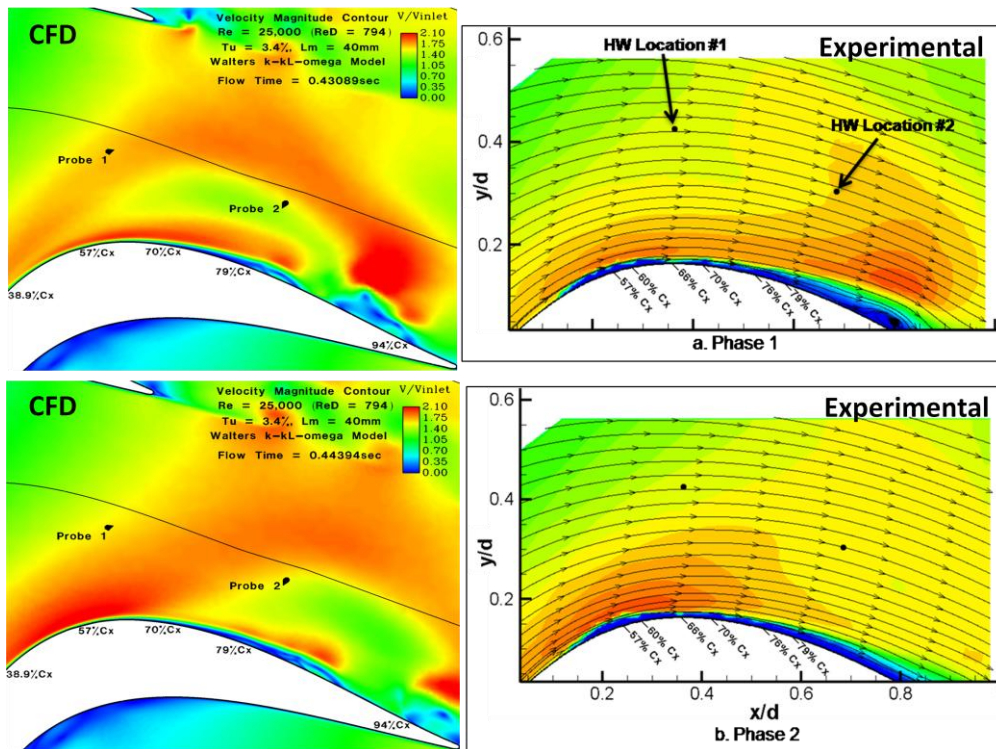
Figure 7.11. Comparison of the velocity magnitude contour plots in the blade passage for the CFD and experimental [37] PIV results at Re = 25,000, Tu = 3.4%, l_m = 40mm for Phase #1 & #2
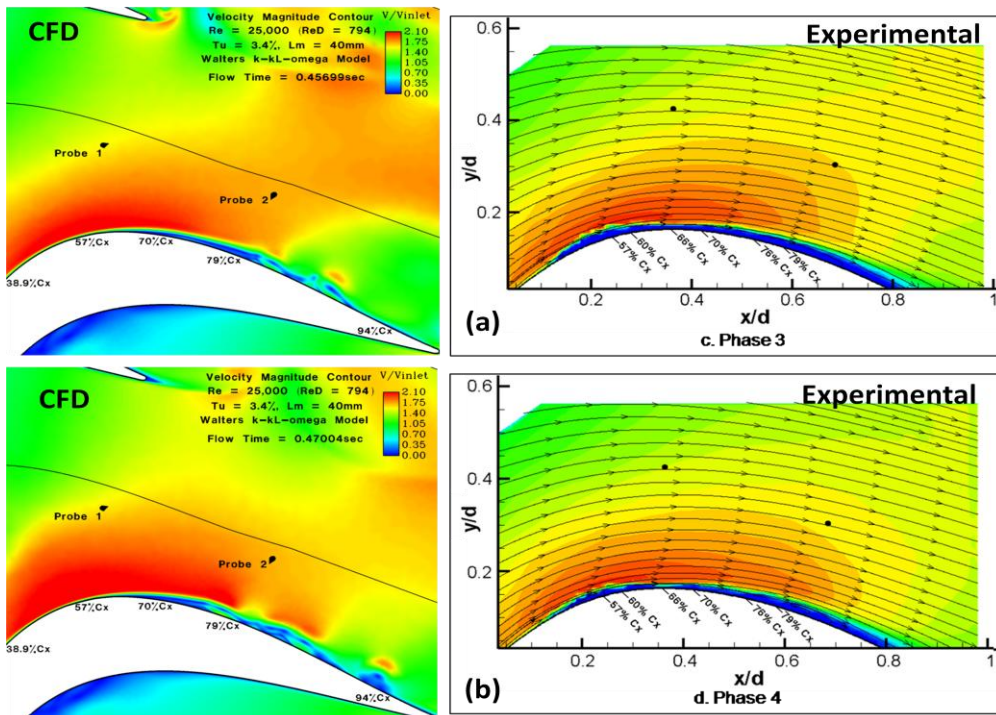
Figure 7.12. Comparison of the velocity magnitude contour plots in the blade passage for the CFD and experimental [37] PIV results at Re = 25,000, Tu = 3.4%, l_m = 40mm for Phase #3 & #4

CFD Modeling of Separation and Transitional Flow in
Low Pressure Turbine Blades at Low Reynolds Numbers
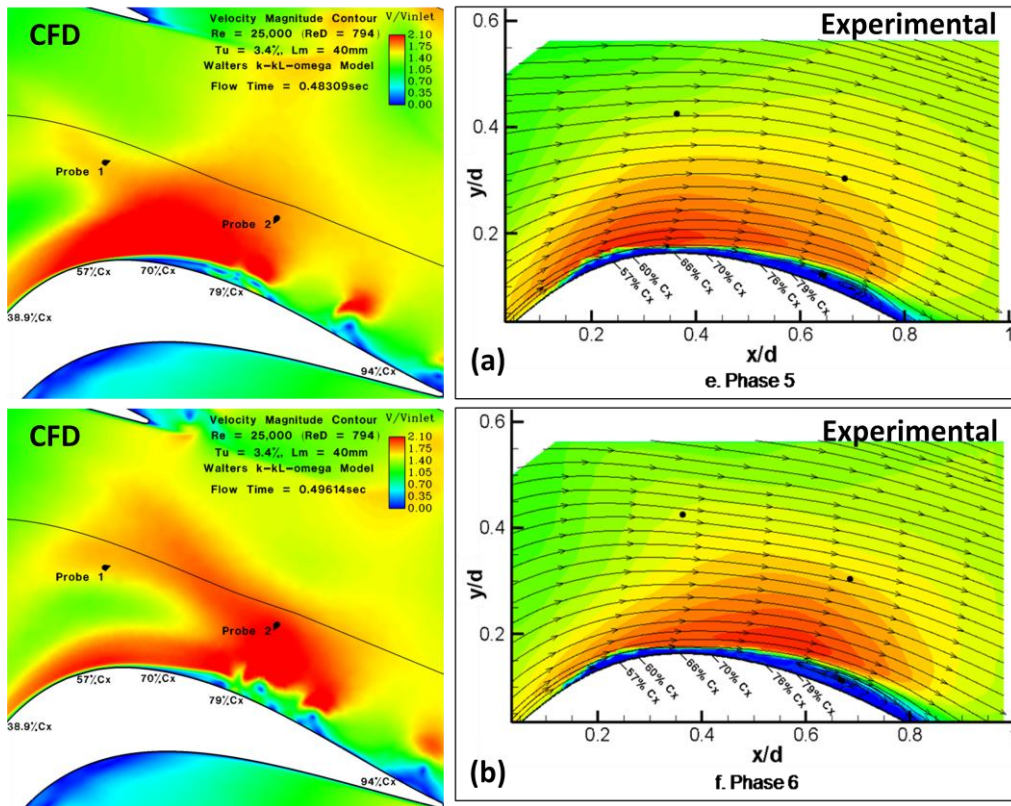
Figure 7.13. Comparison of the velocity magnitude contour plots in the blade passage for the CFD and experimental [37] PIV results at Re = 25,000, Tu = 3.4%, l_m = 40mm for Phase #5 & #6

Instantaneous boundary layer profiles of the axial velocity were obtained at six axial chord locations for Phase #1, #3, and #6 for CFD and experimental results for the Re = 25,000, Tu = 3.4%, l_m = 40mm case as shown in Figure 7.14 - 7.16. For the experimental results, the boundary layer profiles were extracted from PIV measurement of the flowfield for each phase. Phase #1 in Figure 7.14(a) showed the good agreement with the experimental results in the thickness of the boundary layer to the 70.0% axial chord location. Downstream of that location, the CFD result over-predicted the thickness of the boundary to the 85.0% axial chord location (Fig. 7.14(b)). This difference could be attributed to over-prediction of the size of the unsteady vortices produced from the suction surface separated shear layer. Also, the averaging of the instantaneous velocity field completed by the post-processing of the PIV images could have

CFD Modeling of Separation and Transitional Flow in
Low Pressure Turbine Blades at Low Reynolds Numbers

reduced the boundary layer thickness in experimental results. Similar over-prediction of the boundary layer thickness in CFD prediction was observed in Phase #3 (Fig. 7.15(b)) starting at the 74.1% axial chord location. A significant amount of reversed flow was present in the CFD prediction starting at the 70.0% axial chord location for Phase #3 whereas, Phase #1 had the reversed flow beginning more downstream of that location. This indicated that the separation location moved more downstream in Phase #3 as compared to Phase #1. Figure 7.16 shows in Phase #6 that the boundary layer profiles showed a unique shape starting at the 79.4% axial chord location. This was due to the unsteady vortices lifting off the blade surface into the freestream and the boundary layer below reattaching to the blade surface. The amount of reversed flow present in the boundary layer has significantly reduced compared to Phase #1 and Phase #3.
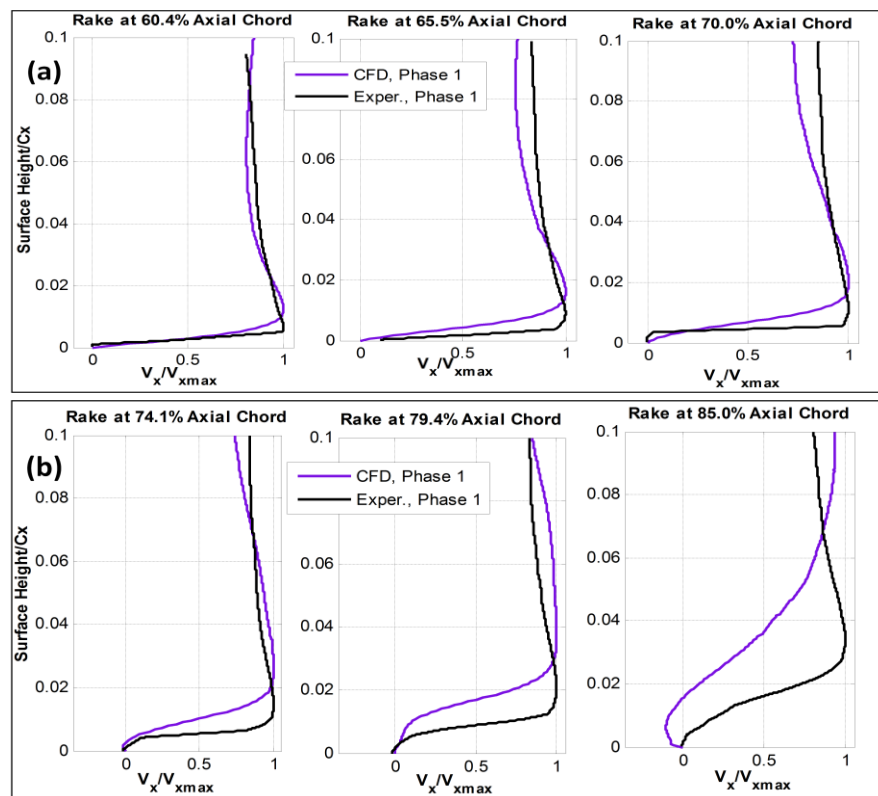
Figure 7.14. Comparison of the instantaneous boundary layer profiles of axial velocity the Aft-Loaded L1A

Figure 7.15. Comparison of the instantaneous boundary layer profiles of axial velocity the Aft-Loaded L1A blade with upstream wake generators to the experimental PIV results for Phase #3 at Tu = 3.4%, l_m = 40mm

Figure 7.16. Comparison of the instantaneous boundary layer profiles of axial velocity the Aft-Loaded L1A blade with upstream wake generators to the experimental PIV results for Phase #6 at Tu = 3.4%, l_m = 40mm

7.2.3   Mean Flow Comparisons of the Surface Static Pressure and Boundary Layer Profiles

In Figure 7.17, the mean static pressure coefficient distributions of the Aft-Loaded L1A blade airfoil were compared to baseline CFD cases at low and high inlet turbulent intensities. Figure 7.17(a) shows that the addition of the upstream wake caused an increase in the pressure peak compared to the baseline case, which resulted a higher blade loading for the $Tu = 0.5\%$ case. The separation point was located more downstream at the 69.9% axial chord location with the addition of the upstream wake, compared to the baseline separation point at 64.4% axial chord. The region of constant pressure downstream of the separation point due to the separation region was smaller in the passing wake case compared to the baseline case, which indicated a smaller separation region. The local peak pressure coefficient at 78% axial chord location was due to the motion of the vortices as they lifted off the blade surface and traveled downstream to

CFD Modeling of Separation and Transitional Flow in
Low Pressure Turbine Blades at Low Reynolds Numbers

the wake region and this peak was smaller and located more upstream compared to the baseline case. This was due to the reduction in size of the vortices created by the separated shear with the addition of the upstream wake. Downstream of this local pressure peak, the static pressure distribution indicated a reattached boundary layer for both the baseline and the passing wake cases. The blade surface static pressure distribution for the high inlet turbulence intensity case in Figure 7.17(b) was similar to the low inlet turbulence intensity case, with similar trends, when compared with the baseline case. This reason for this trend is shown in Figure 7.18 in the turbulence intensity contours for Phase #1, #3, and #6 at both inlet turbulence intensity cases. The turbulence produced by the upstream wake increased to the freestream turbulence to a similar level for both cases and therefore the change in inlet turbulence intensity had no effect prediction of the flowfield with the addition of upstream wakes. Yet, the baseline case showed at higher inlet turbulence intensity a reduction of the separation region. The addition of the upstream wake caused an increase in the blade loading and a decrease in the separated flow present on the blade suction surface for both the low and high inlet turbulence intensity cases.
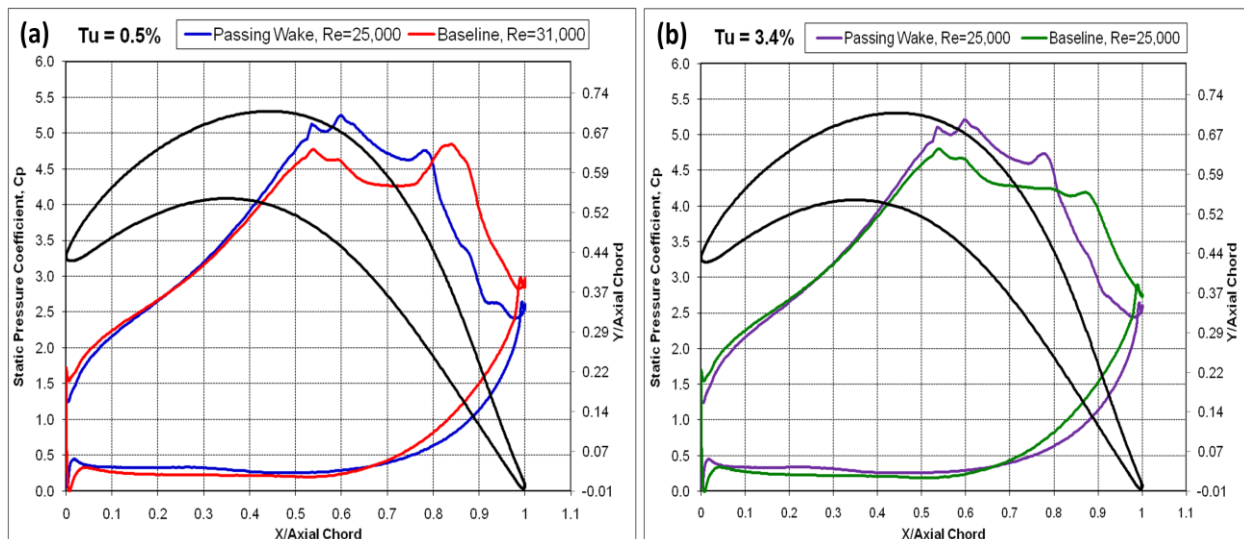
Figure 7.17. Comparison of surface static pressure coefficient of the Aft-Loaded L1A blade with upstream wake generators to the baseline CFD simulation at Re = 25,000 (b) Tu = 0.5% and (b) Tu = 3.4%

CFD Modeling of Separation and Transitional Flow in
Low Pressure Turbine Blades at Low Reynolds Numbers
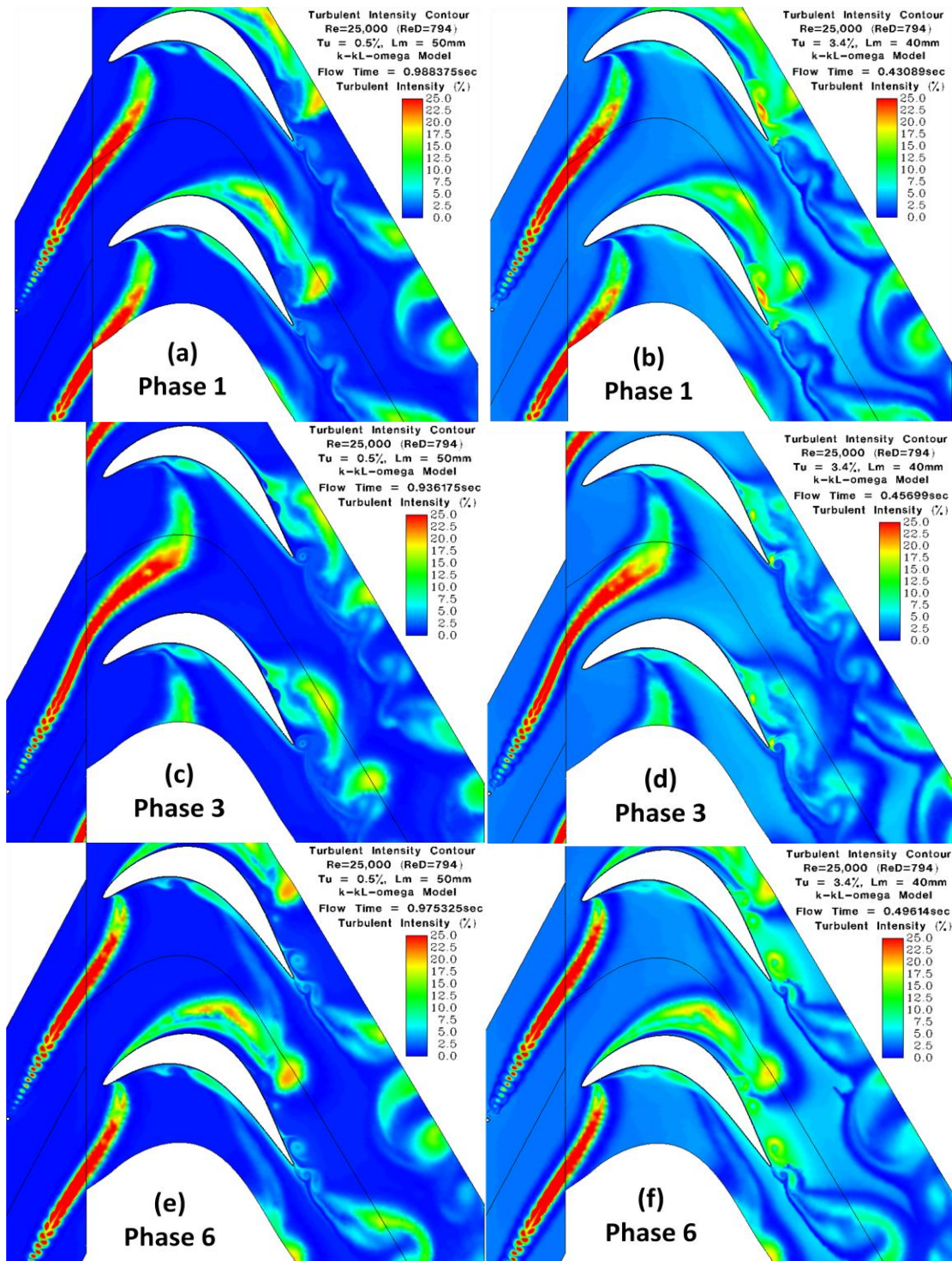
Figure 7.18. Comparisons of the instantaneous turbulence intensity at Phase #1, #3, and #6 for Re = 25,000 with wakes, at Tu = 0.5%, l_m = 50mm and Tu = 3.4%, l_m = 40mm

Chapter 7. The Aft-Loaded L1A Blade with Upstream Wake Generators

Time-averaged values of the boundary layer velocity profiles were obtained at ten axial chord locations normal to the blade surface for both the upstream passing wake cases, at both low and high inlet turbulence intensity. The axial velocity was plotted in order to compare the amount of reversed flow present in the separation region. The result is shown in Figures 7.19 and 7.20. The separation point for the $Tu = 0.5\%$, $l_m = 50$mm case (Fig 7.17(a)) was predicted to occur at the 69.0% axial chord location, which was more downstream than the baseline case separation point at the 64.4% axial chord location. The boundary layer profiles confirmed the trends observed in the surface static pressure coefficient comparisons. There was significantly less separated flow present with the addition of the passing upstream wake compared to the baseline case. Figure 7.19(b) shows the mean flow boundary layer reattached to the blade surface slightly downstream of the 89% axial chord location while the baseline case remained separated to the blade trailing edge. For the high turbulence intensity case, the separation point was located at the 63.3% and 67.3% axial chord position for the baseline case and with upstream passing wakes, respectively. For both the low and high turbulent intensities, the addition of the passing wake caused a significantly smaller separation region as compared to the baseline case as shown in Figure 7.20(a)-(b) for the high inlet turbulence intensity case.
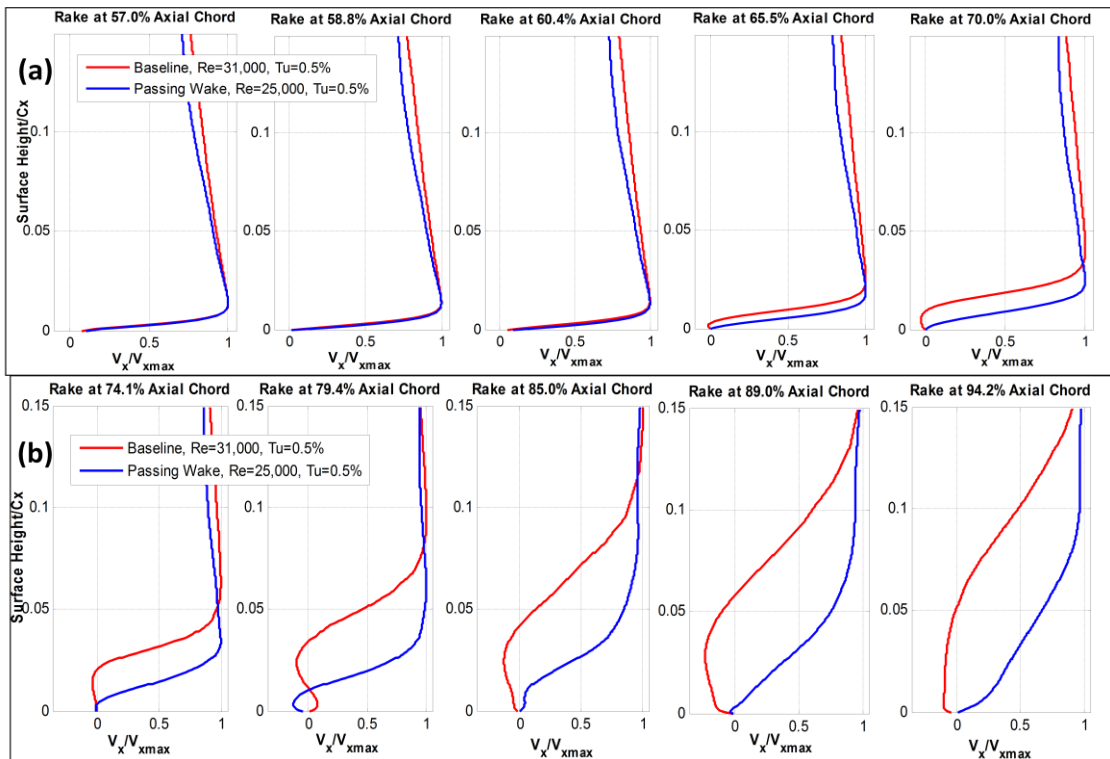
Figure 7.19. Comparison of the mean boundary layer profiles of axial velocity the Aft-Loaded L1A blade with upstream wake generators to the baseline CFD simulation at Re = 25,000, Tu = 0.5%
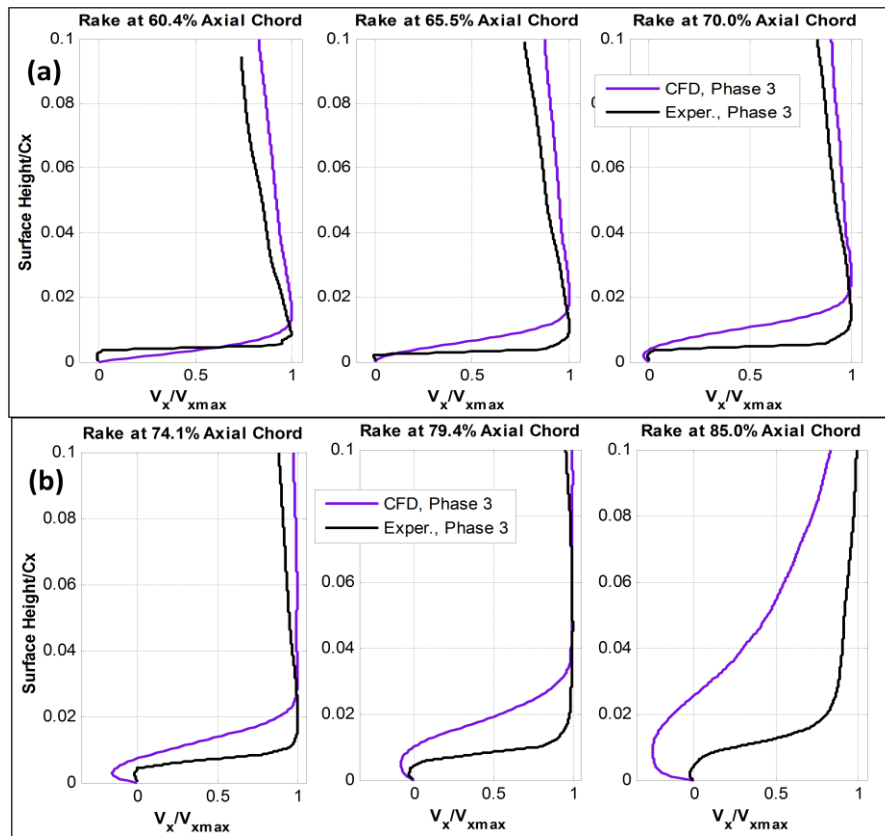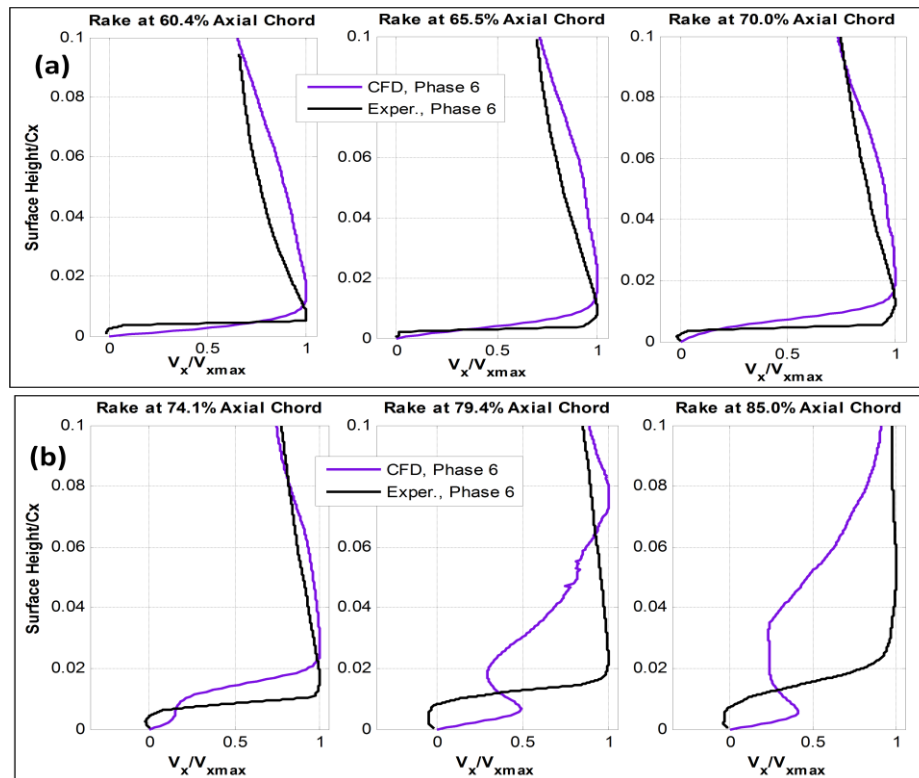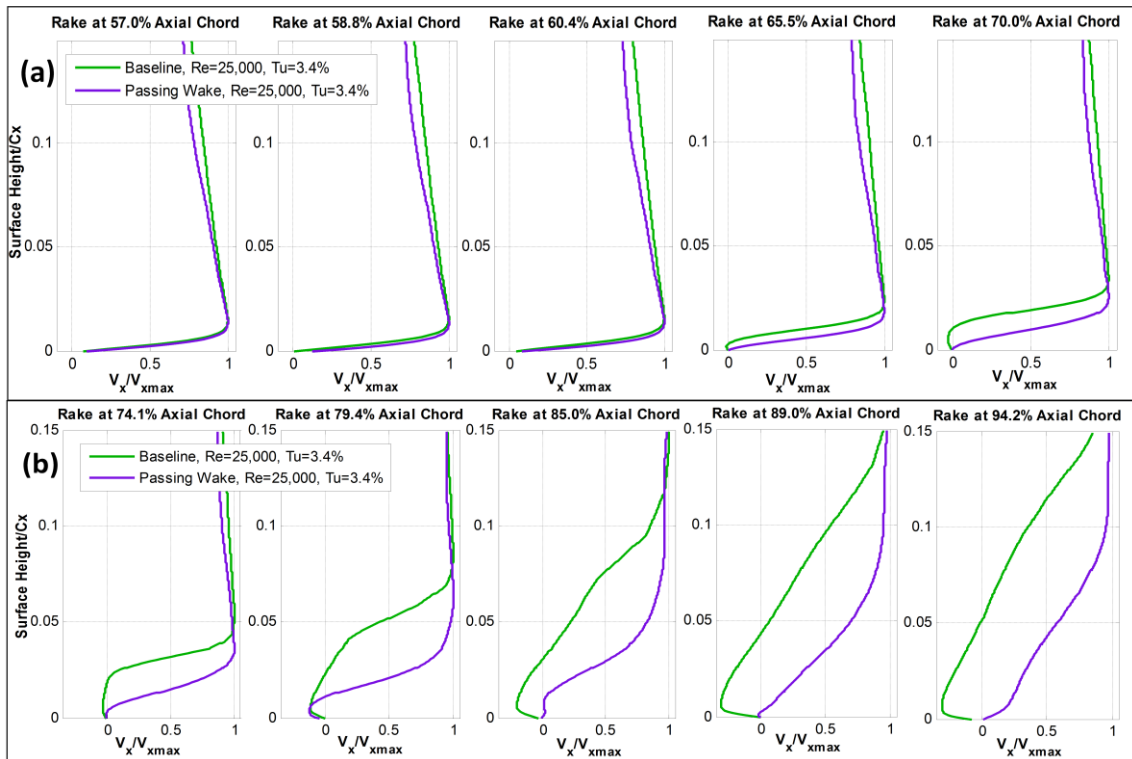

Figure 7.20. Comparison of the mean boundary layer profiles of axial velocity the Aft-Loaded L1A blade with upstream wake generators to the baseline CFD simulation at Re = 25,000, Tu = 3.4%

7.2.4   Total Pressure Loss Coefficient Predictions

The wake total pressure loss coefficient distribution and the integrated value are shown in Figure 7.21 and Table 6.3, respectively. For *Tu* = 0.5% case, the addition of upstream wake caused a 17% and 36% decrease in the peak and integrated loss coefficient, respectively. The increased amount of turbulence produced from the wake re-energized the boundary layer and delayed the separation event. The low turbulence intensity case showed good agreement, 98%, with the experimental loss coefficient measurement and 87% agreement in the integrated loss coefficient. For the *Tu* = 3.4% case, the addition of the upstream wake caused a 3% increase in the peak loss coefficient and 15% decrease in the integrated loss coefficient, respectively. Good agreement with the experimental loss coefficient measurements was achieved, with 95% agreement in the peak loss coefficient and 98% agreement in the integrated value for the high turbulence intensity case. The peak loss coefficients in the baseline cases were significantly under-predicted compared to the experimental results as presented in Section 6.1.4 and 6.2.4. Better comparisons were made with the integrated wake loss coefficients, with 87% and 98% agreement with experimental results for the low and high turbulence intensity baseline cases, respectively.

Chapter 7. The Aft-Loaded L1A Blade with Upstream Wake Generators
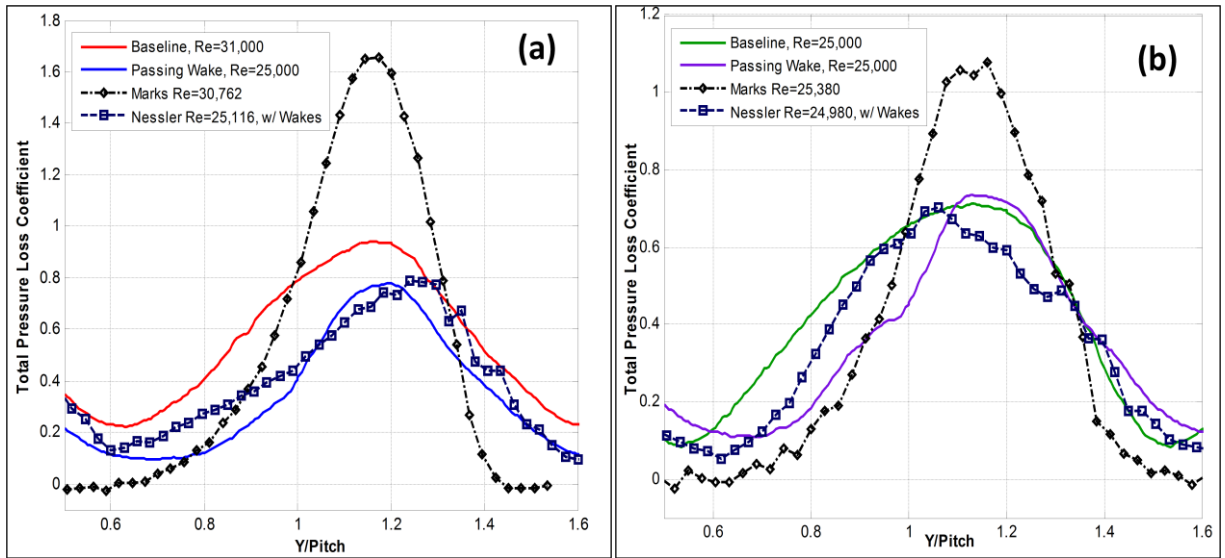
Figure 7.21. Comparison of total pressure loss coefficient with experimental [35,37] for the baseline and addition of wakes (a) Tu = 0.5% and (b) Tu = 3.4% at Re = 25,000for the Aft-Loaded L1A blade airfoil

Re	Tu	$l_m(mm)$	Integrated Loss Coefficient		Maximum Loss Coefficient	
			CFD	Experimental	CFD	Experimental
25,000, Passing Wake	0.5%	50	0.3639	0.4187	0.7793	0.7912
31,000, Baseline	0.5%	50	0.5772	0.5526	0.9391	1.6549
25,000, Passing Wake	3.4%	40	0.3736	0.3804	0.7344	0.7013
25,000, Baseline	3.4%	40	0.4383	0.3893	0.7119	1.0774

Table 7.3. Maximum and integrated total pressure loss coefficient comparison with the experimental [35,37] results for the Aft-Loaded L1A blade with and without upstream wake generators

7.3   Summary of Results

The flowfield of the Aft-Loaded L1A blade airfoil subjected to traversing upstream wakes was simulated using the k-k_L-ω model at an inlet Reynolds number of 25,000. The upstream wakes were generated by a circular cylinder traversing in the pitchwise direction. This setup was used to simulate the periodic flowfield associated with rotor/vane flow interactions encountered in a multistage LPT geometry, where wakes shed from an upstream vane propagate

Chapter 7. The Aft-Loaded L1A Blade with Upstream Wake Generators

and impinge on a downstream rotor. CFD simulations were completed at low and high inlet turbulent intensities and compared to experimental cascade measurements taken by Nessler *et al.* [37,48], and the baseline CFD results.

The flowfield of the upstream wake generator was investigated in order to characterize the wake produced by the circular cylinder impinging upon the downstream Aft-Loaded L1A blade airfoil. The boundary layer on the wake generator surface was predicted as laminar at both the low and high inlet turbulent boundary conditions. The wake generator produced a von Karman vortex street in the wake region that dissipated as the wake reached blade flow passage. Comparisons were made with experimental results of single point velocity measurements placed in the blade passage. The wake produced in the CFD results had a higher velocity deficit as compared to the experimental results. The difference could be attributed to the surface of the experimental wake generator not being perfectly circular and smooth. This could have caused the boundary to become turbulent, reducing the wake peak velocity deficit in the experimental results. Future work will consist of completing simulations with the wake generator ran as a turbulent boundary layer in order achieved better agreement with the experimental wake deficit measurements.

Investigations of the flowfield of the Aft-Loaded L1A blade showed the traversing wakes had a significant effect on the blade loading, behavior of the boundary layer, unsteady vortex shedding, and total pressure loss coefficient. The addition of the wakes increased the blade loading and caused the separation location to be moved further downstream. The traversing wake could be thought of as negative jet flowing toward the origin of the wake superimposed on a uniform freestream [50]. This negative jet causes the fluid in an individual wake segments to

CFD Modeling of Separation and Transitional Flow in
Low Pressure Turbine Blades at Low Reynolds Numbers

convect toward, and impinge on the suction surface. Thus, downstream of wake center the negative jet accelerated the flow, while upstream of the wake center, the negative jet decelerated the flow [51]. The suction surface shear layer produced unsteady vortices that were significantly smaller than the baseline CFD results and caused the separation region in the mean flow to reduce. Similar predictions of the flowfield were made at both the low and high inlet turbulence intensity. Also, the CFD result showed similar unsteady behavior as the experimental results. Good agreement was achieved in the prediction of the both the peak and integrated loss coefficient with over 85% agreement with the experimental measurements. The Walters and Leylek [2] k-k_L-ω transitional flow model successfully demonstrated the ability to predict the separated flowfield of Aft-Loaded L1A blade subjected to an unsteady traversing wake. This shows that the k-k_L-ω flow model can provide the same prediction capability for the more complicated unsteady flowfields found in a multistage LPT blade geometry.

D. Sanders   180
CFD Modeling of Separation and Transitional Flow in
Low Pressure Turbine Blades at Low Reynolds Numbers

CHAPTER EIGHT

8. Summary and Conclusions

The flowfields found in low pressure turbine stages are known to be affected by separation and transitional flow effects associated with operational situations and design factors. Separation and transitional flow can occur when LPT blades are subjugated to low Reynolds number flow effects due to the change in density associated with high altitude operation. Also, there is design pressure to increase the blade airfoil loading level in order to reduce weight and cost of the turbomachinery. Both factors lead to an increased probability of separated and transitional flow in turbine blade passages. High altitude operation and high stage work are known to affect the aerodynamic performance of the low pressure turbine stages. Laminar and transitional flow boundary layers may develop on the blade surface as result of both these situations. The increase in the region of adverse pressure gradients on the aft portion of the blade may cause the laminar flow boundary layer to separate from the surface. Also, the region of the boundary layer that undergoes laminar-to-turbulent boundary layer transition may increase. There is a need for CFD to provide improved prediction of separated and transitional flow for turbomachinary designs, especially for turbines operating at high altitude. The best CFD method must provide a balance between increased fidelity for accurate modeling of the complicated flow physics associated with low Reynolds number effects, and be applicable to complex geometries without being too computationally expensive.

The current study sought to use a selected CFD method to predict both laminar separation and transitional flow effects in low pressure turbine blades at low inlet Reynolds numbers, and to report the accuracy that was achieved. This CFD method was to be based on a RANS turbulence

CFD Modeling of Separation and Transitional Flow in
Low Pressure Turbine Blades at Low Reynolds Numbers

model that was developed to predict aerodynamic flow effects at low Reynolds numbers. Use of

the RANS CFD method was established as a requirement for this study because of its curren

wide adoption and computational efficiency with respect to LES and DNS CFD methods. This

study also sought to find the best RANS turbulence model already implemented into existing

CFD software, in other words, to establish the state of the art for practical CFD predictions of

low Reynolds number turbine flows. Ansys® Fluent was chosen as the CFD software and wide

adoption in the CFD community. Turbulence models available in Fluent were investigated to

determine if they could provide the flow prediction capability to complete the goals of this study.

The k-k_L-ω model developed by Walters and Leylek [2] to model the laminar-to-turbulent

boundary layer transition process was chosen as the turbulence model to complete this study.

Fluent CFD with the Walters and Leylek [2] k-k_L-ω model was applied to flow

predictions for three types of LPT blade airfoils for which cascade tests had been made in the

AFRL Low Speed Wind Tunnel. The LPT blade airfoils were classified based on the blade

loading characteristics defined using the Zweifel blade force coefficient, Z. Experimental flow

measurements of the surface static pressure, boundary layer flow velocities using Particle Image

Velocimetry, and wake losses were made in the cascade test over a wide range of Reynolds

number and freestream conditions. The CFD models simulated the same flow conditions, and

the predictions were compared to the corresponding experimental measurements for each LPT

blade airfoil. Also, additional comparisons were made with predictions available from other

CFD studies.

The Lightly Loaded LPT blade airfoil with $Z = 0.94$ representing a mid-loaded blade

design was used initially to determine the best choice of RANS turbulence model to complete the

objectives of this study. The inlet Reynolds number range of 10,000 – 100,000 was simulated

using the Lightly Loaded blade CFD model. Based on flowfield comparisons with the k-ω(SST) and k-ε models, the Walters and Leylek [2] k-k_L-ω model achieved the best agreement with experimental results for the prediction of the amount of viscous losses produced and the magnitude of the total pressure loss in the wake region. Good agreement was also obtained for the effect of Reynolds number sensitivity of the loss coefficient with the experimental results. Also, a parametric study on the effect of the inlet turbulent boundary conditions showed the inlet freestream turbulence intensity had a strong effect on the turbulent transition point and total pressure loss coefficient. A study on the effect of the inlet turbulent length scale showed a second order sensitivity effect to the turbulent transition location and the peak loss coefficient. The inlet turbulent length scale caused a 10% variation in the integrated loss coefficient due to the changes in the wake region. The boundary layer of the Lightly Loaded blade airfoil was mostly attached and transitional, and showed mild separation at the trailing edge at Reynolds numbers below 50,000 mainly due to its low blade loading level. The k-k_L-ω model successfully demonstrated that it could predict the low Reynolds number aerodynamic effects on the Lightly Loaded blade, and yielded confidence that it could provide same type of prediction capability for highly loaded LPT geometries.

The Walters and Leylek [2] k-k_L-ω model was applied to low Reynolds flow prediction for the Highly Loaded blade airfoil ($Z = 1.07$), an aft-loaded LPT blade design. Flowfield comparisons with experimental cascade data [36,38-40] showed good agreement in prediction of the separation and reattachment at inlet Reynolds numbers of 100,000, 50,000, and 25,000. The k-k_L-ω model showed a better qualitative response to the separated shear layers yet, the two-dimensional CFD predictions showed an over-prediction on the size of the separation region. So, a three-dimensional CFD model of the Highly Loaded blade was simulated to investigate the

addition of the spanwise dimension on the flowfield predictions. The observed unsteady vortex shedding was largely two-dimensional with small spanwise variations in the separation region and produced a similar prediction of the flowfield as the two-dimensional predictions. It is noted that the Walters and Leylek [2] k-k_L-ω model was not specifically design to model boundary layer transition in separated shear layers [30] or due to spanwise instabilities [2]. Yet, overall, it provided effective prediction of the low Reynolds number aerodynamic effects of the Highly Loaded blade.

The most challenging LPT blade design used for the application of the Walters and Leylek [2] k-k_L-ω model was the Aft-Loaded LIA blade airfoil. This geometry with a $Z = 1.23$, was 15% more loaded and had a much stronger adverse pressure gradient present on the aft portion of the suction surface than the Highly Loaded blade airfoil. Simulations were completed at individual inlet Reynolds numbers of 25,000 and 50,000 at low and high inlet turbulent intensities. At low inlet turbulent intensities, good agreement was achieved with experimental results on prediction of the separation locations and the qualitative flow response to the unsteady vortex generation from the separated shear layers. Also, over 80% agreement with the experimental [35] results was achieved in the prediction of the amount of viscous losses present within the wake region, but the higher dissipation predicted with the k-k_L-ω model caused those losses to be distributed more across the wake.

At high inlet turbulent intensities, the loading of the Aft-Loaded L1A blade airfoil was predicted effectively with over 87% agreement with the experimental results [35] for the integrated loss coefficient predictions. Yet, the size of the separation region was under-predicted and the unsteady effects from the vortex shedding were not present compared to the experimental results. The absence of unsteady vortex shedding could be attributed the Reynolds averaging

effect present within all RANS turbulence models where any unsteadiness produced from freestream turbulence will be significantly damped. Overall, the k-k_L-ω model did provide effective prediction of the aerodynamic flow effects for this very challenging LPT blade geometry, but some inaccuracies were observed at high inlet turbulent intensities. Yet, the k-k_L-ω model showed superior flowfield prediction capability compared to the fully turbulent k-ω(SST) model, similar to results obtained for the Lightly Loaded blade airfoil at the low inlet turbulent intensities.

The effect of a periodically passing upstream wake on the separation region of the Aft-Loaded L1A blade airfoil was studied using the k-k_L-ω model. A CFD model of the experimental cascade setup of Nessler *et al.* [37,48] was made to simulate the flowfield. The model and cascade test were designed to generate wake similar what are normally encountered in a multistage LPT geometry, where the wakes shed from one stage travel downstream and impinge on the successive stage. The flowfield of the wake generator was characterized, and the laminar boundary layer produced a von Karman vortex street in the wake region. Differences in the wake deficit were observed compared with the experimental results due the cylindrical wake generators used in cascade setup not being hydraulically smooth, and producing a turbulent boundary layer. Future work will investigate methods of tripping the boundary around the wake generator to turbulent in order to achieve closer agreement with experimental velocity deficit measurements. The addition of the wakes increased the Aft-Loaded L1A blade loading and caused the separation location to be moved further downstream compared to the baseline simulations. The separation region significantly reduced in size when it was impinged upon by the upstream wakes. The influence of the upstream wake caused lower total pressure loss and

improved the aerodynamic performance. Overall good agreement was achieved with the experimental PIV and loss coefficient measurements taken by Nessler *et al.* [37,48].

The prediction capability of Walters and Lekylek [2] k-k_L-ω model was characterized in the prediction of separation and transitional flow in LPT blade airfoils. Greater than 80% agreement with experimental results was achieved on the prediction of several flowfield parameters. The k-k_L-ω model provided good agreement for attached transitional flows in the prediction of the transition location, peak and integrated loss coefficient. When the flow was separated, good agreement was observed in the prediction of the separation location and the integrated loss coefficient. Also, the k-k_L-ω model qualitatively predicted unsteady vortex shedding at low turbulent intensity and the pressure distribution due to the separated shear layers. Differences were observed with less than 80% agreement in the prediction of separation region and the peak loss coefficient. Also, the spanwise variation of the separation region, the unsteady vortex shedding at high turbulent intensities was not well predicted using the k-k_L-ω model. The k-k_L-ω model main limitation was the absence of the unsteady behavior of the small-scale turbulent structures. The prediction capability of the Walters and Leylek [2] k-k_L-ω model is summarized in Table 8.1.

This dissertation has presented a complete evaluation of the Walters and Leylek [2] k-k_L-ω model for the prediction of low Reynolds number flows in low pressure turbine blades. The k-k_L-ω model accuracy was judged to be sufficient for understanding the separation and transition characteristics in the cases studied. The Walters and Leylek [2] k-k_L-ω model provided a more accurate method for aerodynamic loss predictions compared to conventional, widely used RANS turbulence models at low inlet Reynolds numbers. Successful flowfield predictions were

achieved with data from several low Reynolds number turbine flow applications. This research has contributed a characterized and assessed model for improved prediction of low Reynolds number turbine flows and design applications.

	Greater than 80% agreement	Less than 80% agreement
Attached Transitional Flow	Transition Location	
	Peak Loss Coefficient	
	Integrated Loss Coefficient	
Separated Flow	Separation Location	Peak Loss Coefficient
	Integrated Loss Coefficient	Separation Region
	Pressure Distribution	Spanwise Variation of the Separation Region
	Unsteady Vortex Shedding at Low Tu	Unsteady Vortex Shedding at High Tu
		Unsteady Behavior of the Small-Scale Turbulent Structures

Table 8.1. Summary of the prediction capability achieved using Walters and Leylek [2] k-k_L-ω model for the prediction of low Reynolds number effects

8.1   Future Work

Based on the results reported in this study, the Walters and Leylek [2] k-k_L-ω model was applied to a multistage LPT geometry based on the Lightly Loaded blade airfoil operating a low Reynolds numbers [52,53]. Steady flow simulations using the mixing plane numerical method were completed at both a nominal and high altitude operating conditions corresponding to an order of magnitude decrease in the inlet Reynolds number. This model provided a more detailed understanding of the aerodynamic loss mechanisms present in a multistage LPT operating at low Reynolds number. Experimental results are needed to fully validate the CFD predictions using

Chapter 8. Summary and Conclusions

the k-k_L-ω model technique for the multistage LPT geometry. Unsteady CFD simulations are also needed to compare with steady-state predictions using the mixing plane CFD technique.

Additional CFD work could include applying flow control techniques such as vortex generating jets and providing computational support for additional experimental work completed by Woods *et al.* [39] on the Highly Loaded blade airfoil. The CFD model would have to be three-dimensional in order to model the shape of the vortex-generating jet. It could also be used to simulate steady and pulsed jet operation. Additionally, CFD modeling using the k-k_L-ω model in plasma-based flow control could also be completed in support of future experiment that will be completed by Chris Marks at the AFRL LSWT. Since the electric field equations cannot be implemented into the Fluent CFD software, the effect of the plasma flow control can be modeled as an applied body force to the blade surface similar to Thompson [54] and could be used in both two and three-dimensional CFD models.

The Aft-Loaded L1A blade was the most challenging LPT blade airfoil geometry to predict low Reynolds number aerodynamic effects. Simulations could be completed using the more advanced LES CFD method to determine if it could provide better prediction capability compared to Walters and Leylek [2] k-k_L-ω model. This would be first time the LES CFD method would be applied to the Aft-Loaded L1A blade, and would give a unique contribution to low Reynolds number turbine prediction work.

Further improvements of the Walters and Leylek k-k_L-ω model can be explored in order enhance the prediction capability for transitional boundary layer flows. For instance, the k-k_L-ω model could be modified to account for transitional flow due to spanwise instabilities in three-dimensional CFD models. The laminar-to-turbulent transitional flow process is highly three-dimensional, and spanwise instabilities are known to cause initially laminar and coherent

vortices to breakdown into fine-scale turbulent structures [47]. Also, the k-k_L-ω model could be modified to account for transition due to separated flow by including correlations to model this effect such as those included in the Menter *et al*. [26] γ-Re_Θ model and the Praisner and Clark [24] models. The flowfields in both the Highly Loaded and Aft-Loaded L1A blade airfoils were dominated by separated flow and closer agreement with the experiments could likely be achieved if this modification were implemented in the k-k_L-ω model.

References

[1]   Sharma, O., "Impact of Reynolds Number on LP Turbine Performance". Minnowbrook II 1997 Workshop on Boundary Layer Transition in Turbomachines, NASA/CP-1998-206958, 1998.

[2]   Walters, D.K., and Leylek, J.H., "A New Model for boundary Layer Transition Using a Single Point RANS Approach", *Journal of Turbomachinery*, Vol. 126, January 2004, pp 193–202.

[3]   Halstead, D.E., D.C. Wisler, T.H. Okiishi, G.J. Walker, H.P. Hodson and H.W. Shin, "Boundary Layer Development in Axial Compressors and Turbines Part 1 of 4: Composite Picture." ASME Paper No. 95-GT-461, 1995.

[4]   Hodson H.P. and Dawes W.N., "On the Interpretation of Measured Profile Loses in Unsteady Wake-Turbine Blade Interaction Studies", ASME Paper No. 96-GT-494, 1996.

[5]   Dietz, A.J. and Ainworth, R.W., "Unsteady Pressure Measurements on the Rotor of a Model Turbine Stage in a Transient Flow Facility", ASME Paper No. 92-GT-156, 1992.

[6]   Langston, L.S., "Secondary Flows in Axial Turbines- A Review", *Annals of the New York Academy of Sciences*, pp. 11-26, 2001.

[7]   Munson, B.R., Young, D.F., and Okiishi, T.H., "Fundamental of Fluid Mechanics", 4th Edition, John Wiley & Sons, Inc., 2002.

[8]   White, F., "Fluid Mechanics", 4th Edition, McGraw-Hill, 1999.

[9]   Schetz J.A.,"Foundations of Boundary Layer Theory for Momentum, Heat, and Mass Transfer", Prentice –Hall, Inc., 1984.

[10]   VKI Lectures Series, "Advances in Laminar-Turbulent Transition Modeling", Wright State University, Dayton, OH, January 12-15, 2009.

[11]   Wilcox, D.C., "Turbulence Modeling for CFD", DCW Industries, Inc., 2005.

[12]   Cebeci, T., "Analysis of Turbulent Flows", 2nd Revised and Expanded Edition, Elsevier Publishing, 2004.

[13]   Tannehill, J.C., Anderson, D.A., and Pletcher, R.H., "Computational Fluid Mechanics and Heat Transfer", 2nd Edition, Tayler & Francis, In., 1997.

[14]   Enomoto, S., Hah, C., and Loelbach, J., "Numerical Investigation of a Low Reynolds Number Flow Field in a Turbine Blade Row", AIAA 2001-0524.

[15]   Singh, N., Ghia, K., and Ghia, U., "Simulation of Separated Flow inside a Low-Pressure Turbine Cascade", AIAA 2005-1273.

[16]   Rizzetta, D.P., and Visbal M.R., "Numerical Investigation of Active Flow Control for a Transitional Highly-Loaded Low Pressure Turbine", AIAA 2005-5020

[17]   Rizzetta, D.P., and Visbal M.R., "Numerical Investigation of Plasma-Based Flow Control for a Transitional Highly-Loaded Low Pressure Turbine", AIAA 2007-938.

[18]   Lake, J.P., "Flow Separation Prevention on a Turbine Blade in Cascade at Low Reynolds Number" *PhD Dissertation*, Air Force Institute of Technology, AFIT/DS/ENY/99-01, 1999.

[19]   Mittal, R., Venkatasubramanian, S., and Najjar, F.M., "Large-Eddy Simulation of Flow Through a Low-Pressure Turbine Cascade", AIAA 2001-2560.

[20] Raverdy, B., Mary, I., Sagaut, P., and Liamis, N., "High-Resolution Large-Eddy Simulation of Flow Around Low-Pressure Turbine Blade", *AIAA Journal*, Vol. 41, No. 3, March 2003, pp. 390-397.

[21] Sekar, S., and Voke, P.R., "Large-Eddy Simulation of Unsteady Surface Pressure Over a Low-Pressure Turbine Blade due to Interaction of Passing Wakes and Inflexional Boundary Layer", *Journal of Turbomachinery*, Vol. 128, April 2006, pp 221–231.

[22] Dorney, D.J., Lake, J.P., King P.I., and Ashpis, D.E., "Experimental and Numerical Investigation of Losses in Low Pressure Turbine Blade Rows", AIAA 2000-0737.

[23] Suzen, Y.B., Huang, P.G., Volino, R.J., Corke, T.C., Thomas, F.O., Huang, J., Lake, J.P., and King, P.I., "A Comprehensive CFD Study of Transitional Flows in Low-Pressure Turbines Under a Wide Range of Operating Conditions", AIAA Paper No. 2003-3591.

[24] Praisner, T.J., and Clark, J.P., "Predicting Transition in Turbomachinery, Part I – A Review and New Model Development", ASME Paper No. GT-2004-54108.

[25] Praisner, T.J., Grover, E.A., Rice, M.J., and Clark, J.P., "Predicting Transition in Turbomachinery, Part II – Model Validation and Benchmarking", *Journal of Turbomachinery*, Vol. 129, January 2007, pp 14 – 22.

[26] Menter, F.R., Langtry, R.B., Likki, S.R., Suzen, Y.B., Huang, P.G., and Volker, S., "A Correlation-Based Transition Model Using Local Variables- Part I: Model Formulation", *Journal of Turbomachinery*, Vol. 128, July 2006, pp 413 – 422.

[27] Langtry, R.B., Menter, F.R., Likki, S.R., Suzen, Y.B., Huang, P.G., and Volker, S., "A Correlation-Based Transition Model Using Local Variables- Part II: Test Cases and Industrial Applications", *Journal of Turbomachinery*, Vol. 128, July 2006, pp 423 – 434.

[28] Moore, J.G. and Moore, J., "High Turbulence Turbine Cascade Performance Using the MARV Reynolds Stress Model", AIAA 2009-1322.

[29] Holloway, D.S., Walters, D.K., and Leylek, J.H., "Prediction of Unsteady, Separated Boundary Layer over a Blunt Body for Laminar, Turbulent, and Transitional Flow", *International Journal for Numerical Methods in Fluids*, Vol. 45, March 2004, pp 1291-1351.

[30] Walters, D.K., and Leylek, J.H., "Prediction of Boundary-Layer Transition on Turbine Airfoil Profile Losses", ASME Paper No. IMECE 2003-41420.

[31] Walters, D.K., and Leylek, J.H., "Computational Fluid Dynamics Study of Wake-Induced Transition on a Compressor-Like Flat Plate", *Journal of Turbomachinery*, Vol. 127, January 2005, pp 52–63.

[32] Yocum, A.M., O'Brien W.F., "Separated Flow in a Low Speed Two-Dimensional Cascade: Part I- Flow Visualization and Time-Mean Velocity Measurements. *Journal of Turbomachinery*, Vol. 115, 409-420, 1993.

[33] Hill P., and Peterson C, "Mechanics and Thermodynamics of Propulsion" 2nd edition, Addison-Wesley Publishing Company Inc., 1992.

[34] McQuilling, M., "Design and Validation of a High-Lift Low-Pressure Turbine Blade", PhD Dissertation, Wright State University, Dayton, OH, August 2007.

[35] Marks, C., Sondergaard, R., Wolff, M., and Estevadeordal, J., "PIV Investigation of a Highly-Loaded LPT Blade Using a Curved Laser-Sheet", AIAA 2009-301.

[36] Garmoe, T.L., "Characterization of the GH1R Low Pressure Turbine" *Master Thesis*, Air Force Institute of Technology, AFIT/DS/ENY/05-S02, 2005.

[37] Nessler, C., Marks, C., Sondergaard, R., and Wolff, M., "Investigation of Losses on a Highly Loaded Low Pressure Turbine with Unsteady Wakes", AIAA 2009-302.

[38] Bons, J.P., Sondergaard, R., and Rivir, R.B., "Control of Low-Pressure Turbine Separation Using Vortex Generator Jets", AIAA 1999-0367.

[39] Woods, N., Sondergaard, R., McQuilling, M., and Wolff, M., "Investigation of Separation Control in Low Pressure Turbine using Pulsed Vortex Generator Jets", AIAA 2006-4450.

[40] Casey, J.P., "Effect of Dimple Pattern on the Suppression of Boundary Layer Separation on a Low Pressure Turbine Blade", *Master's Thesis*, Air Force Institute of Technology, 2004. AFIT/GAE/ENY/04-M05.

[41] Estevadeordal J., Gorrell S., Copenhaver W., "PIV study of wake-rotor phenomena in a transonic compressor under various operating conditions", *Journal of Propulsion and Power*, Volume 23, No. 1, pp. 235-242, Jan-Feb 2007.

[42] Curtis, E., Hodson, H., Banieghbal, M., Denton, J., Howell, R., and Harvey, N., "Development of Blade Profiles for Low-Pressure Turbine Applications", *Journal of Turbomachinery*. Vol. 119, 531-538, 1997.

[43] Clark, J. and Koch, P. "Benchmark Turbines for the Guidance of Design System Improvements", 2006 Turbine Engine Technology Symposium, Dayton, OH., September 14, 2006.

[44] Sondergaard, R., Rivir, R., Bons, J., "Control of Low-Pressure Turbine Separation Using Vortex Generator Jets", *Journal of Propulsion and Power*, Vol. 18, No. 4, pp. 889-895, 2002.

[45] Rizzetta, D.P., and Visbal M.R., "Numerical Investigation of Transitional Flow through a Low Pressure Turbine Cascade", AIAA 2003-3587.

[46] ANSYS Fluent® User's Manual Version 6.3.26, 2006.

[47] Visbal, M.R., "High Fidelity Simulations of Transitional Flows Past a Plunging Airfoil", AIAA 2009-391.

[48] Nessler, C., Marks, C., Sondergaard, R., and Wolff, M., "PIV Investigation of Periodic Unsteady Wakes over a Highly Loaded LPT Blade", AIAA 2009-5107.

[49] Schlichting, H., "Boundary Layer Theory", 6th Edition, McGraw-Hill Book Company Inc., 1968.

[50] Meyer R.X., "The Effect of Wakes on the Transient Pressure and Velocity Distribution in Turbomachines", *AMSE Journal of Basic Engineering*. Vol. 80, pp. 1544-1552, 1958.

[51] Hodson, H.P. and Howell, R.J., "Bladerow Interaction, Transition, and High-Lift Aerofoil in Low-Pressure Turbines", *Annual Review of Fluid Mechanics*. Vol. 37, pp. 71-98, 2005.

[52] Sanders, D.D., O'Brien, W.F., Sondergaard, R., Polanka, M.D., and Rabe, D.C., "A Mixing Plane Model Investigation of Separation and Transitional Flow at Low Reynolds Numbers in a Multistage Low Pressure Turbine", AIAA Paper No. 2009-1467.

[53] Sanders, D.D., O'Brien, W.F., Sondergaard, R., Polanka, M.D., and Rabe, D.C., "Turbulence Model Comparisons for Mixing Plane Simulations of a Multistage Low Pressure Turbine Operating at Low Reynolds Numbers", AIAA Paper No. 2009-4928.

[54] Thompson C.T., "Investigations and Simulation of Ion Flow Control over a Flat Plate and Compressor Cascade", M.S. Thesis, Virginia Tech, May 2009.

Appendix I. Comparisons of the Fluent Formulations of Walters and Leylek's Transitional Flow Model

As previous discussed in Section 4.3.1, an updated version of the k-k_L-ω model has been fully integrated in the newest software release as Ansys[®] Fluent 12.0. All of the Aft-Loaded L1A blade simulations were completed with the Fluent 12.0 k-k_L-ω model because Fluent 6.3 version was not implemented as to be used in combination with the sliding mesh model. This model was needed for the Aft-Loaded L1A blade with upstream wake generators simulation. The Lightly Loaded and the Highly Loaded blade airfoil were completed using the Fluent 6.3 k-k_L-ω model because it was the only version of the model that was available at the time of those simulations.

It was discovered through private conversations with Prof. Walters that the main difference between the two versions of the k-k_L-ω model was a tuning of the model constants and reformulations of some of the secondary equations. The model was reformulated because the Fluent 12.0 k-k_L-ω model consistently performed better for several of his CFD test cases. So, flowfield comparisons of the Aft-Loaded L1A blade were made using the different versions of the Walters and Leylek [2] k-k_L-ω model in order to understand the differences in the prediction flow transition and separation at low Reynolds numbers. Two-dimensional simulations were completed at Re = 50,000 at high and low inlet turbulent intensities and compared to experimental results of Marks *et al.* [35] and Clark *et al.* [25] CFD results.

A.1 Fluent Formulations of the k-k_L-ω Model

This section describes the two formulations of the k-k_L-ω model inherent in the Fluent CFD software. Walters and Leylek [2] k-k_L-ω model was first implemented as a beta addition to the Fluent 6.3 CFD software. It was learned that the k-k_L-ω model was not programmed to function in conjunction with the sliding mesh or mixing plane numerical methods. The k-k_L-ω model was fully integrated in the Fluent 12.0 release of the CFD software. The sliding mesh numerical method was needed for Aft-Loaded L1A blade simulations using the passing wake generators so the Fluent 12.0 formulation was used for Aft-Loaded L1A blade airfoil simulations. The next section presents the transport equations for each of the k-k_L-ω model formulations.

A.1.1 Fluent 6.3 k-k_L-ω Model

The transport equations for the Fluent 6.3 model for the turbulent kinetic energy (k_T), laminar kinetic energy (k_L), and the specific dissipation rate (ω) which were given as

$$\frac{Dk_T}{Dt} = P_{k_T} + R + R_{NAT} - \omega k_T - D_T + \frac{\partial}{\partial x_j}\left[\left(\nu + \frac{\alpha_T}{\sigma_k}\right)\frac{\partial k_T}{\partial x_j}\right] \tag{A.1}$$

$$\frac{Dk_L}{Dt} = P_{k_L} - R - R_{NAT} - D_L + \frac{\partial}{\partial x_j}\left[\nu\frac{\partial k_T}{\partial x_j}\right] \tag{A.2}$$

$$\frac{D\omega}{Dt} = P_\omega + C_{\omega R}\frac{\omega}{k_T}\left(R + R_{NAT}\right) - C_{\omega 2}\omega^2 - C_{\omega 3}f_\omega\alpha_T\left(\frac{\lambda_{eff}}{\lambda_T}\right)^{4/3}\frac{\sqrt{k_T}}{d^3} + \frac{\partial}{\partial x_j}\left[\left(\nu + \frac{\alpha_T}{\sigma_\omega}\right)\frac{\partial\omega}{\partial x_j}\right] \tag{A.3}$$

A detailed description of all the model variables and dependencies was given in Walters and Leylek [2]. The constants for the Fluent 6.3 formulation of the k-k_L-ω model are given in Table A.1.

Summary of Model Constants		
$A_0 = 4.04$	$C_{INT} = 0.75$	$C_{\omega1} = 0.44$
$A_s = 2.12$	$C_{TS,crit} = 1000$	$C_{\Delta P} = 0.15$
$A_v = 6.75$	$C_{R,NAT} = 0.04$	$C_{\omega3} = 0.3$
$A_{BP} = 3$	$C_{11} = 3.4\times10^{-6}$	$C_\lambda = 2.495$
$A_{NAT} = 60$	$C_{12} = 1.0\times10^{-9}$	$C_{\mu,std} = 0.09$
$A_{TS} = 200$	$C_R = 0.08$	$Pr_\theta = 0.85$
$C_{BP,crit} = 12$	$C_{\alpha,\theta} = 0.035$	$\sigma_k = 1$
$C_{NAT,crit} = 440$	$C_{\tau,1} = 4360$	$\sigma_\omega = 1.17$

Table A.1. Fluent 6.3 k-k_L-ω model constants

A.1.2   Fluent 12.0 k-k_L-ω Model

The transport equations for the Fluent 12.0 model for the turbulent kinetic energy (k_T), laminar kinetic energy (k_L), and the specific dissipation rate (ω) which were given as

$$\frac{Dk_T}{Dt} = P_{k_T} + R + R_{NAT} - \omega k_T - D_T + \frac{\partial}{\partial x_j}\left[\left(\nu + \frac{\alpha_T}{\sigma_k}\right)\frac{\partial k_T}{\partial x_j}\right] \tag{A.4}$$

$$\frac{Dk_L}{Dt} = P_{k_L} - R - R_{NAT} - D_L + \frac{\partial}{\partial x_j}\left[\nu\frac{\partial k_T}{\partial x_j}\right] \tag{A.5}$$

$$\frac{D\omega}{Dt} = C_{\omega1}\frac{\omega}{k_T}P_{k_T} + \left(\frac{C_{\omega R}\lambda_T}{\lambda_{eff}} - 1\right)\frac{\omega}{k_T}(R + R_{NAT}) - C_{\omega2}\omega^2 - C_{\omega3}f_\omega\alpha_T\left(\frac{\lambda_{eff}}{\lambda_T}\right)^2\frac{\sqrt{k_T}}{d^3} + \frac{\partial}{\partial x_j}\left[\left(\nu + \frac{\alpha_T}{\sigma_\omega}\right)\frac{\partial\omega}{\partial x_j}\right] \tag{A.6}$$

A detailed description of all the model variables and dependencies was given in the Fluent 12.0 User Manual [46]. The constants for the Fluent 12.0 formulation of the k-k_L-ω model are given in Table A.2.

Summary of Model Constants		
$A_0 = 4.04$	$C_{INT} = 0.75$	$C_{\omega 1} = 0.44$
$A_s = 2.12$	$C_{TS,crit} = 1000$	$C_{\omega 2} = 0.92$
$A_v = 6.75$	$C_{R,NAT} = 0.02$	$C_{\omega 3} = 0.3$
$A_{BP} = 3$	$C_{11} = 3.4 \times 10^{-6}$	$C_{\omega R} = 1.5$
$A_{NAT} = 200$	$C_{12} = 1.0 \times 10^{-10}$	$C_\lambda = 2.495$
$A_{TS} = 200$	$C_R = 0.12$	$C_{\mu,std} = 0.09$
$C_{BP,crit} = 1.2$	$C_{\alpha,\theta} = 0.035$	$Pr_\theta = 0.85$
$C_{NC} = 0.1$	$C_{SS} = 1.5$	$\sigma_k = 1$
$C_{NAT,crit} = 1250$	$C_{\tau,1} = 4360$	$\sigma_\omega = 1.17$

Table A.2. Fluent 12.0 k-k_L-ω model constants

Both Table A.1 and A.2 showed that the model constants are significantly different for the both formulations of the k-k_L-ω model. Also, the transport equation for the specific dissipation rate (ω) has changed which indicates that distribution of specific dissipation should be different for each of the formulations. The next section compared the flowfield predictions obtained from both the Fluent 12.0 and 6.3 formulations of the k-k_L-ω model at high and low inlet turbulent intensities.

A.2 CFD Predictions at Low Inlet Turbulence intensity

The two-dimensional cascade CFD model of Aft-Loaded L1A blade airfoil (Fig. 3.5(c)) was simulated at an inlet Reynolds number of 50,000. Unsteady simulations were ran using both Fluent versions of the k-k_L-ω model at $Tu = 0.5\%$ with an inlet turbulent length scale, $l_m = 50mm$. The next sections present the comparisons of the static pressure coefficient, boundary layer profiles, and total pressure loss coefficient with the experimental measurements taken by Marks et al. [35] in the LSWT. Also comparisons were made with CFD result of Clark et al. [25] which used the Prasnier and Clark [24] correlation based transitional flow model. A total of

*CFD Modeling of Separation and Transitional Flow in
Low Pressure Turbine Blades at Low Reynolds Numbers*

191,589 and 221,549 time-steps were used for averaging of mean flow quantities with the Fluent 6.3 and 12.0 version of the k-k_L-ω model using time step of 2 μsec.

A.2.1   Mean Surface Static Pressure Coefficient

In Figure A.1, the mean static pressure coefficient distributions were compared to the measurements of Marks *et al.* [35] and CFD results of Clark [25].   At the Re = 50,000, both Fluent versions of the k-k_L-ω model results showed good agreement to the 55% and 42% axial chord suction surface location with Clark's [25] CFD and experimental results, respectively. There was only a slight difference in the predicted static pressure distribution to the 80% axial chord location using both versions of the k-k_L-ω model. The Fluent 6.3 k-k_L-ω model predicted a higher local pressure peak at the approximately 82% axial chord location compared to the Fluent 12.0 k-k_L-ω model. The difference was attributed to the behavior of the vortices created from the separated shear layer as they moved downstream to the wake region.   Both k-k_L-ω model formulations predicted a lower peak pressure than the Clark [25] CFD result but both over-predicted the peak pressure compared to the experimental results.   The results indicated the prediction of the blade loading using the k-k_L-ω model was independent of the Fluent model formulation at low turbulent intensities.
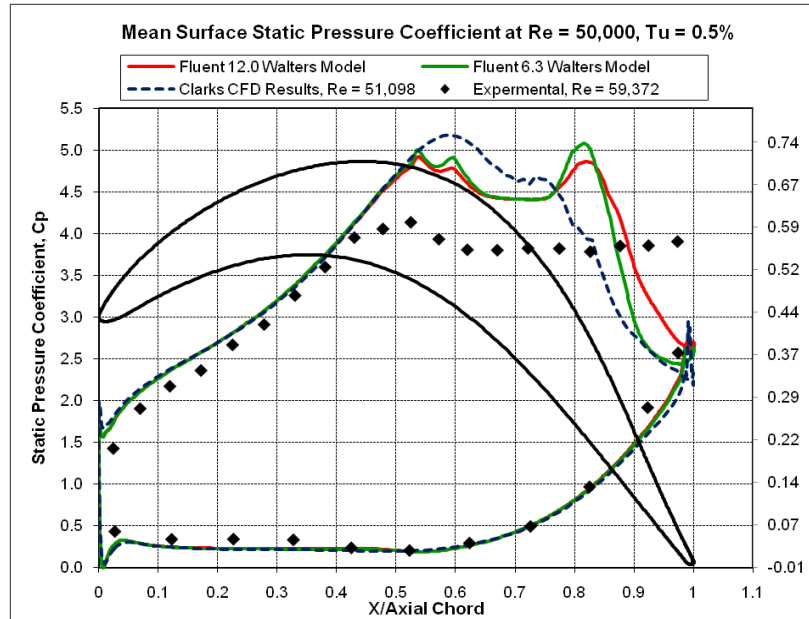
Figure A.1. The k-k_L-ω model formulation comparison of surface static pressure coefficient with Clark *et al.* [25] CFD simulations and experimental results [35] at Re = 50,000, Tu =0.5% for the Aft-Loaded L1A blade airfoil

A.2.2   Velocity Contours and Boundary Layer Profiles

Mean velocity magnitude contour plots from both version of the k-k_L-ω model were compared to the PIV contour plots taken by Marks *et al.* [35] in Figure A.2. All contour plots showed flowfields on the suction surface of the blade starting at approximately 50.0 - 94% axial chord location. Both of the k-k_L-ω model formulations predicted separated flow on the suction surface trailing edge as in the experimental [35] PIV result. The mean flow characteristics were very similar in both k-k_L-ω model predictions, but the Fluent 12.0 version did predict a slightly larger separation region. The contours plots indicated the size of the suction surface separation region was significantly under-predicted compared to the experimental [35] PIV result.
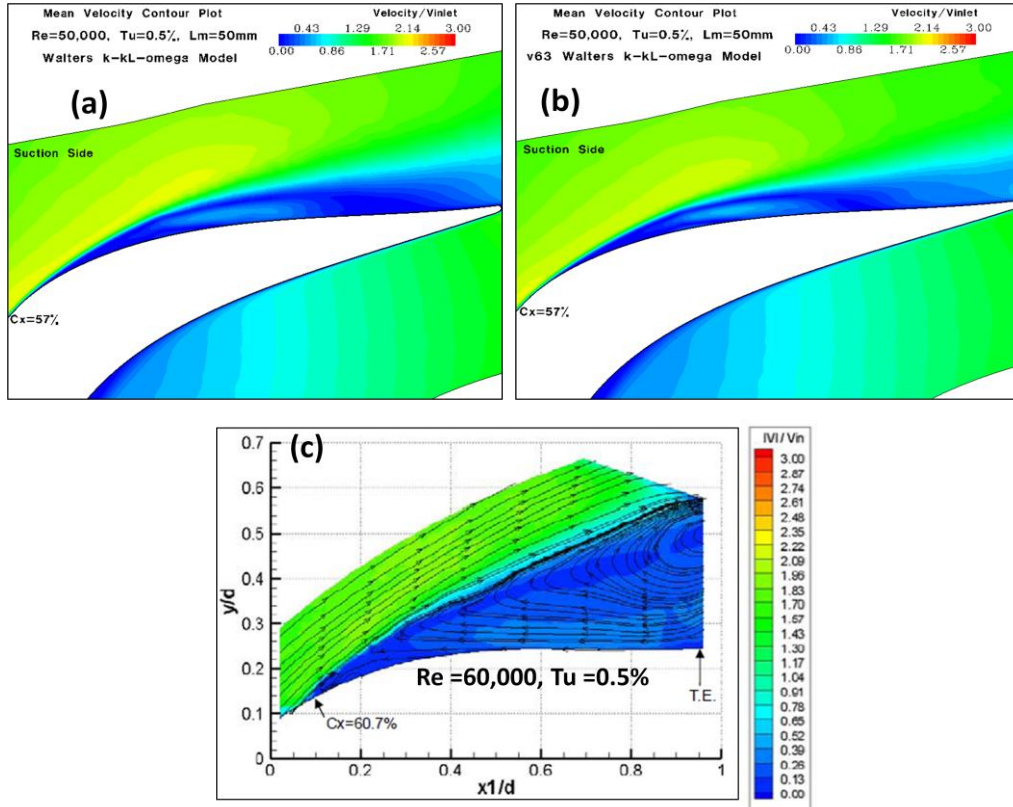
CFD Modeling of Separation and Transitional Flow in
Low Pressure Turbine Blades at Low Reynolds Numbers

Figure A.2. Mean velocity contours plots of the (a) Fluent 12.0, and (b) Fluent 6.3 formulation of the k-k_L-ω model at Re = 50,000, and (c) PIV results [35] at Re = 60,000, Tu = 0.5% for the Aft-Loaded L1A blade airfoil

The mean axial velocity boundary layer profiles confirmed the trends observed in the blade suction surface contour plot comparisons. Figure A.3 shows identical boundary layer profiles using both k-k_L-ω model formulations to the 60.4% axial chord location. The separation location for the Fluent 6.3 model result at 64.4% axial chord was more downstream than the Fluent 12.0 version of the k-k_L-ω model which was located at the 62.8% axial chord location. This resulted in a larger separation region starting at the 65.5% axial chord location (Fig A.3(a)) in the Fluent 12.0 k-k_L-ω model prediction. Figure A.3(b) shows the reversed flow present in the boundary layer extended to the 95% axial chord location in the Fluent 12.0 k-k_L-ω model prediction. This indicated that the Fluent 12.0 model formulation predicted a larger influence of the adverse pressure gradient on the aft portion of the blade, causing more reversed flow. Both

CFD Modeling of Separation and Transitional Flow in
Low Pressure Turbine Blades at Low Reynolds Numbers

model formulations under-predicted the separation region compared to the experimental results starting at the 60.4% axial chord location and continued for every downstream location (Fig. A.3(a)-(b)).
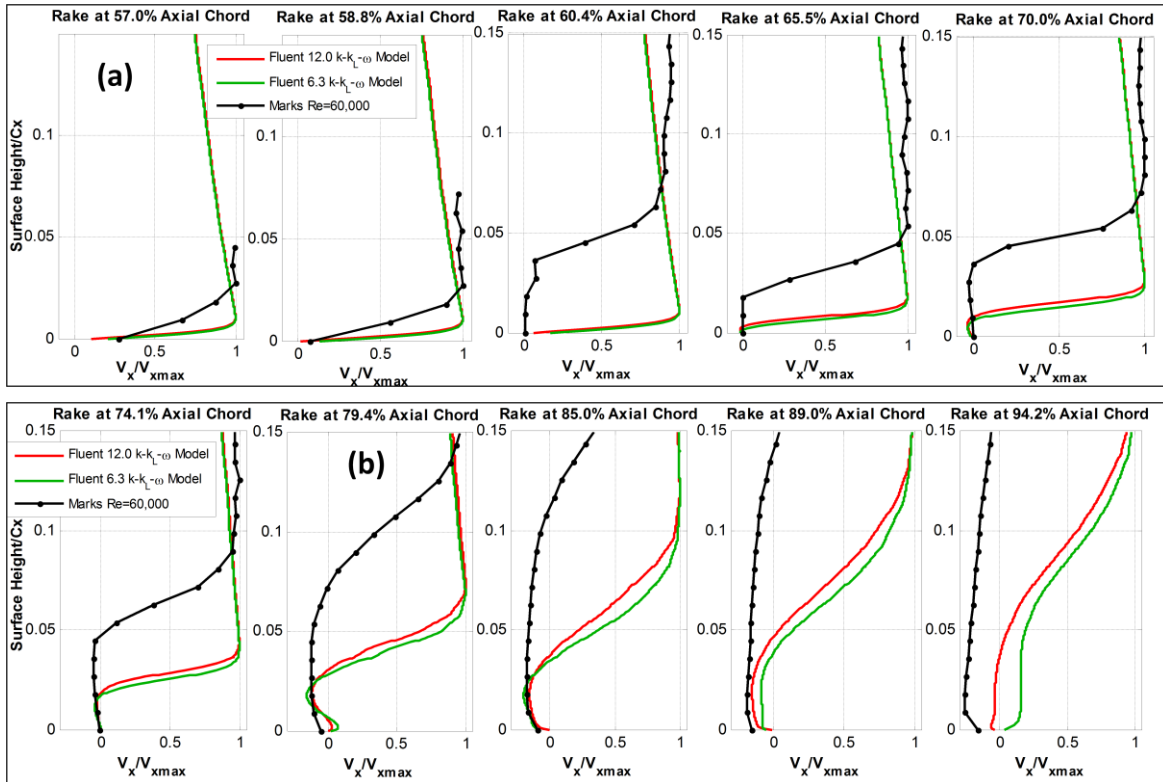

Figure A.3. The k-k_L-ω model formulation comparison of the mean axial velocity boundary layer profiles with experimental (Re=60,000) results [35] at inlet Re = 50,000, Tu = 0.5% for the Aft-Loaded L1A blade airfoil

A.2.3 Unsteady Features of the Flowfield

The k-k_L-ω model formulation comparisons were made in the prediction of the unsteady features of the flowfield. Instantaneous contour plots of vorticity were used to visualize the features of the flowfield as shown in Figure A.4. The overall unsteady vortex shedding behavior was similar for both the Fluent 12.0 and 6.3 versions of the k-k_L-ω model. The separated shear layer on blade suction surface consistently produced a clockwise vortex, while smaller counter-clockwise vortices were present beneath main vortex produced by the separated shear layer. The

CFD Modeling of Separation and Transitional Flow in
Low Pressure Turbine Blades at Low Reynolds Numbers

Fluent 12.0 k-k_L-ω model consistently produced slightly larger vortices from the suction surface shear layer. Also, the behavior of the small counter-clockwise vortices shed at the trailing edge was similar in both k-k_L-ω model formulations. The main difference between both k-k_L-ω model formulation was that the Fluent 12.0 k-k_L-ω model prediction extended the vortices across the wake region compared to the Fluent 6.3 k-k_L-ω model prediction.
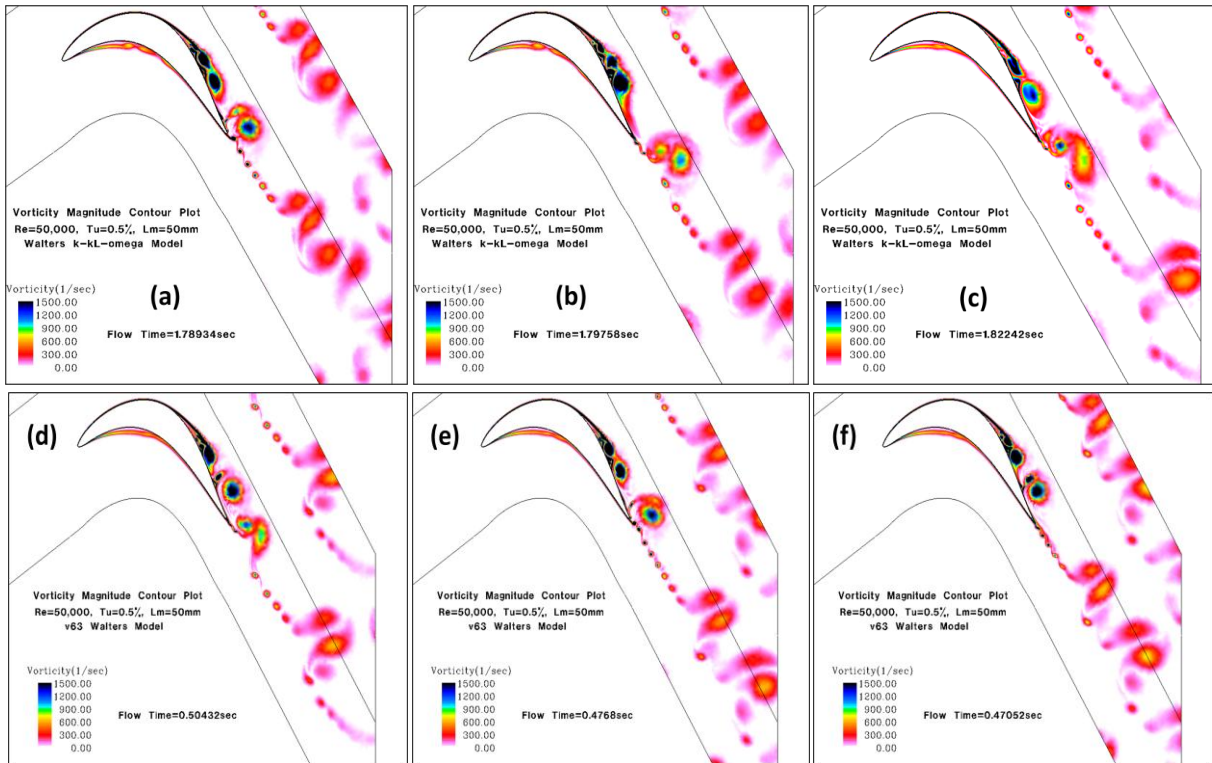

Figure A.4. Instantaneous vorticity contours at Re = 50,000, Tu = 0.5% for (a)-(c) Fluent 12.0 and (d)-(f) Fluent 6.3 of the k-k_L-ω model for the Aft-Loaded L1A blade airfoil

The time signal and the FFT of the drag coefficient were calculated for each simulation completed with the two k-k_L-ω model formulations. The frequency resolution was 2Hz and 3Hz for the Fluent 12.0 and Fluent 6.3 formulation of the k-k_L-ω model, respectively. Figure A.5(a) shows the unsteady behavior of the drag coefficient differed depending on which version of the k-k_L-ω model was implemented, which was attributed to the behavior of the vortex shedding. Yet

CFD Modeling of Separation and Transitional Flow in
Low Pressure Turbine Blades at Low Reynolds Numbers

when comparing the FFT calculation, it showed that each k-k_L-ω model formulations was in good agreement on the frequency peaks present in the FFT calculation, given the frequency resolution. This quantitatively confirmed the finding observed in the vorticity contour plots in Fig. A.4 that the prediction of the overall unsteady behavior of the vortex shedding at Re = 50,000 was similar for both k-k_L-ω model formulations.
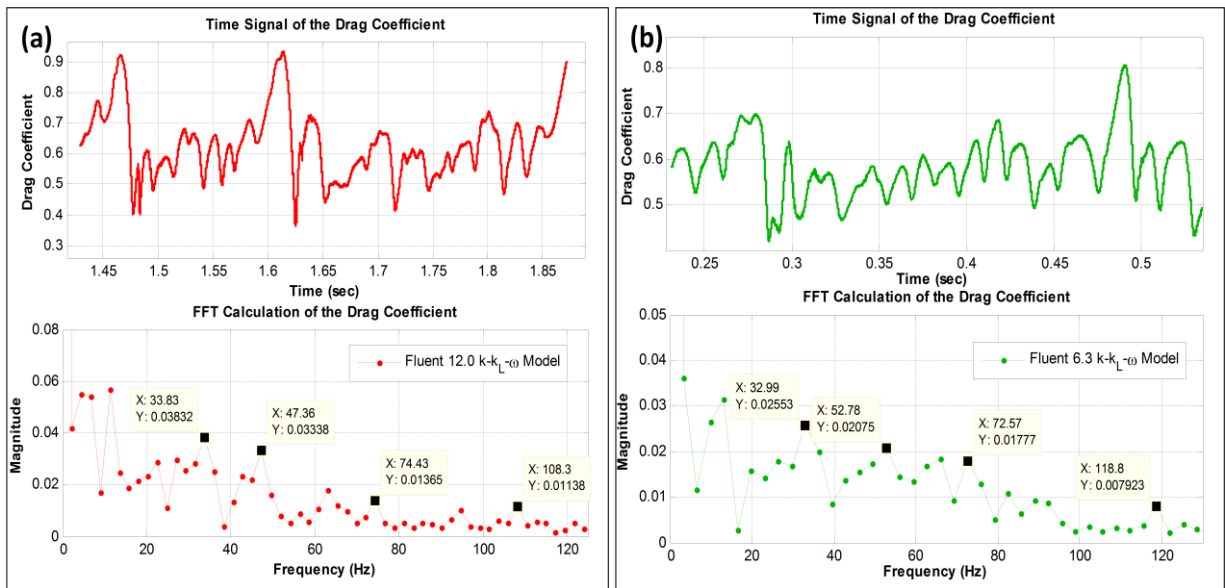

Figure A.5. Time signal and FFT calculation of the drag coefficient for the Aft-Loaded L1A blade airfoil using the (a) Fluent 12.0 and (b) Fluent 6.3 formulation of the k-k_L-ω model

A.2.4   Total Pressure Loss Coefficient

The total pressure loss coefficient obtained from both k-k_L-ω model formulations was compared to the experimental results of Marks *et al.* [35] as shown in Figure A.6. Both the formulations of the Walters and Leylek [2] k-k_L-ω transitional model significantly under-predicted the maximum value of the loss coefficient compared to the experimental results due to the over-prediction of the dissipation from the unsteady vortices in the wake region. The Fluent 6.3 k-k_L-ω model predicted a 14% higher value of the peak loss coefficient achieving 49% agreement with the experimental results compared to the Fluent 12.0 k-k_L-ω model prediction

CFD Modeling of Separation and Transitional Flow in
Low Pressure Turbine Blades at Low Reynolds Numbers

with 43% agreement. The distribution of the loss coefficient indicated that the Fluent 12.0 k-k_L-ω model predicted the effect of the wake to extend further across the wake region than the Fluent 6.3 k-k_L-ω model prediction.   Table A.1 shows that 81% agreement was achieved with the Fluent 12.0 k-k_L-ω model when comparing the integrated loss coefficient to the experimental results.   This indicated that the Fluent 12.0 k-k_L-ω model predicted an adequate amount of viscous losses, but the distribution of the viscous losses across the wake region was inaccurate.
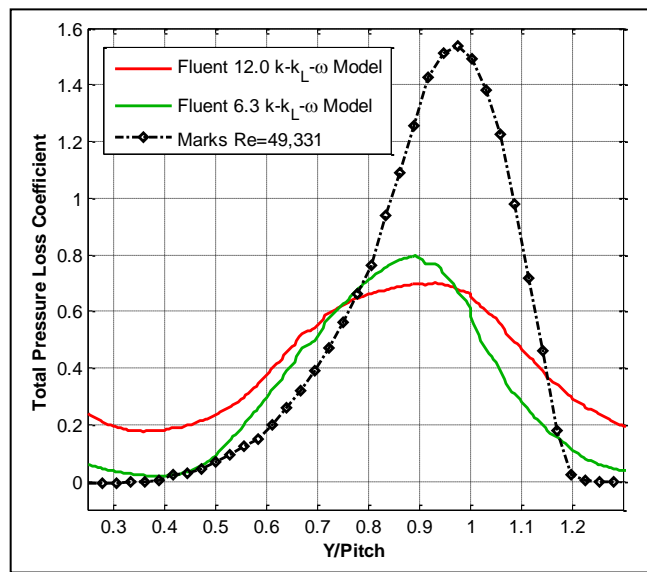

Figure A.6.   The k-k_L-ω model formulation comparison of total pressure loss coefficient with experimental [35] result at inlet Re = 50,000, Tu = 0.5% for the Aft-Loaded L1A blade airfoil

Re	Fluent Model	l_m(mm)	Integrated Loss Coefficient		Maximum Loss Coefficient	
			CFD	Marks *et al.* [35]	CFD	Marks *et al.* [35]
50,000	12.0	50	0.4131	0.5099	0.7001	1.5974
50,000	6.3	50	0.3434		0.7955	

Table A.3. Maximum and integrated total pressure loss coefficient comparison with the experimental [35] results at Re =50,000, Tu = 0.5% for the Aft-Loaded L1A blade airfoil

A.3 CFD Predictions at High Inlet Turbulence intensity

Unsteady simulations were completed at an inlet Tu = 3.4% using both formulations of the k-k_L-ω model at Re = 50,000. The inlet turbulent length scale was set as l_m = *4mm* for both simulations. Similar to the low turbulence intensity cases, comparisons were made using the static pressure coefficient, boundary layer profiles, and total pressure loss coefficient with the experimental measurements and Clark *et al.* [25] CFD results. A total of 11,000 time-steps using t_{step} = 10μsec were used for averaging of mean flow quantities with the Fluent 6.3 k-k_L-ω model simulation whereas the Fluent 12.0 simulation used a total 50,000 time-steps with t_{step} = 40 μsec.

A.3.1 Mean Surface Static Pressure Coefficient

The mean surface static pressure coefficient shown in Figure A.7 compared the blade loading predicted with the Fluent 12.0 and 6.3 formulations of the k-k_L-ω model at high inlet turbulence intensity. The Fluent 12.0 k-k_L-ω model predicted a similar pressure distribution due to flow separation and turbulent reattachment which was comparable to Clark's [25] CFD and the experimental [35] results. The closed separation region was indicated to be larger in the Fluent 12.0 formulation results as compared to the experimental [35] and Clark's [25] CFD results. The Fluent 6.3 k-k_L-ω model predicted a fully turbulent flow static pressure distribution with no indication of a separation bubble which was not observed in the experimental results. So, this indicated the Fluent 12.0 k-k_L-ω model provides more effective prediction of the Aft-Loaded L1A blade loading at this inlet turbulence intensity.
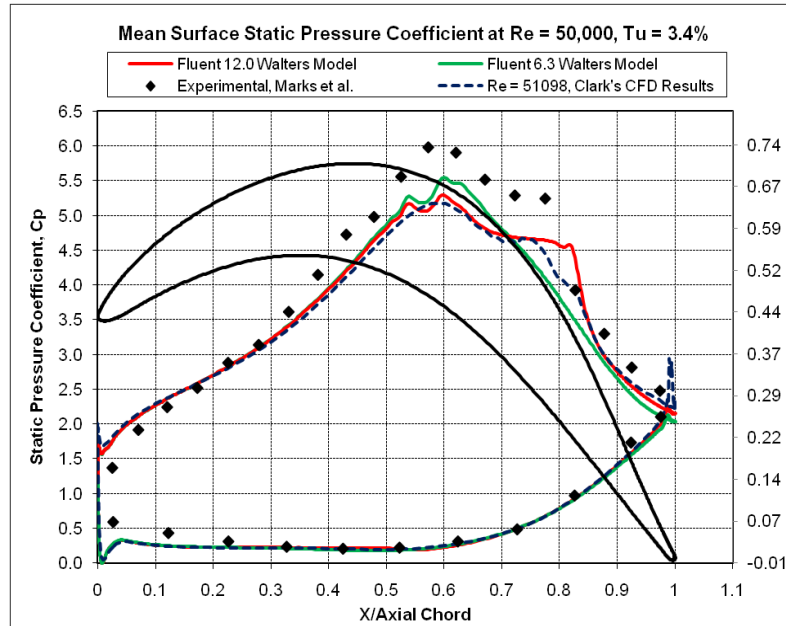
Figure A.7. The k-k_L-ω model formulation comparison of surface static pressure coefficient with Clark *et al.* [25] CFD simulations and experimental results [35] at Re = 50,000, Tu = 3.4% for the Aft-Loaded L1A blade airfoil

A.3.2 Velocity Contours and Boundary Layer Profiles

The velocity contours and boundary layer profiles were compared at high inlet turbulence intensity obtained from both formulations of the k-k_L-ω model. The velocity contours in Figure A.8(a) confirmed the presence of a closed separation region starting at approximately the 60% axial chord location in the Fluent 12.0 prediction which was observed in the experimental PIV contour plot in Figure A.8(c). The Fluent 6.3 k-k_L-ω model indicated an attached turbulent boundary layer which was not observed in the experimental results (Fig. A.8(b) & Fig. A.9). The boundary layer profiles for the Fluent 12.0 version of the k-k_L-ω model predicted the separation point at the 65.9% axial chord location and reattaching by the 89% axial chord location as shown in Figure A.9. The separation region was under-predicted in the Fluent 12.0 prediction compared to the experimental result [35]. The separation point was reported to be near 62% axial chord location. Reattachment occurred between the 79.4 and 85% axial chord

CFD Modeling of Separation and Transitional Flow in
Low Pressure Turbine Blades at Low Reynolds Numbers

position in the experimental [35] result, which was predicted to be more downstream in the

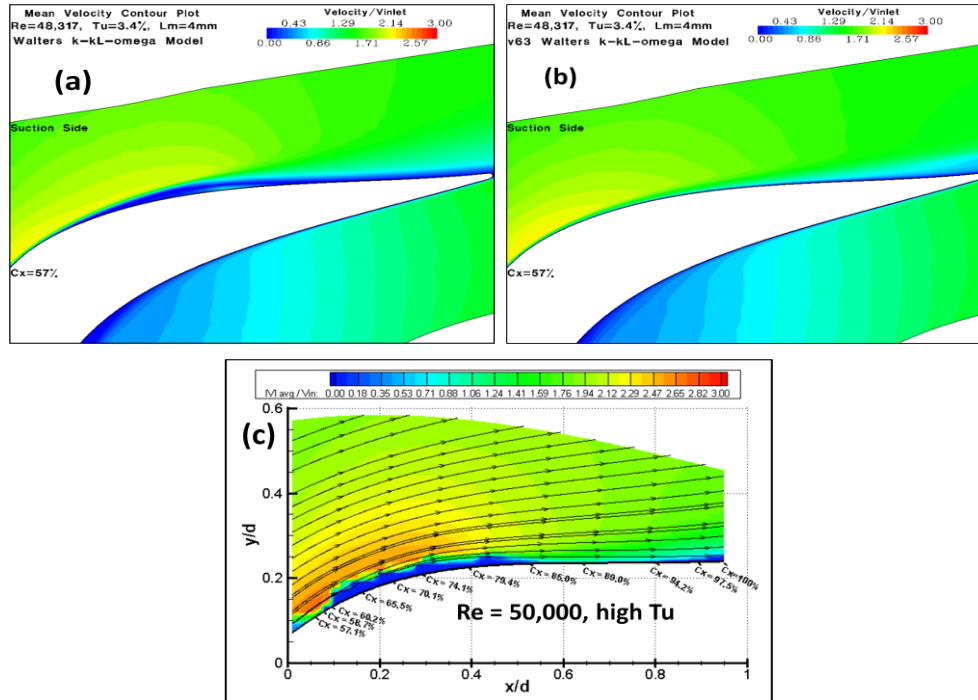Fluent 12.0 formulation of the k-k_L-ω model.

Figure A.8. Mean velocity contours plots of the (a) Fluent 12.0, (b) Fluent 6.3 formulation of the k-k_L-ω model and (c) PIV [35] results at Re = 50,000, Tu = 3.4% for the Aft-Loaded L1A blade airfoil
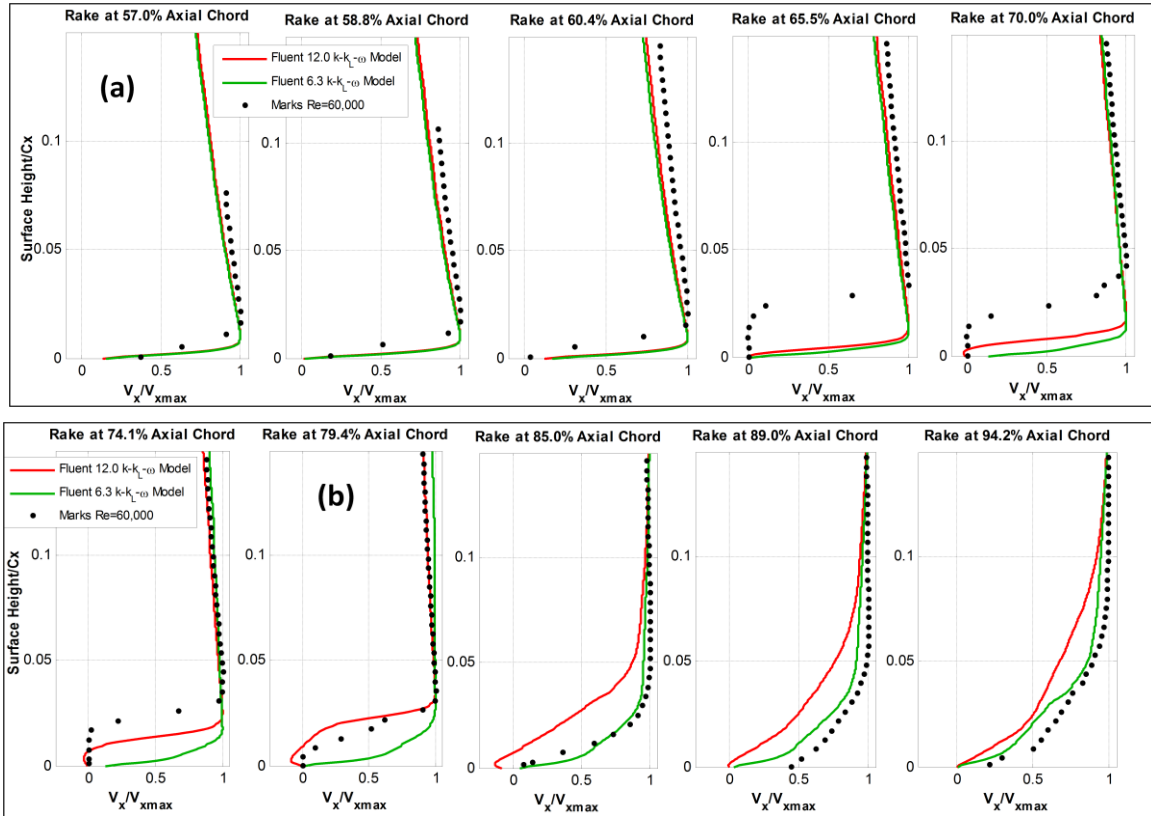
Figure A.9. The k-k_l-ω model formulation comparison of the mean axial velocity boundary layer profiles with experimental results [35] at inlet Re = 50,000, Tu = 3.4% for the Aft-Loaded L1A blade airfoil

A.3.3   Total Pressure Loss Coefficient

The total pressure loss coefficient obtained from both k-k_L-ω model formulations was compared to the experimental results of Marks *et al.* [35] as shown in Figure A.10. Both the formulations of the Walters and Leylek [2] k-k_L-ω transitional model significantly under-predicted the maximum value of the loss coefficient compared to the experimental results. The Fluent 6.3 k-k_L-ω model predicted a 34% higher peak loss coefficient and a narrower wake region compared to the Fluent 12.0 k-k_L-ω model. Better agreement to the experimental results of 63% was achieved in the integrated loss coefficient prediction with the Fluent 12.0 k-k_L-ω model.

CFD Modeling of Separation and Transitional Flow in
Low Pressure Turbine Blades at Low Reynolds Numbers

In summary, the Fluent 12.0 k-k_L-ω model was used in the Aft-Loaded L1A blade airfoil simulations because in gave similar flow predictions at the lower inlet turbulence intensity, and better agreement with the experimental results at the high inlet turbulence intensity. The difference in the prediction in the Fluent 12.0 and 6.3 the k-k_L-ω model was attributed the formulation of the transport equations in the k-k_L-ω model. The Lightly and Highly Loaded blade airfoil simulation completed with the Fluent 6.3 k-k_L-ω model were still considered valid because those simulation were done at a low inlet turbulence intensity where the Fluent 12.0 and 6.3 formulation of the k-k_L-ω model obtained similar results in the prediction of the flowfield.
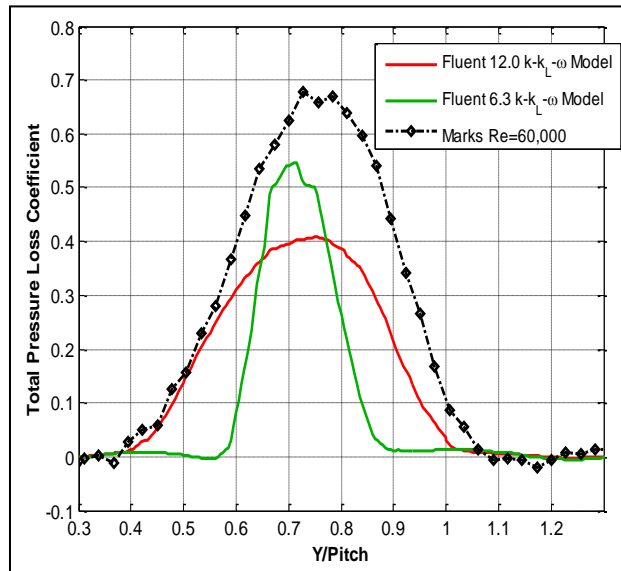

Figure A.10. The k-k_L-ω model formulation comparison of total pressure loss coefficient with experimental [35] result at inlet Re = 50,000, Tu = 3.4%, for the Aft-Loaded L1A blade airfoil

Re	Fluent Model	l_m(mm)	Integrated Loss Coefficient		Maximum Loss Coefficient	
			CFD	Marks *et al.* [35]	CFD	Marks *et al.* [35]
50,000	12.0	4	0.1502	0.2397	0.4083	0.6791
50,000	6.3	4	0.0944		0.5475	

Table A.4. Maximum and integrated total pressure loss coefficient comparison with the experimental [35] results at Re =50,000, Tu = 3.4% for the Aft-Loaded L1A blade airfoil